14 December 2002 | $10

Science

Reefs in TROUBLE

AAAS

EDITED BY STELLA HURTLEY AND PHIL SZUROMI

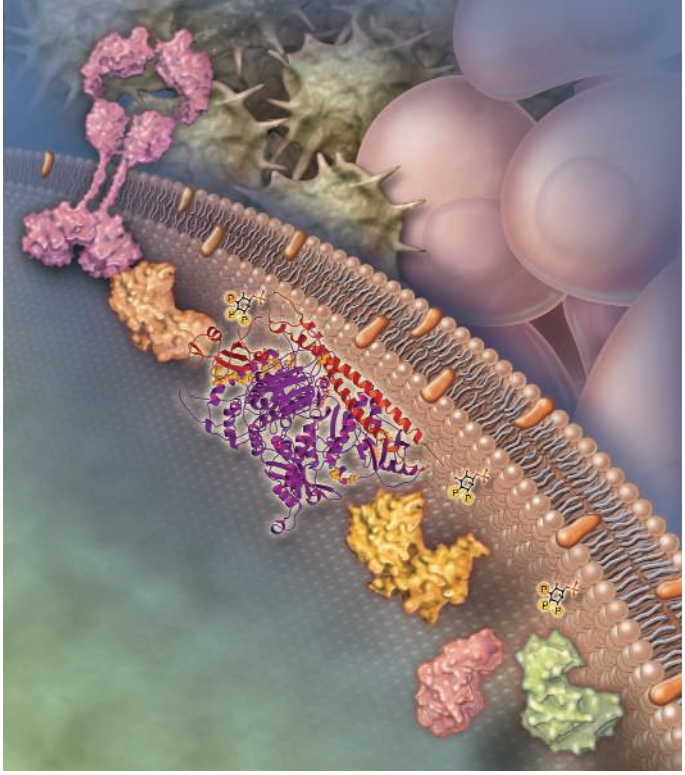

<< PIKing Oncogenic Mutations

Phosphoinositide 3-kinases (PI3Ks) are lipid kinases that can initiate a variety of signaling events. Many human cancers involve mutations that activate PI3Kα, a heterodimer comprised of a catalytic subunit, p110α, and a regulatory subunit, p85α, both of which contain multiple domains. **Huang *et al.*** (p. 1744) describe the crystal structure of a complex between the full-length human p110α catalytic subunit and the binding and activation domains of the p85α regulatory subunit. The structure provides insight into how oncogenic mutations affect enzyme activity and could assist in the future design of isoform- or mutation-specific inhibitors.

Deeper Understanding of the MJO

The Madden-Julian Oscillation (MJO) is a large-scale (1000-kilometer) atmospheric disturbance that propagates slowly eastward through the tropics from the Indian Ocean to the western Pacific during the course of 30 to 60 days. The MJO affects precipitation over the tropical monsoon regions and has been implicated as a trigger of El Niño–Southern Oscillation events. It is coupled with the upper ocean through its effects on surface fluxes of solar radiation caused by changes in cloudiness, and on evaporation from the ocean surface caused by surface wind speed changes, which can heat or cool the ocean mixed layer by up to 1°C during a strong MJO event. Nonetheless, important aspects of the MJO still are unclear, such as how deep into the ocean its influence extends, in part because the range of scales of the processes it involves have made it difficult to simulate in models (see the Perspective by **Hartmann and Hendon**). **Matthews *et al.*** (p. 1765) used a data set of unprecedented size obtained from autonomous, free-drifting instruments, called Argo floats, to show that the surface wind stress associated with the MJO can force eastward-propagating oceanic Kelvin waves that extend to a depth of 1500 meters and that have amplitudes of as much as six times those of annual-cycle Kelvin waves. These amplitudes are significantly greater than those predicted by ocean models, so that the MJO could affect a much larger volume of the Pacific Ocean than just the ocean surface. **Miura *et al.*** (p. 1763) address one of the shortcomings of contemporary global meteorological models—cumulus cloud parameterization—by using a model that allows direct coupling of atmospheric circulation and clouds to simulate an MJO event. Their results show that MJO predictions extending 1 month into the future soon may be possible.

Storing Light in Optic Fiber

Communication with optical pulses is fast, but direct storage of optical signals for later processing is challenging. There are routes for stopping and storing light that make use of quantum gases, but the wavelengths that can be used are fixed by the excitation levels of the atoms or ions of the gas. **Zhu *et al.*** (p. 1748; see the news story by **Cho**) show that stimulated Brillouin scattering can be used to write a sequence of optical pulses as an acoustic signal in a fiber and retrieve the signal on demand with a read pulse. Thus, variable delays can be achieved with commonly used components. The induced time delays are limited by the lifetime of the acoustic signal, but can be on the order of several nanoseconds. The authors also show that a small number of pulses can be stored simultaneously within the optic fiber.

Close-Ups of Phase Transitions

The study of phase transitions is often done with macroscopic probes that can average out some underlying microscopic inhomogeneities. **Qazilbash *et al.*** (p. 1750) report on the development of a new spectroscopic method that combines the high accuracy and sensitivity of spectral ellipsometry with the high spatial resolution of near-field microscopy. They used this method to study the metal-insulator transition in VO_2 and identified an inhomogeneous state with metallic and insulating regions near the transition regime. Within the metallic regions, they observed a divergent electron mass, an effect predicted by one of the competing scenarios of the transition in which correlation effects play a dominant role.

A Magnesium(I) Dimer

The partially reduced +1 state has rarely been observed for magnesium or any of its heavier alkaline-earth congeners, calcium, strontium, and barium. **Green *et al.*** (p. 1754, published online 8 November) used potassium metal to reduce a pair of Mg(II) compounds and thereby isolate and crystallographically characterize stable dimers in which two Mg(I) centers are connected by a single bond. Coordination of bulky bidentate nitrogen-based ligands helped stabilize these unusual complexes.

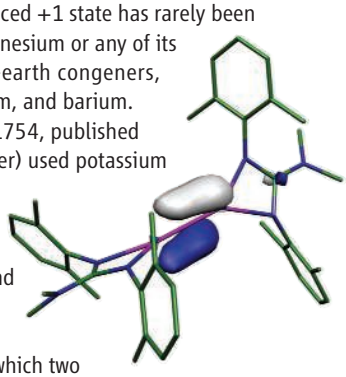

Mud Formation on the Move

Mudstones make up the majority of the geological record and have been thought to record the quies-

Continued on page 1693

CREDITS (TOP TO BOTTOM): LAUREN O'MALLEY; GREEN *ET AL.*

Published by AAAS

Continued from page 1691

cent conditions of offshore and deeper water environments. However, it is difficult to reconstruct the complex processes of mud deposition in the laboratory, such as the clumping of particles into floccules. Using flume experiments, **Schieber *et al.*** (p. 1760; see the Perspective by **Macquaker and Bohacs**) investigated the transport and deposition of clay floccules and find that this process occurs at flow velocities that transport and deposit sand. Floccules form and are deposited over a wide range of experimental conditions. The floccules form ripples that develop into mud beds and appear laminated after compaction. These results bear not only on interpretations of paleoenvironments that mudstones record, but also on current problems such as hydrocarbon exploration and the management of sediment accumulation.

Reefs Run to Rubble

With no immediate prospect of slowing anthropogenic climate change, the long-term outlook for the survival of coral reefs is bleak. **Hoegh-Guldberg *et al.*** (p. 1737; see the cover, the editorial by **Kennedy**, and the special News report) review three scenarios for the fate of coral reefs, none of which offer much solace for human societies dependent on their resources and protection. To maintain the status quo requires urgent implementation of conservation measures to reduce stress on corals, but even small further increases in atmospheric carbon dioxide could tip many reef systems into ecological and structural collapse.

Invasion of the Whitefly

Individuals of closely related but geographically isolated populations of organisms are often able to interbreed when brought together by human activities. **Liu *et al.*** (p. 1769, published online 8 November; see the Perspective by **Reitz**) report the behavioral mechanisms underlying the recent widespread, rapid invasion of the B biotype of the whitefly *Bemisia tabaci* in China and Australia. Biotype B is one of the top 100 invasive species in the world and is more harmful to crops than other biotypes. Asymmetric mating between closely related but previously geographically separated biotypes appears to drive the invasion of alien populations. Contrary to expectation, the indigenous individuals helped to increase the competitiveness of the invaders and accelerated the process of invasion and displacement.

Human Impacts on Fish and Frogs

Farmed fish are reared under conditions that promote transmission of pathogens among the stock, notably crustacean parasites called salmon lice. Salmon lice are highly damaging to juvenile salmon and can cause in excess of 90% mortality. **Krkošek *et al.*** (p. 1772; see the news story by **Stokstad**) now show that fish farms are a fatal source of salmon lice infestation to juvenile fish off the coast of Canada and are rapidly driving populations of wild fish to extinction in some rivers. A concerted decline in amphibian populations and species worldwide has been evident for at least a decade. Various causes have been implicated, including fungal disease, habitat loss, and pollution. **Becker *et al.*** (p. 1775) show that in the Brazilian Atlantic Forest, amphibian population loss is determined by the mismatch in the landscape between the location of aquatic breeding sites and the remnants of natural terrestrial vegetation across which they migrate. This result helps explain why population declines are biased toward amphibian species with aquatic larvae and suggests that conservation management of riverside vegetation could help to reduce the rate of amphibian decline.

Serine and the CTD Code

The carboxyl-terminal domain (CTD) of the large subunit of mammalian polymerase II (pol II) has a unique structure comprising 52 repeats of a consensus serine-rich heptapeptide. Phosphorylation of serine-2 and serine-5 is known to be critical for cotranscriptional RNA processing steps that are required for maturation of pol II transcripts (see the Perspective by **Corden**). **Chapman *et al.*** (p. 1780) use monoclonal antibodies to show that serine-7 is phosphorylated on transcribed genes, and **Egloff *et al.*** (p. 1777) show that this phosphorylation event plays a specific role in recruitment of the Integrator complex to genes for noncoding small nuclear RNAs. This gene type–specific requirement for a residue within the CTD heptapeptide reinforces the notion of a CTD code.

CREDIT: ALEXANDRA MORTON

Published by AAAS

Donald Kennedy is the Editor-in-Chief of *Science*.

Year of the Reef

THE CORAL REEFS OF THE WORLD, ON WHICH THE NEWS FOCUS SECTION OF THIS ISSUE OF *Science* concentrates, are important for all sorts of reasons. For many, exploration by diving provides a unique connection with a fascinating natural ecosystem. For scientists, including climate scientists, the health of reefs provides insight into the physical and biological welfare of the oceans as a whole. And for conservation biologists, shallow-water reefs are remarkable hot spots of biodiversity; those that surround oceanic islands often include a level of specialized endemic species that rivals that on the islands themselves. But the corals of the world are in trouble, and that's why we need the International Year of the Reef (IYOR) in 2008.

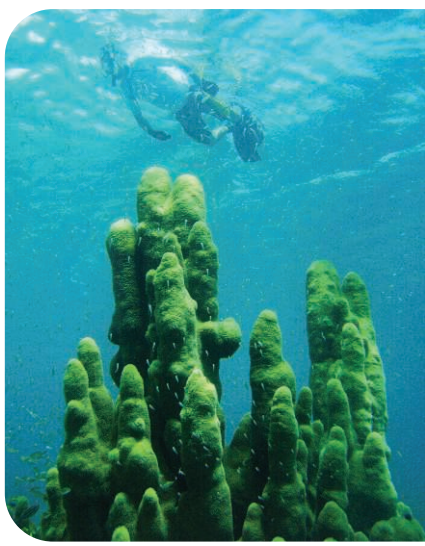

There are two problems, both of them serious. The addition of carbon dioxide and other greenhouse gases to the atmosphere has altered both the ocean's temperature and its acidity. Because most shallow-water corals exist near their temperature optimum, some are becoming heat-bleached. The more problematic concomitant of climate change is that when carbon dioxide is absorbed by the oceans, as 30% of global industrial production is, it forms bicarbonate and hydrogen ions, which lower ocean pH and threaten the carbonate structure of the reef with dissolution. Since the industrial revolution, average ocean pH has been reduced by about 0.1 unit, and models predict further loss of 0.3 or 0.4 unit by the end of the century. Thomas Lovejoy, president of the H. John Heinz III Center for Science, Economics, and the Environment, calls it "the single most profound environmental change I've learned about in my entire career." In Australia, which has the best-managed reefs in the world, the Institute of Marine Science conducts continuous monitoring to document these changes.

If only those were the only problems. In many areas, coral reefs that are unprotected or inadequately protected are being harvested. In Indonesia 10 years ago, the minister of the environment showed me a video taken of poachers applying cyanide to a reef to harvest stunned but living Napoleon wrasse and other delicacies bound for upscale restaurants in Hong Kong and Singapore. Other harvesters are after species of *Corallium*, the beautiful living red or pink corals that are traded globally. Because the United States imports 60% of that commodity, mainly for use as aquarium decorations, we ought to be pushing to have them listed for sanctions.

Given the reasons for caring about coral and the threats to its survival, it's not surprising that a large number of people and organizations are interested in reef protection. The IYOR has gathered interest and support from many of these. SeaWeb, a long-lived and effective conservation group, has a strategy of teaming with fashion editors and journals to remind everyone that coral is "too precious to wear" as jewelry. Although shallow reefs are the central concern, a symposium at next year's annual meeting of the American Association for the Advancement of Science will address the role of deep-sea corals, species that are under threat from disruption by bottom trawling or other harvesting.

Some good things are happening already. The U.S. House of Representatives passed, on 22 October, the Coral Reef Conservation Act (H.R. 1205). A Senate bill is out of committee. Final legislation should include strict provisions regulating coral trade, and scientists should continue to make recommendations, including supporting a listing of corals under the Convention on International Trade in Endangered Species (CITES), denied last year by secret ballot in The Hague. Alas, the next Conference of the Parties to CITES won't happen till 2010.

Scientists meanwhile have some good work to do. Data on monitoring and changes in status, along with modeling predictions of temperature and pH effects, should be brought to governments and the public. The failure to gain a CITES listing through political efforts should be rectified. Finally, the United States could grab the front end of the problem by taking serious steps to mitigate carbon dioxide emissions: the root cause of global warming and the reef problem. Experience suggests that for this, we might have to await an election.

– Donald Kennedy

10.1126/science.1153230

CREDIT: ANDY ARRISON

Spores produced from a fungus-infected ant.

BEHAVIOR

Prosocial Ants

The threat from infectious diseases is a major concern not only for humans but also for other highly social animals. Organisms that live in close quarters are particularly susceptible to infection because of the intrinsically favorable disease transmission dynamics; hence, systems that prevent or ameliorate the spread of disease are likely to be beneficial. Indeed, social insects have evolved a number of behaviors—for example, nursing sick individuals or excluding them from the nest—that help to limit the spread of infection. Uglevig and Cremer demonstrate that in small colonies of the garden ant *Lasius neglectus*, introducing workers infected with living fungal spores (but not dead spores) promptly produced two changes in behavior. First, the infected ants almost immediately reduced their interaction with ant larvae in the brood chamber, apparently helping to protect the most valuable or susceptible individuals in a colony. The absence of aggression by uninfected worker ants toward afflicted individuals suggests that such standoffishness may be due to self-restraint. Second, the uninfected workers increased their brood-care activities, primarily via grooming to remove spores from the infected individuals. Rather than increasing their own incidence of infection, the naïve ants acquired a higher level of resistance to the fungus—providing a form of "social prophylaxis." — GR

Curr. Biol. **17,** 1967 (2007).

MATERIALS SCIENCE

Extra-Strong Sleeves

The sponge-like structure of metallic foams (up to 80% void fraction) has fostered applications in impact-absorbing materials, acoustic insulation, and lightweight structural materials. More recent attention has focused on periodic cellular materials (PCMs), wherein the remaining mass exclusively forms load-bearing trusses that are loaded in tension or compression rather than bending. A second design strategy for strengthening metals is to reduce grain size to the nanometer scale and thereby localize a larger number of atoms at grain boundaries, reducing their mobility. Suralvo *et al.* created a PCM by stretching a square punched aluminum sheet to displace half the nodes above and the other half below the initial starting plane. They then electroplated a nanocrystalline alloy of nickel and iron to form a sleeve around the struts and nodes of the trusses, with the thickness controlled over a 75- to 400-μm range by the deposition time. The loading stiffness more than doubled and the peak strength increased 10-fold. The specific strength, which accounts for changes in density, also increased almost threefold. — MSL

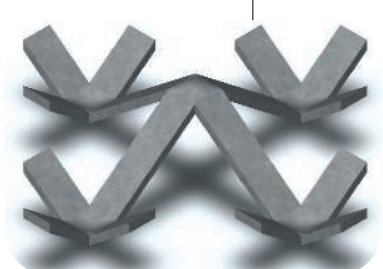

Scripta Mater. **58**, 247 (2008).

CELL BIOLOGY

Live Long and Prosper

Autophagy, the degradation of intracellular components that occurs in response to starvation, is also important in the response to stress and in development and disease—both as a defense mechanism and as a pathological consequence. Simonsen *et al*. found that *Drosophila* lacking key autophagy-related genes had a reduced life span, and then went on to examine to what extent the promotion of autophagy in the nervous system could affect aging. During aging in the normal fly, the levels of autophagy within neurons fall, leading to the accumulation of ubiquitinated protein aggregates. By increasing the levels of expression of an autophagy-related gene, *Atg8a*, in aging neurons, the authors were able to increase adult life span by more than 50% and saw a concomitant reduction in the levels of ubiquitinated aggregates in the aging brains. Further, these engineered flies were also more resistant to oxidative stress. — SMH

Autophagy, in press: www.landesbioscience.com/journals/autophagy/article/5269

ECOLOGY/EVOLUTION

Disturbing Patterns

Forest habitats around the world vary widely in the nature of the influence that humans have had on them. Some forests are primary (more or less undisturbed), others are secondary (regrown after human disturbance), and some are entirely artificial (plantations). In our era, the balance of forested area tilts ever more to the secondary and managed end of the spectrum. In this context, Barlow *et al.* assessed the conservation value of primary, secondary, and plantation forests in the tropics by comparing the species richness of major invertebrate, vertebrate, and plant taxa across replicated sites in Amazonia. A range of patterns was observed. A few taxa (scavenger flies, moths, and grasshoppers) appeared to be more species-rich in the secondary and plantation forests; unsurprisingly, at the other extreme, amphibians, birds, and woody plants were far better represented in the undisturbed forest; small mammals, orchid bees, and fruit flies appeared to be relatively unaffected by habitat type. These data help to

Continued on page 1699

CREDITS (TOP TO BOTTOM): UGLEVIG AND CREMER, *CURR. BIOL.* 17, 1967 (2007); SURALVO *ET AL.*, *SCRIPTA MATER.* 58, 247 (2008)

Published by AAAS

Continued from page 1697

build a picture of the consequences of land-use change for biodiversity in the tropics and elsewhere, and to suggest ways of ameliorating its effects. — AMS

Proc. Natl. Acad. Sci. U.S.A. **104**, 18555 (2007).

BIOPHYSICS

Congested Corpuscles

Sickle cell disease results from a mutation in the gene encoding the β chain of hemoglobin; the mutant protein tends to polymerize, especially so in its deoxygenated form. The extended polymers (HbS) forcibly alter the elasticity of the red blood cell, changing it from a biconcave disc into the sickle shape that gives the condition its name. One outcome is a logjam of corpuscles (known as a vascular occlusion) in small blood vessels. Although there is a clear link between occlusion and the irregular shape of the sickle red blood cell, other factors are likely to influence the process as well. To test for the minimal

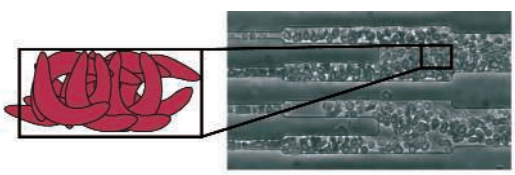

Microfluidic occlusion of HbS cells.

requirements for occlusion events in the absence of inflammation or coagulation, Higgins *et al.* have developed a microfluidic device that allows independent control of geometry (channel size), physics (applied hydrostatic pressure), and chemistry (oxygen tension) under conditions of steady flow. The times to occlusion and resolution (de-occlusion) were measured and used to generate a phase-space representation, revealing that the capacity of blood cells to flow through capillaries was determined by the mechanical properties of the cell and by geometric and hydrodynamic factors. The device was also used to quantitate the improvement in blood flow in samples taken from a patient before and after infusion of (normal) HbA-containing erythrocytes. — SJS

Proc. Natl. Acad. Sci. U.S.A. **104**, 10.1073/pnas.0707122104 (2007).

APPLIED PHYSICS

Tinker-Free Interferometry

The interference of waves, be they photons, atoms, or electrons, and the measured phase shift induced as the waves take a different route around the arms of an interferometer are widely used in applications ranging from global positioning systems and gravity wave detectors down to the more mundane characterization of optical materials. The sensitivity of the interferometer in measuring the phase shift is affected by noise contributions to the signal. To combat this noise, piezoelectric actuators are typically used to adjust the system to an optimum measuring point for maximum sensitivity. This approach has drawbacks, however, for certain applications where the determination of arbitrary phase shifts is important. Pezzé *et al.* introduce a method and protocol of photon counting at the output paths to determine the phase. They show that the classical, or thermal, noise can be eliminated without bias (i.e., no tinkering with the phase shift is necessary). At this quantum limit, only quantum uncertainty affects the precision of the phase measurement. — ISO

Phys. Rev. Lett. **99**, 223602 (2007).

Science STKE AAAS

www.stke.org

<< Looking After Polysialic Acid

In some cases, the effects of neuronal activity are restricted to particular developmental stages. For instance, the loss of visual input from one eye early in life leads to a shift in the responsiveness of neurons in the visual cortex toward the functional eye. The onset and time course of this critical period for ocular dominance plasticity are influenced by the maturation of GABAergic innervation, which is itself regulated by visual input and neuronal activity. Di Cristo *et al*. found that polysialic acid [PSA, a homopolymer of sialic acid that attaches to neural cell adhesion molecule (NCAM) and modulates intercellular bonds] and NCAM were abundant in the neonatal mouse visual cortex but that PSA underwent a steep decline after eye opening. Pups reared in the dark showed increased PSA as compared with pups reared under conventional light/dark cycles. Injection of endoneuramidase (which cleaves off PSA) into the visual cortex promoted both perisomatic GABAergic innervation and the frequency of miniature inhibitory postsynaptic currents. Moreover, it stimulated the early onset of the critical period for ocular dominance plasticity. Thus, maturation of GABAergic inhibition—and thereby the initiation of ocular dominance plasticity—is regulated by an activity-dependent decrease in PSA. — EMA

Nat. Neurosci. **10**, 1569 (2007).

CREDIT: HIGGINS *ET AL., PROC. NATL. ACAD. SCI. U.S.A.* **104**, 10.1073/PNAS.0707122104 (2007)

Tiger tracked to this 2002 poster.

Flat Cat: Act II

Suspicions about purported photographs of a presumed-extinct South China tiger (*Science*, 9 November, p. 893) were confirmed last month when a netizen found the apparent source of the image: a 2002 Chinese lunar New Year poster. But China's obsession with the issue has continued. The China Photographers Association convened a team including biologists and forensic scientists who met in Beijing for 5 days pondering 40 digital photos of the beast. On 2 December, they noted, among other things, that the tiger was in exactly the same position in all the photos and that its eyes did not reflect the camera's flash.

Both the photographer and the State Forestry Administration (SFA), however, continue to maintain that a tiger exists in the mountains of Zhengping County. At a 4 December press conference, an SFA spokesperson reiterated that the agency plans to look for it. After the first snowfall, 10 large-carnivore experts will comb a 200,000-hectare forested region for signs of tigers, leopards, and bears. As for the photos, an SFA official offered this logic: "There are a lot of photographs of the Loch Ness monster [in Scotland]. … People care about the existence of the monster rather than the authenticity of the photos."

MIT: Completely Online

It took 5 years, but the Massachusetts Institute of Technology in Cambridge has put all its courses online. Free materials for all 1800 courses are available at ocw.mit.edu—everything from full video talks about aerospace engineering to anthropology lecture notes about "Intersubjectivity, Phenomenology, Emotion, and Embodiment." The site has drawn 35 million visitors since 2002, most from outside North America, says MIT's Stephen Carson. "It's unprecedented to have all the courses available at a university this deeply and openly available on the Web. … It's an extension of the public-service function of the university."

Sale of Rare Astrolabe Halted

This 14th century brass astrolabe probably belonged to an educated gentleman about 1388, the time Geoffrey Chaucer was writing *The Canterbury Tales*. Now the owner wants to sell it to a foreigner, and the U.K. government is moving to keep it in Britain.

Found in 2005 under the floors of a 17th century inn just outside Canterbury, the pocket-sized instrument, valued at about £350,000, has been in the possession of the landowner. The name of the purchaser is confidential, according to a spokesperson for the Department for Culture, Media, and Sports. The department has put a temporary ban on the astrolabe's export to give U.K. institutions time to raise money to buy it.

Used for timekeeping, surveying, and performing astronomical calculations, this quadrant is one of only eight such instruments known to exist in the world, the culture department says. A horizon line positioned at 52° N shows that it was made for use in southern England.

Dehydrated DNA

Here's a new item for your family album: your genes. For $175, DNA Direct, a clinical genetic testing outfit in San Francisco, California, will provide a kit you can use to swab your cheek and mail in a sample. A week or two later, you'll receive three vials containing your air-dried and chemically stabilized DNA, which can be stored indefinitely at room temperature and reactivated with a few drops of water.

The samples have more than sentimental value. The company suggests they might come in handy for genealogy, family medical histories, settling inheritance suits, determining paternity in the face of an elusive male, or—in a pinch—identifying your remains should some dire mishap render them unrecognizable.

Oh, to Live in Iceland

Iceland has the most well-developed humans of any country on Earth, according to the 2007/2008 United Nations Human Development Index, which rates life expectancy, income, and education in 177 countries and regions. The land of geysers and glaciers displaced Norway, which has led the ranking for 6 years. Although not first in any category, Iceland ranked third in life expectancy (81.5 years), 13th in combined school and college enrollment (95.4%), and fifth in per capita gross domestic product (U.S. $36,510). Australia, Canada, and Ireland round out the top 5, with the United States slipping from eighth to 12th. All 22 countries in the Low Human Development category are in Africa.

Demographer Elwood "Woody" Carlson of Florida State University, Tallahassee, notes that it's not fair to compare small countries to the United States. "We probably should be comparing Iceland to Connecticut or something. … If you average together all the European countries, the continent as a whole doesn't look much different from the U.S.A."

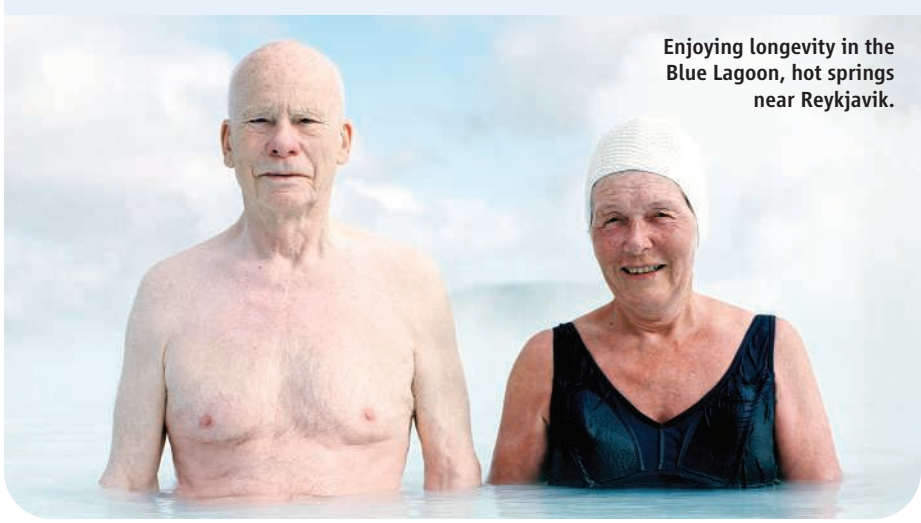

Enjoying longevity in the Blue Lagoon, hot springs near Reykjavik.

CREDITS (TOP TO BOTTOM): WWW.YWXINLONG.COM; COURTESY OF MLA; JENS NIETH/CORBIS

Storing light 1710

Lousy salmon 1711

Hot property. The much-coveted site behind the British Public Library and next to the St. Pancras railway station may house 1500 scientists by 2013.

BIOMEDICAL RESEARCH FACILITIES

London's Super-Lab Faces Hurdles

Imagine that the National Institutes of Health and the Howard Hughes Medical Institute teamed up with a megacharity and a university to buy land in the heart of New York City next to Grand Central Station and agreed to spend more than $1 billion to build a biomedical research facility there. And as part of the project, the famed Cold Spring Harbor Laboratory on Long Island would close, with only some of its labs relocated to the new facility.

That suggests the scope, and controversy, of the ambitious project U.K. Prime Minister Gordon Brown unveiled last week when he announced the sale of a key central London site to a coalition composed of the government's Medical Research Council (MRC), two medical charities, the Wellcome Trust and Cancer Research UK, and University College London (UCL). Next to the reopened St. Pancras station, which has high-speed rail links to the rest of Europe, the groups plan to build a £500 million-plus facility—£85 million for the land, about £350 million for the building, and the rest for equipment—that will house some 1500 scientists, many of them from MRC's celebrated National Institute for Medical Research (NIMR). "This is going to be great for British medical science, European medical science, and world medical science," says UCL Vice-Provost Edward Byrne.

Although there's no guarantee the project will live up to that promise, Richard Lerner, president of the Scripps Research Institute in San Diego, California, says the effort does signify that the prime minister believes "biological science is important to the future of the country."

Still, to achieve Brown's goal of improving the U.K. economy and the health of its citizens, the project will have to overcome major hurdles. London officials, who had designated the land for affordable housing, may try to stop it, as may those fearful of research on dangerous infectious pathogens being performed in central London near rail links to Europe. And it's not clear how the new center will blend labs from UCL, Cancer Research UK, and NIMR, which is being forced to close, to the dismay of many of its scientists. "Making it a single entity rather than a collage of contrasting colors is a strong challenge," says Frank Gannon, Science Foundation Ireland's director general and former head of the European Molecular Biology Organization. "It's not simply having great scientists in the same location."

The proposed facility has emerged out of the struggle over NIMR, whose 19-hectare campus in north London is home to more than 500 scientists and support staff. MRC has long wanted to strengthen NIMR's efforts in translational medicine by marrying it to a research university and hospitals. In 2005, it announced that NIMR would relocate to a 0.3-hectare central London site in a project with UCL. NIMR scientists protested the move, arguing that it was an attempt to downsize their institute (*Science*, 4 February 2005, p. 652).

When the hectare-sized lot near St. Pancras became available, however, MRC and UCL joined forces with Cancer Research UK, which was looking to relocate some 550 scientists specializing in cell growth, signal transduction, and genome maintenance from its aging London Research Institute (LRI). "Pooling our resources helps us invest in technologies we might not on our own," says Harpal Kumar, Cancer Research UK's chief executive. The charity and MRC will also shift technology-transfer units to the new center, a move they hope will speed research findings to the clinic. With Cancer Research UK, the project "became much more exciting," says MRC Executive Director Nick Winterton. "This is a new vision."

UCL will enable access to its teaching and specialist hospitals and has committed about £50 million for construction. UCL will also embed some 150 scientists at the new center. "The relatively small number of UCL scientists will be a bridge to the whole university," says Byrne. Researchers will be able to "interact with almost every imaginable discipline."

The Wellcome Trust, the U.K.'s largest nongovernmental funder of biomedical research, has also committed at least £100 million. Wellcome Director Mark Walport notes that the St. Pancras location will encourage international collaboration and educational outreach through the British Library. "We immediately saw it as an important opportunity," he says.

Now comes the hard part. The project has a site, partners, estimated completion date—2013—but little more. MRC, for instance, won't detail its financial contribution yet, although the previous plan with UCL would have required it to contribute more than £200 million. And will one scientist run a unified institute? "Exactly how the governance will work has to be dealt with quite soon," says LRI Director Richard Treisman, noting that Cancer Research UK needs to have a visible presence, as it depends on public donations. ▶

CREDIT: TROIKA

British Nobel laureate Paul Nurse, president of Rockefeller University in New York City, heads a committee that will develop science plans for the project by next year. "The aim of this group is to be as ambitious as possible," says Byrne. What to incorporate from NIMR will likely be the stickiest topic Nurse faces. MRC has said that the new site will have animal research facilities comparable to those at NIMR now and that NIMR's World Influenza Centre will be part of the project, but it has made no assurances to other labs. "Not everyone will relocate. That's clear," says Winterton.

Although not agreeing that relocation is needed, several NIMR scientists who talked to *Science* acknowledge that the new proposal has much more appeal than the smaller union with UCL. Yet MRC, they note, hasn't said how many NIMR labs will be eliminated. Given the potential uncertainty during the next 7 years, they worry that colleagues will simply leave. Some even wonder whether the institute's name will live on at the new facility. "I don't know if this will mean the real end of NIMR," says Jonathan Stoye, a virologist at the institute.

–JOHN TRAVIS

SPACE SCIENCE

China's Crystal-Sharp Moon Map Sets the Internet Abuzz

BEIJING—Last month, China feted its space scientists for sending the Chang'e-1 spacecraft to the moon, the nation's first mission beyond Earth orbit. Last week, however, the Chinese space establishment found itself on the defensive, after anonymous individuals in Internet forums attacked the authenticity of Chang'e-1's first mosaic view of the lunar surface.

The critiques have touched a sore spot. Chinese Premier Wen Jiabao, who unveiled the picture at a celebratory event on 26 November, hailed Chang'e-1 as "the third milestone in China's space exploration," after placing its first satellite in orbit in 1970 and its first astronaut in orbit in 2003. Some Chinese scientists have equated questioning the veracity of the picture—a mosaic of 19 scan strips of the lunar surface taken over 3 days and processed and stitched together by an army of imaging specialists—with an attack on China itself. "Doubting the authenticity of the Chang'e moon photo is insulting the country," the mission's chief scientist, Ouyang Ziyuan, told the newspaper *Guangzhou Daily* last week.

Chang'e-1, named after a legendary fairy who flew to the moon, is the first stage of a China National Space Administration (CNSA) program to orbit the moon, land a probe, and return a sample to Earth. It is also the second of four planned missions—others are from Japan, India, and the United States—aiming to learn about the moon's origins and composition (*Science*, 31 August, p. 1163).

Launched on 24 October, Chang'e-1 maneuvered into a polar orbit, 200 kilometers above the surface, on 7 November, according to the Beijing Aerospace Command and Control Center. It travels above Japan's Kaguya spacecraft, launched in September in a polar orbit 100 kilometers above the surface.

Chang'e-1's payload includes a microwave radiometer to measure soil depth, gamma ray and x-ray spectrometers to determine soil composition, a solar plasma detector to chart the distribution of solar particles impinging on the moon, and a charge-coupled device (CCD) stereo camera for mapping. "All the sensors are working well," says Wu Ji, director of the Center for Space Science and Applied Research of the Chinese Academy of Sciences, which managed the payload and developed the radiometer and plasma detector. Wu is particularly proud of the radiometer, the first of its kind on a lunar mission.

The moon image, too, is a source of pride. The sharp resolution of the mosaic, representing a swath of lunar surface between 57° and 83° longitude east and 54° and 70° latitude south, surprised even some project scientists. After seeing the first photo sent back by Chang'e-1, the camera's chief designer, Zhao Baochang, told the Chinese newspaper *Science Times*, "everybody at the unveiling scene was dumbstruck. … We absolutely did not expect the photo to be this clear!" Space administrators and scientists reportedly received bonuses totaling more than $1 million for "meritorious service." Western experts are also impressed. "To be able to match the 19 images and remove the seams, they produced a very aesthetically pleasing mosaic," says Mark Rosiek of the U.S. Geological Survey's Planetary Geomatics Group in Flagstaff, Arizona.

Within hours after the picture's release, however, critics were chipping away at it. In the "Beautiful Science" forum of People Net, one anonymous individual drew attention to a tiny rectangular shadow and asked, facetiously, whether it is the ▶

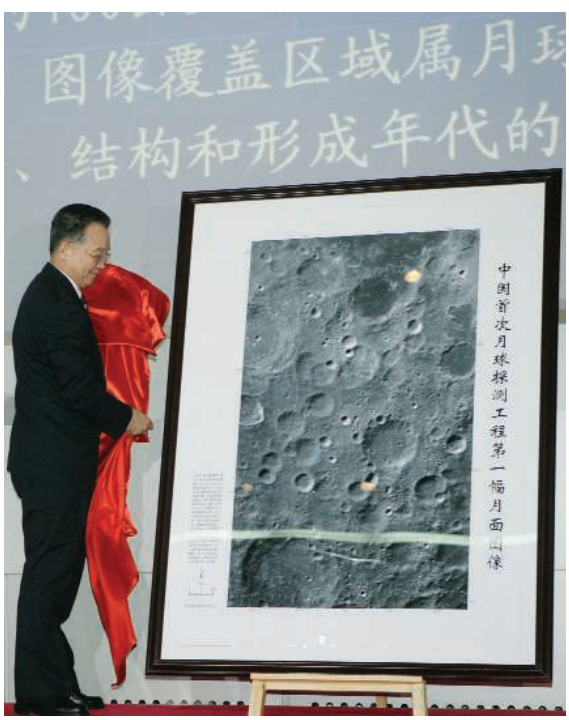

CREDIT: XINHUA/LANDOV

Picture perfect. Chinese Premier Wen Jiabao unveils the Chang'e-1 composite at a 26 November press conference.

U.S. lunar rover that was abandoned on the moon. On other Internet sites, critics pointed out that the mosaic is similar to images and maps from earlier lunar missions, including a 1994 image from Clementine, a U.S. probe. Some even alleged that the mosaic is a fake.

Chinese space officials came out fighting. In a forum held live on SpaceChina Net on 29 November, Ye Peijian, designer-in-chief of the Chang'e-1 mission, said that Chang'e-1 obtained the map "using our own equipment—it is absolutely true." He lambasted critics for doubting the image's authenticity. "This kind of speech is either irresponsible, or with ulterior motives."

Western analysts view the Chang'e-1 mosaic as bona fide. The Chang'e-1 and Clementine mosaics are "evidently not the same," says Emily Lakdawalla, a blogger for the Planetary Society. She points out that the lighting angle is different: "The Clementine image is lit from the top [north], while the Chang'e image is lit from the northwest," she wrote on her blog, referring to her high-resolution image (planetary.org/blog/article/00001248).

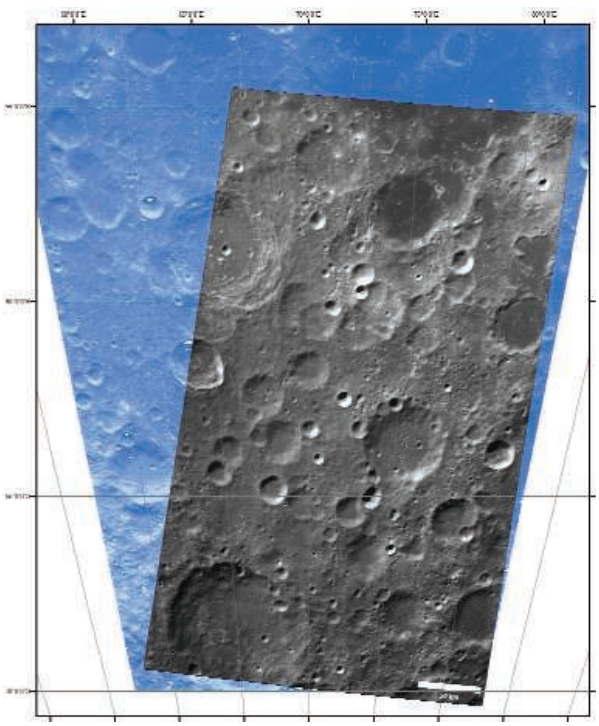

Like a glove. Sinusoidal projection of Chang'e-1 mosaic (gray) overlaid on a Clementine base map.

CREDIT: MARK ROSIEK/USGS

However, it's not clear how this Chang'e-1 mosaic is oriented. Mapmaking involves projecting craters and other three-dimensional features onto a flat surface. In a Mercator projection, the north and south poles are spread out, resulting in a map with equally spaced longitudes and latitudes, and a constant compass bearing. Google Moon uses a Mercator projection.

The Chang'e-1 image Lakdawalla analyzed includes no frame and no indication of whether it is a Mercator projection. Matthew Hancher, a researcher at NASA's Ames Research Center in Mountain View, California, on the other hand, looked at a framed Chang'e-1 moon image—the one unveiled by the government—and concluded that "the map is perfectly clear" in representing a sinusoidal projection. In a sinusoidal projection, longitudes converge at the poles and latitudes are parallel. A low-resolution image is available from the CNSA Web site (www.cnsa.gov.cn/n615708/n620172/n677078/n751578/images/1798046.jpg). Rosiek came to a similar conclusion after finding that a sinusoidal projection of the Chang'e-1 mosaic almost matched a sinusoidal Clementine base map, but with a small slant, which Hancher estimated to be 5° from north.

The peculiar presentation of the Chang'e-1 mosaic and its similarities to the Clementine base map do not mean that it is a fake. "The forgery idea just doesn't make very much sense," Hancher says. "The Chinese would be backing themselves into a corner from which it is unclear how they could possibly hope to escape." He and others point out that Chang'e-1's mosaic has a finer resolution than Clementine's. And Ouyang, who told *Science* he's still "angry" at the doubters, says new Chang'e-1 images, including a view of the moon's dark side, have been posted to the lunar program's Web site (www.clep.org.cn/index.asp?modelname=index%5Fzt%5Fkxtc&titleno=cggxiang).

Wu and his colleagues hope to put the controversy behind them as they plan an encore: launch of the backup Chang'e spacecraft in late 2009 or early 2010. The duplicate probe would be equipped with a higher resolution CCD camera to help determine a landing site for the planned 2012 lander mission. A decision on the payload and launch date of the second probe is expected in early 2008, Wu says.

–HAO XIN AND RICHARD STONE

With reporting by Andrew Lawler.

Stretching NSF Dollars

Three years after abolishing requirements that National Science Foundation (NSF) grantees share the cost of funded research, the foundation's National Science Board is taking a second look. Congress asked for a review after hearing that the policy was discouraging companies from participating in certain programs in which an industry role was essential. Lawmakers also worried that NSF might be leaving good money on the table.

Legislation passed this summer restores a 30% cost-sharing requirement for NSF's Major Research Instrumentation Program, and the review "will tell us if the new across-the-board policy is the right way to go," says an aide to the House Science and Technology Committee, which requested the study. Last week, a board task force explored the perennially thorny issue, and it plans to give Congress a draft report in February. **–JEFFREY MERVIS**

2007 Brings Near-Record Heat

With data through November, NASA's Goddard Institute for Space Studies (GISS) has determined that 2007 will likely be Earth's second-warmest year on record. The strongest warming signal occurred in the Arctic, where temperatures were more than 3°C above the 1951–1980 mean. And the planet's global mean temperature was 0.6°C above the average, despite this year's low solar radiance and strong La Niña phenomena, which both tend to lower Earth's temperature. "Given that both of these natural effects were in their cool phases in 2007, it makes the unusual warmth this year all the more notable," says an analysis GISS provided *Science*. The six warmest years in Goddard's 128-year record occurred in the past decade, with 2005 leading the list.

–ELI KINTISCH

Shuttle Shuffle

Eager European scientists must wait until the new year for astronauts to attach the Columbus research module to the international space station. NASA postponed last week's planned launch of the space shuttle carrying the European Space Agency laboratory after fuel sensors on the external tank failed twice in a row. Agency officials may need to roll the Atlantis orbiter back for repairs. The earliest new launch date is 2 January. The delay is not expected to affect NASA's ability to put the first piece of the Japanese Kibo module into orbit in February. A short delay is no big deal for European and Japanese scientists, who have been waiting since 2004. **–ANDREW LAWLER**

CLIMATE CHANGE

Senate Bill Would Provide Billions For Deploying Cleaner Technologies

A Senate panel has approved a sweeping climate change measure that would provide billions of dollars annually to commercialize energy sources that emit little or no carbon. Utility companies have long regarded the type of cap-and-trade system contained in the legislation (S. 2191) as a stick that punishes them for generating energy that the country needs. But lawmakers are also hoping that vast numbers of technological carrots will help curb the global rise in greenhouse gas emissions. "Many have said that we need a Manhattan Project for energy," said Senator Max Baucus (D–MT) during the panel's 5 December markup of the bill. "This is it."

So far, the debate about climate legislation has focused on who should pay as the United States overhauls its energy system. The question of how to allocate the vast sums that a federally managed system might produce, however, has received little attention. Neither has promoting synergy between the public sector and industry, on whose shoulders rests most of the burden for reducing emissions.

The Climate Security Act of 2007, approved on a vote of 11 to 8 by the Senate Environment and Public Works Committee, would require greenhouse polluters—refineries, factories, and fuel importers, as well as power companies—to procure emission permits in order to operate. Some of the permits would be provided for free, and others would be sold through a yearly auction. (Over time, the total number of permits issued would decrease, as an incentive to reduce the level of emissions, and a larger fraction would be sold.) The bill, which the Senate is expected to take up next year, would lower U.S. greenhouse emissions by an estimated 70% by 2050. Economists have calculated that an auction could generate as much as $3 trillion between 2012 and 2050.

Some lawmakers, such as Senator Bernie Sanders (I–VT), see those revenues as a golden opportunity to stimulate the development and use of green technologies such as solar and wind power, along with more energy-efficient products. "Sustainable energy is and will be the future of this country. We need to give it a fair shake," he told *Science*.

Just what is fair, however, is a key unresolved question. Sanders had criticized an earlier version that would have forced renewables to compete for deployment funds ▶

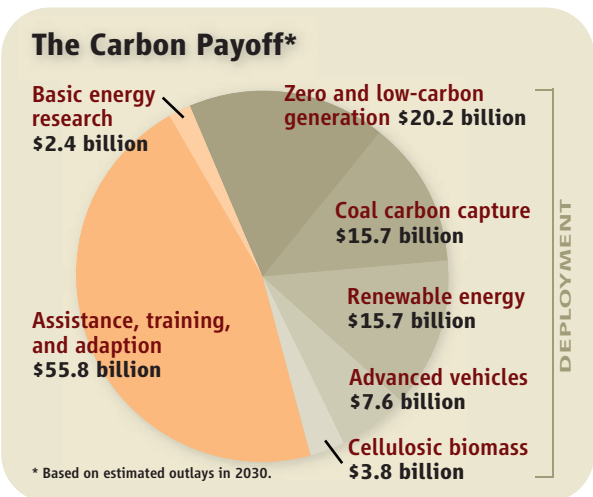

Making allowances. Proceeds from a carbon credit auction would be distributed among a number of programs. The amounts assume a carbon dioxide equivalent price of $49 per ton.

SOURCE: S. 2191 AND CLEAN AIR TASK FORCE

RESEARCH POLICY

NIH Weighs Big Changes in Peer Review

Peer review, a cornerstone of biomedical science, appears headed for an overhaul, to judge by a sweeping examination unveiled at the National Institutes of Health (NIH) last week. Since July, scientists have flooded two working groups established by NIH Director Elias Zerhouni with several thousand comments and ideas. This outpouring indicates that the community is frustrated by the system's administrative burden and deeply concerned about the fate of talented new investigators. Zerhouni has promised quick action.

At a meeting of the advisory committee to the NIH director on NIH's Bethesda, Maryland, campus last week, leaders of this review highlighted the recommendations they may deliver to Zerhouni in February. No final decisions have been made, however, and the committees are weighing everything, including shortening grant applications to seven pages from the current 25 pages and recommending an "editorial board" model that would refer some grant proposals to outside experts.

Molecular biologist Keith Yamamoto of the University of California, San Francisco, who also serves as co-chair of the external working group that solicited comments from outside NIH, suggested ways to ease a reviewing backlog. (Lawrence Tabak, director of the National Institute of Dental and Craniofacial Research, co-chaired the internal group.) Currently, Yamamoto noted, most applicants are permitted to resubmit their proposal twice if it's rejected the first time around, which happens most of the time. But the appeals, Zerhouni said at the meeting, have created a "traffic jam" and a system that "penalizes the new entrant to a very extreme degree."

Yamamoto thinks reviewers ought to assess applications first for their scientific impact and, in cases that seem hopeless, communicate that unequivocally to the applicant without allowing resubmissions. "Right now, if an application is triaged"—left unscored—"many times it's unclear what the reason is," said Yamamoto in a conversation after the meeting. "Here, the goal is to say, 'Let's stop all that.' "

Streamlining applications—perhaps by vastly reducing the amount of preliminary data that's included—is also a possibility, as is eliminating the current scoring system and having reviewers rank only the top 10 grant proposals that they consider. Some study sections, the working groups believe, have too many members, having ballooned from the usual 15 or 20 members to as many as 80, to accommodate the increasingly specialized science being proposed. Sending applications containing certain technical details to outside experts, who would consider those elements alone and report back to the study section, is one way to slim study sections down. Shorter grant proposals, meanwhile, could allow each one to be evaluated by four people instead of the usual two.

with nuclear plants, which have been subsidized by the government for decades. The bill would now create a separate pool specifically for renewables (see chart, p. 1708).

Elizabeth Salerno of the American Wind Energy Association in Washington, D.C., applauds that change, although she says coal and nuclear plants will still retain "a competitive advantage." Solar-energy researcher Nathan Lewis of the California Institute of Technology in Pasadena likes the fact that hundreds of millions of dollars in revenue each year would be allocated for basic research at the Department of Energy's new Advanced Research Projects Agency–Energy. "That's a step in the right direction but not nearly enough to make up for the deficiencies in basic research over the last 3 decades," he says. Lewis thinks the government should spend as much on basic and applied energy research as it provides the National Institutes of Health, whose annual budget is $30 billion.

But experts believe what's on the shelf right now could have a significant impact. A recent study estimated that current technologies, if deployed widely, could reduce U.S. carbon emissions to 80% of 2005 levels by mid-century. "We need to take the solutions we have today and apply them," says mechanical engineer Charles Kutscher of the National Renewable Energy Laboratory in Golden, Colorado, who led the study.

Others, including some advocates of renewables, believe the government shouldn't be charging companies for permits at all. George Sterzinger of the Renewable Energy Policy Project in Washington, D.C., complains that an auction would favor utilities in low-carbon-emitting regions, such as hydropower operators in the Pacific Northwest, whereas consumers in coal-dependent Ohio would pay 15% more, he estimates, as companies pass along the cost of their permits. Oil giant Shell complained earlier this year in a letter to lawmakers that forcing companies to pay for emission permits in addition to the cost of cleaning up their act could "withdraw capital from the industries and firms" involved and harm consumers.

Sterzinger prefers incentives, including tax breaks, as a way to spur renewables. That approach is part of an energy bill that the House of Representatives passed last week. (Senate action was pending as *Science* went to press.) An aide to Senator Joseph Lieberman (I–CT), who co-sponsored the Senate bill, agrees that companies, spurred by emissions caps, will have to do most of the heavy lifting if the country hopes to lower its carbon pollution. "The private investment will actually dwarf the public funds available," he says. "That's the big way this bill is a Manhattan Project."

–ELI KINTISCH

Zerhouni and his advisory committee seemed enthusiastic, but several members wondered if the proposed changes went far enough. "The biggest [issue] on the minds of the people I talk to is getting the best people to serve on study sections," said advisory committee member Thomas Kelly, director of the Sloan-Kettering Institute in New York City. And, he added, "I'm skeptical" whether the incentives proposed will be sufficient to coax these people to serve. Bioengineer Annelise Barron of Stanford University in Palo Alto, California, worried that slimming down the applications might mean those from less prestigious universities would not fare as well, because with shorter applications, name recognition could carry more weight. The NIH system cannot allow such a bias or must find a way to manage it, agreed David Botstein of Princeton University, who's working with Yamamoto on reviewing peer review. Some wondered whether blinding the names and affiliations of grantees would be possible.

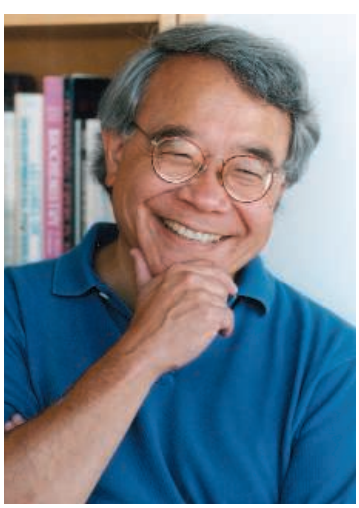

CREDIT: UCSF

Plain speaking. NIH adviser Keith Yamamoto sees merit in blunt reviews.

No matter what the working groups decide, it's critical that NIH retains the scientists it's helped train and gives investigators "a sense of commitment that's real," says pharmacologist and cardiologist Garret FitzGerald of the University of Pennsylvania, an NIH adviser not directly involved in this review. "Otherwise," as the average age of first-time grantees continues to rise, says FitzGerald, "what rational person would choose to go into a career where you begin to be independent when you're 45?"

–JENNIFER COUZIN

CIRM in Turmoil

The California Institute for Regenerative Medicine (CIRM) is having a rough holiday season. California's Fair Political Practices Commission is investigating a conflict-of-interest complaint against board member John Reed, president of the Burnham Institute for Medical Research in San Diego, and the state controller plans to audit CIRM. The commission is examining a letter Reed wrote to CIRM—on the advice of its board chair, Robert Klein—to appeal its rejection of a Burnham research application. CIRM policies ban board members from "us[ing] their official position to influence a decision regarding a grant."

In addition, the institute last week eliminated 10 applications from four universities because they had been signed by deans who serve on CIRM's governing board. "This is unfortunate," says stem cell researcher Renee Reijo Pera of Stanford University in Palo Alto. Those applications "were from some of our best young scientists in the state." Klein said in a press release that board members will be given more legal guidance on the institute's procedures. CIRM spokesperson Ellen Rose says the institute may hold a second competition to give the failed applicants another chance. "CIRM is not a private foundation and cannot be run as if it were," says John Simpson of the Foundation for Taxpayer and Consumer Rights, the organization that complained to the state commission.

–CONSTANCE HOLDEN

Cornell's Collider Lives

After cranking out data for nearly 3 decades, Cornell University's storied Cornell Electron Storage Ring (CESR) collider in Ithaca, New York, will stop smashing particles in March. But the machine won't come to a crashing halt. Last week, the National Science Foundation announced that it will become a test bed for the proposed 30-kilometer-long, multibillion-dollar International Linear Collider. ILC, which will fire beams of electrons and positrons at each other, will need circular accelerators called damping rings to cool and compress the beams. CESR is "the closest thing we have to a damping ring right now," says Cornell's Maury Tigner.

Started up in 1979, CESR paced the world in the study of particles called B mesons. Since 2003, it has refined measurements of more familiar D mesons. It's the last remaining particle physics machine at a university and the only one of three U.S. colliders with a new mission lined up. And even as CESR joins the push for ILC, cash-strapped officials in the United Kingdom have announced that they may pull out of the project.

–ADRIAN CHO

NEUROBIOLOGY

Immune Molecules Prune Synapses In Developing Brain

The complement cascade is part of the body's innate immune defense: a protein work crew whose duties include tagging bacteria and other bad guys for elimination. A new study suggests that complement proteins may have a surprising yet analogous function in the developing brain, tagging unwanted synapses for removal. The work also hints that these proteins may promote synapse loss in early stages of neurodegenerative disease.

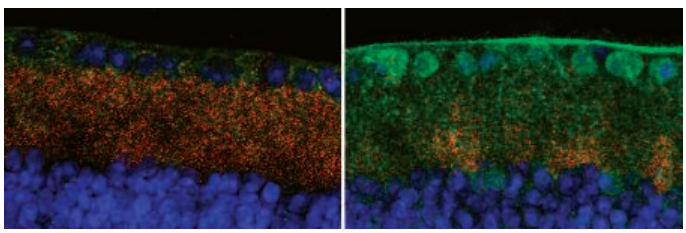

Early indicator. C1q (green) can be seen early in glaucoma (*left*), even before synapses (red) and neurons (blue) disappear as the disease progresses (*right*).

"It's a pretty provocative finding," says Greg Lemke, a neurobiologist at the Salk Institute for Biological Studies in San Diego, California. "This is part of a growing body of evidence that many molecules of the immune system have a second set of jobs in the brain," says Lisa Boulanger, a neurobiologist at the University of California, San Diego.

The new study, which appears in the 14 December issue of *Cell*, began as an attempt to determine whether neural support cells called astrocytes have a role in refining synaptic connections between neurons during development, says senior author Ben Barres of Stanford University in Palo Alto, California. Postdoc Beth Stevens and colleagues used gene chips to look for changes in gene expression in neurons from the developing retinas of rats when the neurons were cultured with astrocytes.

To their surprise, astrocytes spurred the neurons to crank out a complement protein called C1q, which elsewhere in the body kicks off a cascade of chemical events that culminates in the destruction of an intruding cell. In experiments with mice, the researchers found that C1q concentrations in the retina and brain peaked a week or so after birth and dropped dramatically as mice matured. The peak coincided with the period when unwanted synapses are pruned. More intriguing, C1q seemed to concentrate ▶

PHYSICS

Simple Scheme Stores Light by Converting It Into Vibration and Back

A few years ago, physicists slowed light to a crawl and then stopped it entirely (*Science*, 26 January 2001, p. 566). To do that, they exploited strange quantum-mechanical interactions between light and atoms in a gas, converting a pulse of light into a subtle arrangement of spinning atoms. On page 1748, three physicists report a simpler way to hit the brakes: They convert light in an optical fiber into a slow-moving vibration and then back into light.

"This has the enormous advantage of simplicity," says Stephen Harris, an applied physicist at Stanford University in Palo Alto, California, and a pioneer of the atomic techniques. "Conversely, it can't do some things that the other techniques can."

To store a pulse of laser light in a cloud of atoms, researchers shine a second laser into the cloud at the same time. The overlapping light fields interact with the atoms in a way that greatly decreases the light's speed. The light also nudges each atom into a strange quantum-mechanical condition in which it spins in two different directions at once. The precise spin mixture varies from point to point in the cloud, effectively freezing the light pulse into the atoms when the reference laser is turned off and holding it until the laser comes back on. Others have managed to store light by shunting it into tiny optical "resonators" for a fraction of a nanosecond.

To find another way, Zhaoming Zhu and Daniel Gauthier of Duke University in Durham, North Carolina, and Robert Boyd of the University of Rochester, New York, opted for an optical fiber. They fed a "data" pulse in one end and a short, intense "write" pulse in the other. When the two collided, the data pulse disappeared and was replaced by a vibration crawling along at just 1/40,000 the speed of light in a fiber. To convert the vibration back to light, the researchers hit it with a "read" pulse identical to the write pulse.

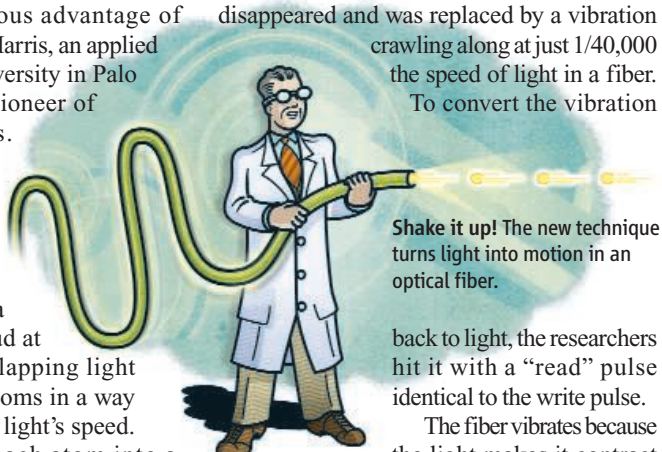

Shake it up! The new technique turns light into motion in an optical fiber.

The fiber vibrates because the light makes it contract in the spots where the light is most intense. To make the conversion efficient, the team tuned the frequency of light in the read pulse slightly lower than that in the data pulse. The two had to differ by the frequency of the vibration, which was fixed by the properties of the fiber. The researchers showed they could store a train of three 2-nanosecond pulses and retrieve it as much as 12 nanoseconds later.

The new technique works for any frequency of light that will pass through the fiber, Gauthier says. The atomic and resonator techniques generally work at one frequency.

The conversion doesn't depend on quantum mechanics, notes Lene Hau, a physicist at Harvard University and one of the first to stop light. That should make the effect more robust but rules out truly bizarre embellishments. For example, Hau and colleagues have encoded a light pulse in one cloud of atoms and revived it in another cloud by letting a few atoms drift between the two, as they reported 8 February in *Nature*. Such a feat would be impossible with the fiber technique. Still, Hau says, "it's very important to try different systems."

The atomic systems might someday provide the memory for quantum computers, Harris says. Gauthier sees more immediate uses for the fiber-optic approach. For example, it might be used to measure the correlations between signals in optical networks. But first researchers must increase the storage time and reduce the power in the read and write pulse from a walloping 100 watts. That's enough to shake up anybody. **–ADRIAN CHO**

at puny, immature-looking synapses in the developing nervous system.

When the researchers examined the brains of mice lacking a functional *C1q* gene, they found that development had gone awry in the lateral geniculate nucleus, a relay station in the brain that receives synaptic inputs directly from retinal neurons. In normal mice, geniculate neurons initially receive inputs from both eyes and then prune them so that they only receive input from one eye or the other. In the mutant mice, geniculate neurons maintained extraneous inputs from both eyes into adulthood.

That's a striking finding, Boulanger says: "When you get rid of these proteins that we thought just functioned in the immune system, it disrupts a very specific event that we think is involved in making the precise, final connections in the developing visual system." Many questions remain, however. Barres suspects that complement proteins mark unwanted synapses for removal by microglia, immune cells in the brain. More work is needed to demonstrate that, Boulanger says, and to figure out why only certain synapses are flagged for removal.

Finally, Barres and colleagues collaborated with Simon John's group at the Jackson Laboratory in Bar Harbor, Maine, to investigate whether C1q might have a role in synapse loss in a mouse model of glaucoma. Compared to normal adult mice, adult glaucoma mice exhibited elevated C1q levels: The protein accumulates at retinal synapses early in the disease, even before synapses disappear and neurons die off.

Synapse loss precedes cell death in Alzheimer's and other neurodegenerative diseases, Barres notes. He speculates that drugs that block the complement cascade may forestall neurodegeneration in a number of disorders. It's an exciting idea, says Monica Vetter, a neurobiologist at the University of Utah in Salt Lake City: "There's good evidence that these complement components are upregulated in other diseases."

–GREG MILLER

ECOLOGY

Parasites From Fish Farms Driving Wild Salmon to Extinction

A new study suggests that fish farming could rapidly wipe out some populations of wild salmon in British Columbia. Although some researchers are calling for dramatic controls on the industry, others say the risk hasn't been established firmly enough. At stake is the $450 million aquaculture business.

One of the top concerns about aquaculture is the spread of disease and parasites to wild species. On page 1772, the first population-level analysis suggests that sea lice from farmed salmon will cause several populations of one species of salmon in British Columbia to plummet by 99% within 8 years. "It's a shocking number," says salmon conservation expert John Reynolds of Simon Fraser University in Burnaby, Canada, who was not involved in the research. But environmental physiologist Scott McKinley of the University of British Columbia in Vancouver worries about rushing to judgment. "You cannot conclude anything from a correlation," he says.

Sea lice are small crustaceans that latch onto salmon and other fish. They feed on tissue and create lesions that make it hard for fish to regulate their body fluids. The saltwater parasites naturally occur on adult salmon in the sea but not on juveniles, which hatch in fresh water and then swim to the sea. In 2001, however, researchers found significant numbers of sea lice on wild juveniles that had passed by fish farms in British Columbia. The situation was alarming because young pink salmon are more vulnerable to damage from lice than adult salmon are.

Graduate student Martin Krkošek of the University of Alberta, Edmonton, started studying the problem in 2003. In previous papers, he and colleagues calculated that juvenile pink salmon are 73 times more likely to be infected with sea lice after they passed by salmon farms than are fish that didn't pass by and that lice can kill between 9% and 95% of juvenile pink salmon, depending on how many fish farms they must swim by. Some researchers are unconvinced, however, and point to other studies that suggest lower mortality from sea lice.

Ouch! Young pink salmon suffer from sea lice, which dig in when salmon swim past fish pens.

CREDIT: M. KRKOŠEK *ET AL.*, *SCIENCE*

In the new work, Krkošek and colleagues investigated the extent to which sea lice are affecting pink salmon populations throughout the Broughton Archipelago near Vancouver Island. They analyzed 35 years of records from the Canadian fisheries agency on the number of salmon in seven rivers that flow into marine channels with fish farms. They also looked at 64 rivers from which migrating salmon do not pass by fish farms. Using a standard model, they calculated that pink salmon not exposed to fish farms showed the same range of population size for all 35 years, varying from year to year.

The pink salmon that swam past salmon farms showed the same pattern, until the lice infestations began in 2001. Then all seven populations shrank year after year. If these populations continue to decline at this rate, they will be 99% gone within four generations. "It's very fast," says Krkošek, who says immediate conservation steps are necessary. "We can't sit around and do more research, because these fish will be gone." Senior author Mark Lewis of the University of Alberta in Edmonton and another co-author were among 18 scientists who in September called for requiring salmon farms to be surrounded by barriers to prevent the spread of parasites or disease.

As with previous papers, the reaction to the new finding is polarized. McKinley and others say that there are too many unknowns to conclude that sea lice from farms harm wild salmon. Many factors influence their abundance, including fluctuations in ocean nutrients. But fisheries biologist Ray Hilborn of the University of Washington, Seattle, says it is too risky to farm fish in open pens near wild relatives: "The bigger concern is that [sea lice] are just one of many pathogens. There could be other things out there that we don't know about."

–ERIK STOKSTAD

Spawning for a Better Life

With our planet's besieged corals the focus of the International Year of the Reef in 2008, scientists are racing to decipher the riddles of coral reproduction

The numbers aren't working in Michael Henley's favor. Two months earlier, this invertebrates aquarist at the National Zoo in Washington, D.C., returned from Puerto Rico with three Nalgene bottles brimming with coral larvae—12,000 or so of the tiny creatures—to do his part in an international bid to grow an endangered coral species from scratch. He hopes to nurse the elkhorn coral (*Acropora palmata*) larvae through the fragile swimming stage of their life cycle and entice them to build miniature reefs in a saltwater tank.

Henley has labored to make the baby corals feel right at home. Inside the 350-liter aquarium, two underwater jets pulse, simulating surges, and a pair of 400-watt lamps suspended over the tank are stand-ins for the blazing Caribbean sun. He's fine-tuned the filtering system to get the turbidity just right, and he nourishes the coral with newly hatched brine shrimp, oyster eggs, and rotifers. Henley spices up the cuisine with algae, which adult coral polyps host as symbionts that provide carbohydrates and other nutrients. "If they don't take [the algae] up, they won't live long," says Henley.

Despite Henley's tender care, many did not live long. One month after the larvae arrived at the zoo, only 158 found safe haven in tiny grooves etched into ceramic tile terraces in the tank. Another month later, Henley has found just two millimeter-long animals. "It doesn't look good," he says.

Like coral lovers around the world, Henley feels a sense of crisis. Climate change, disease, and human activities such as overfishing and coastal development have destroyed 20% of the world's 285,000 square kilometers of known reefs, threatening biodiversity hot spots that generate an estimated $30 billion a year in revenue, mostly from fisheries and tourism. In the Caribbean, populations of elkhorn and staghorn corals have dropped so low that in May 2006, the United States listed them as threatened species. Last September, for the first time, corals were inscribed on the Red List of Threatened Species. Two coral species from the Galápagos—Floreana coral (*Tubastraea floreana*) and Wellington's solitary coral (*Rhizopsammia wellingtoni*)—are considered critically endangered, and a third, Galápagos coral (*Polycyathus isabela*), is designated as vulnerable. According to the *Status of Coral Reefs of the World: 2004*, nearly half of remaining reefs are imperiled and could collapse as soon as 20 years from now.

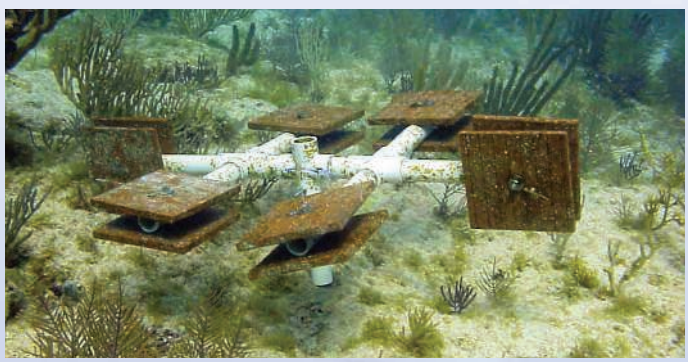

Home, sweet home. Ceramic tiles attached to reefs at various angles help determine where coral larvae prefer to settle after spawning.

Prospects for recovery are grim. With more frequent and severe spikes in ocean temperatures, corals seem to be having an ever-harder time reproducing and surviving. Although reefs are built in large part through asexual cloning, "sexual reproduction is possibly the most important process in the replenishment of degraded reefs," says James Guest, a marine biologist at the University of Newcastle upon Tyne, U.K. Larvae can migrate to where conditions are more amenable, and the mixing of gene pools may be critical to survival in a rapidly changing world.

Henley, part of a consortium called SECORE, short for Sexual Coral Reproduction, hopes that by growing corals in aquaria, he and his colleagues can keep beleaguered species from disappearing. Marine biologists, too, want to jump-start new reefs. "Our vision is to do for coral reefs what [others] do for forests" by developing seedlings for reforestation, says Alina Szmant, a marine biologist at the University of North Carolina, Wilmington. Other teams are blending old-fashioned husbandry and 21st century science to work out how corals know when to spawn and what fate befalls larvae. "A lot of our state of knowledge is an accumulation of hunches," laments Margaret Miller, a marine biologist with the National Marine Fisheries

CREDITS (TOP TO BOTTOM): OVE HOEGH-GULDBERG, UNIVERSITY OF QUEENSLAND; TONYA SHEARER

Service Southeast Fisheries Science Center in Miami, Florida.

Some hunches are paying off. By combining satellite climate data and spawning records, one team has begun to overturn the long-held view that surface water temperatures regulate the spawning clock. DNA studies have uncovered proteins that help detect light and fine-tune the spawning schedule. Studies are revealing the molecular pas de deux of coral-algal partnerships. And genetic tags are making it possible to trace reef genealogies to find out which are the fittest and likeliest to withstand environmental perturbations that are devastating more vulnerable reefs.

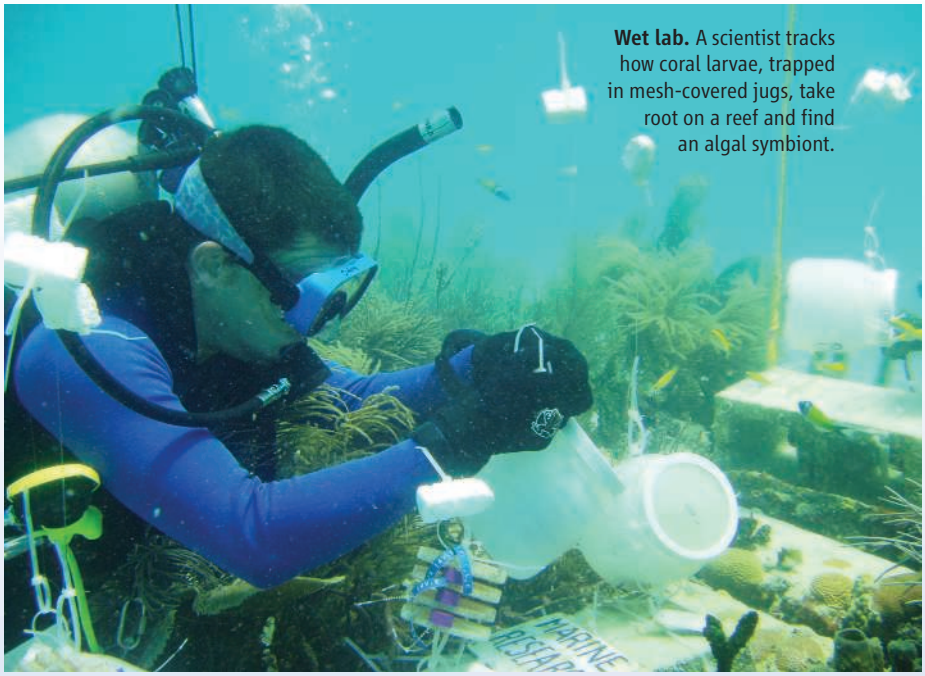

Wet lab. A scientist tracks how coral larvae, trapped in mesh-covered jugs, take root on a reef and find an algal symbiont.

CREDIT: CINDY LEWIS

Time to spawn

Until recently, catching corals in the act has been more art than science. Spawn-chasers must contend with bad weather, miscalculated spawning times, problems with permits to transport live corals, and a host of unknowns about conditions conducive to survival of young coral (see sidebar, p. 1715).

Although coral clones form the bulk of the pillars and billowing mounds of healthy reefs, after a few years' growth, individuals in the colonies become sexually active. Most species spew gametes into the water in a milky frenzy of fertilization en masse. For many corals, this is a once-a-year event. Thus, "spawning together is a biological imperative," says Miller.

To ensure sufficient concentrations of egg and sperm for fertilization, corals need to know the right month, the right day, even the right hour to release gametes. For decades, researchers assumed that warming sea surface temperatures stimulate the production and maturation of gametes, which burst forth a few days after the full moon, at a precise time after sunset.

The role of temperature as the seasonal cue never felt quite right to Robert van Woesik, an ecologist at the Florida Institute of Technology in Melbourne. "The problem for decades has been that we have been studying coral spawning at mid-latitudes," he explains. In the tropics, water temperatures vary by only about 3°C—not much of a cue, he contends. At higher latitudes, corals off western Australia spawn in late summer, whereas those off the east coast spawn in spring, even though water temperatures peak in both regions in summer.

From September 2002 until February 2003, van Woesik and research fellow Lolita Penland kept tabs on two tropical reefs in Palau. They discovered that multiple species spawned multiple times over the course of the year. Temperature didn't seem to matter. Rather, most of the time, spawning coincided with the spring and fall equinoxes, when the amount of insolation, or sunlight hitting any one spot, is highest. A literature review revealed that spawning schedules in the Great Barrier Reef and off Japan also track insolation.

Van Woesik and his colleagues next looked at spawning in the Caribbean. They combed the literature and got timing information for 12 species, including elkhorn, brain, and star corals, from Venezuela to Bermuda. Again, insolation seemed to set the spawning clocks. It could be that insolation fluctuations affect symbiont productivity, periodically fueling gonad growth, van Woesik says.

Some reef researchers are dubious. "We need experimental work to understand how these environmental cues are translated into physiological change by the organisms," says Guest. And

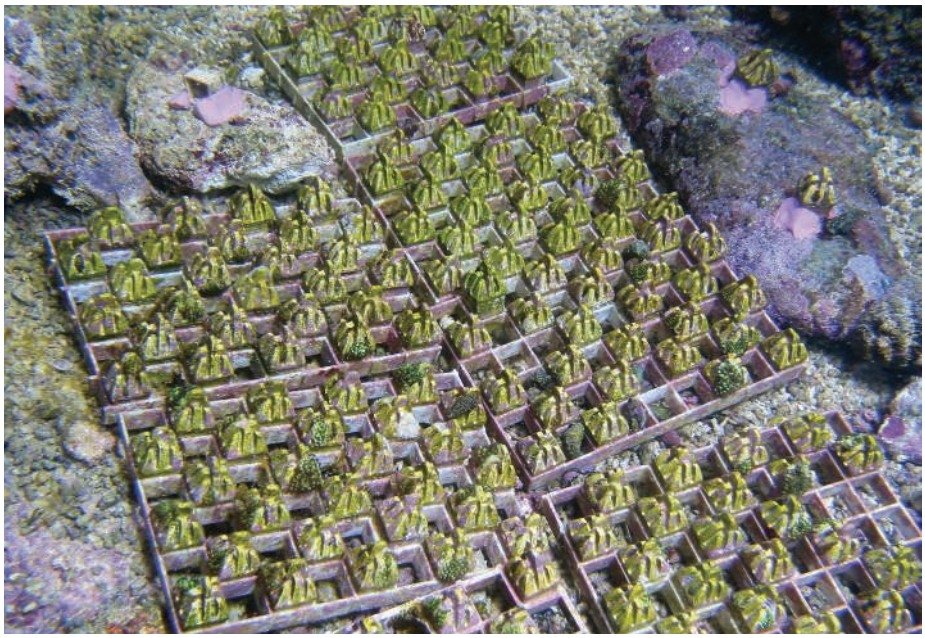

Corralled. Young corals grow on blocks that can be removed for examination under a microscope.

although the Caribbean data are "pretty solid," adds Andrew Baird, an ecologist at James Cook University in Townsville, Australia, he is not convinced that the same patterns prevail elsewhere. "It's possible that these cues differ among regions," says Baird, who in the past 5 years has sampled gametes from 20 sites in the Indian and Pacific oceans. He has found two peaks of spawning activity, loosely tied to the start and finish of the monsoon season.

No matter what puts corals in the mood, the spark that ignites a reproductive melee is moonlight. Most corals spawn within a week of the full moon. Yet corals lack eyes of any sort. Researchers have recently discovered that at least one species "sees" moonlight thanks to cryptochromes, proteins that sense blue light (*Science*, 19 October, p. 467).

After locating cryptochrome genes in the fingerlike coral *Acropora millepora*, Oren Levy, a marine biologist at the University of Queensland in St. Lucia, Australia, and his colleagues monitored the activity of two of those genes. One revved up protein production at dawn, whereas the other stirred hours later. When kept in constant darkness, the genes were quiet. One gene's activity tracked the moon's phase; protein production soared during the full moon. Szmant thinks these data are inconclusive. Yet if they hold up, the findings "provide an important mechanistic link in how mass spawning in corals is cued," says Miller.

Settling down

Nailing the timing is making it easier to predict and witness mass spawnings and to begin to understand this stage of the coral life cycle. Typically, spawning corals disgorge eggs and sperm packaged in a mucous bundle that floats to the surface and bursts, freeing the gametes. A cnidarian orgy ensues. Within a few days, the free-swimming larval progeny disperse and colonize.

The larvae are a weak link in the coral life cycle—a frailty exacerbated by climate change. Two years ago, Szmant and Miller gathered the larvae of elkhorn and mountainous star coral in the Caribbean and allowed them to settle on limestone plates that had been left for weeks or months on the reef to approximate natural surfaces and then brought back to the lab. They noted where the larvae preferred to land, put the plates back on the reefs, and watched what happened.

In lab experiments, the larvae tended to take root where there was encrusting red algae, but often new settlers would be overrun by the expanding algal patch. Star coral preferred the undersides of plates—even if the plates were put back upside down. This species fared poorly: Three-quarters of individuals disappeared within a month, and none survived a year. Elkhorn coral populated the top of the plates, and 3% remained alive after 9 months.

Puzzled about why coral would tempt fate by settling near the aggressive algae, Andrew Negri of the Australian Institute of Marine Science in Townsville took a closer look at this odd dynamic. He and his colleagues now argue that bacteria associated with the algae are the true cues for larval settlement. Szmant has evidence supporting this contention. Knowing the right cues, she says, "could lead to the development of targeted restoration measures."

Temperature, too, is a huge factor. Szmant and her colleagues have utilized a fluorescent protein found in larvae to follow them as they put down roots. In the summer, if seawater temperatures climb 1 or 2 degrees Celsius above normal, larval survival and settlement plummet, she and her colleagues are finding. Similarly, a team led by Paul Sammarco, a marine biologist at the Louisiana Universities Marine Consortium in Chauvin, has found that larvae of the species he studies—such as the Atlantic brain coral (*Diploria strigosa*) and reef-building and soft corals on the Great

continued on p. 1716 ▶

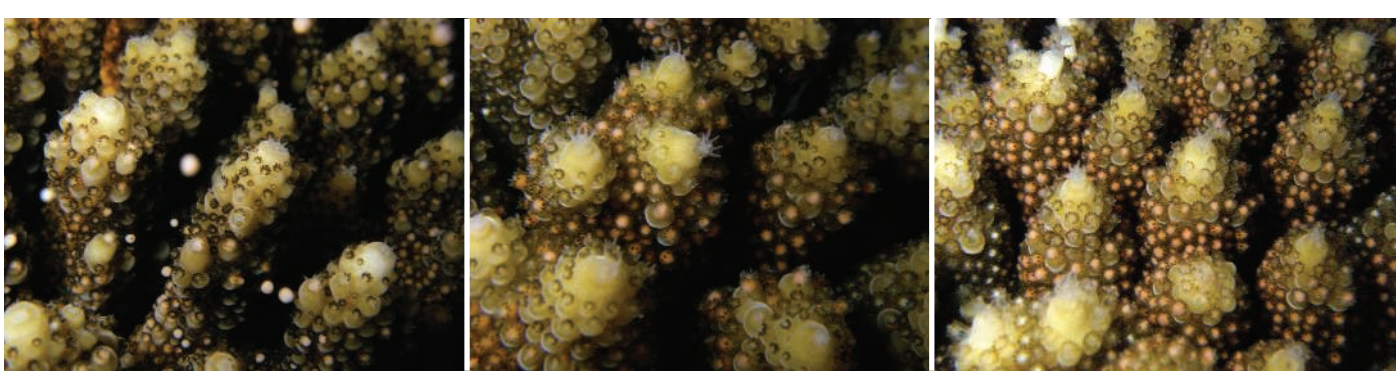

Let the spawning begin. Pink egg and sperm bundles are released by *Acropora digitifera* polyps.

CREDITS (TOP TO BOTTOM): DIRK PETERSEN; MAKATO KITAMURA

All ashore! Anticipating that spawning is about to begin, researchers haul small colonies of *Acropora millepora* onto Magnetic Island in seawater bins.

MOONLIGHT SONATA ON THE REEF

MAGNETIC ISLAND, AUSTRALIA—On the night of the full moon last October, a couple of dozen scientists from around the world converged on this tropical island off Townsville in northeastern Australia to witness a marvel of nature: an upside-down snowstorm.

Decades of observations suggested that *Acropora millepora*, a common coral of Australia's Great Barrier Reef, would erupt in an hourlong frenzy of reproduction precisely 5 days after the full moon. But the corals ad-libbed, releasing a blizzard of male and female sex cells into the warm tropical waters 2 days earlier than expected. "Coral rarely reads the script; this is biology," says David Miller, a molecular biologist with the Australian Research Council (ARC) Centre of Excellence for Coral Reef Studies at James Cook University (JCU) in Townsville, Australia.

Fortunately, Miller and his colleagues were tipped off. They had on hand a sample of *A. tenuis*, which spawns a few hours before *A. millepora*. When the researchers saw *A. tenuis* spawn, they sped out to the reef to bring coral samples ashore in tubs of water. On the beach under a gibbous moon and amid the wails of the bush curlew, *A. millepora* released egg-sperm bundles in delicate mucous sacs into the "baby baths." Later that night, the researchers, working in a makeshift lab in a seaside guesthouse, divided the egg-sperm bundles between plastic tubs in which they would raise larvae over the next few days.

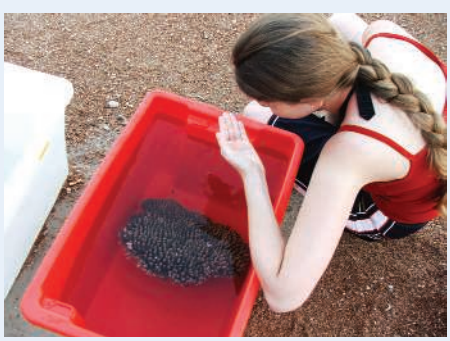

Primed. Graduate student Yvonne Weiss examines an *Acropora* colony a few hours before the big event.

The researchers hope that work on *A. millepora*—the species that has been most extensively studied at the molecular level—will point to ways to minimize global warming–inflicted damage to the 2000-kilometer-long Great Barrier Reef, which generates $4 billion a year in revenue. Diseases, most of them poorly understood (see sidebar, p. 1716), and urban runoff are among the villains. A looming threat is acidification of the seawater from dissolved carbon dioxide (*Science*, 4 May, p. 678, and p. 1737 of this issue).

To address these critical issues, four teams came to Magnetic Island to raise larvae. There's no magic formula. Some scientists filter and change water regularly, whereas others say this stunts larval growth. In an even simpler approach, a team led by ecologist Andrew Baird of JCU raises larvae in $1 buckets for studies about how temperature affects the larvae's ability to latch onto energy-giving algal symbionts.

A group led by Miller and Eldon Ball of the ARC Centre for the Molecular Genetics of Development has the big picture in focus. They are using high-throughput sequencers to compile a catalog of expressed genes as part of a "poor man's coral genome project." They hope to get most of the coding sequence out next year. Already, their labs have identified about 10,000 genes in *A. millepora*. Some, including genes critical to the vertebrate immune system, were once thought to be vertebrate innovations because they were absent from the fruit fly and the nematode worm, the archetype of invertebrates. "It's a vertebrate-centric view of the world," says William "Bill" Leggat of JCU.

Miller and Ball hope to find out which proteins among coral's repertoire of tens of thousands are expressed at various stages of development and in response to environmental shocks. In one fine-grained study, Miller is using genomic data to zoom in on the molecular basis of symbiont uptake and calcification. The research will include a comparison of coral genes with the full genome sequence of the sea anemone (*Science*, 6 July, p. 86). Another project, by Victor Hugo Beltrán Ramírez of JCU, is probing two proteins that turn on corals' vivid green and red fluorescence. The proteins may be involved in either photosynthetic enhancement or photoprotection in adult corals.

Leggat and François Seneca are investigating coral bleaching, a phenomenon in which coral polyps expel their algal symbionts if water exceeds the seasonal average temperature by 2°C for a couple of weeks. They want to find out which genes are switched on during the crises, which can wipe out entire reefs. The Magnetic Island reefs were hit hard by bleaching in 2002. One hypothesis is that free radicals generated by the heat-stressed symbionts disable their ability to photosynthesize. Coral somehow senses this and ousts its partners.

Two days after the spawning at Magnetic Island, Lubna Ukani, a molecular biologist in Miller's group, was bent over a microscope in the guesthouse-cum-laboratory. The ground floor was covered with baby baths, and tables strained under a mass of microscopes and chemicals. Ukani was chemically preserving 1-millimeter-diameter, pear-shaped white larvae for the genetic research.

"Tomorrow, they'll start swimming," Ukani says. After reaching this stage out on the reef, some larvae corkscrew down to the bottom, looking for a patch of sea floor that they will call home for the rest of their lives—as long as 100 years. Other larvae drift for months, eventually settling far away. That wanderlust, an evolutionary adaptation to cope with changing sea conditions, may be the key to survival for coral reefs as the planet warms. **–CHERYL JONES**

Cheryl Jones is a science writer based in Canberra, Australia.

CREDITS (TOP TO BOTTOM): YUYANG ZHANG; LUBNA UKANI

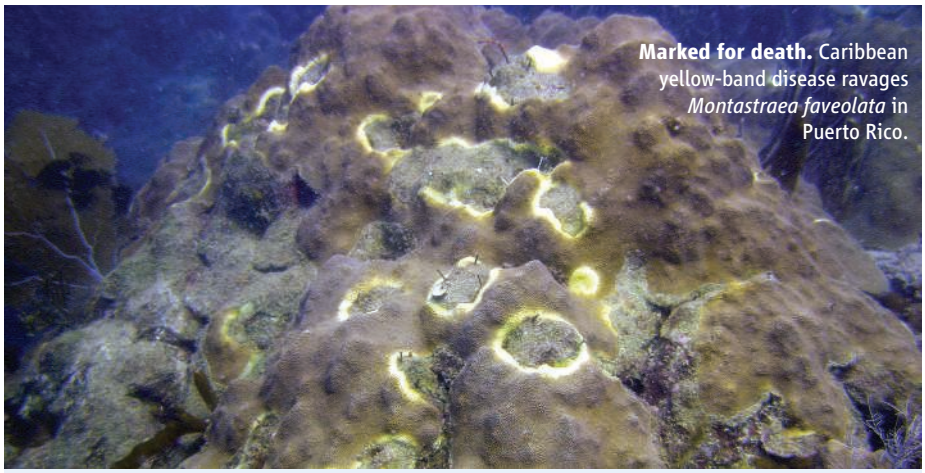

Marked for death. Caribbean yellow-band disease ravages *Montastraea faveolata* in Puerto Rico.

WHITER SHADES OF PALE

Disease is an unsung villain in the global degradation of coral reefs. Here are a few of the nastiest plagues that experts are keeping an eye on. All are expected to worsen as global warming nudges up average ocean temperatures.

Caribbean yellow-band disease is hitting reefs hard. "In Puerto Rico, some of the reefs that I have been studying for 8 years have lost 60% of their live coral tissue," says Ernesto Weil of the University of Puerto Rico. The disease has struck large, old colonies of *Montastraea*, or star coral, the main reef builder in the region. Scientists have not pinned down the pathogen that leaves yellow rings as it chews through a colony, nor do they know if it targets the coral or its algal symbionts. Outbreaks, once confined to summer, are now "permanent," says Weil, and assaults have been quicker and deadlier than in the late 1990s, when the disease first appeared. The increased ferocity seems to be correlated with a rise in average minimum water temperatures, Weil says.

The **Caribbean white diseases** are a group of bacterial diseases that show up as bands or patches of bare white skeleton. In the early 1980s, **white-band disease** wiped out as much as 95% of the acroporid corals throughout the Caribbean. **White plague** first struck in the late 1970s in Florida. Since then, it has appeared regularly across the Caribbean, afflicting 42 of the region's 60 coral species. The disease advances and retreats in sync with seasonal changes in water temperature. Although white plague remains "a major concern," Weil says, yellow band is emerging as a bigger threat.

Aspergillosis, caused by the soil fungus *Aspergillus sydowii*, exacted a heavy toll on Caribbean sea-fan corals in the mid-1990s. The disease is now entrenched but at low levels, says C. Drew Harvell of Cornell University. Studies suggest that the pathogen will thrive in warming oceans, she says. One glimmer of hope is that the sea fans are fighting back. They are "resilient," says Harvell, "and may have evolved increased resistance."

Denuded. White plague afflicts *Dichocoenia stokesii*.

White syndrome is a single disease—or a suite of diseases—that was first spotted about 10 years ago on the Great Barrier Reef and later detected in the Marshall and Hawaiian islands and in Palau. It can wipe out entire colonies in weeks or months. Although the causes are unknown, there is evidence for both bacterial infections and runaway cell death. A 6-year study of 48 reefs spanning 1500 kilometers of the Great Barrier Reef linked outbreaks to rises in sea surface temperatures and to coral density, says Bette Willis of James Cook University in Townsville, Australia. Global warming is likely to trigger more outbreaks, she says.

Scientists are warily eyeing **Montipora white syndrome**, which is attacking one of the three main coral genera in the Hawaiian Islands. "Changes in disease levels are starting to concern us," says Greta Aeby of the Hawaii Institute of Marine Biology in Kaneohe. She and others suspect that urban runoff, especially in Oahu's south Kaneohe Bay, is fueling a slow but sure advance of the disease, the cause of which is eluding scientists. Says Aeby, "This is one disease we expect will get worse." **–C.J.**

◀ continued from p. 1714

Barrier Reef—succumb to above-average water temperatures.

Not every species is under siege. Even where key reef-builders are in trouble, "weedy" corals, such as mustard hill coral (*Porites astreoides*) and lettuce coral (*Agaricia agaricites*), are doing okay. Most of these corals brood their young, and Szmant hopes to zero in on differences that gird brooders against environmental forces that hit spawners hard.

And there is plenty of geographic variability. In the Caribbean, for example, the prognosis is not bleak for every reef. Larvae seem to settle just fine near Bonaire and Curaçao, even where development has resulted in pollution and high sediment loads. Szmant and Miller are panning for clues to these reefs' secrets to success.

In the Florida Keys, Miller has teamed up with molecular ecologist Iliana Baums of Pennsylvania State University in State College to probe whether survival depends on having the right parents. In 2005, Baums developed a genetic test that distinguishes individual elkhorn corals. The test uses short bits of variable DNA called microsatellites. Last summer, Miller and Baums collected egg and sperm from elkhorn and mountainous star coral, looked at their microsatellite makeup, and cross-fertilized gametes from a number of individuals. They tallied how many larvae of each cross settled on plates coated with various communities of microbes and algae. "We saw incredible differences in the performance of different crosses," says Baums. Some crosses yielded few offspring, whereas others were prolific. Reef restoration may depend on collecting gametes from the hardiest parent colonies, says Baums.

Matchmaking

Larvae lucky enough to find turf to colonize can't go it alone: They must latch onto a symbiont. They tend to be picky about which microscopic zooxanthellae algae will get a cozy intracellular home in return for generating a stable food supply. Mary Alice Coffroth, a marine biologist at the University at Buffalo, New York, and her colleagues have been teasing out the molecular signals that underlie a successful match.

Researchers suspect that larvae recruit algal partners from the water column. Coffroth and others are showing that larvae are selective but not dead set on particular species. Coffroth evaluated the potential of free-living *Symbiodinium* to join forces with young corals called octocorals by suspending trays of newly settled

CREDITS (TOP TO BOTTOM): ERNESTO WEIL

larvae 20 meters above a reef. At the beginning of the experiment, none of the larvae had algae, but by the end, Coffroth and her colleagues found that just three of the many *Symbiodinium* varieties in the water had taken up residence in coral polyps. They found a similar pattern with algae from reef rubble and other bottom surfaces where octocoral colonies live, they reported in the 5 December 2006 issue of *Current Biology*.

It remains a mystery how corals and zooxanthellae strike up a relationship. To eavesdrop on the molecular signals of courtship, Mónica Medina, a geneticist at the University of California, Merced, and her colleagues have collected larvae, extracted DNA, and pulled out bits of genes called expressed sequence tags (ESTs), which allow researchers to study genes without knowing the full sequence. So far they have 10,000 ESTs for each of two coral species and about 900 zooxanthellae genes represented. They are putting the DNA to work on chips that can monitor changes in expression in thousands of genes at a time. In 2006, Medina and others collected eggs and sperm of elkhorn and mountainous star coral from a Florida reef, then used DNA chips to monitor gene expression after fertilization. When they expose larvae to zooxanthellae, "the corals go wild," says Medina, switching on scads of genes.

Virginia Weis, a cell biologist at Oregon State University in Corvallis, has some ideas about which genes are important. In studies of the sea anemone, a coral cousin that also has symbionts, she discovered that a nascent relationship hinges on run-of-the-mill genes involved in programmed cell death and cell division.

Planned parenthood

Understanding the molecular details of symbiosis should one day help guide efforts to save coral species. But the National Zoo's Henley and his three dozen SECORE partners aren't waiting for answers. Nor are Szmant and Miller. They are taking coral sexual reproduction into their own hands.

In 2001, Dirk Petersen and Michael Laterveer of the Rotterdam Zoo in the Netherlands set up SECORE to encourage aquarists to bring coral reproduction in-house rather than depend on harvesting coral from the sea. Working with larvae of two species, Atlantic brain coral and boulder star coral (*Montastraea annularis*) from Curaçao, Petersen figured out how to gather and fertilize gametes and raise larvae.

Coral nurseries. SECORE divers collect spawned gametes (*above*) and rear fertilized eggs in containers flushed with saltwater.

CREDITS (TOP TO BOTTOM): DIRK PETERSEN

Last year, SECORE researchers and aquarists netted 900,000 elkhorn larvae in Puerto Rico. Each night during the spawning season that August, divers collected gametes and quickly returned them to shore or boat, where others would mix gametes from different spots, gently rocking coolers to encourage fertilization. "The whole crew had to work in 2-hour shifts, 24 hours a day for 4 days," Petersen recalls.

They wound up with far more larvae than they could handle. Convention on International Trade in Endangered Species of Wild Fauna and Flora permits did not come through in time for the European participants. And there were fresh hassles. Previously, Petersen had transported larvae in carry-on luggage. But last year, new security rules relegated corals to baggage, and 100,000 larvae destined for the Columbus Zoo and Aquarium in Ohio got lost in transit for 2 days and perished. Months later, only corals under the care of Mitch Carl of the Henry Doorly Zoo in Omaha, Nebraska, had survived. He distributed many to other SECORE members, and 821 colonies are now thriving.

The second time around, last August, Henley and other SECORE colleagues each took home about 10,000 larvae. Once again, only Carl had the magic touch: He is raising some 900 incipient colonies. "I'll be happy if I have one colony left after 1 year," says Henley.

Likewise, Szmant and Miller have little to show for their efforts to collect and fertilize gametes during spawning expeditions. They release some larvae right away and put others on the reef after these have settled on ceramic plates in the lab. "We have been trying various things to increase survivorship, but no major breakthrough yet," says Szmant. Baums's findings suggest that a breakthrough may come through "breeding" corals that produce hardy offspring.

The stakes are high to get it right. "If the larvae can survive and settle and grow into adults," Szmant says, "then there's hope that the reefs will recover."

–ELIZABETH PENNISI

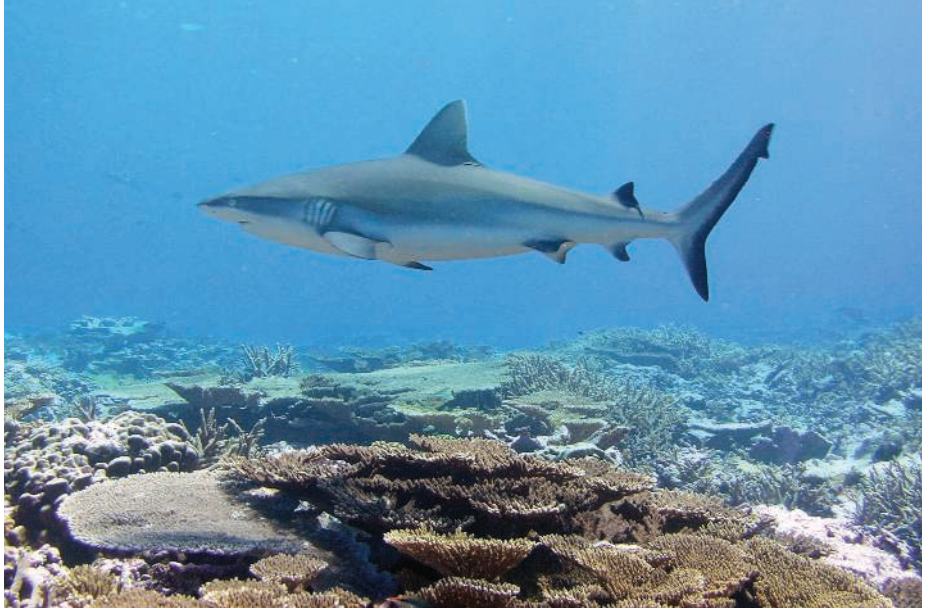

Splendid isolation. A shark patrols Kingman Atoll.

ECOLOGY

Life on the Mean Reefs

The short, nasty existence for reef-dwelling fish at two primeval atolls suggests that intensive fishing elsewhere has skewed predator-prey dynamics

Imagine an atoll in the time of Eden. It would be teeming with fish, a few big ones and a lot of little ones swarming among the coral reefs.

Think again, says a group of marine biologists who have been studying the Line Islands south of Hawaii. Led by researchers at the Scripps Institution of Oceanography in San Diego, California, they are comparing Kingman and neighboring Palmyra—U.S. possessions that are among a handful of Pacific atolls virtually untouched by humans—with Fanning and Christmas, which belong to Kiribati and respectively have some 3000 and 6000 residents.

To their surprise, the scientists found that life at Kingman is anything but idyllic. The ecosystem is dominated by large predators to an extraordinary degree: About 85% of the estimated mass of all fish is made up of apex predators such as sharks, large jacks, and snappers. For the prey fish, life in the real Edens of Kingman and Palmyra is just as the English philosopher Thomas Hobbes had described it for humankind without society: "Nasty, brutish, and short."

"Inverted pyramids have been documented in plankton but never within a community of large animals," says Scripps's Stuart Sandin, the project's coordinator. "The intensity of predation is new." The more familiar pyramid occurs at Christmas Island, where sharks have been fished for their fins and jacks and snappers for food. There, apex predators make up only 15% of the biomass. Their findings are in review at two publications.

To begin to understand the future of reefs in a warming world, it's not only important to unravel the mysteries of coral but also essential to work out the dynamics of reef communities. The more researchers learn, the more acutely they feel the need to restore reefs to a state resembling primeval Kingman and Palmyra. "If we don't protect these places, it will be the end of true natural selection in the oceans," says Alan Friedlander of the National Oceanic and Atmospheric Administration's biogeography branch in Hawaii.

When the cat's away … Fewer predators near Fiji mean hordes of small fish out and about, like these fairy basslets—but less total fish mass than at Kingman and Palmyra.

Seen underwater, Kingman, a mostly sunken atoll 15 kilometers long, "looks like a small town at the start of a classic Western movie," Friedlander says. "There's nobody out on the street except for a few big bullies, and the basements are crowded with petrified locals."

"It looks weirdly empty," agrees Sandin. "In Fiji, you'll see hundreds of colorful fish milling around, even though there's 20 times more fish [by weight] at Kingman." Crevices are so precious that when one occupant ventures out to feed, another takes its place. "It's hot-bunking," says Friedlander, referring to the Navy custom of having three men occupy one bunk in 8-hour shifts. As a result of this lopsided structure, a Kingman denizen from a prey species has little chance of reaching puberty. "That's why these fish are evolutionarily so important," says Sandin. "Only the very fittest survive."

How can so many predators live off so few prey? Because prey reproduce and grow much faster than predators do. "It's like your lawn," says Friedlander. "The more you mow it, the faster and thicker it grows." At Kingman, half-pints like surgeonfish, wrasses, and damselfish live about half as long as counterparts at Christmas, where the average prey is 20% bigger.

Still, life is literally no picnic at the top of the food chain. Examining predators' stomachs, the scientists found them mostly empty. "Kingman has shown us that unlike mammals, fish can survive with very little food. They simply grow slower," Sandin says. And they don't turn on each other, he says, because they don't want to risk injury. Nowhere else has Sandin observed the voracious scrutiny that spearing elicits at Kingman and Palmyra. "Your buddy shoots his spear against a rock—ping!—and you notice that all the predators in the neighborhood turn around. He shoots a fish and they all come closer. If the fish gets away with an injury, it will be eaten within a minute," he says. Desperation has made the predators fearless. "They nip at anything that moves: ears, ponytails, even pencils," Sandin says.

Such primeval reefs need not be kept in pristine isolation: They could be a test bed for sustainable approaches to fishing, researchers say. "We need to study more pristine reefs to see how much you can fish without reducing the fish stocks," Sandin says. "That's the key question we need to answer."

–CHRISTOPHER PALA

Christopher Pala is a writer based in Honolulu.

CREDITS (TOP TO BOTTOM): JENNIFER SMITH; STUART WESTMORLAND/CORBIS

Economics and terrorism 1726

Implementation science 1728

When whiteflies attack 1733

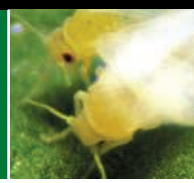

LETTERS | BOOKS | POLICY FORUM | EDUCATION FORUM | PERSPECTIVES

LETTERS

edited by Jennifer Sills

Switch to Corn Promotes Amazon Deforestation

THE UNITED STATES IS THE WORLD'S LEADING PRODUCER OF SOY. HOWEVER, MANY U.S. FARMERS are shifting from soy to corn (maize) in order to qualify for generous government subsidies intended to promote biofuel production (*1*); since 2006, U.S. corn production has risen 19% while soy production has fallen by 15% (*2*). This in turn is helping to drive a major increase in global soy prices (*3*), which have nearly doubled in the past 14 months.

The rising price for soy has important consequences for Amazonian forests and savanna-woodlands (*4*). In Brazil, the world's second-leading soy producer, deforestation rates (*5*) and especially fire incidence (*6*) have increased sharply in recent months in the main soy- and beef-producing states in Amazonia (and not in states with little soy production). Although dry weather is a contributing factor, these increases are widely attributed to rising soy and beef prices (*5*, *7*), and studies suggest a strong link between Amazonian deforestation and soy demand (*8*, *9*).

Deforestation. The aftermath of forest burning in central Amazonia.

Some Amazonian forests are directly cleared for soy farms (*8*). Farmers also purchase large expanses of cattle pasture for soy production, effectively pushing the ranchers farther into the Amazonian frontier or onto lands unsuitable for soy production (*9*). In addition, higher soy costs tend to raise global beef prices because soy-based livestock feeds become more expensive (*10*), creating an indirect incentive for forest conversion to pasture. Finally, the powerful Brazilian soy lobby is a key driving force behind initiatives to expand Amazonian highways and transportation networks in order to transport soybeans to market, and this is greatly increasing access to forests for ranchers, loggers, and land speculators (*11*, *12*).

In a globalized world, the impacts of local decisions about crop preferences can have far-reaching implications. As illustrated by an apparent "corn connection" to Amazonian deforestation, the environmental benefits of corn-based biofuel might be considerably reduced when its full and indirect costs are considered.

WILLIAM F. LAURANCE

Smithsonian Tropical Research Institute, Apartado 0843-03092, Balboa, Ancón, Panama. E-mail: laurancew@si.edu

References and Notes

1. P. C. Westcott, "U.S. ethanol expansion driving changes throughout the agricultural sector" (www.ers.usda.gov/amberwaves/september07/features/ethanol.htm).
2. National Agricultural Statistics Service Acreage Report, U.S. Department of Agriculture (www.usda.gov/nass/PUBS/TODAYRPT/acrg0607.pdf).
3. USDA-ERS (www.ers.usda.gov/data/priceforecast/data/futmodsoybeans.xls). Growing global demands for soy for edible oil, livestock feed, and biodiesel are also contributing to high soy prices.
4. The corn-soy-deforestation link was evidently first noted by D. C. Nepstad *et al.*, *The Amazon in a Changing Climate: Large-Scale Reductions of Carbon Emissions from Deforestation and Forest Impoverishment* [Amazon Institute for Environmental Research (IPAM), 2006].
5. C. Angelo, Desmatamento cresce 8% na Amazonia, *Folha de São Paulo Online* (www1.folha.uol.com.br/folha/ambiente/ult10007u337678.shtml).
6. ImazonGeo (http://imazongeo.org.br/alerta2.php).
7. R. A. Butler, "Is the Amazon more valuable for carbon offsets than cattle or soy?" (mongabay.com, 17 October 2007); http://news.mongabay.com/2007/1017-amazon.html.
8. D. C. Morton *et al.*, *Proc. Nat. Acad. Sci. U.S.A.* **103**, 14637 (2006).
9. D. C. Nepstad *et al.*, *Conserv. Biol.* **20**, 1595 (2006).
10. D. L. Hard, in *Protein Sources for the Animal Feed Industry* (Animal and Production Health Proceedings, FAO, Rome, 2002), pp. 125–140.
11. W. F. Laurance *et al.*, *Science* **291**, 438 (2001).
12. P. M. Fearnside, *Environ. Conserv.* **28**, 23 (2001).

CREDIT: WILLIAM F. LAURANCE

NASA Funding Slow, Not Steady, After Space Race

AFTER READING D. KENNEDY'S EDITORIAL "Sputnik nostalgia" (5 October, p. 17), I find myself in a state I did not expect—one of disappointment. Kennedy writes about the positive effects the launch of Sputnik had on education and the nation's educational community. These improvements resulted largely from an increase in federal sponsorship that came as part of the backlash from Sputnik. Yet, there lies within this seemingly fine outcome an issue that needs to be addressed.

The National Aeronautics and Space Administration (NASA) was formed along with a dramatic increase in federal funding for science and science education in response to the former Soviet Union's incredible achievement (*1*). When Neil Armstrong became the first person to set foot on the moon, the government's interest in science dropped almost immediately. Because of the sudden lack of funding, the Apollo program was discontinued just 6 years after Apollo 11 landed in the Sea of Tranquility, in order to save funds for the shuttle and Skylab programs (*2*). Lately, NASA has received additional funding to attempt a second series of missions to the moon as part of the Constellation Program (*3*), but the long-awaited increase is the bittersweet result of an imaginary space race (*4*).

It seems that only when faced with the threat of looking stupid or coming in second place does our government open its wallet to science (*1*, *4*).

MICHAEL J. GOLDSTEIN

Department of Biology, Rutgers University, Camden, NJ 08102, USA.

References

1. J. F. Kennedy, Special Message to the Congress on Urgent National Needs, Washington, DC, 25 May 1961.
2. R. W. Orloff, *Apollo by the Numbers* (NASA History Division, Washington, DC, 2000).
3. W. Gerstenmaier, paper presented before the Subcommittee on Space, Aeronautics, and Related Sciences, Washington, DC, 28 March 2007.
4. R. Block, "NASA points to foreign competition to spark support," *Orlando Sentinel*, 23 October 2007.

Memory Suppression in PTSD Treatment?

IN THEIR RESEARCH ARTICLE "PREFRONTAL regions orchestrate suppression of emotional memories via a two-phase process" (13 July, p. 215), B. E. Depue *et al.* suggest possible "implications for therapeutic approaches" for emotionally distressing memories. They speculate that the results "provide the possibility for approaches to controlling memories by suppressing sensory aspects of memory." As experimental psychopathologists, we applaud the elegant experimental approach and welcome new ideas for clinical innovation. However, the proposal that suppression would be a beneficial strategy for clinical intrusive memories is directly counter to treatment outcome data. For example, the gold standard treatment for posttraumatic stress disorder (PTSD) is cognitive behavior therapy that involves repeatedly and intentionally bringing the trauma memory and associated affect to mind—a technique that is antithetical to suppression (*1*).

Empirically supported theories of PTSD implicate cognitive avoidance (e.g., via thought suppression) in its persistence (*2*), with avoidance of trauma memories in the acute phase predicting PTSD at one year (*3*). While suppression may reduce distress in the short term, it predicts symptom maintenance (i.e., exacerbated trauma memories) in the long term.

The tension between epidemiological and treatment data and the apparent implications of the Depue *et al.* observations are worthy of attention, and may provide a more sophisticated understanding of both areas. In the meantime, there is a need for caution and for careful consideration of the relevant literature before inferring clinical implications from experimental studies such as these, particularly when a suggestion is liable to harm patients.

EMILY A. HOLMES,[1] MICHELLE L. MOULDS,[2] DAVID KAVANAGH[3]

[1]Department of Psychiatry, University of Oxford, Warneford Hospital, Oxford OX3 7JS, UK. [2]School of Psychology, The University of New South Wales, Sydney, NSW 2052, Australia. [3]School of Medicine, The University of Queensland, Herston, QLD 4029, Australia.

References

1. NICE, "Post-traumatic stress disorder (PTSD): The management of PTSD in adults and children in primary and secondary care" *Tech. Report No. CG026* (National Institute for Clinical Excellence, 2005).
2. A. Ehlers, D. M. Clark, *Behav. Res. Ther.* **38**, 319 (2000).
3. A. Ehlers, R. A. Mayou, B. Bryant, *J. Abnorm. Psychol.* **107**, 508 (1998).

Response

HOLMES *ET AL*. RAISE THE EXCELLENT POINT that suppression seems antithetical to the use of cognitive behavior therapy (CBT), especially exposure therapy, for disorders like

Letters to the Editor

Letters (~300 words) discuss material published in *Science* in the previous 3 months or issues of general interest. They can be submitted through the Web (www.submit2science.org) or by regular mail (1200 New York Ave., NW, Washington, DC 20005, USA). Letters are not acknowledged upon receipt, nor are authors generally consulted before publication. Whether published in full or in part, letters are subject to editing for clarity and space.

CORRECTIONS AND CLARIFICATIONS

Reports: "DNA double-strand breaks trigger genome-wide sister-chromatid cohesion through Eco1 (Ctf7)" by E. Ünal *et al.* (13 July, p. 245). In the print and HTML versions, the labels on the red and green shapes in Fig. 4 are missing. The corrected figure appears here. The labels appear in the PDF version.

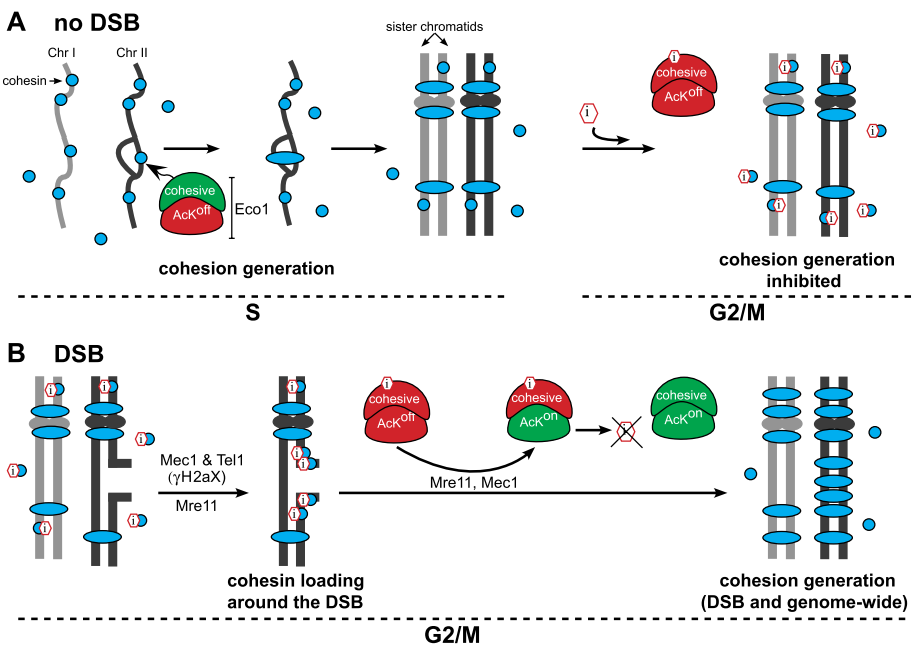

TECHNICAL COMMENT ABSTRACTS

COMMENT ON "Tumor Growth Need Not Be Driven by Rare Cancer Stem Cells"

James A. Kennedy, Frédéric Barabé, Armando G. Poeppl, Jean C. Y. Wang, John E. Dick

Kelly *et al.* (Brevia, 20 July 2007, p. 337) questioned xenotransplant experiments supporting the cancer stem cell (CSC) hypothesis because they found a high frequency of leukemia-initiating cells (L-IC) in some transgenic mouse models. However, the CSC hypothesis depends on prospective purification of cells with tumor-initiating capacity, irrespective of frequency. Moreover, we found similar L-IC frequencies in genetically comparable leukemias using syngeneic or xenogeneic models.

Full text at www.sciencemag.org/cgi/content/full/318/5857/1722c

RESPONSE TO COMMENT ON "Tumor Growth Need Not Be Driven by Rare Cancer Stem Cells"

Jerry M. Adams, Priscilla N. Kelly, Aleksandar Dakic, Stephen L. Nutt, Andreas Strasser

A critical issue for cancer biology and therapy is whether most tumor cells or only rare "cancer stem cells" sustain tumor growth. Although the latter model seems supported by the minute proportion of human leukemia cells that can grow in immunodeficient mice, evidence that more than 10% of cells in many mouse leukemias and lymphomas are transplantable challenges its generality.

Full text at www.sciencemag.org/cgi/content/full/318/5857/1722d

PTSD. In responding, we need to consider complexities in the treatment of these disorders that we could only briefly allude to in our Research Article (13 July, p. 215) (*1*).

First, Holmes *et al*. note that PTSD patients who characteristically avoid their traumatic memories have a poorer prognosis. However, unsystematic avoidance by a patient is not the same as a systematic therapeutic process of directed suppression, which involves the acquisition of neural suppression over a number of trials. Second, we do not advocate suppression as a sole means of treatment for PTSD, but rather as a complementary treatment with other methods. For example, it may be necessary to revisit an emotionally distressing memory before it can be controlled [our Research Article and (*1*)].

Currently, only about 30 to 70% of PTSD patients respond successfully to exposure therapy alone. Even these "responders" are only classified as such because they experience reductions in just one or two key symptoms (*2*). Other symptoms may still be vivid, and patients may suffer from relapses.

Few long-term comprehensive studies of the relapse rate of PTSD symptoms have been reported beyond 6 months. Furthermore, because PTSD research lacks rigorous randomized clinical trials, "responder" levels have been overreported (*3*). We believe, therefore, that conceptualization and testing of complementary therapeutic approaches is needed.

Some forms of CBT may tap into the brain mechanisms underlying suppression. Research suggests that cognitive restructuring could benefit sufferers of PTSD (*4*). Cognitive restructuring processes may involve attaching a new emotional significance to a negative memory or cognition, as well as lessening physiological arousal (*5*, *6*). Furthermore, new responses paired with an original conditioned stimulus may have inhibitory influences over the amygdala via a pathway from the medial prefrontal cortex to the basolateral amygdala to the central amygdala (*7*, *8*). In addition, research examining the cognitive manipulation of emotional significance, known as reappraisal, has shown increased activation in areas of the middle and inferior frontal gyri and decreased activation in the amygdala (*9*). These are the specific prefrontal areas involved in suppression in our Research Article. Perhaps all of these findings explain why it may be necessary to revisit an emotionally distressing memory before it can be controlled via suppression. In any case, such processes may provide part of the biological basis for exposure and restructuring CBT methods.

BRENDAN E. DEPUE,[1,2]* TIM CURRAN,[1,2,3] MARIE T. BANICH[1,2,3,4]

[1]Department of Psychology, University of Colorado, Boulder, CO 80309, USA. [2]Center for Neuroscience, University of Colorado, Boulder, CO 80309, USA. [3]Institute of Cognitive Science, University of Colorado, Boulder, CO 80309, USA. [4]Department of Psychiatry, University of Denver Health Sciences, Denver, CO 80208, USA.

*To whom correspondence should be addressed. E-mail: depue@colorado.edu

References

1. B. E. Depue, T. Curran, M. T. Banich, *Psychol. Sci.* **17**, 441 (2006).
2. R. Bradley *et al*., *Am. J. Psychiatr.* **162**, 214 (2005).
3. G. Harvey, R. A. Bryant, N. Tarrier, *Clin. Psychol. Rev.* **23**, 501 (2003).
4. B. Nemeroff *et al*., *J. Psychiatr. Res.* **40**, 1 (2006).
5. J. Debiec, V. Doyere, K. Nader, J. E. Ledoux, *Proc. Natl. Acad. Sci. U.S.A.* **103**, 3428 (2006).
6. I. Izquierdo, M. Cammarota, *Science* **304**, 829 (2004).
7. G. J. Quirk *et al*., *J. Neurosci.* **23**, 8800 (2003).
8. M. R. Milad, G. J. Quirk, *Nature* **420**, 70 (2002).
9. N. Ochsner *et al*., *J. Cognit. Neurosci.* **14**, 1215 (2002).

Comment on "Tumor Growth Need Not Be Driven by Rare Cancer Stem Cells"

James A. Kennedy,[1,2] Frédéric Barabé,[3,4,5] Armando G. Poeppl,[1] Jean C. Y. Wang,[1,6,7] John E. Dick[1,2]*

Kelly *et al*. (Brevia, 20 July 2007, p. 337) questioned xenotransplant experiments supporting the cancer stem cell (CSC) hypothesis because they found a high frequency of leukemia-initiating cells (L-IC) in some transgenic mouse models. However, the CSC hypothesis depends on prospective purification of cells with tumor-initiating capacity, irrespective of frequency. Moreover, we found similar L-IC frequencies in genetically comparable leukemias using syngeneic or xenogeneic models.

Kelly *et al*. (*1*) observed that more than 10% of the bulk tumor cells in several transgenic mouse models of leukemia and lymphoma were capable of initiating malignant growth upon transplantation into histocompatible mice. These values clearly contrast with the leukemia-initiating cell (L-IC) frequency on the order of 1 in 10^4 to 10^7 that has been reported for primary human acute myeloid leukemia (AML) after intravenous transplantation of bulk blast cells at limiting doses into severe combined immunodeficient (SCID) or nonobese diabetic (NOD)/SCID mice (*2*–*4*). Kelly *et al*. proposed that this quantitative difference arises from an inability of the human cells to grow efficiently in the murine bone marrow (BM) microenvironment and leads to a routine underestimation of the frequency of tumor-initiating cells in xenotransplantation assays. Based on these observations, the authors called into question the main conclusion of these and subsequent studies, namely that both human leukemias and solid tumors are hierarchically organized and sustained by a population of biologically distinct cancer stem cells (CSC) (*2*, *3*, *5*). Kelly *et al*. clearly demonstrated that in some experimental cancer models, tumorigenic growth need not be driven by rare CSCs; however, their criticism of xenotransplantation assays and their challenge of the generality of the CSC hypothesis merit some discussion.

Undoubtedly, human cell engraftment in xenotransplant models is limited by residual elements of the recipient immune system, the absence of cross-species reactivity of some cytokines, and other components of the murine microenvironment. The first-generation models used to perform the aforementioned calculations of L-IC frequency presented substantial barriers to human cell engraftment. Since these initial reports, improvements including depletion of residual immune activity, direct injection of cells into bone cavities, and transgenic expression of human cytokines have increased the sensitivity of detection of normal human hematopoietic stem cells, warranting a reassessment of L-IC frequency in primary human leukemias (*6*–*8*). Our unpublished work and that of others (*8*) suggests that optimized assays increase L-IC detection by 1 to 2 orders of magnitude; nevertheless, L-ICs in primary human AML remain relatively rare, with high variation in frequency from sample to sample.

Using these improved xenograft assays, we recently developed a genetically induced model of human B cell acute lymphoblastic leukemia (B-ALL) by transplanting primary human umbilical cord blood stem/progenitor cells expressing the *mixed lineage leukemia–eleven-nineteen leukemia* (*MLL-ENL*) oncogene into immunodeficient mice (*9*). To determine L-IC frequency in this model, limiting numbers of BM cells from primary leukemic mice were transplanted into secondary recipients. As summarized in Table 1, the L-IC frequency in the bulk leukemic blast population was on the order of 1%. Interestingly, our L-IC frequency was comparable to that reported for a murine retroviral transduction/transplantation model of MLL-AF9–induced AML (1 in 150) (*10*). Furthermore, purification of human leukemic cells from the BM of primary mice on the basis of CD19 and CD34 expression showed that L-ICs were enriched in the $CD19^+CD34^+$ fraction compared with the $CD19^+CD34^-$ fraction and were absent in the $CD19^-CD34^-$ fraction (table S1). Thus, these data prove the existence of discrete L-IC in this model and demonstrate that these cells can be detected at high frequencies in xenograft systems despite barriers to human cell growth. Furthermore, these studies indicate that when genetically comparable leukemia models are studied, syngeneic and xenogeneic approaches can yield similar calculations of L-IC frequency.

In addition to Kelly *et al*. (*1*) and the studies discussed above, demonstration of functional heterogeneity and assessment of L-IC frequencies have been reported in the literature for many decades. For example, in 1963, Bruce and van der Gaag (*11*) reported that the frequency of clonogenic lymphoma cells from spontaneously occurring murine lymphomas ranged from 0.001% to 1% in syngeneic recipients. In a MOZ-TIF retroviral transduction/transplantation model, the L-IC frequency was on the order of 1 in 10^4 (*12*), whereas it was 1 in 6×10^5 in a *Pten* deletion model of AML (*13*). Thus, it is evident that L-IC frequencies can vary widely between different cancers regardless of whether they are quantified using xeno- or syngeneic transplant assays. We hypothesize that different cancers will exhibit variable degrees of functional heterogeneity as a consequence of the specific oncogenic pathways operating within the neoplasm, resulting in different CSC frequencies. However, we must emphasize that the fundamental concept underlying the CSC hypothesis is not related to the absolute frequency of these cells; instead, this model proposes that the basis of the functional heterogeneity within tumors is the presence of a distinct population of cells that

Table 1. Limiting dilution analysis of *MLL-ENL* B-precursor ALL. Leukemia was defined as ≥20% $CD19^+CD20^-$ blasts in the BM. The data from leukemia 1 have appeared previously (*9*).

	Cell dose	Frequency of leukemia	Median disease latency
MLL-ENL leukemia 1	250,000	2/2	77
	50,000	2/2	85
	10,000	5/5	85
	2,000	4/4	104
	400	0/3	n/a
MLL-ENL leukemia 2	125,000	2/2	57
	25,000	2/2	64
	5,000	5/5	85
	1,000	4/4	92
	200	3/4	125

[1]Division of Cell and Molecular Biology, University Health Network, Toronto, Canada. [2]Department of Molecular and Medical Genetics, University of Toronto, Toronto, Canada. [3]Department of Medicine, Laval University, Québec, Canada. [4]Department of Hematology, Enfant-Jesus Hospital, Québec, Canada. [5]Research Center in Infectious Diseases, Centre Hospitalier Universìtaire de Québec/Centre Hospitalier de l'Université Laval, Québec, Canada. [6]Division of Medical Oncology and Hematology, Department of Medicine, University Health Network, Toronto, Canada. [7]Department of Medicine, University of Toronto, Toronto, Canada.

*To whom correspondence should be addressed. E-mail: jdick@uhnres.utoronto.ca

can be prospectively isolated and can initiate malignant growth in vivo while the remaining cells cannot. The therapeutic implications of CSCs remain the same regardless of their absolute frequency: These cells, which may have growth or therapeutic resistance properties that differ from those of the bulk tumor, must be effectively targeted to achieve definitive curative benefits.

Kelly *et al*. (*1*) raise the important point that some experimental cancer models may not follow the CSC hypothesis. Accordingly, some human cancers may be found that also do not adhere to this model. However, it is important to consider that, similar to many cell lines that have lost the hierarchical structure of the primary leukemia from which they originated, some experimental mouse models may not accurately reflect spontaneously occurring human malignancies. For example, one could argue that some of the models used by Kelly *et al*. (i.e., the *N-Ras* lymphoma) have limited human antecedents.

Finally, Kelly *et al*. state that the term "cancer stem cell" designates an origin from normal tissue stem cells, a point that has long been a source of confusion in the literature. Recently, an AACR panel made up of experts in the stem cell field agreed that the term "cancer stem cell" does not speak to the cell of origin (the normal cell type that becomes transformed and gives rise to the cancer). Instead, this term, albeit imperfect, encompasses the notion that the cell type that sustains the growth of many cancers possesses stem cell properties, such as a capacity for self-renewal, and lies at the pinnacle of a neoplastic hierarchy, giving rise to "differentiated" progeny that lack these same properties (*14*).

References

1. P. N. Kelly, A. Dakic, J. M. Adams, S. L. Nutt, A. Strasser, *Science* **317**, 337 (2007).
2. T. Lapidot *et al*., *Nature* **367**, 645 (1994).
3. D. Bonnet, J. E. Dick, *Nat. Med.* **3**, 730 (1997).
4. L. E. Ailles, B. Gerhard, H. Kawagoe, D. E. Hogge, *Blood* **94**, 1761 (1999).
5. N. A. Lobo, Y. Shimono, D. Qian, M. F. Clarke, *Annu. Rev. Cell Dev. Biol.* **23**, 675 (2007).
6. T. Yahata *et al*., *Blood* **101**, 2905 (2003).
7. J. L. McKenzie, O. I. Gan, M. Doedens, J. E. Dick, *Blood* **106**, 1259 (2005).
8. M. Feuring-Buske *et al*., *Leukemia* **17**, 760 (2003).
9. F. Barabé, J. A. Kennedy, K. J. Hope, J. E. Dick, *Science* **316**, 600 (2007).
10. A. V. Krivtsov *et al*., *Nature* **442**, 818 (2006).
11. W. R. Bruce, H. van der Gaag, *Nature* **199**, 79 (1963).
12. B. J. Huntly *et al*., *Cancer Cell* **6**, 587 (2004).
13. O. H. Yilmaz *et al*., *Nature* **441**, 475 (2006).
14. M. F. Clarke *et al*., *Cancer Res.* **66**, 9339 (2006).

22 August 2007; accepted 9 November 2007
10.1126/science.1149590

Response to Comment on "Tumor Growth Need Not Be Driven by Rare Cancer Stem Cells"

Jerry M. Adams,[1*] Priscilla N. Kelly,[1,2] Aleksandar Dakic,[1,2] Stephen L. Nutt,[1] Andreas Strasser[1*]

A critical issue for cancer biology and therapy is whether most tumor cells or only rare "cancer stem cells" sustain tumor growth. Although the latter model seems supported by the minute proportion of human leukemia cells that can grow in immunodeficient mice, evidence that more than 10% of cells in many mouse leukemias and lymphomas are transplantable challenges its generality.

A key unresolved issue for cancer biology and therapy is whether the relentless growth of a tumor is driven by most of its cells or, as proposed by the cancer stem cell hypothesis, exclusively by a minor subpopulation capable of self-renewal, akin to the numerically rare normal stem cells that maintain tissues (*1*). The impetus for that hypothesis has come primarily from experiments in which human tumor cells are transplanted at limit dilution into immunodeficient mice. The most widely cited evidence is that, in human acute myelogenous leukemia (AML), only a minute proportion of the cells (10^{-4} to 10^{-7}) could seed leukemia growth in immunodeficient nonobese diabetic (NOD)/severe combined immunodeficient (SCID) mice (*2*). Xenotransplantation is problematic, however, because the incompatibility of many cytokine-receptor interactions between mouse and man may prevent critical relationships with the microenvironment. In striking contrast to human AML, with three types of primary monoclonal mouse tumors from genetically modified mice (B lymphomas, T lymphomas, and AML), we found that >10% of the cells readily seeded tumor growth in nonconditioned congenic recipients, and three of eight single-cell transfers attempted with a B lymphoma succeeded (*3*).

Other mouse leukemia models (albeit not all) have yielded similar results. Pertinently, in mouse AML induced by the *MLL-AF9* translocation gene, the leukemia growth-sustaining cells represented 25% of all myeloid cells (*4*). Similarly, as few as 20 BCR-ABL-transduced Arf-deficient pre-B cells could rapidly induce acute lymphocytic leukemia (*5*). Notably, in all these studies the cells that seeded leukemia resembled relatively mature cell types and not hematopoietic stem cells or primitive progenitors (*3*–*5*). Although an early study of an AKR mouse thymoma cited by Kennedy *et al*. (*6*) reported that <1% of cells were tumorigenic (*7*), it used a less sensitive, indirect assay (spleen colony formation rather than tumor growth), and the retroviral etiology of AKR tumors may well have caused their immunological rejection. In more relevant classical studies with both myeloid and lymphoid tumors, the leukemia growth-sustaining cells have typically ranged from >1 in 100 to the majority of cells, and some single-cell transfers have succeeded (*8*, *9*).

Thus, many mouse lymphomas and leukemias, including ones closely modeling human counterparts and involving equivalent genetic changes and stochastic onset, seem to be sustained by a substantial proportion of their cells (probably at least 1 to 30%). Hence, xenotransplantation may reveal only a minute fraction of the human AML cells that drive those leukemias. Supporting that view, 50% of human AML samples did not engraft NOD/SCID mice even when 10^7 or 10^8 cells were introduced (*10*). The new data from Kennedy *et al*. (*6*) showing that 10^{-2} to 10^{-3} of the cells in a human B cell acute lymphoblastic leukemia (B-ALL) model can initiate tumors in secondary transfers does not answer our major reservation about xenotransplantation, because the initial generation of these tumors within mice may have allowed selection for growth in that milieu. Also, the evidence that those tumors are maintained by a defined subpopulation of cells appears limited.

Kennedy *et al*. and other cancer stem cell advocates argue that the proof of the model is that cell populations prospectively isolated from human AML samples by surface markers initiate leukemia in mice, whereas the cell population lacking those markers does not (*1*, *2*). Two considerations question this argument. First, a human tumor cell population may fail to propagate in mice not from lack of self-renewal capacity but because of the lack of a receptor responsive to murine growth factors or the inability to home to a nurturing microenvironment. Second, rather than possessing unique self-renewal capacity, the NOD/SCID-transplantable population in human AML may have inadvertently acquired addressing molecules that target them to favorable niches in the mouse. With some types of mouse leukemias, no functionally distinct tumorigenic subpopulations have been discerned (*3*–*5*). Nevertheless, with other types, subpopulations enriched for leukemogenic cells have been identified (*11*–*13*), so the cancer stem cell model may well hold for some types of leukemia but not others. Interestingly, however, the reported phenotypes of the mouse leukemogenic subpopulations are variable and more similar to relatively mature cells than hematopoietic stem cells (*11*–*13*).

The evidence for cancer stem cells in solid tumors is less advanced than for AML (*1*) and is subject to the same reservations regarding xenotransplantation. The cancer-propagating cells are often found within subpopulations (e.g., $CD133^+$) that can contain up to 20% of the cells within a tumor (*14*, *15*). In some instances, the transplantable population might also contain essential support cells. For example, co-transfer of $CD133^+$ support cells might explain the puzzle that the colon cancer $CD133^+$ population appeared to contain 20 times as many cancer growth–sustaining cells as the unfractionated population (*16*). Much of the heterogeneity in tumors may well result from the subclonal genetic and epigenetic variation produced during tumor evolution, without the need to invoke a strict hierarchical relationship between subpopulations.

We agree with Kennedy *et al*. (*6*) that tumors are likely to fall on a spectrum in which the tumor-propagating cells range from infrequent to the dominant population. However, the marked disparities between most transplant results with human and mouse leukemias suggests that current xenotransplantation systems seriously underestimate the frequency of cells that can maintain the growth of human tumors. Several mouse tumor models challenge the generality of the cancer stem cell hypothesis, and more compelling tests with human tumors presumably will require transfer into mice installed with all the requisite human support cells and support factors. Much of the excitement about the cancer stem cell hypothesis arises from the possibility that the putative stem cell population will prove to be uniquely responsible for the relapses that so frequently follow conventional therapy (*1*). On the available evidence, however, we suggest that curative therapy will require targeting all the tumor subpopulations.

[1]Walter and Eliza Hall Institute of Medical Research, Melbourne 3050, Australia. [2]Department of Medical Biology, University of Melbourne, Melbourne 3050, Australia.

*To whom correspondence should be addressed. E-mail: adams@wehi.edu.au (J.M.A.); strasser@wehi.edu.au (A.S.)

References

1. M. F. Clarke *et al*., *Cancer Res.* **66**, 9339 (2006).
2. D. Bonnet, J. E. Dick, *Nat. Med.* **3**, 730 (1997).
3. P. N. Kelly, A. Dakic, J. M. Adams, S. L. Nutt, A. Strasser, *Science* **317**, 337 (2007).
4. T. C. Somervaille, M. L. Cleary, *Cancer Cell* **10**, 257 (2006).
5. R. T. Williams, W. den Besten, C. J. Sherr, *Genes Dev.* (2007).
6. J. A. Kennedy, F. Barabé, A. G. Poeppl, J. C. Y. Wang, J. E. Dick, *Science* **318**, 1722 (2007); www.sciencemag.org/cgi/content/full/318/5857/1722c.

7. W. R. Bruce, H. Van Der Gaag, *Nature* **199**, 79 (1963).
8. J. Furth, M. C. Kahn, *Am. J. Cancer* **31**, 276 (1937).
9. H. B. Hewitt, E. R. Blake, A. S. Walder, *Br. J. Cancer* **33**, 241 (1976).
10. D. J. Pearce *et al*., *Blood* **107**, 1166 (2006).
11. S. J. Neering *et al*., *Blood* **110**, 2578 (2007).
12. B. J. Huntly *et al*., *Cancer Cell* **6**, 587 (2004).
13. A. J. Deshpande *et al*., *Cancer Cell* **10**, 363 (2006).
14. M. Al-Hajj, M. S. Wicha, A. Benito-Hernandez, S. J. Morrison, M. F. Clarke, *Proc. Natl. Acad. Sci. U.S.A.* **100**, 3983 (2003).
15. L. Ricci-Vitiani *et al*., *Nature* **445**, 111 (2007).
16. C. A. O'Brien, A. Pollett, S. Gallinger, J. E. Dick, *Nature* **445**, 106 (2007).

11 September 2007; accepted 13 November 2007
10.1126/science.1149672

POLITICAL ECONOMICS

Why People Turn to Bombs

Ethan Bueno de Mesquita

What Makes a Terrorist
Economics and the Roots of Terrorism

by Alan B. Krueger

Princeton University Press, Princeton, NJ, 2007. 192 pp. $24.95, £14.95. ISBN 9780691134383.

In *What Makes a Terrorist: Economics and the Roots of Terrorism*, Alan Krueger (a professor of economics and public policy at Princeton University and adviser to the U.S. National Counterterrorism Center) addresses a key question in the academic and policy debates sparked by 9/11: What are the individual and societal causes of terrorism? The book's great strength is its focus on new sources of data examined in new ways. Somewhat less satisfying are the conclusions drawn from the evidence. Krueger seems overly confident that correlations in the data have simple causal interpretations. As a result, although the book makes real contributions to our understanding of the empirical landscape of terrorism, I remain skeptical of the author's inferences and policy conclusions.

The most compelling analysis in the book is of biographical information on operatives from Hezbollah and Hamas. This is a substantial contribution, offering insight into who becomes a terrorist and, as important, pushing terrorism studies in a productive new direction, toward microlevel data. Not surprisingly, these data yield Krueger's most provocative results: Terrorist operatives are neither poor nor poorly educated. Rather, their economic and educational statuses tend to lie around, or even slightly exceed, the averages in their societies. Moreover, terrorists are not especially likely to emerge from the world's poorest countries.

Following 9/11, many policy-makers took as self-evident that poverty and ignorance were at the root of terrorism. Krueger quotes President Bush: "We fight against poverty because hope is an answer to terror." The book provides a valuable service in dispelling the stereotype of the poor, ignorant terrorist. And Krueger takes the argument one step further, concluding, "A wealth of evidence now shows that any effect of education and poverty on terrorism is indirect, complicated, and probably quite weak."

The reviewer is at the Harris School of Public Policy Studies, University of Chicago, 1155 East 60th Street, Suite 108, Chicago, IL 60637, USA. E-mail: bdm@uchicago.edu

What, then, are the root causes of terror? Krueger suggests two. First, across countries, the absence of political freedom is positively correlated with terror attacks. Thus, Krueger argues, "a lack of civil liberties seems to be a main cause of terrorism around the world." Second, democracies are more often the victims of terrorism than autocracies. The reason, Krueger suggests, is that democratic leaders are more responsive than autocratic leaders to public opinion, making terrorism—a tactic designed to create mass panic—more effective in democracies.

Terror in the streets. This depiction of a bomb exploding on Paris's Avenue de la Republique appeared in the February 1905 issue of *Le Petit Journal*.

Krueger concludes that alleviating poverty is unlikely to reduce terrorism and that counterterrorism operations that violate civil liberties may be counterproductive. "The importance of guaranteeing civil liberties has been underemphasized as a means of prosecuting the war on terrorism and the war in Iraq," he argues. Krueger also suggests that terrorism "only matters in a big way if we let it matter." If the media and the government minimize the public panic that terrorist attacks engender, the negative consequences of such attacks will be diminished.

There are good reasons to be skeptical of Krueger's interpretations of his findings and, ultimately, of his policy conclusions. Ironically, most of the grounds for skepticism revolve around lessons that many social scientists learned from Krueger himself, in his pathbreaking work in labor economics on how to draw causal inferences from observational data—an approach made famous by another economist in the bestseller *Freakonomics* (*1*). In particular, one needs to be cautious in drawing even intuitive conclusions based on simple patterns in the data. Occasionally, Krueger acknowledges such concerns. Often, however, he seems overly confident of his conclusions, given the evidence.

One example relates to Krueger's argument that democracies suffer more terrorist attacks than autocracies because democratic leaders are more responsive to terrorism, making democracies attractive targets. Other scholars offer a different interpretation: the empirical relationship between regime type and terrorism is spurious and actually reflects systematic underreporting of terrorist incidents in nondemocracies (*2*). If they are correct, this calls Krueger's theoretical inference into question.

Critiques with more substantial policy implications can be made of other of Krueger's arguments. As I have discussed elsewhere (*3*), Krueger's important observation that terrorist operatives are neither poor nor poorly educated does not justify his conclusion that socioeconomic factors are irrelevant for terrorist mobilization. As Krueger himself notes, terrorist organizations screen potential recruits, preferring educated candidates because they are more effective in carrying out difficult assignments (*4*). To see the problem this creates for Krueger's logic, suppose that terrorist organizations accept recruits only over some competence threshold and that, as suggested by the data, competence is positively correlated with income or education. Suppose, further, that economic downturns increase mobilization (perhaps by decreasing opportunity costs). In such a world, because of screening, the terrorists actually observed will be neither poor nor poorly educated, just as in Krueger's data. Yet, Krueger's conclusion will not be true: the supply of acceptable operatives and, therefore, the expected level of violence will be affected by economic factors. Of course, this theoretical argument does not establish that poverty causes terrorism. But it does suggest that the data Krueger presents on the socioeconomic status of terrorists do not entail his inference that "there is not much question that poverty has little to do with terrorism."

For similar reasons, I am not as convinced as Krueger that the data show that limited political freedoms are a root cause of terror. The negative correlation between political freedom and terrorism could be due to causal forces that run in either direction—repression could spark violence or violence could lead a government to repress (a point that arises in the question-and-answer section at the end of the book). This causal uncertainty is important. In many conflict situations, counterterrorism operations necessitate an infringement on the rights and interests of civilians. As a result, sometimes civil liberties cannot be increased in the presence of a terrorist threat without a concomitant security trade-off. Before reaching strong conclusions about how to balance such concerns, we should seek more compelling evidence of the causal link between political freedom and political violence.

References

1. S. D. Levitt, S. J. Dubner, *Freakonomics: A Rogue Economist Explores the Hidden Side of Everything* (Morrow, New York, 2005).
2. K. Drakos, A Gofas, *J. Conflict Resolut.* **50**, 714 (2006).
3. E. Bueno de Mesquita, *Am. J. Polit. Sci.* **49**, 515 (2005).
4. E. Benmelech, C. Berrebi, *J. Econ. Perspect.* **21**(3), 223 (2007).

10.1126/science.1151192

MICROBIOLOGY

Life in the Really Hard Places

Tom Schmidt

In the classic *Microbe Hunters* (*1*), microbiologist Paul de Kruif provided an enthralling account of scientists who had devoted their careers to pursuing the unseen world of microbes. His tales of their difficult but rewarding work that identified bacteria and viruses as the causative agents of many of the medical scourges plaguing humanity inspired many current researchers in the field. *The Third Domain* has the potential to similarly enthrall readers and inspire future generations of microbiologists. Rather than recounting discoveries about the relatively few microbes that cause disease, Tim Friend takes readers on a journey that begins with the discovery of the Archaea—a fundamental discovery that challenged the paradigm that life splits neatly into two distinct groups, one prokaryotic and the other eukaryotic. As Friend so deftly explains, instead there are three primary lineages (or domains) of evolutionary descent: Bacteria, Eukarya, and Archaea.

The Third Domain
The Untold Story of Archaea and the Future of Biotechnology
by Tim Friend
Joseph Henry Press, Washington, DC, 2007. 312 pp. $27.95, C$32.95. ISBN 9780309102377.

The journey begins in the 1960s at the University of Illinois, where Carl Woese, driven by a vision of the tremendous value that would be derived from a phylogenetic tree encompassing all forms of life, developed the means to assess the evolutionary relatedness of microbes. (Friend gained an insider's historical perspective through conversations with many of the scientists featured in the book, including Woese.) We learn of the combination of insight and persistence that led to Woese's discovery of the Archaea. Perhaps not surprisingly, serendipity played a part as well: Ralph Wolfe—the world expert on methane-producing "bacteria"—occupied a lab just down the hall from Woese and suggested that he take a look at these unusual microbes. Those methanogens offered the first evidence that there was more to life than bacteria and eukaryotes. As in any engaging history of science, it is not just the discovery that is recounted; in addition, readers are offered a view into the politics of science. We find that Woese's discovery of the Archaea was greeted with skepticism by many and ridicule by others, including some very influential scientists.

Along the way, readers meet some of the researchers who recognized early on the dramatic consequences of Woese's discovery. These include the swashbuckling Karl Stetter, hunter extraordinaire of microbes that prefer life in boiling, sulfide-rich waters, and Norman Pace, who combined molecular phylogenetics with strategies to cull DNA sequences directly from natural communities of microbes. Pace's approach to exploring the microbial world without requiring that the organisms of interest be maintained in cultures unleashed a revolution in microbial ecology that continues to reverberate.

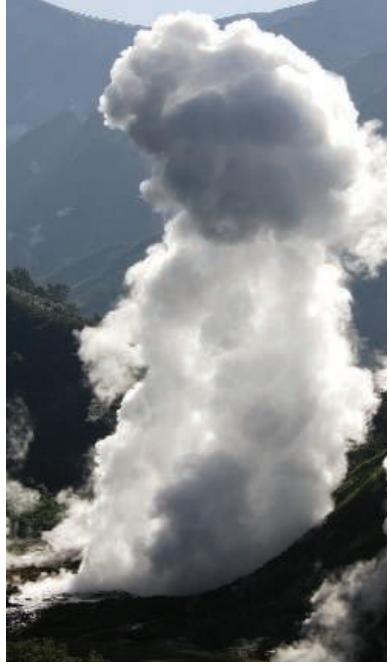

CREDIT: IGOR SHPILENOK/RUSSIAN NATURE PHOTOGRAPHY/WWW.SHPILENOK.COM

Hot home for extremophiles. Velikan ("Giant") geyser survived the 3 June 2007 landslide that seriously damaged Kamchatka's Valley of the Geysers.

Friend himself apparently developed a taste for exploring the world of microbes and quit his job as a science journalist for *USA Today* in order to devote his full attention to the Archaea. The book offers readers excursions through Yellowstone National Park to scuba dive for hyperthermophilic microbes, into Costa Rican rainforests to collect termites that house a microbial community in their gut that may be the world's best bioreactor for degrading cellulose, and on a helicopter-assisted foray into Russia's Valley of the Geysers. Along the way, we learn of biotechnological applications that stem from these exotic microbes, including the potentials to minimize our reliance on fossil fuels and to remediate some rather nasty chemical dumps.

These travelogues are sprinkled with primers in microbiology and chemistry that are needed to fully appreciate life's third domain. For example, while riding a submersible to view the microbial assault under way on the *Titanic*'s hull, Friend takes the opportunity to explain how the vast diversity of microbes in the world's ocean is being cataloged and how genomic methods revealed a previously unrecognized type of photosynthesis in the seas. He also weaves into the adventure stories relevant vignettes from the history of microbiology that set the stage for the archaeal revolution.

It is easy to be swept along with Friend's wild ride through the world of microbes. In his exuberance for explaining the pivotal roles of microbes on Earth, there are some minor errors in details (as there would be in the first edition of any textbook that tackles complex topics), but these are easy to overlook and do not interrupt the excitement of the hunt for new forms of life.

The Third Domain brings deserved acclaim to the discovery of the Archaea as one of the 20th century's most dramatic developments in biology. I suspect many readers will be persuaded to join Friend in his recently acquired fondness for these spectacular microbes.

Reference

1. P. de Kruif, *Microbe Hunters* (Harcourt, Brace, New York, 1926).

10.1126/science.1150506

The reviewer is at the Department of Microbiology and Molecular Genetics, 6180 Biomedical and Physical Sciences Building, Michigan State University, East Lansing, MI 48824, USA. E-mail: tschmidt@msu.edu

CORRECTED 25 JANUARY 2008; SEE LAST PAGE

PUBLIC HEALTH

Implementation Science

Researchers and funders need to use systems approaches that are beginning to translate research not only to the bedside but also to global health programs.

Temina Madon, Karen J. Hofman,* Linda Kupfer, Roger I. Glass

We face a formidable gap between innovations in health (including vaccines, drugs, and strategies for care) and their delivery to communities in the developing world. As a result, nearly 14,000 people in sub-Saharan Africa and South Asia die daily from HIV, malaria, and diarrheal disease (*1*), even though scientific advances have enabled prevention, treatment, and, in some cases, elimination of these diseases in developed countries.

Many evidence-based innovations fail to produce results when transferred to communities in the global south, largely because their implementation is untested, unsuitable, or incomplete. For example, rigorous studies have shown that appropriate use of insecticide-treated bed nets can prevent malaria (*2*), yet, in 2002, fewer than 10% of children in 28 sub-Saharan African countries regularly slept with this protection (*3*). Newer studies have shown that malaria incidence is decreased by distribution of free nets, but further research is needed to promote cost-effective, sustained access—particularly for the poor living in rural areas (*4*).

The same is true of strategies to prevent mother-to-child transmission of HIV. Although interventions like prophylactic antiretroviral therapy and replacement feeding have worked well in hospitals and clinics, increasing coverage in rural areas (where women have limited access to clean water and formal health care) may require testing of novel approaches, such as self-administration of drugs (*5*, *6*). Similarly, the scale-up of male circumcision, which has been shown to protect against HIV transmission in recent clinical trials (*7*), will require development of safe, culturally acceptable, and accessible methods for surgery and care (*8*).

The Implementation Research Gap

Why is effective implementation, particularly in resource-poor countries, such an intractable problem? The reasons are complex. First, scientists have been slow to view implementation as a dynamic, adaptive, multiscale phenomenon that can be addressed through a research agenda. Although randomized, controlled experiments are the gold standard for testing safety and efficacy of pharmaceuticals, health delivery schemes are less likely to be subject to rigorous scientific analysis.

Second, people living in poverty face a bewildering constellation of social constraints and health threats that make prevention and treatment more difficult. They often have limited knowledge of preventive health practices and insufficient or sporadic access to quality care. Their health systems are underfinanced, underregulated, and crippled by health-worker shortages. Even for those with access to care, health is routinely undermined by heavy pathogen loads, environmental exposures, inadequate sanitation infrastructure, and socioeconomic barriers to behavior change. Faced with such challenges, it is not surprising that public-health professionals have found it difficult to successfully adapt, implement, and sustain new interventions.

Although a few rigorous studies of implementation could advance the delivery of health care in low-income countries, recent billion-dollar increases in budgets for global health have provided only limited support for studies needed to ensure maximum impact (*9*). Instead, planners often assume that clinical research findings can be immediately translated into public health impact, simply by issuing "one-size-fits-all" clinical guidelines or best practices without engaging in systematic study of how health outcomes vary across community settings.

A doctor seeing a patient through Progresa, Mexico's incentive-based development program that targets the very poor. By improving children's growth and nutrition, it has especially benefited those who lack health care. Its success in improving health outcomes depends on rigorous, scientific studies that established the effectiveness of new strategies.

CREDIT: INTERAMERICAN DEVELOPMENT BANK

A Framework for Research Translation

Realizing the need for a quantitative, scientific framework to guide health-care scale-up in developing countries, researchers in health, engineering, and business are building interest in implementation science (*10*–*14*). Unlike routine applied (or operations) research, which may identify and address barriers related to performance of specific projects, implementation science creates generalizable knowledge that can be applied across settings and contexts to answer central questions. Why do established programs lose effectiveness over days, weeks, or months? Why do tested programs sometimes exhibit unintended effects when transferred to a new setting? How can multiple interventions be effectively packaged to capture cost efficiencies and to reduce the splintering of health systems into disease-specific programs? Answering questions like these will require analysis of biological, social, and environmental factors that impact implementation, both to develop and test communitywide, multisector interventions that are not testable in clinical settings, and to identify how proven clinical interventions should be modified to achieve sustained health improvements in the "real world." A few innovative studies have begun to appear (*15*).

One example is the research program coordinated with implementation of Mexico's 1997 reform of health and social services. Before reform, food subsidies and health care were provided by the Mexican government, largely without gains in public health and welfare.

Division of Advanced Science and Policy Analysis, The John E. Fogarty International Center, U.S. National Institutes of Health, Bethesda, MD 20892, USA.

*Author for correspondence. E-mail: hofmank@mail.nih. gov

Frustrated with poor outcomes, the government worked with scientists to develop a multisector antipoverty program, *Progresa*, to help increase the uptake of existing nutrition and health services.

The new initiative provided conditional financial incentives for poor rural families, on the basis of their use of prenatal, child health, and nutritional services provided by local clinics. Because researchers were involved in the initial design, they were able to build a prospective, cluster-randomized experiment into the program's roll-out, revealing statistically significant improvements in child development as a result of the new initiative (*16*). Because these and other quantitative studies showed sustained effectiveness (*17*), conditional cash transfers have enjoyed continuous support of the Mexican government, despite radical changes in political leadership. Similar programs are being adopted by policy-makers throughout Latin America.

The West African Onchocerciasis Control Programme (OCP) is another example of how rigorous implementation research can amplify the public health impact of proven interventions. This decades-long initiative has used established vector elimination methods and communitywide drug treatment campaigns to control the nematode parasite that causes river blindness. However, the program is unique in that it has, from the beginning, integrated mathematical modeling into every aspect of implementation and ongoing operation (*18*). Modeling of strategies has enabled the OCP to package together tested interventions, without direct experimentation. It has also helped optimize interventions to match field conditions and has enabled scientists to better understand parasite transmission and host-vector interactions.

Many implementation experiments—particularly cluster-randomized trials and agent-based models that compare the population-level health impacts of different delivery strategies—can be coupled with the planning and roll-out of new programs by health ministries, making the cost of research marginal. They can also be used to model the potential gains of health-system designs, policies, and multisector interventions that cannot be tested experimentally. These approaches all require the involvement of scientists in early planning to ensure that research questions are incorporated into program design.

Identifying New Research Opportunities

Opportunities for learning about implementation are particularly promising for initiatives like the Global Fund to Fight AIDS, Tuberculosis, and Malaria; the U.S. President's Emergency Plan for AIDS Relief (PEPFAR); and the President's Malaria Initiative. To date, these programs have focused on trial-and-error optimization of health services, using descriptive studies, process evaluations, and monitoring to measure program outputs. More recently, they have expanded to include targeted evaluations, which use comparison groups to infer the likely impacts of interventions on community health. Among the questions they need to address are those relating to behavior change and HIV prevention; the effectiveness of orphan care services; the risk of drug resistance in the scale-up of antiretroviral and antimalarial therapy; and the packaging together of interventions for HIV/AIDS, tuberculosis, and malaria. Questions that focus on health-care providers and systems include how pay-for-performance schemes impact quality and cost of care, and how agent-based modeling of clinic and hospital operations can inform development of human resources for health.

Implementation Science for Global Health

There are three additional imperatives facing the research community. First, we must advance theoretical models and new analytic methods that apply to resource-poor settings. This may include, for example, developing frameworks for implementation that rely on existing social networks and markets for sustained health-care delivery, rather than the training of health workers—a limited resource in most developing countries. Multiple disciplines, from systems science and computer simulation to public health and behavioral economics, need to be integrated.

The World Health Organization's Special Programme for Research and Training in Tropical Diseases (TDR) has begun to address this need, through support of collaborative research grants in implementation research (*19*). For example, with funds from the ExxonMobil Foundation, TDR researchers are currently testing the impacts of health-care franchising (based on a micro-enterprise business model) on access to antimalarial drugs in Kenyan villages (*20*, *21*). Programs like these should be expanded. The U.S. National Institutes of Health is actively soliciting international research proposals for its ongoing initiative in Dissemination and Implementation Research in Health (*22*).

Second, we need to train a generation of researchers who can effectively bridge the implementation gap. This will require new curricula and interdisciplinary, systems-oriented approaches. Because some features of implementation are context-specific, it also calls for strengthening of research institutions in low-income countries.

A final imperative is for researchers to collaborate with developing country governments, nongovernmental organizations (NGOs), and communities. For example, the George Washington University School of Public Health and Health Services recently announced a partnership with the Elizabeth Glaser Pediatric AIDS Foundation, to help capture opportunities to integrate research into the delivery of HIV/AIDS prevention and treatment services supported by the foundation (*23*).

Although implementation experiments and computational modeling may be more complex—in terms of study design and data analysis—than the monitoring and observational studies currently funded by donors, any inconvenience is outweighed by the profound ability of scientifically rigorous findings to focus limited health resources and to save more lives.

References and Notes

1. A. D. Lopez, C. D. Mathers, M. Ezzati, D. T. Jamison, C. J. L. Murray, Eds., *Global Burden of Disease and Risk Factors* (Oxford Univ. Press, New York, 2006).
2. C. Lengeler, "Insecticide-treated bednets and curtains for preventing malaria" (Cochrane Review, update software, Cochrane Library, issue 4, Oxford, 2001).
3. R. Monasch *et al.*, *Am. J. Trop. Med. Hyg.* **71** (suppl.), 232 (2004).
4. A. M. Noor, A. A. Amin, W. S. Akhwale, R. W. Snow, *PLoS Med.* **4**, e255 (2007).
5. D. J. Jackson *et al.*, *AIDS* **21**, 509 (2007).
6. J. Kagaayi *et al.*, *J. Acquir. Immune Defic. Syndr.* **39**, 121 (2005).
7. B. Auvert *et al.*, *PLoS Med.* **2**, e298 (2005).
8. T. C. Quinn, *Curr. Opin. Infect. Dis.* **20**, 33 (2007).
9. W. D. Savedoff, R. Levine, N. Birdsall, *When Will We Ever Learn? Improving Lives Through Impact Evaluation* (Report of the Evaluation Gap Working Group, Center for Global Development, Washington, DC, 2006).
10. M. P. Eccles, B. S. Mittman, *Implement. Sci.* **1**, 1 (2006).
11. D. Sanders, A. Haines, *PLoS Med.* **3**, e186 (2006).
12. D. L. Fixsen *et al.*, *Implementation Research: A Synthesis of the Literature* [Florida Mental Health Institute (FMHI) publ. no. 231, Louis de la Parte FHMI, University of South Florida, The National Implementation Research Network, Tampa, FL, 2005].
13. R. G. A. Feachem, *Trop. Med. Int. Health* **9**, 1139 (2004).
14. E. A. McCarthy, M. E. O'Brien, W. R. Rodrigues, *PLoS Med.* **3**, e304 (2006).
15. P. Buekens, G. Keusch, J. Belizan, Z. A. Bhutta, *JAMA* **291**, 2639 (2004).
16. E. Skoufias, *PROGRESA and Its Impacts of the Welfare of Rural Households in Mexico* (Research report 139, International Food Policy Research Institute, Washington, DC, 2005).
17. E. Gakidou *et al.*, *Lancet* **368**, 1920 (2006).
18. F. E. McKenzie, E. M. Samba, *Am. J. Trop. Med. Hyg.* **71** (suppl.), 94 (2004).
19. Special Programme for Research and Training in Tropical Diseases (TDR), www.who.int/tdr/topics/ir/default.htm.
20. "Shopkeepers to deliver health to Africa? Trust the people," *RealHealthNews* (Global Forum for Health Research, Geneva, May 2007).
21. Additional details re (*20*) available at www.cfwshops.org/news_exxon_mobil_foundation.html.
22. Announcement of request for proposals, http://grants.nih.gov/grants/guide/pa-files/PAR-07-086.html.
23. Elizabeth Glaser Pediatric AIDS Foundation, www.pedaids.org/

10.1126/science/1150009

CIRCADIAN RHYTHMS

Daily Watch on Metabolism

Plants and animals adjust responses to their environments through small molecules, including metabolites, which interact with their circadian clocks

Takato Imaizumi, Steve A. Kay, Julian I. Schroeder

Most organisms enhance fitness by coordinating their development with daily environmental changes through molecular timekeepers known as circadian clocks. In eukaryotes, these clocks comprise interlocking loops of transcriptional feedback and protein turnover (*1*). This system of multiple connected loops increases the clock's robustness and provides numerous points of input and output to the clock. Many metabolic pathways are regulated by circadian clocks in plants and animals (*2*, *3*). Two papers in this issue, Dodd *et al.* on page 1789 (*4*) and Yin *et al*. on page 1786 (*5*), provide evidence that clock feedback mechanisms in plants and animals incorporate small metabolites and signaling molecules. This represents yet another complex layer of feedback regulation within circadian networks, and how the clock maintains metabolic homeostasis in response to external conditions.

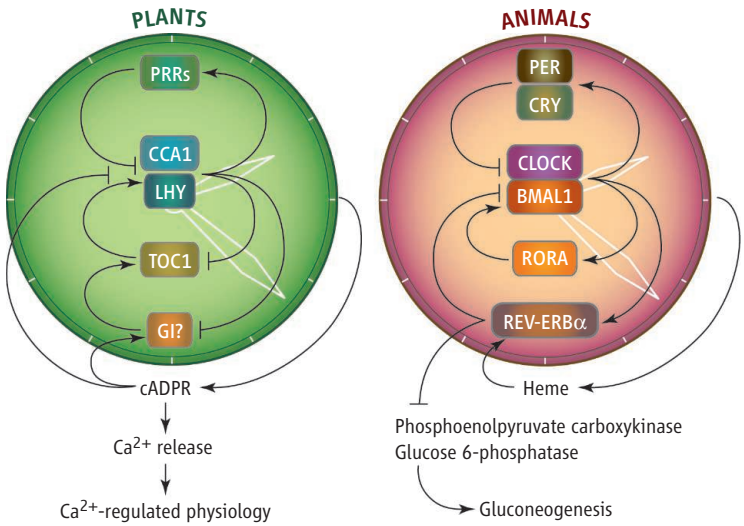

Metabolic feedback to clocks. (**Left**) The plant circadian clock comprises interlocking loops of the clock components CIRCADIAN CLOCK ASSOCIATED 1 (CCA1), LATE ELONGATED HYPOCOTYL (LHY), PSEUDO-RESPONSE REGULATORs (PRRs), TIMING OF CAB EXPRESSION 1 (TOC1), and GIGANTEA (GI). The clock controls the concentration of cADPR, which in turn regulates circadian oscillation in the cytosolic free Ca^{2+} concentration. (**Right**) In the mammalian clock, the CLOCK/BMAL1 heterodimer regulates expression of PERIOD (PER), CRYPTOCHROME (CRY), RORA, and REV-ERBα. REV-ERBα is a heme sensor that forms a transcriptional repressor complex. Heme provides feedback to the circadian clock and influences gluconeogenesis.

In plant and animal cells, the concentration of intracellular free calcium ions ($[Ca^{2+}]_i$) shows a diurnal oscillation (*6*). Because Ca^{2+} is a signaling molecule in various physiological responses, its daily oscillation could encode circadian clock signaling information (*7*, *8*). Analyses in the model plant *Arabidopsis thaliana* suggest that the extracellular Ca^{2+}-sensing receptor contributes to generating this oscillation. This pathway involves inositol 1,4,5,-trisphosphate (IP_3), which triggers Ca^{2+} release from intracellular stores (*9*). In animal cells, cyclic adenosine diphosphate ribose (cADPR) is another signaling molecule that induces Ca^{2+} release by binding to the ryanodine receptor present on intracellular stores (*10*). Although there is not yet an obvious ryanodine receptor counterpart in plant genomes, cADPR triggers $[Ca^{2+}]_i$ increase in plants as well (*11*, *12*).

Dodd *et al.* determined that cADPR concentration peaks during the early hours of the day. This fluctuation was abolished in plants with defective clock function, indicating that the circadian clock regulates cADPR concentration. cADPR is synthesized from nicotinamide adenine dinucleotide by the enzyme ADP ribosyl cyclase (*10*). Nicotinamide, at 10 to 50 mM concentrations, inhibited ADP ribosyl cyclase and weakened circadian $[Ca^{2+}]_i$ oscillation in plant cells. Dodd *et al*. also found a correlation between the expression of circadian- and cADPR-regulated genes. Moreover, decreasing the cellular concentration of cADPR lengthened the period of circadian gene expression. The authors suggest that circadian-regulated cADPR-derived Ca^{2+} signaling may configure part of the feedback loop that controls the clock (see the figure).

The results of Dodd *et al.* raise interesting questions. The phytohormone abscisic acid, thought to lengthen the clock period (*13*), induces cADPR production (*11*), and cADPR gene expression overlaps with that of genes controlled by abscisic acid (*14*). Does abscisic acid affect the clock partly through cADPR-derived signals? Also, assuming that both IP_3- and cADPR-dependent pathways are involved in generating circadian $[Ca^{2+}]_i$ oscillation, do they interact with each other? Dodd *et al.* found that a pharmacological inhibitor (U73122 at 1 μM) of IP_3 production did not affect daily $[Ca^{2+}]_i$ oscillation. Because IP_3 concentrations were not analyzed, more research is needed to understand the relative roles of both cADPR and IP_3. In particular, identification of the plant genes that encode the enzymes that produce cADPR and the proteins that control Ca^{2+} release by cADPR and IP_3 are required to analyze the functions of these signaling molecules in plants.

The circadian clock also controls daily metabolic homeostasis in mammals. Indeed, mice with a dominant mutation in *Clock*, the gene that encodes a core clock component, develop various metabolic syndromes (*15*). Many enzymes that catalyze diverse metabolic reactions require heme as a cofactor. The circadian clock regulates the heme metabolic pathway partly by controlling expression of 5-aminolevulinic acid synthase, the rate-limiting enzyme in heme biosynthesis (*3*). Yin *et al.* show that the circadian clock may also monitor heme metabolism through the clock component REV-ERBα. Heme binds to REV-ERBα and regulates its function by promoting its assembly with two proteins that repress transcription—nuclear receptor co-repressor and histone deacetylase 3 complex.

Heme suppresses the expression of genes involved in gluconeogenesis in the liver. Yin *et al.* show that in the presence of heme, REV-ERBα decreased the expression of genes encoding phosphoenolpyruvate carboxykinase and glucose 6-phosphatase, both of which control glucose production, in human hepatoma cells. Heme also augmented transcriptional repression of the core clock gene *Bmal1* by REV-ERBα. Therefore, REV-ERBα couples the circadian clock with glucose metabolism. It would be intriguing to

The authors are in the Division of Biological Sciences, Section of Cell and Developmental Biology, University of California, San Diego, La Jolla, CA 92093–0116, USA. E-mail: timaizumi@ucsd.edu

study whether REV-ERBα–dependent regulation contributes to the transcriptional regulation of phosphoenolpyruvate carboxykinase and glucose 6-phosphatase genes in *Rev-erbα*–deficient mice.

At first glance, the studies by Dodd *et al*. and Yin *et al*. appear unrelated. However, they propose that both plant and animal clocks possess a mechanism for implementing cellular signaling or redox status in the fine-tuning of daily transcriptional regulation. Thus, a common theme emerges in which small molecules provide feedback mechanisms between the circadian clock network and clock-controlled metabolic pathways to maintain metabolic homeostasis.

References

1. H. Wijnen, M. W. Young, *Annu. Rev. Genet.* **40**, 409 (2006).
2. S. L. Harmer *et al.*, *Science* **290**, 2110 (2000).
3. S. Panda *et al.*, *Cell* **109**, 307 (2002).
4. A. N. Dodd *et al.*, *Science* **318**, 1789 (2007); published online 15 November 2007 (10.1126/science.1146757).
5. L. Yin *et al.*, *Science* **318**, 1786 (2007); published online 15 November 2007 (10.1126/science.1150179).
6. T. Imaizumi *et al.*, *Sci. STKE* **2007**, pe32 (2007).
7. C. H. Johnson *et al.*, *Science* **269**, 1863 (1995).
8. J. Love *et al.*, *Plant Cell* **16**, 956 (2004).
9. R. H. Tang *et al.*, *Science* **315**, 1423 (2007).
10. H. C. Lee, *Physiol. Rev.* **77**, 1133 (1997).
11. Y. Wu *et al.*, *Science* **278**, 2126 (1997).
12. C. P. Leckie *et al.*, *Proc. Natl. Acad. Sci. U.S.A.* **95**, 15837 (1998).
13. S. Hanano *et al.*, *Genes Cells* **11**, 1381 (2006).
14. J. P. Sanchez *et al.*, *Plant J.* **38**, 381 (2004).
15. F. W. Turek *et al.*, *Science* **308**, 1043 (2005).

Published online 15 November 2007;
10.1126/science.1151360
Include this information when citing this paper.

ATMOSPHERIC SCIENCE

Resolving an Atmospheric Enigma

Data and modeling are helping to explain what drives an important atmospheric oscillation in the tropics.

Dennis L. Hartmann and Harry H. Hendon

In 1971, meteorologists Roland Madden and Paul Julian studied weather data from near-equatorial Pacific islands. To their surprise, tropospheric winds, pressure, and rainfall oscillated with a period of about 40 to 50 days (*1*). The oscillation in clouds and precipitation tends to be confined to the tropical Indian and Pacific oceans, but the oscillation in winds and pressure is felt throughout the tropics (see the figure). The search for a single robust theory for this Madden-Julian Oscillation (MJO) continues today.

The MJO is not a true oscillation, in the sense that its period varies and its appearance is episodic, but it is the largest source of tropical weather variability on subseasonal time scales, especially in the Indian and Pacific oceans. On page 1765 of this issue, Matthews *et al.* (*2*) use observations from the new Argos system of profiling floats to reveal the deep-ocean response to the MJO. Also in this issue, Miura *et al*. on page 1763 report an advance in modeling the MJO (*3*).

Because of its large amplitude and long period, the MJO affects many people. It causes prolonged dry and wet episodes during the Asian Summer Monsoon and modulates the intensity, frequency, and location of tropical storms in the Indian, Pacific, and Atlantic oceans (*4*, *5*). The strong and persistent surface winds associated with the MJO drive a large response in the upper ocean (*6*). Matthews *et al.* have measured the deep ocean response to wind surges associated with the oscillation. It is as yet unclear what effect this has on the deep ocean. The MJO also influences the onset and intensity of El Niño events and may underlie the very existence of the El Niño–Southern Oscillation (*7*).

In climate models, the MJO is typically weaker and moves faster than is observed. Weather prediction models cannot sustain the MJO. Coupled ocean-atmosphere models tend to produce more realistic simulations, because the MJO interacts strongly with the upper ocean, but this coupling is not essential for the existence of the oscillation (*8*, *9*).

Observations show that a wide range of scales interact within the MJO, ranging from the scale of individual convective cells a few kilometers across and a few hours in duration to the 10,000-km planetary scale of the 40- to 50-day variation (*10*). Similar to a hurricane but on a much larger scale, the release of latent heat in moist convection drives the planetary-scale wind variations of the MJO. The planetary wind variations in turn provide organization to the convective-scale phenomena, suppressing convection in some regions and enhancing it in others.

Because the MJO arises from the interaction of convective and planetary scales, it serves as a probe into our ability to understand and model the interaction of convection and clouds with climate. This interaction remains one of the largest uncertainties in climate projections (*11*). The inability to properly simulate the MJO indicates inaccurate treatment of the interaction between the scale of convection—perhaps 1 km or

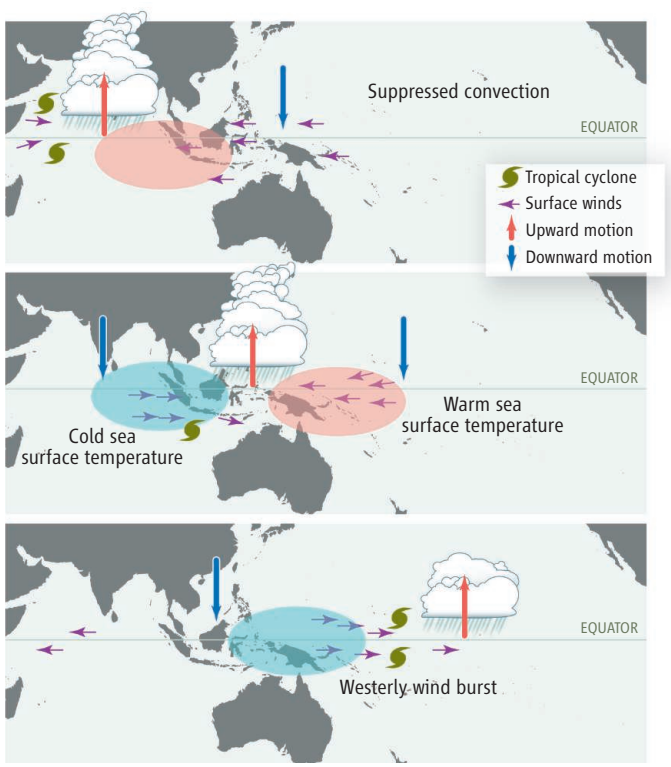

The Madden-Julian Oscillation. Precipitation first develops in the Indian Ocean and moves eastward with a speed of about 5 m s^{-1}. Surface winds converge under the convection, and a burst of eastward surface winds follows the passage of the heaviest rainfall. This burst is an important driver for ocean dynamics. Each panel is separated by ~15 days.

D. L. Hartmann is in the Department of Atmospheric Sciences, University of Washington, Seattle, WA 98195, USA. H. H. Hendon is with the Centre for Australian Weather and Climate Research, Bureau of Meteorology, Melbourne, 3001 Victoria, Australia. E-mail: dennis@atmos.washington.edu; h.hendon@bom.gov.au

less—and the resolved scales of global models, which currently have grid points separated by ~25 km for global weather forecasting models and ~100 km for climate models.

Miura *et al.* use a global model in which the horizontal grid spacing is 7 km. To perform their simulation they used the Earth Simulator, a Japanese supercomputer developed for running more realistic global simulations (*12*). In the simulation, the MJO appears to be sustained with realistic structure over a period of 1 month. This result suggests that a transition to more realistic behavior may occur for grid spacing as large as 7 km, rather than 1 km.

Increasing the resolution of weather prediction models to 7 km would require an increase in computing power of about a factor of 100, which might be achieved in less than a decade. Thus, increasing the spatial resolution of operational models may provide a brute-force solution to a critical problem in weather and climate research. In the near term, tools such as the Earth Simulator should be used to better understand the scale interactions that underlie the MJO.

References

1. R. A. Madden, P. R. Julian, *J. Atmos. Sci.* **28**, 702 (1971).
2. A. J. Matthews *et al.*, *Science* **318**, 1765 (2007).
3. H. Miura *et al.*, *Science* **318**, 1763 (2007).
4. B. Liebmann *et al.*, *J. Meteorol. Soc. Jpn.* **72**, 401 (1994).
5. E. D. Maloney, D. L. Hartmann, *Science* **287**, 2002 (2000).
6. M. C. Spillane *et al.*, *J. Phys. Oceanogr.* **17**, 313 (1987).
7. M. J. McPhaden, *Science* **283**, 950 (1999).
8. C. Zhang *et al.*, *Clim. Dyn.* **27**, 573 (2006).
9. J. L. Lin *et al.*, *J. Clim.* **19**, 2665 (2006).
10. T. Nakazawa, *J. Meteorol. Soc. Jpn.* **66**, 823 (1988).
11. D. Randall *et al.*, *Bull. Am. Meteorol. Soc.* **84**, 1547 (2003).
12. See www.es.jamstec.go.jp/index.en.html.

10.1126/science.1152502

MICROBIOLOGY

A Fifth Pathway of Carbon Fixation

Genome sequence analyses and enzymatic studies reveal a novel CO_2 fixation cycle in some autotrophic archaea.

Rudolf K. Thauer

Autotrophs are organisms that can grow using carbon dioxide (CO_2) as their sole source of carbon. Among them are plants, algae, cyanobacteria, purple and green bacteria, and also some bacteria and archaea that do not obtain energy from light. Autotrophs generate the biomass on which all other organisms—including humans—thrive. They also play an important role in Earth's nitrogen and sulfur cycles. Four mechanisms are known by which autotrophic organisms fix carbon (see the figure). On page 1782 of this issue, Berg *et al.* (*1*) describe a fifth autotrophic CO_2 fixation pathway in archaea that may have been used by some of the earliest organisms on Earth.

The first autotrophic CO_2 fixation pathway was elucidated by Calvin about 50 years ago (*2*). In this pathway, CO_2 reacts with a five-carbon sugar, yielding two carboxylic acids, from which the sugar is regenerated in a cyclic process. The Calvin cycle operates in plants, algae, and cyanobacteria (which all perform oxygenic photosynthesis) and in autotrophic proteobacteria, some of which do not tolerate oxygen (anaerobes). The key enzyme of the cycle—RuBisCO (*3*)—is also found in several other bacteria and some archaea, but these either lack another enzyme crucial for the cycle and/or there is no evidence for autotrophic growth.

In 1966, Evans *et al.* proposed that the green sulfur bacterium *Chlorobium* uses a second cycle for autotrophic CO_2 fixation (*4*). It took until 1990 until all the details of this reductive citric acid cycle were worked out (*5*). The cycle also operates in several other groups of bacteria and archaea. Because it involves enzymes that are sensitive to oxygen, this cycle is only found in anaerobes or in organisms that tolerate oxygen only at levels below those found in air (microaerophiles). At the beginning of the 1980s, a third pathway of autotrophic CO_2 fixation was found in certain Gram-positive bacteria and methane-forming archaea. In these organisms, one CO_2 molecule is reduced to CO and one to methanol (bound to a carrier); subsequently, acetyl–coenzyme A (CoA) is synthesized from CO and methanol (*6*). This reductive acetyl-CoA pathway is also found in several other bacteria and archaea. It involves one of the most oxygen-sensitive enzymes known and is thus only found in strict anaerobes.

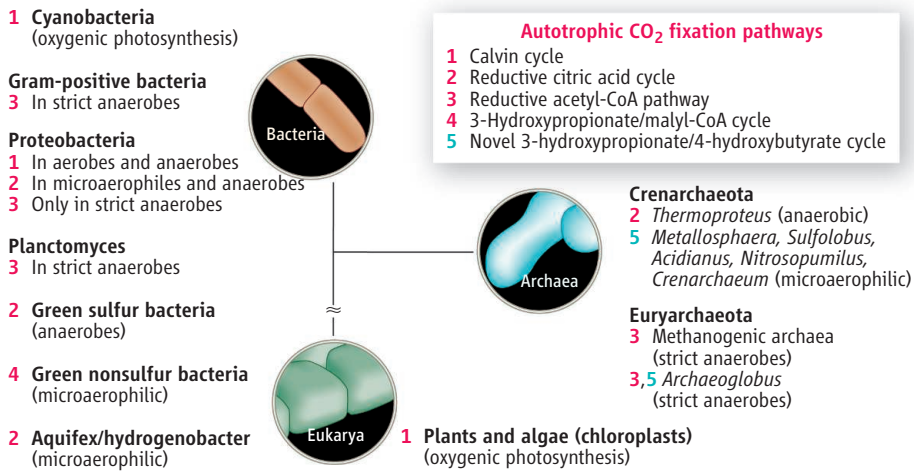

A novel pathway of CO_2 fixation found by Berg *et al.* (*1*) in Archaea. Four other pathways are known by which autotrophic representatives of Bacteria, Archaea, and Eukarya fix carbon.

The fourth pathway was discovered in the green nonsulfur bacterium *Chloroflexus*. Here, CO_2 fixation starts with the carboxylation of acetyl-CoA; the CO_2 acceptor is then regenerated in a cyclic process, with 3-hydroxypropionate and malyl-CoA as characteristic intermediates (*7*). The 3-hydroxypropionate/malyl-CoA cycle appears to be restricted to *Chloroflexus* species. None of the enzymes involved in this cycle are inherently sensitive toward oxygen; one of them is sensitive to ultraviolet-A light, which, however, does not reach the ecological niches in which the green bacteria thrive.

The novel autotrophic CO_2 fixation pathway described by Berg *et al.* has some of the same intermediates as the 3-hydroxypropionate/malyl-CoA cycle. Succinyl-CoA is also formed from acetate and 2 CO_2 mol-

The author is at the Max Planck Institute for Terrestrial Microbiology, 35043 Marburg, Germany. E-mail: thauer@mpi-marburg.mpg.de

ecules via 3-hydroxypropionate. However, the enzymes involved appear not to be phylogenetically related, indicating convergent evolution. From succinyl-CoA on, the two pathways are different.

Berg *et al.* show that the novel cycle is operative in *Metallosphaera* growing on H_2 and O_2 as the energy source. The genes for this cycle are also present in other archaea. All these organisms are either microaerophiles or, as in the case of *Archaeoglobus*, strict anaerobes. The cycle involves 4-hydroxybutyryl-CoA dehydratase, a radical enzyme sensitive to oxygen (*8*).

Why do different autotrophs use different pathways of CO_2 fixation? According to one hypothesis, the first organisms on Earth were strict anaerobes and autotrophs that used a reductive acetyl-CoA pathway very similar to that found today in some strictly anaerobic archaea and bacteria (*9*, *10*). After the emergence of oxygenic photosynthesis, the atmospheric oxygen concentration increased slowly and the reductive acetyl-CoA pathway could no longer operate in most organisms due to the extreme oxygen sensitivity of one of its key enzymes. Autotrophy thus had to be reinvented after the major phyla had already evolved, leading to different pathways of autotrophic CO_2 fixation in different organisms dependent on their genetic outfit and living conditions.

Lateral gene transfer helped to spread the new inventions. Some were lost again. The reductive citric acid cycle and the 3-hydroxypropionate/4-hydroxybutyrate cycle could only survive in organisms that live under anaerobic or microaerophilic conditions due to the inherent oxygen sensitivity of the enzymes involved. Only the Calvin cycle made it into the aerobic world of plants, one reason being that it does not use enzymes that are inactivated by O_2 or by light.

References

1. I. A. Berg *et al.*, *Science* **318**, 1782 (2007).
2. M. Calvin, *Nature* **192**, 799 (1961).
3. RuBisCO stands for ribulose-1,5-bisphosphate carboxylase-oxygenase.
4. M. C. W. Evans, B. B. Buchanan, D. I. Arnon, *Proc. Natl. Acad. Sci. U.S.A.* **55**, 928 (1966).
5. B. B. Buchanan, D. I. Arnon, *Photosynth. Res.* **24**, 47 (1990).
6. S. W. Ragsdale, *Crit. Rev. Biochem. Mol. Biol.* **26**, 261 (1991).
7. S. Herter *et al.*, *J. Biol. Chem.* **277**, 20277 (2002).
8. B. M. Martin *et al.*, *Proc. Natl. Acad. Sci. U.S.A.* **44**, 15645 (2004).
9. G. Wächtershäuser, *Chem. Biodivers.* **4**, 584 (2007).
10. W. Martin, M. J. Russel, *Philos. Trans. R. Soc. B* **362**, 1887 (2007).

10.1126/science.1152209

ECOLOGY

Invasion of the Whiteflies

An invading whitefly is successful because invading males interfere with mating by native males and invading females produce more female offspring.

Stuart R. Reitz

Invasive alien species—organisms that have become established and so abundant in new geographic areas as to cause harm—are one of the most pressing global environmental concerns (*1*). As invasive alien species spread, they often displace indigenous species, thus altering ecological communities and adversely affecting agricultural pest management, human well-being, and biodiversity. To successfully invade a new geographic area, a species must have the opportunity to enter that area, and then it must become an established member of its new community, from which it can spread over large geographic areas (see the figure).

The routes for introductions of alien species are fairly well understood. Most organisms achieve this first step in the invasion process with the assistance of human movement (*2*). Less well understood are the processes enabling species to become established, spread, and displace indigenous species. On page 1769 of this issue, Liu *et al.* (*3*) provide unique insights into how one subtype of the sweet potato whitefly spread through China and Australia and displaced two indigenous subtypes of this species.

CREDIT: TOM PERRING/UNIVERSITY OF CALIFORNIA, RIVERSIDE

Asymmetric warfare. A successful invasion, such as accomplished by the B biotype of the sweet potato whitefly, reflects the completion of three contingent stages: (i) the opportunity to enter a new geographic area, from which the invader (ii) must establish in the new habitat, and then (iii) spread extensively enough to cause harm. Liu *et al.* address how biotype B of the whitefly, as shown here mating, has accomplished the second and third stages through interfering with mating by indigenous whitefly biotypes and increasing their own female offspring in the presence of males of other biotypes.

The sweet potato whitefly *Bemisia tabaci* consists of some 12 genetically distinct subtypes (termed "biotypes") distributed throughout tropical and subtropical regions of the world (*4*), of which the B biotype is considered one of the most invasive organisms in the world (*5*). Although the question of whether these biotypes are unique species has been intensely debated (*6*, *7*), it is clear that within just the past 20 years, biotype B has become one of the world's most damaging agricultural pests (*8*). As with other invasive alien species, biotype B has been transported by humans through the movement of agricultural products, which has given it the opportunity to invade new areas. Yet this raises the question of how this biotype has been so successful as an invader, even in areas with indigenous whitefly biotypes.

By combining DNA analyses to distinguish the biotypes, long-term field surveys, and controlled experimentation, Liu *et al.* reach the striking conclusion that the key to biotype B success is mating interference and facilitation. Biotype B males reduce the reproductive success of indigenous whiteflies by readily courting the indigenous females and by disrupting courtships among the indigenous males and females. In contrast, whereas biotype B females mate only with biotype B males, they can facilitate their reproductive success by producing more female offspring in the presence of multiple males, regardless of the additional males' biotypes.

Sexual interference by invaders has been linked with displacements of other animal species, such as between species of *Aedes* mosquitoes or *Hemidactylus* geckos (*9*, *10*), but mating facilitation by an indigenous species had not previously been implicated in aiding the success of an invader. Although the size of the invading "army" is important (*11*), Liu *et al.* raise the interesting possibility that relatively small introductions of biotype B can succeed by rapidly producing female offspring, and thus contribute to its overall invasiveness.

The author is at the Agricultural Research Service, U.S. Department of Agriculture, Tallahassee, FL 32308, USA. E-mail: stuart.reitz@ars.usda.gov

A valuable aspect of the study by Liu *et al*. is that they documented the process of establishment and displacement as it occurred over time in different areas within China and Australia. Rarely has this approach been possible or undertaken: Invasions and displacements often are not detected or studied until they are widespread and complete. Consequently, much of our information on these historical events is derived from retrospective studies, which can be confounded by rapid evolutionary changes in both invading and indigenous populations (*12*).

In turn, these displacements should not be regarded as total victory for the invaders. Some authors argue that invasive competitors may cause local extinctions of indigenous species but are unlikely to cause the complete extinction of indigenous species (*13*). Further, some invasive populations have undergone seemingly unexplained crashes, which open opportunities for additional changes in invaded communities (*14*, *15*). It remains to be seen whether remnant populations of the indigenous biotypes exist and may respond evolutionarily to the invasive biotype B.

Liu *et al.* conclude that invasions bring about intense interactions between previously geographically isolated species. In such asymmetric interactions, the B biotype is competitively superior and indigenous biotypes suffer more from interactions with the B biotype than the B biotype suffers from interactions with the indigenous types. It still would be of interest to compare invasive populations of biotype B with populations in its indigenous habitats of the Middle East and Asia Minor to determine whether biotype B inherently has invasive characteristics, or whether populations have been selected for through previous invasions. Such questions of how invasive populations compare with their original source populations are among the most pertinent in invasion biology today (*16*).

Maintaining a long-term perspective is important, as the results of Liu *et al*. show. Brief snapshots of the event may not have led to the same conclusions as did their longer-term study. Clearly, invasions provide opportunities for dramatic ecological and evolutionary experimentation. Unfortunately, invasions come at tremendous environmental and economic costs, yet understanding interactions between invaders and residents will continue to be necessary for more effective control of invasive species (*9*).

References

1. D. Pimentel, *et al.*, *Ecol. Econ.* **52**, 273 (2005).
2. A. K. Sakai *et al.*, *Annu. Rev. Ecol. Syst.* **32**, 305 (2001).
3. S.-S. Liu *et al.*, *Science* **318**, 1769 (2007); published 8 November 2007 (10.1126/science.1149887).
4. L. M. Boykin *et al.*, *Mol. Phylogenet. Evol.* **44**, 1306 (2007).
5. International Union for the Conservation of Nature and Natural Resources (IUCN), Invasive Species Specialist Group, "100 of the World's Worst Invasive Alien Species" (www.issg.org).
6. T. M. Perring, *Crop Prot.* **20**, 725 (2001).
7. P. J. De Barro, J. W. H. Trueman, D. R. Frohlich, *Bull. Entomol. Res.* **95**, 193 (2005).
8. J. K. Brown *et al.*, *Annu. Rev. Entomol.* **40**, 511 (1995).
9. E. A. Dame, K. Petren, *Anim. Behav.* **71**, 1165 (2006).
10. S. R. Reitz, J. T. Trumble, *Annu. Rev. Entomol.* **47**, 435 (2002).
11. J. M. Levine, *Science* **288**, 852 (2000).
12. S. Y. Strauss *et al.*, *Ecol. Lett.* **9**, 357 (2006).
13. M. A. Davis, *Bioscience* **53**, 481 (2003).
14. D. Simberloff, L. Gibbons, *Biol. Invasions* **6**, 161 (2004).
15. D. L. Strayer *et al.*, *Trends Ecol. Evol.* **21**, 645 (2006).
16. P. Alpert, *Biol. Invasions* **8**, 1523 (2006).

10.1126/science.1152124

GEOLOGY

On the Accumulation of Mud

Joe H. S. Macquaker and Kevin M. Bohacs

Mudstones can be deposited under more energetic conditions than widely assumed, requiring a reappraisal of many geologic records.

On page 1760 of this issue, Schieber *et al.* (*1*) document a mechanism for depositing mud that is at odds with perceived wisdom. Geoscientists tend to assume that most mud accumulates directly from suspension in the water column, that mud deposition requires quiet bottom-water conditions, and that mudstones containing closely spaced, parallel laminae represent continuous deposition (see the first figure, top panel). In contrast, the authors show that mud can accumulate as current ripples composed of grain aggregates under currents that can transport very fine sand (see the first figure, bottom panel). Thus, a layer of muddy sediment can be eroded and transported laterally without showing obvious signs of such disturbance and may record surface-water conditions elsewhere in the basin. The results call for critical reappraisal of all mudstones previously interpreted as having been continuously deposited under still waters. Such rocks are widely used to infer past climates, ocean conditions, and orbital variations.

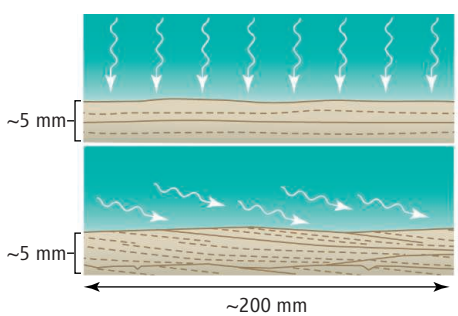

Not so simple. Mud deposition via suspension settling (wavy vertical arrows) (**top**) and the advective sediment transport processes close to the sediment-water interface (wavy close-to-horizontal arrows) identified by Schieber *et al.* (**bottom**). Bedding planes are indicated by solid lines, laminae by dotted lines. The vertical scale is exaggerated relative to the horizontal scale. In mudstone successions, the expression of these two very different physical processes can only be distinguished by detailed inspection of the textures present.

Fine-grained sedimentary rocks such as shales or mudstones—with an average grain size of less than 62.5 μm—are by far the most common sedimentary rocks preserved close to Earth's surface. Most were deposited on lake or ocean floors, where they provide a record of Earth's history. These rocks also play an important part in the global carbon budget, groundwater flow, and landfill containment and contribute important resources such as oil, shale gas, minerals, and metals.

Mudstones typically consist of various materials, including clays, quartz, organic matter, remains of organisms, and chemical precipitates formed when the sediment was buried. Because of their very fine grain size, they appear homogeneous in hand specimens; moreover, their high clay content makes them very susceptible to weathering. Thus, they do not reward casual inspection and are poorly understood relative to other rock types. Researchers typically resort to analysis of attributes such as fossil content, chemical composition, and electromagnetic characteristics to deduce the conditions under which the mudstone was deposited.

Patterns of change in these proxy data are typically attributed to variations in ocean circulation, water chemistry, plankton growth,

J. Macquaker is in the School of Earth, Atmospheric and Environmental Sciences, The University of Manchester, Manchester M13 9PL, UK. K. M. Bohacs is with the ExxonMobil Upstream Research Company, Houston, TX 77027, USA. E-mail: Joe.Macquaker@Manchester.ac.uk; Kevin.M.Bohacs@exxonmobil.com

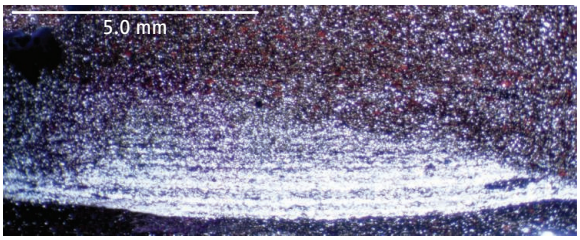

Beyond suspension settling. Thin-section scan of a mudstone collected from the Kimmeridge Clay Formation (Upper Jurassic). The sample is mainly composed of silt and clay and contains a ripple. The existence of this ripple indicates that the sediment was not simply delivered by suspension settling, but rather was deposited from traction currents operating close to the sediment-water interface.

climate, or Earth-Sun distance. It is commonly assumed—but not always explicitly stated—that fine-grained sediment was delivered more or less continuously from buoyant plumes produced by storms and river floods, zones of high primary productivity, or turbidity currents before settling out of suspension as individual grains in still waters.

This paradigm appears to fit available proxy data and is consistent with the few sedimentary structures that are readily visible. It is, however, at odds with observations in modern oceans and lakes (*2*), where environments and water-column chemistries can change rapidly and a variety of sediment transport processes have been observed. Fine-grained sediment is seldom deposited as individual grains but commonly organized into grain aggregates. Doubts about the validity of the paradigm have also emerged from imaging studies of ancient fine-grained rocks (*3*), which have revealed the presence of millimeter-scale sedimentary structures, including localized erosion, progressively fine-grained beds, and low-angle ripple laminae (see the second figure).

The laboratory investigations reported by Schieber *et al.* now provide direct evidence of advective sediment transport of mud-sized material, using apparatus designed to maintain the integrity of the floccules. In the experiments, clay aggregates formed migrating ripples that deposited sediment under much higher current velocities than previously assumed. These floccule ripples have low crests (2 to 20 mm) and very long spacings (300 to 400 mm); they deposit nonparallel inclined laminae that could be easily misinterpreted as parallel-laminated.

Together, these studies indicate that many of our preconceptions about fine-grained rocks are naïve. First, mud accumulation can occur in higher-energy conditions than most researchers had assumed. Second, Schieber *et al.* suggest that advective traction currents commonly erode, transport, and deposit substantial volumes of fine-grained sediment; as a result, fine-grained successions in the sedimentary record are much less complete than commonly assumed. Third, most researchers did not consider it important that floccules can be stable under traction transport, although some, including coastal engineers, have recognized the vital role that floccules probably play (*4*). Most models of mudstone deposition do not incorporate any of these factors. Geologists will have to revisit these rocks and generate much subtler models to explain their variability.

These results come at a time when mudstone science is poised for a paradigm shift. Observations accumulated over the past 30 years (*3*, *5*–*9*) indicate that deposition and burial of mud is as dynamic and complex as that of sand or limestone—or possibly even more so, because of myriad processes—including grain-size changes due to aggregate growth and decay, presence of biofilms, reworking, and cement precipitation—that occur in mudstones to control their variability. We can now recognize traces of bottom currents in very fine-grained rocks, supported by laboratory, modern mud, and ancient rock studies.

The study by Schieber *et al.* enables us to critically reexamine existing databases and to extract maximal information from new ones. Such studies will reward us with deeper insights into the inner workings of the dominant sediment type on Earth.

References

1. J. Schieber *et al.*, *Science* **318**, 1760 (2007).
2. C. A. Nittrouer, *Marine Geology* **154**, 3 (1999).
3. J. H. S. Macquaker, K. G. Taylor, R. L. Gawthorpe, *J. Sediment. Res.* **77**, 324 (2007).
4. R. B. Krone, *Flume Studies of the Transport of Sediment in Estuarial Shoaling Processes* (Final Report, Hydraulic Engineering Laboratory and Sanitary Engineering Research Laboratory, University of California, Berkeley, 1962).
5. I. N. McCave, *J. Sediment. Petrology* **41**, 89 (1971).
6. R. M. Cluff, *J. Sediment. Petrology* **50**, 767 (1980).
7. K. M. Bohacs, in *Mudstones and Shales, vol. 1, Characteristics at the Basin Scale*, J. Schieber, W. Zimmerle, P. Sethi, Eds. (Schweizerbart'sche Verlagsbuchhandlung, Stuttgart, 1998), pp. 32–77.
8. N. R. O'Brien, in *Palaeoclimatology and Palaeoceanography from Laminated Sediments*, A. E. S. Kemp, Ed. (Special Publications v. 116, Geological Society, London, 1996), pp. 23–36.
9. J. Schieber, *Sediment. Res.* **69**, 909 (1999).

10.1126/science.1151980

TRANSCRIPTION

Seven Ups the Code

Jeffry L. Corden

Patterns of phosphorylation in a region of RNA polymerase II may constitute a code that controls the recruitment of regulatory factors to control gene expression.

Eukaryotic RNA polymerase II, the enzyme that converts DNA information into RNA, couples this transcriptional activity to both modifying the DNA template (chromatin) and to processing nascent RNA transcripts into mature forms. Proteins that carry out the latter two functions are tethered to the catalytic core of polymerase II by a flexible carboxyl-terminal domain (CTD) that harbors tandem repeats of the consensus amino acid sequence Tyr^1-Ser^2-Pro^3-Thr^4-Ser^5-Pro^6-Ser^7 (*1*–*3*). Actively transcribing polymerase II is phosphorylated on different sites within this heptapeptide sequence, and the pattern of phosphorylation has been proposed as a code that controls the binding of different regulatory factors to the enzyme (*4*). Two papers in this issue, by Chapman *et al.* on page 1780 (*5*) and by Egloff *et al.* on page 1777 (*6*), provide evidence that expands the number of potential CTD phosphorylation states, supporting the notion of a CTD code. Together, the papers show that CTD phosphorylation is more complicated than previously thought and link, for the first time, expression of specific genes with a distinct CTD phosphorylation pattern.

CTD heptapeptides are tandemly repeated from 17 to 52 times in different eukaryotes and these sequences are modified by phosphorylation, glycosylation, and proline isomerization (*2*, *3*). In principle, CTD modification could dictate many aspects of polymerase II function including assembly of the multisubunit enzyme, its transport to the nucleus, its localization either on the DNA template or within subnuclear domains, and its eventual destruction.

Most work to date has focused on the role of CTD phosphorylation during transcription. The pattern of phosphorylation is established

The author is in the Department of Molecular Biology and Genetics, Johns Hopkins Medical School, Baltimore, MD 21205, USA. E-mail: jcorden@jhmi.edu

by the balanced activities of enzymes that phosphorylate (kinases) and dephosphorylate (phosphatases) the CTD (*3*). Earlier work showed that serine-2 and serine-5 are phosphorylated (*7*). More recent studies have shown that serine-5 is phosphorylated when the polymerase passes through the 5′ end of a gene, whereas serine-2 phosphorylation is prominent when the enzyme reaches the gene's 3′ end (*8*). When polymerase II is in the middle of a gene, both serine-2 and serine-5 are phosphorylated. Capping enzymes that modify the 5′ end of nascent RNA polymerase II transcripts bind to phosphorylated serine-5 repeats, whereas RNA cleavage and polyadenylation factors prefer phosphorylated serine-2 repeats near the 3′ end of RNA (*3*).

Chapman *et al*. created antibodies that recognize these and other forms of phosphorylated CTD. The most surprising result indicates that serine-7 is phosphorylated on actively transcribing polymerase II, increasing the number of possible heptapeptide serine-phosphorylation states from four to eight (see the figure). If each individual heptapeptide repeat is independently modified in human cells, this could lead to nearly 8^{52} different CTD serine phosphorylation patterns.

How many different CTD serine phosphorylation patterns are present in cells, and are these phosphorylated isomers functionally distinct? Given the similarity of multiple repeats, it seems unlikely that kinases and phosphatases can discriminate sufficiently to independently modify most repeats. The pattern of modified repeats is thus likely to be more uniform depending on which kinase or phosphatase is brought close to the CTD. Chapman *et al*. provide evidence for at least two distinct populations of polymerase II primarily phosphorylated at either serine-2 or serine-5. What about multiply phosphorylated repeats? Mutation of serine-7 to alanine in multiple repeats reduces the abundance of a form of polymerase II that binds an antibody specific to phosphorylated serine-5, suggesting that phosphorylation of both residues may be linked. Intriguingly, serine-7 mutations seem to have different effects on polymerase activity when they are located in the proximal or distal repeats within the CTD, suggesting that differential modification may direct the functional specialization of different repeats within the CTD array. The antibody reagents described by Chapman *et al*. are ideal for further characterizing the different CTD serine-phosphorylated forms that constitute part of the CTD code.

What role does serine-7 play in gene expression? Chapman *et al*. show that serine-7 is phosphorylated when polymerase II is present on several protein-coding genes, but mutation of this serine to alanine does not reduce gene expression. In contrast, Egloff *et al*. show that serine-7 is required for expression of the U2 small nuclear RNA gene in mammalian cells. These data are consistent with earlier work showing that distal CTD repeats—which are degenerate and include lysine or threonine at position 7 (*1*)—are less effective at directing U2 processing relative to the proximal repeats (*9*). In the Egloff *et al*. study, mutation of serine-7 to alanine does not block recruitment of polymerase II to genes, but blocks the processing of nascent RNA transcripts. Moreover, the authors show that the integrator complex, which is required for 3′-end processing of small nuclear RNAs (*10*), binds specifically to phosphorylated serine-7 in the CTD. The kinase that phosphorylates this residue when polymerase II is on the U2 gene has not been identified but is presumed to be part of the transcription complex that drives expression of small nuclear RNA genes. The requirement for serine-7 phosphorylation is the first example of a specifically modified form of polymerase II involved in expressing a particular type of gene, and is the strongest evidence yet for a gene-specific CTD code.

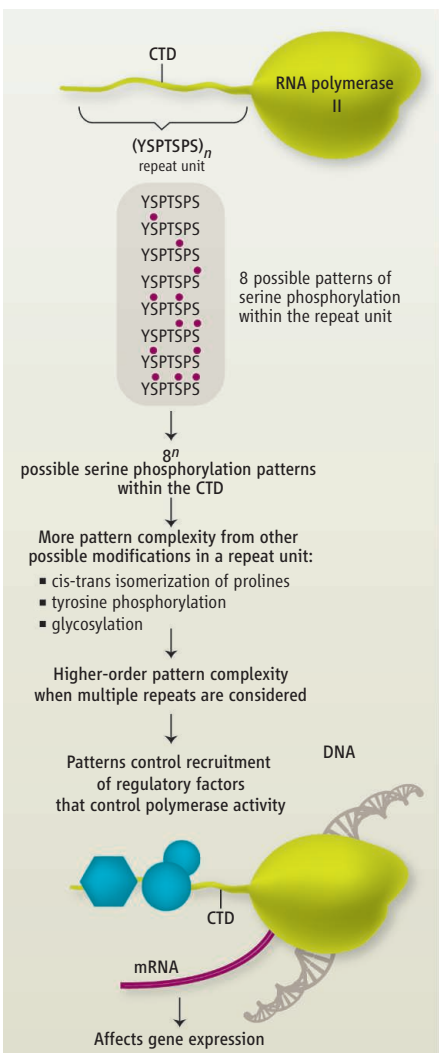

The CTD code. The carboxyl-terminal domain (CTD) of RNA polymerase II contains repeats of a consensus sequence that can be differentially modified. Different patterns of modification may constitute a code that directs the various polymerase activities.

The CTD may be more broadly involved in gene-specific regulation. For example, a large number of unexpressed human protein-coding genes contain an engaged polymerase II at their 5′ end (*11*). Although the state of CTD phosphorylation at these inactive genes was not determined, these genes showed evidence of transcription initiation. It is possible that regulation of CTD phosphorylation is required for polymerase II to proceed along the DNA template beyond a promoter-proximal block; polymerase activation may occur through promoter-specific recruitment of appropriate kinases to act on the CTD. Another possibility is that the CTD code could in some cases be linked to the histone code, which also regulates gene expression. For example, when polymerase II passes through the middle of a gene, the histone methyltransferase Set2 recognizes repeats in the CTD containing both phosphorylated serine-2 and phosphorylated serine-5 (*3*). Set2 methylates histone H3, and this modification recruits a histone deacetylase. The resulting histone hypoacetylation may alter DNA conformation such that polymerase II cannot initiate transcription at cryptic (and potentially regulatory) promoters located within a gene.

The biological role of CTD phosphorylation remains to be fully elucidated, but the emerging picture is that the pattern of CTD phosphorylation changes during RNA synthesis, allowing dynamic modification of the DNA template and processing of the nascent RNA transcript. The studies by Chapman *et al*. and by Egloff *et al*. provide both the tools to fully document CTD phosphorylation patterns and the best evidence to date that these patterns constitute a code that intersects, at the most fundamental level, with the regulation of different classes of eukaryotic genes.

References

1. J. L. Corden, *Trends Biochem. Sci.* **15**, 383 (1990).
2. A. Meinhart *et al*., *Genes Dev.* **19**, 1401 (2005).
3. H. P. Phatnani, A. L. Greenleaf, *Genes Dev.* **20**, 2922 (2006).
4. S. Buratowski, *Nat. Struct. Biol.* **10**, 679 (2003).
5. R. D. Chapman *et al*., *Science* **318**, 1780 (2007).
6. S. Egloff *et al*., *Science* **318**, 1777 (2007).
7. M. Patturajan *et al*., *J. Biol. Chem.* **273**, 4689 (1998).
8. P. Komarnitsky *et al*., *Genes Dev.* **14**, 2452 (2000).
9. J. E. Medlin *et al*., *EMBO J.* **22**, 925 (2003).
10. D. Baillat *et al*., *Cell* **123**, 265 (2005).
11. M. G. Guenther *et al*., *Cell* **130**, 77 (2007).

10.1126/science.1152624

Coral Reefs Under Rapid Climate Change and Ocean Acidification

O. Hoegh-Guldberg,[1*] P. J. Mumby,[2] A. J. Hooten,[3] R. S. Steneck,[4] P. Greenfield,[5] E. Gomez,[6] C. D. Harvell,[7] P. F. Sale,[8] A. J. Edwards,[9] K. Caldeira,[10] N. Knowlton,[11] C. M. Eakin,[12] R. Iglesias-Prieto,[13] N. Muthiga,[14] R. H. Bradbury,[15] A. Dubi,[16] M. E. Hatziolos[17]

Atmospheric carbon dioxide concentration is expected to exceed 500 parts per million and global temperatures to rise by at least 2°C by 2050 to 2100, values that significantly exceed those of at least the past 420,000 years during which most extant marine organisms evolved. Under conditions expected in the 21st century, global warming and ocean acidification will compromise carbonate accretion, with corals becoming increasingly rare on reef systems. The result will be less diverse reef communities and carbonate reef structures that fail to be maintained. Climate change also exacerbates local stresses from declining water quality and overexploitation of key species, driving reefs increasingly toward the tipping point for functional collapse. This review presents future scenarios for coral reefs that predict increasingly serious consequences for reef-associated fisheries, tourism, coastal protection, and people. As the International Year of the Reef 2008 begins, scaled-up management intervention and decisive action on global emissions are required if the loss of coral-dominated ecosystems is to be avoided.

Coral reefs are among the most biologically diverse and economically important ecosystems on the planet, providing ecosystem services that are vital to human societies and industries through fisheries, coastal protection, building materials, new biochemical compounds, and tourism (*1*). Yet in the decade since the inaugural International Year of the Reef in 1997 (*2*), which called the world to action, coral reefs have continued to deteriorate as a result of human influences (*3*, *4*). Rapid increases in the atmospheric carbon dioxide concentration ($[CO_2]_{atm}$), by driving global warming and ocean acidification, may be the final insult to these ecosystems. Here, we review the current understanding of how anthropogenic climate change and increasing ocean acidity are affecting coral reefs and offer scenarios for how coral reefs will change over this century. The scenarios are intended to provide a framework for proactive responses to the changes that have begun in coral reef ecosystems and to provoke thinking about future management and policy challenges for coral reef protection.

[1]Centre for Marine Studies, The University of Queensland, St. Lucia, 4072 Queensland, Australia. [2]Marine Spatial Ecology Laboratory, School of BioSciences, University of Exeter, Prince of Wales Road, Exeter EX4 4PS, UK. [3]AJH Environmental Services, 4900 Auburn Avenue, Suite 201, Bethesda, MD 20814, USA. [4]University of Maine, School of Marine Sciences, Darling Marine Center, Walpole, ME 04573, USA. [5]The Chancellery, University of Queensland, St. Lucia, 4072 Queensland, Australia. [6]Marine Science Institute, University of the Philippines, Diliman, Quezon City, Philippines. [7]Ecology and Evolutionary Biology, E321 Corson Hall, Cornell University, Ithaca, NY 14853, USA. [8]International Network on Water, Environment and Health, United Nations University, 50 Main Street East, Hamilton, Ontario L8N 1E9, Canada. [9]School of Biology, Ridley Building, University of Newcastle, Newcastle upon Tyne, NE1 7RU, UK. [10]Department of Global Ecology, Carnegie Institution of Washington, 260 Panama Street, Stanford, CA 94305, USA. [11]National Museum of Natural History, Smithsonian Institution, Washington, DC 20013, USA. [12]National Oceanic and Atmospheric Administration, Coral Reef Watch, E/RA31, 1335 East West Highway, Silver Spring, MD 20910–3226, USA. [13]Unidad Académica Puerto Morelos, Instituto de Ciencias del Mar y Limnología, Universidad Nacional Autónoma de México, Apdo. Postal 1152, Cancún 77500 QR, México. [14]Wildlife Conservation Society, 2300 Southern Boulevard, Bronx, New York, NY 10460, USA. [15]Resource Management in Asia-Pacific Program, Australian National University, Canberra, 0200 Australia. [16]Institute of Marine Sciences, University of Dar es Salaam, Tanzania. [17]Environment Department, MC5-523, The World Bank, 1818 H Street, NW, Washington, DC 20433, USA.

*To whom correspondence should be addressed. E-mail: oveh@uq.edu.au

Warming and Acidifying Seas

The concentration of carbon dioxide in Earth's atmosphere now exceeds 380 ppm, which is more than 80 ppm above the maximum values of the past 740,000 years (*5*, *6*), if not 20 million years (*7*). During the 20th century, increasing $[CO_2]_{atm}$ has driven an increase in the global oceans' average temperature by 0.74°C and sea level by 17 cm, and has depleted seawater carbonate concentrations by ~30 μmol kg^{-1} seawater and acidity by 0.1 pH unit (*8*). Approximately 25% (2.2 Pg C $year^{-1}$) of the CO_2 emitted from all anthropogenic sources (9.1 Pg C $year^{-1}$) currently enters the ocean (*9*), where it reacts with water to produce carbonic acid. Carbonic acid dissociates to form bicarbonate ions and protons, which in turn react with carbonate ions to produce more bicarbonate ions, reducing the availability of carbonate to biological systems (Fig. 1A). Decreasing carbonate-ion concentrations reduce the rate of calcification of marine organisms such as reef-building corals, ultimately favoring erosion at ~200 μmol kg^{-1} seawater (*7*, *10*).

We used global $[CO_2]_{atm}$ and temperature data from the Vostok Ice Core study (*5*) to explore the ocean temperature and carbonate-ion concentration (*10*) seen today relative to the recent past for a typical low-latitude sea maintaining a mean temperature of 25°C during the past 420,000 years (Fig. 1B). The results show a tight cluster of points that oscillate (temperature ±3°C; carbonate-ion concentration ±35 μmol kg^{-1}) between warmer interglacial periods that had lower carbonate concentrations to cooler glacial periods with higher carbonate concentrations. The overall range of values calculated for seawater pH is ±0.1 units (*10*, *11*). Critically, where coral reefs occur, carbonate-ion concentrations over the past 420,000 years have not fallen below 240 μmol kg^{-1}. The trends in the Vostok ice core data have been verified by the EPICA study (*6*), which involves a similar range of temperatures and $[CO_2]_{atm}$ values and hence extends the conclusions derived from the Vostok record to at least 740,000 years before the present (yr B.P.). Conditions today ($[CO_2]_{atm}$ ~380 ppm) are significantly shifted to the right of the cluster points representing the past 420,000 years. Sea temperatures are warmer (+0.7°C), and pH (−0.1 pH units) and carbonate-ion concentrations (~210 μmol kg^{-1}) lower than at any other time during the past 420,000 years (Fig. 1B). These conclusions match recent changes reported for measurements of ocean temperature, pH, and carbonate concentration (*8*). In addition to the absolute amount of change, the rate at which change occurs is critical to whether organisms and ecosystems will be able to adapt or accommodate to the new conditions (*11*). Notably, rates of change in global temperature and $[CO_2]_{atm}$ over the past century are 2 to 3 orders of magnitude higher than most of the changes seen in the past 420,000 years (Table 1). Rates of change under both low (B1) and high (A2) Intergovernmental Panel on Climate Change (IPCC) emission scenarios are even higher, as are recent measurements of the rate of change of $[CO_2]_{atm}$ (*9*). The only possible exceptions are rare, short-lived spikes in temperature seen during periods such as the Younger Dryas Event (12,900 to 11,500 yr B.P.) (*12*). Given that recent and future rates of change dwarf even those of the ice age transitions, when biology at specific locations changed dramatically, it is likely that these changes will exceed the capacity of most organisms to adapt.

Ocean Acidification and Reef Accretion

Many experimental studies have shown that a doubling of pre-industrial $[CO_2]_{atm}$ to 560 ppm decreases coral calcification and growth by up to 40% through the inhibition of aragonite formation (the principal crystalline form of calcium carbonate deposited in coral skeletons) as carbonate-ion concentrations decrease (*13*). Field studies confirm that carbonate accretion on coral reefs approaches zero or becomes negative at aragonite saturation values of 3.3 in today's oceans (Fig. 4), which occurs when $[CO_2]_{atm}$ approaches 480 ppm and carbonate-ion concentrations drop below 200 μmol kg^{-1} in most of the global ocean (*10*, *13*). These findings are supported by the observation that reefs with net carbonate accretion today (Fig. 4, 380 ppm) are restricted to waters where aragonite saturation

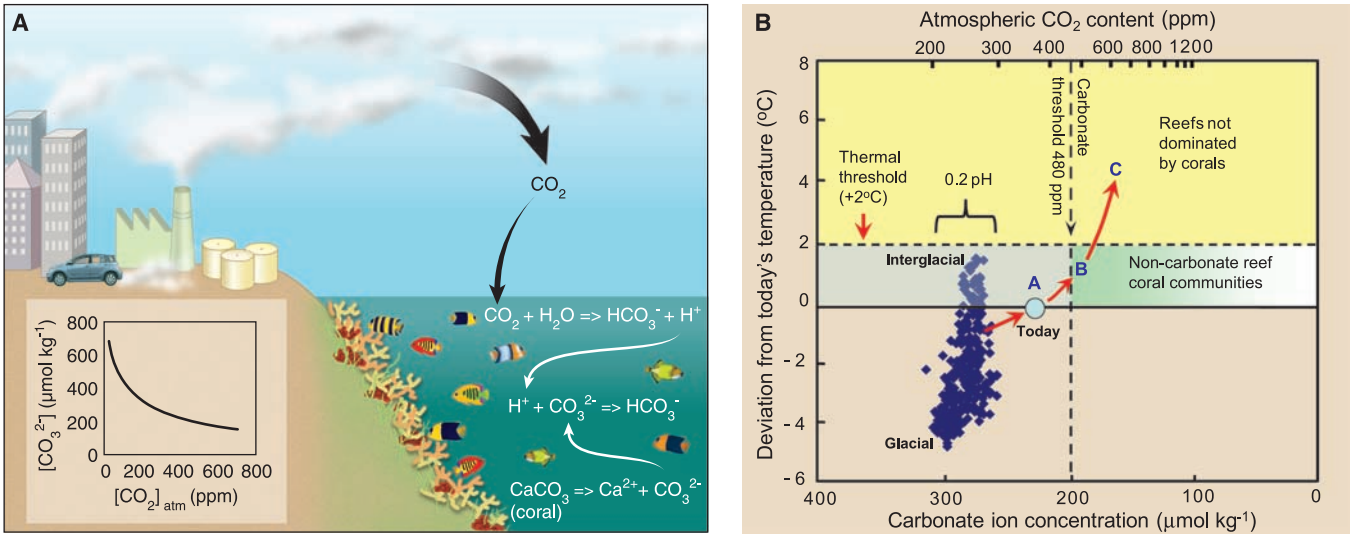

Fig. 1. (**A**) Linkages between the buildup of atmospheric CO_2 and the slowing of coral calcification due to ocean acidification. Approximately 25% of the CO_2 emitted by humans in the period 2000 to 2006 (*9*) was taken up by the ocean where it combined with water to produce carbonic acid, which releases a proton that combines with a carbonate ion. This decreases the concentration of carbonate, making it unavailable to marine calcifiers such as corals. (**B**) Temperature, $[CO_2]_{atm}$, and carbonate-ion concentrations reconstructed for the past 420,000 years. Carbonate concentrations were calculated (*54*) from $CO_{2\ atm}$ and temperature deviations from today's conditions with the Vostok Ice Core data set (*5*), assuming constant salinity (34 parts per trillion), mean sea temperature (25°C), and total alkalinity (2300 mmol kg^{-1}). Further details of these calculations are in the SOM. Acidity of the ocean varies by ± 0.1 pH units over the past 420,000 years (individual values not shown). The thresholds for major changes to coral communities are indicated for thermal stress (+2°C) and carbonate-ion concentrations ([carbonate] = 200 μmol kg^{-1}, approximate aragonite saturation ~$\Omega_{aragonite}$ = 3.3; $[CO_2]_{atm}$ = 480 ppm). Coral Reef Scenarios CRS-A, CRS-B, and CRS-C are indicated as A, B, and C, respectively, with analogs from extant reefs depicted in Fig. 5. Red arrows pointing progressively toward the right-hand top square indicate the pathway that is being followed toward $[CO_2]_{atm}$ of more than 500 ppm.

exceeds 3.3 (*10*). Geological studies report a notable gap in the fossil record of calcified organisms, including reef-building corals (*14*) and calcareous algae (*15*), during the early Triassic when $[CO_2]_{atm}$ increased dramatically and reached levels at least five times as high as today's (*16*). Phylogenetic studies suggest that corals as a group survived the Permian-Triassic extinction event (*14*) but may have done so through forms lacking calcified skeletons (*17*, *18*). Although Scleractinian (modern) corals arose in the mid-Triassic and lived under much higher $[CO_2]_{atm}$, there is no evidence that they lived in waters with low-carbonate mineral saturation. Knoll *et al.* succinctly state that "it is the rapid, unbuffered increase in $[CO_2]_{atm}$ and not its absolute values that causes important associated changes such as reduced $[CO_3^{2-}]$, pH, and carbonate saturation of sea water" (*19*). The rate of $[CO_2]_{atm}$ change is critical given that modern genotypes and phenotypes of corals do not appear to have the capacity to adapt fast enough to sudden environmental change.

Reef-building corals may exhibit several responses to reduced calcification, all of which have deleterious consequences for reef ecosystems. First, the most direct response is a decreased linear extension rate and skeletal density of coral colonies. The massive coral *Porites* on the Great Barrier Reef has shown reductions in linear extension rate of 1.02% $year^{-1}$ and in skeletal density of 0.36% $year^{-1}$ during the past 16 years (*20*). This is equivalent to a reduction of 1.29% $year^{-1}$ or a 20.6% drop in growth rate (the product of linear extension rate and skeletal density) over the 16-year period. While at present it is not possible to confidently attribute the observed decrease in growth and calcification to ocean acidification, it is consistent with changes reported in oceanic pH and carbonate-ion concentrations.

Second, corals may maintain their physical extension or growth rate by reducing skeletal density. However, erosion could be promoted by the activities of grazing animals such as parrotfish, which prefer to remove carbonates from lower-density substrates. Increasingly brittle coral skeletons are also at greater risk of storm damage (*21*); thus, if rates of erosion outstrip calcification, then the structural complexity of coral reefs will diminish, reducing habitat quality and diversity. A loss of structural complexity will also affect the ability of reefs to absorb wave energy and thereby impairs coastal protection.

Third, corals may maintain both skeletal growth and density under reduced carbonate saturation by investing greater energy in calcification. A likely side effect of this strategy is the diversion of resources from other essential processes, such as reproduction, as seen in chronic stress (*21*), which could ultimately reduce the larval output from reefs and impair the potential for recolonization following disturbances.

Table 1. Rates of change in atmospheric CO_2 concentration ($[CO_2]_{atm}$, ppm/100 years) and global temperature (°C/100 years) calculated for the past 420,000 yr B.P. using the Vostok Ice Core data (*5*) and compared to changes over the last century and those projected by IPCC for low-emission (B1) and high-emission (A2) scenarios (*8*). Rates were calculated for each successive pair of points in the Vostok Ice Core record by dividing the difference between two sequential values (ppm or °C) by the time interval between them. Rates were then standardized to the change seen over 100 years. Ratios of each rate relative to the mean rate seen over the past 420,000 years are also calculated.

Period	$[CO_2]_{atm}$ (ppm $century^{-1}$)	Ratio (relative to past 420,000 years)	Temperature (°C $century^{-1}$)	Ratio (relative to past 420,000 years)
Past 420,000 years (99% confidence interval; n = 282)	0.07 + 0.223	1	0.01 + 0.017	1
Past 136 years (1870–2006)	73.53	1050	0.7	70
IPCC B1 scenario: 550 ppm at 2100	170	2429	1.8	180
IPCC A2 scenario: 800 ppm at 2100	420	6000	3.4	420

Resilience and Tipping Points

Maintaining ecological resilience is the central plank of any strategy aiming to preserve coral reef

ecosystems. Ecological resilience (*4*) is a measure of the rate at which an ecosystem returns to a particular state (e.g., coral-dominated communities) after a perturbation or disturbance (e.g., hurricane impacts). Recent changes to the frequency and scale of disturbances such as mass coral bleaching, disease outbreaks, and destructive fishing, coupled with a decreased ability of corals to grow and compete, are pushing reef ecosystems from coral- to algal-dominated states (*4*, *22*). If pushed far enough, the ecosystem may exceed a "tipping point" (*22*) and change rapidly into an alternative state with its own inherent resilience and stability, often making the possibility of returning to a coral-dominated state difficult.

To examine the ecological implications of the 20.6% reduction in coral growth rate that Cooper *et al.* measured in Great Barrier Reef *Porites* (*20*), we simulated a similar reduction in the growth of massive brooding and spawning corals on exposed Caribbean forereefs specifically to investigate what happens to the balance between corals and macroalgae in a system of high primary production (Fig. 2). The ecological model (*22*) simulated a 50-year time series for a wide range of initial coral cover and grazing rates by fish on benthic algae while holding all other factors (e.g., nutrient concentrations) constant. Each time series revealed the underlying trajectory of coral recovery, stasis, or degradation between major disturbances, and the final equilibrium values of coral cover were plotted to illustrate potential resilience (Fig. 2). The unstable equilibria represent thresholds, and for recovery to outweigh mortality reefs must lie either above or to the right of the threshold. For example, if coral cover is low (<5%), the intensity of fish grazing on benthic algal competitors needed to shift the reef into a state where recovery is possible (i.e., to the right or above the unstable equilibrium) moves from 30% to almost a half of the reef having to be grazed. This implies that in the absence of invertebrate grazers like the sea urchin, *Diadema antillarum*, which essentially disappeared from Caribbean reefs in the early 1980s after a massive disease outbreak, highly productive reefs would likely require the highest levels of parrotfish grazing (i.e., ~40% of the reef being grazed) for a reef to be able to recover from disturbance. The loss of ecological resilience occurs because coral cover increases more slowly after disturbance and competitive interactions with macroalgae become more frequent and longer in duration (Fig. 3) (*23*) (table S1). Although the ecological model only represents a single Caribbean reef habitat in a very productive physical environment and has not incorporated several other putative consequences of acidification such as a loss of rugosity, sensitivity analyses reveal that changes to coral growth rate have a relatively large impact on model predictions (*22*), and therefore the conclusions of a reduction in resilience appear to be robust.

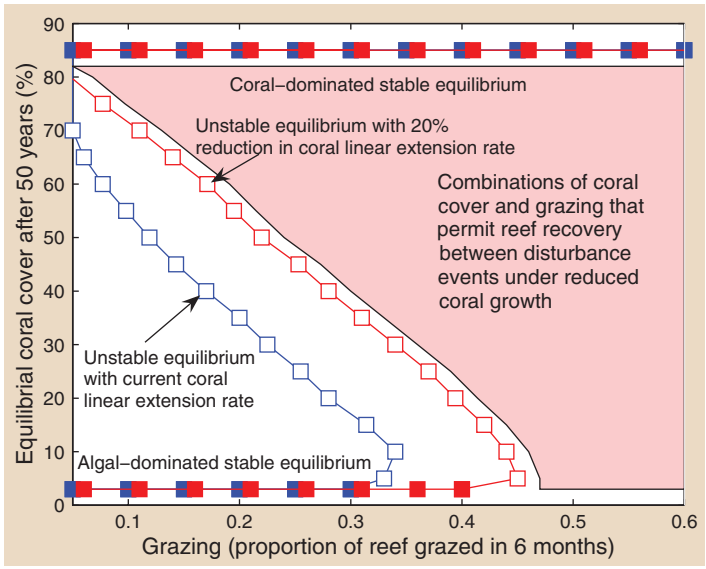

Fig. 2. Reduction in the resilience of Caribbean forereefs as coral growth rate declines by 20%. Reef recovery is only feasible above or to the right of the unstable equilibria (open squares). The "zone of reef recovery" (pink) is therefore more restricted under reduced coral growth rate and reefs require higher levels of grazing to exhibit recovery trajectories.

Thermal Stress, Synergies, and Ecological Feedback Loops

The sensitivity of corals and their endosymbiotic dinoflagellates (*Symbiodinium* spp.) to rising ocean temperatures has been documented extensively (*24*). *Symbiodinium* trap solar energy and nutrients, providing more than 95% of the metabolic requirements of the coral host, which

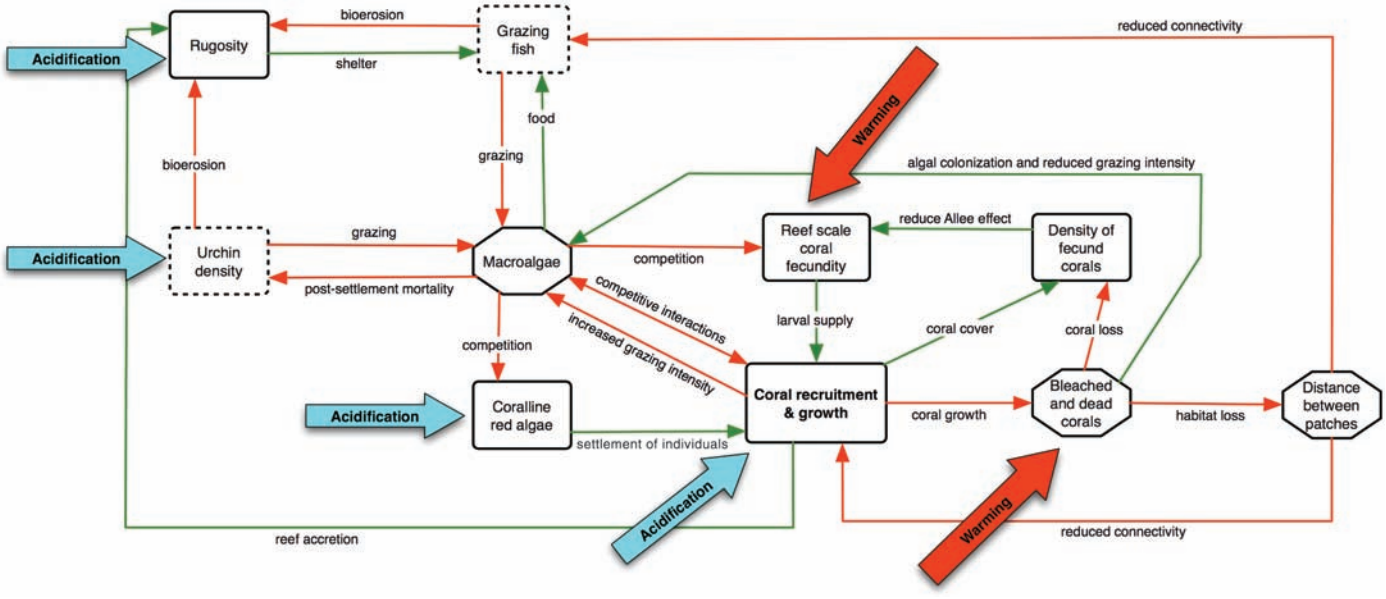

Fig. 3. Ecological feedback processes on a coral reef showing pathways of disturbance caused by climate change. Impact points associated with ocean acidification (e.g., reduced reef rugosity, coralline algae) are indicated by the blue arrows, and impact points from global warming (e.g., bleached and dead corals) by the red arrows. Boxes joined by red arrows denote that the first factor has a negative (decreasing) influence on the box indicated. Green arrows denote positive (increasing) relationships. Over time, the levels of factors in hexagonal boxes will increase, whereas those in rectangular boxes will decline. Boxes with dashed lines are amenable to local management intervention.

is consequently able to maintain high calcification rates. When temperatures exceed summer maxima by 1° to 2°C for 3 to 4 weeks, this obligatory endosymbiosis disintegrates with ejection of the symbionts and coral bleaching (*24*). Bleaching and mortality become progressively worse as thermal anomalies intensify and lengthen (*24*). Indeed, mass coral bleaching has increased in intensity and frequency in recent decades (*24*–*27*). At the end of the International Year of the Reef in 1997, mass bleaching spread from the Eastern Pacific to most coral reefs worldwide, accompanied by increasing coral mortality during the following 12 months (*24*). Corals may survive and recover their dinoflagellate symbionts after mild thermal stress, but typically show reduced growth, calcification, and fecundity (*24*) and may experience greater incidences of coral disease (*28*, *29*).

To illustrate the combined effects of acidification and bleaching on reefs, we simplified the coral ecosystem into the nine features required to model feedback mechanisms (Fig. 3). Although it is not comprehensive, the model provides a theoretical framework indicating that acidification and bleaching enhance all deleterious feedbacks, driving the coral ecosystems toward domination by macroalgae and noncoral communities (Fig. 3) (table S1).

Trajectories in Response to Climate Change

Global temperatures are projected to increase rapidly to 1.8°C above today's average temperature under the low-emission B1 scenario of the IPCC, or by 4.0°C (2.4° to 6.4°C) under the higher-emission A1F1 scenario (Table 1) (*8*). Increases in the temperature of tropical and subtropical waters over the past 50 years (*24*) have already pushed reef-building corals close to their thermal limits. Projections for ocean acidification include reductions in oceanic pH by as much as 0.4 pH units by the end of this century, with ocean carbonate saturation levels potentially dropping below those required to sustain coral reef accretion by 2050 (Fig. 4) (*7, 10, 13*). Changes in ocean acidity will vary from region to region, with some regions, such as the Great Barrier Reef and Coral Sea, and the Caribbean Sea, attaining risky levels of aragonite saturation more rapidly than others (Fig. 4). Just as carbonate coral reefs do not exist in waters with carbonate-ion concentrations < 200 μmol kg^{-1} (*10*), they are likely to contract rapidly if future $[CO_2]_{atm}$ levels exceed 500 ppm. Similarly, unless thermal thresholds change, coral reefs will experience an increasing frequency and severity of mass coral bleaching, disease, and mortality as $[CO_2]_{atm}$ and temperatures increase (*24*–*27*).

We have projected three scenarios for coral reefs over the coming decades and century. In doing so, we recognize that important local threats to coral reefs, such as deterioration of water quality arising from sediment and nutrient inputs associated with coastal development and deforestation, and the overexploitation of marine fishery stocks, may produce synergies and feedbacks in concert with climate change (*30*) (Fig. 3) [supporting online material (SOM)]. How quickly we arrive at or how long we stay within each of the three scenarios will depend on the CO_2 emission rate, with each scenario highlighting the context against which management and policy actions must be devised.

If conditions were stabilized at the present $[CO_2]_{atm}$ of 380 ppm, that is, Coral Reef Scenario CRS-A (Figs. 1B and 5A), coral reefs will continue to change but will remain coral dominated and carbonate accreting in most areas of their current distribution. Local factors—i.e., those not directly related to global climate change, such as changes to water quality—affecting levels of sediment, nutrients, toxins, and pathogens, as well as fishing pressure, will be important determinants of reef state and should demand priority attention in reef-management programs. However, as we move toward higher $[CO_2]_{atm}$, coral-community compositions will change with some areas becoming dominated by more thermally tolerant corals like the massive *Porites* (*31*) and others potentially dominated by thermally sensitive but rapidly colonizing genera, such as the tabulate *Acropora*. Under the current rate of increase in $[CO_2]_{atm}$ (>1 ppm $year^{-1}$), carbonate-ion concentrations will drop below 200 μmol kg^{-1} and reef erosion will exceed calcification at $[CO_2]_{atm}$ = 450 to 500 ppm, i.e., Scenario CRS-B (Figs. 1 and 5B). The density and diversity of corals on reefs are likely to decline, leading to vastly reduced habitat complexity and loss of biodiversity (*31*), including losses of coral-associated fish and invertebrates (*32*).

Coralline algae are a key settlement substrate for corals, but they have metabolically expensive high-magnesium calcite skeletons that are very sensitive to pH (*33*). Hence, coral recruitment may be compromised if coralline algal abundance declines. Coral loss may also be compounded by an increase in disease incidence (*34*). Ultimately, the loss of corals liberates space for the settlement of macroalgae, which in turn tends to inhibit coral recruitment, fecundity, and growth because they compete for space and light, and also produce antifouling compounds that deter settlement by potential competitors. Together these factors allow macroalgae to form stable communities that are relatively resistant to a return to coral domination (Figs. 2 and 3) (*22*, *23*, *35*). As a result of weakening of coral growth and competitive ability, reefs within the CRS-B scenario will be more sensitive to the damaging influence of other local factors, such as declining water quality and the removal of key herbivore fish species.

Increases in $[CO_2]_{atm}$ > 500 ppm (*11*) will push carbonate-ion concentrations well below

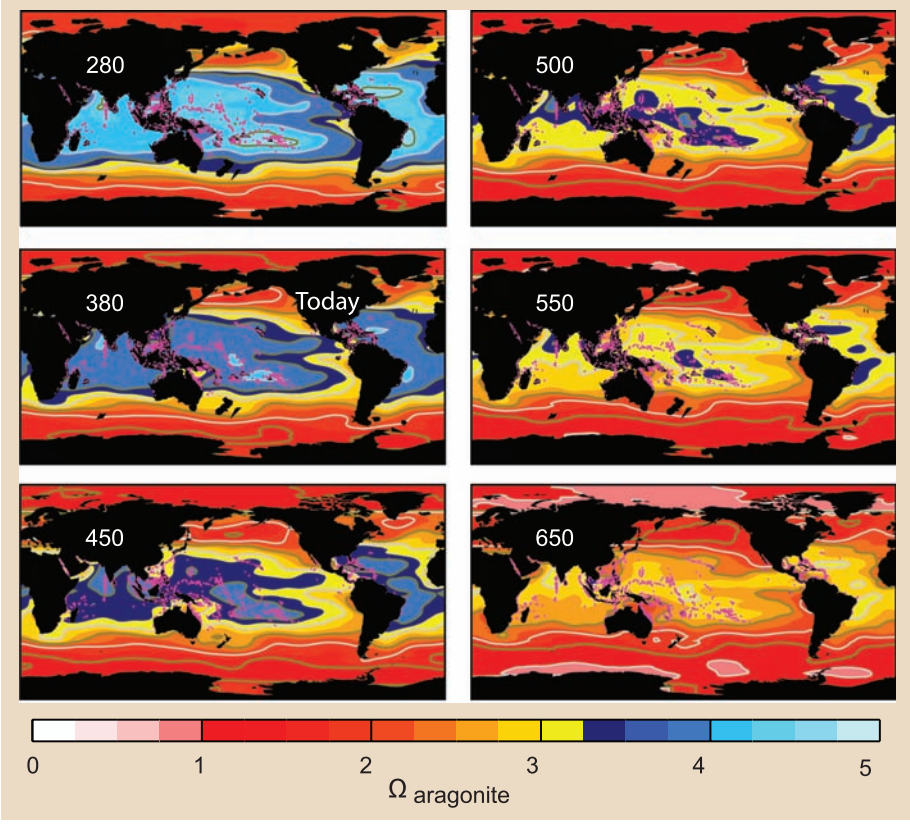

Fig. 4. Changes in aragonite saturation {$\Omega_{aragonite}$ = ($[Ca^{2+}].[CO_3^{2-}]/K_{sp\ aragonite}$)} predicted to occur as atmospheric CO_2 concentrations (ppm) increase (number at top left of each panel) plotted over shallow-water coral reef locations shown as pink dots (for details of calculations, see the SOM). Before the Industrial Revolution (280 ppm), nearly all shallow-water coral reefs had $\Omega_{aragonite}$ > 3.25 (blue regions in the figure), which is the minimum $\Omega_{aragonite}$ that coral reefs are associated with today; the number of existing coral reefs with this minimum aragonite saturation decreases rapidly as $[CO_2]_{atm}$ increases. Noticeably, some regions (such as the Great Barrier Reef) attain low and risky levels of $\Omega_{aragonite}$ much more rapidly than others (e.g., Central Pacific).

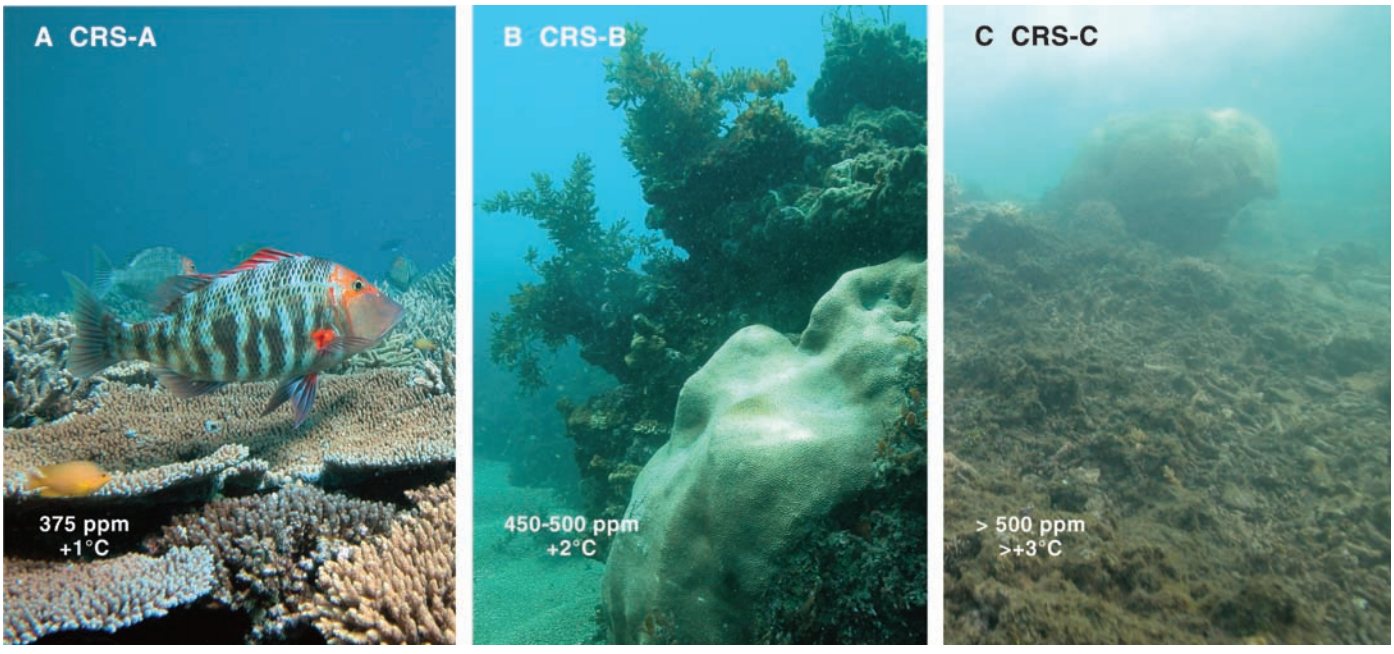

Fig. 5. Extant examples of reefs from the Great Barrier Reef that are used as analogs for the ecological structures we anticipate for Coral Reef Scenarios CRS-A, CRS-B, and CRS-C (see text). The $[CO_2]_{atm}$ and temperature increases shown are those for the scenarios and do not refer to the locations photographed. (**A**) Reef slope communities at Heron Island. (**B**) Mixed algal and coral communities associated with inshore reefs around St. Bees Island near Mackay. (**C**) Inshore reef slope around the Low Isles near Port Douglas. [Photos by O. Hoegh-Guldberg]

200 μmol kg^{-1} (aragonite saturation < 3.3) and sea temperatures above +2°C relative to today's values (Scenario CRS-C, Fig. 1). These changes will reduce coral reef ecosystems to crumbling frameworks with few calcareous corals (Fig. 5C). The continuously changing climate, which may not stabilize for hundreds of years, is also likely to impede migration and successful proliferation of alleles from tolerant populations owing to continuously shifting adaptive pressure. Under these conditions, reefs will become rapidly eroding rubble banks such as those seen in some inshore regions of the Great Barrier Reef, where dense populations of corals have vanished over the past 50 to 100 years. Rapid changes in sea level (+23 to 51 cm by 2100, scenario A2) (*8*), coupled with slow or nonexistent reef growth, may also lead to "drowned" reefs (*36*) in which corals and the reefs they build fail to keep up with rising sea levels.

The types of synergistic impacts on coral and reef-dependent organisms defined for Scenario CRS-B (Fig. 5B) will be magnified substantially for CRS-C (Fig. 5C), with probably half, and possibly more, of coral-associated fauna becoming rare or extinct given their dependence on living corals and reef rugosity (*37*). Macroalgae may dominate in some areas and phytoplankton blooms may become more frequent in others, as water quality declines owing to the collateral impact of climate change on associated coastal areas, drying catchments and causing episodic heavy rainfall that transports nutrients and sediments into coastal areas. Whether or not one defines the transition from CRS-B to CRS-C and $[CO_2]_{atm}$ of 450 to 500 ppm as the tipping point for coral reefs, it is clear that coral reefs as we know them today would be extremely rare at higher $[CO_2]_{atm}$.

We recognize that physiological acclimation or evolutionary mechanisms could delay the arrival of some scenarios. However, evidence that corals and their symbionts can adapt rapidly to coral bleaching is equivocal or nonexistent. Reef-building corals have relatively long generation times and low genetic diversity, making for slow rates of adaptation. Changes in species composition are also possible but will have limited impact, as even the most thermally tolerant corals will only sustain temperature increases of 2° to 3°C above their long-term solar maxima for short periods (*24*, *31*). However, such changes come at a loss of biodiversity and the removal of important redundancies from these complex ecosystems. Some studies have shown that corals may promote one variety of dinoflagellate symbiont over another in the relatively small number of symbioses that have significant proportions of multiple dinoflagellate types (*38*). These phenotypic changes extend the plasticity of a symbiosis (e.g., by 1° to 2°C) (*21*) but are unlikely to lead to novel, long-lived associations that would result in higher thermal tolerances (*39*). The potential for acclimation even to current levels of ocean acidification is also low given that, in the many studies done to date, coral calcification has consistently been shown to decrease with decreasing pH and does not recover as long as conditions of higher acidity persist (*13*).

Socioeconomic Impacts of Coral Reef Decline

The scenarios presented here are likely to have serious consequences for subsistence-dependent societies, as well as on wider regional economies through their impact on coastal protection, fisheries, and tourism. These consequences become successively worse as $[CO_2]_{atm}$ increases, and unmanageable for $[CO_2]_{atm}$ above 500 ppm. Although reefs with large communities of coral reef-related organisms persist under CRS-A and CRS-B, they become nonfunctional under CRS-C, as will the reef services that currently underpin human welfare. Climate change is likely to fundamentally alter the attractiveness of coral reefs to tourists (compare Fig. 5, A and C), which is an important consideration for the many low-income coastal countries and developing small island states lying within coral reef regions. Under-resourced and developing countries have the lowest capacity to respond to climate change, but many have tourism as their sole income earner and thus are at risk economically if their coral reefs deteriorate (*40*). For instance, tourism is a major foreign exchange earner in the Caribbean basin and in some countries accounts for up to half of the gross domestic product (*40*). Coral reefs in the United States and Australia may supply smaller components of the total economy, but still generate considerable income (many billions of U.S. $ per year) from reef visitors that are increasingly responsive to the quality of reefs (*41*).

Reef rugosity is an important element for the productivity of all reef-based fisheries, whether subsistence, industrial, or to supply the aquarium trade. The density of reef fish (*32*) is likely to decrease as a result of increasing postsettlement mortality arising from a lack of hiding places and appropriate food for newly settled juveniles (*42*). Regardless of future climate-change influences, the total landing of coral reef fisheries is already 64% higher than

can be sustained, with an extra 156,000 km^2 of coral reef estimated as being needed to support anticipated population growth by 2050 (*43*). For example, in Asia alone coral reefs provide about one-quarter of the annual total fish catch and food to about 1 billion people (*43*). Climate-change impacts on available habitat will only exacerbate already overstretched fisheries resources.

The role of reefs in coastal protection against storms (*44*) has been highlighted in analyses of exposed and reef-protected coastlines (*45*, *46*). We do not yet have estimates for how fast reef barriers will disappear (*47*), but we can anticipate that decreasing rates of reef accretion, increasing rates of bioerosion, rising sea levels, and intensifying storms may combine to jeopardize a wide range of coastal barriers. People, infrastructure, and lagoon and estuarine ecosystems, including mangroves, seagrass meadows, and salt marshes, will become increasingly vulnerable to growing wave and storm impacts. Observations of increasingly intense tropical hurricanes and cyclones in all oceans (*48*) suggest that losses of beach sand from coastal zones are likely to increase (*49*). Further losses may occur from reduced sand production, formed in many cases by coral reefs, as a consequence of ocean acidification and thermal stress on calcareous algae and other sand producers. Beaches are also under threat of erosion from rising sea levels. The combination of these factors will lead to less stable beaches and impacts on other organisms, such as turtles and sea birds that depend on beach habitats for reproduction, as well as leading to economic impacts on tourism and coastal fishing communities.

Opportunities for Management Intervention

The inherent inertia of the atmosphere and of our attempts to mitigate CO_2 emissions suggest that reef managers and coastal resource policies must first reduce the influence of local stressors such as declining water quality, coastal pollution, and overexploitation of key functional groups such as herbivores (*4*). These types of action are most likely to assist coral reefs through the decades of stress that inevitably face them. There may be opportunities for using coral restoration to reduce the risk that reefs will shift into a non–coral-dominated state (Fig. 3); however, the efficacy of coral restoration methods to increase rugosity and coral cover remains unclear, and further evaluation of methods is badly needed. With respect to the latter, there is a mismatch between the feasible scale of restoration (hectares) and that of the extent of degradation (many thousands of km^2). Nevertheless, new techniques for the mass culture of corals from fragments and spat may assist local restoration or the culture of resistant varieties of key organisms (*44*).

At the 100- to 1000-km scale of coral reefs, one of the most practical interventions is to facilitate grazing by fish and invertebrate herbivores. This is likely to play an important role in situations like that of the Caribbean where densities of one important herbivore, the sea urchin *Diadema antillarum*, were decimated by disease in the early 1980s (*50*). Clearly, the improved management of reef fish, especially grazers such as parrotfish, would be expected to result in an improved ability of coral reefs to bounce back from disturbances (*51*), as long as other factors such as water quality are not limiting. Unfortunately, with the exception of marine reserves, there is negligible explicit management of herbivores in most countries, but this could be improved by setting catch limits (*52*). Diversification of the herbivore guild to include modest densities of invertebrates like sea urchins will also enhance the resilience of coral reef ecosystems.

Conclusion

It is sobering to think that we have used the lower range of IPCC scenarios in our analysis yet still envisage serious if not devastating ramifications for coral reefs. Emission pathways that include higher $[CO_2]_{atm}$ (600 to 1000 ppm) and global temperatures of 3° to 6°C defy consideration as credible alternatives. Equally important is the fact that IPCC scenarios are likely to be cautious given scientific reticence and the inherently conservative nature of consensus seeking within the IPCC process (*53*). Consequently, contemplating policies that result in $[CO_2]_{atm}$ above 500 ppm appears extremely risky for coral reefs and the tens of millions of people who depend on them directly, even under the most optimistic circumstances.

References and Notes

1. F. Moberg, C. Folke, *Ecol. Econ.* **29**, 215 (1999).
2. International Year of the Reef (IYOR), www.iyor.org/ (2008).
3. J. F. Bruno, S. E. Selig, *PLoS ONE* **2**, e711 (2007).
4. T. P. Hughes *et al*., *Science* **301**, 929 (2003).
5. D. A. Petit *et al*., *Nature* **399**, 429 (1999).
6. EPICA community members, *Nature* **429**, 623 (2004).
7. J. Raven *et al*., "Acidification due to increasing carbon dioxide." Policy Document 12/05 (The Royal Society, London, 2005).
8. IPCC, *Climate Change 2007: The Physical Science Basis. Contribution of Working Group I to the Fourth Assessment Report of the Intergovernmental Panel on Climate Change*, S. Solomon *et al*., Eds. (Cambridge Univ. Press, Cambridge, UK, and New York, 2007).
9. J. G. Canadell *et al*., *Proc. Natl. Acad. Sci. U.S.A.* **104**, 18866 (2007).
10. J. A. Kleypas, J. W. McManus, L. A. B. Meñez, *Am. Zool.* **39**, 146 (1999).
11. J. H. Connell, *Coral Reefs* **16** (suppl.), S101 (1997).
12. IPPC, *Climate Change 2001. The Scientific Basis. The Contribution of Working Group I to the Third Assessment Report of the Intergovernmental Panel on Climate Change*, J. T. Houghton *et al*., Eds. (Cambridge Univ. Press, New York, 2001).
13. J. A. Kleypas, C. Langdon, *Coast. Estuar. Stud.* **61**, 73 (2006)
14. G. D. Stanley Jr., *Earth-Sci. Rev.* **60**, 195 (2003).
15. J. L. Wray, *Proc. N. Am. Paleontol. Conv.* Pt. **J**, 1358 (1969)
16. R. A. Berner, Z. Kothavala, Am. *J. Sci.* **301**, 182 (2001).
17. M. Medina, A. G. Collins, T. L. Takaoka, J. V. Kuehl, J. L. Boore, *Proc. Natl. Acad. Sci. U.S.A.* **103**, 9096 (2007).
18. M. Fine, D. Tchernov, *Science* **315**, 1811 (2007)
19. A. H. Knoll, R. K. Bambach, J. L. Payne, S. Pruss, W. W. Fischer, *Earth Planet. Sci. Lett.* **256**, 295 (2008)
20. T. F. Cooper, G. De'ath, K. E. Fabricius, J. M. Lough, *Global Change Biol.*, in press.
21. A. M. Szmant, N. J. Gassman, *Coral Reefs* **8**, 217 (1990).
22. P. J. Mumby *et al*., *Nature* **450**, 98 (2007).
23. P. J. Mumby *et al*., *Proc. Natl. Acad. Sci. U.S.A.* **104**, 8362 (2007).
24. O. Hoegh-Guldberg, *Mar. Freshw. Res.* **50**, 839 (1999).
25. O. Hoegh-Guldberg, *J. Geophys. Res.* **110**, C09S06 (2005).
26. T. J. Done *et al*., "Global Climate Change and Coral Bleaching on the Great Barrier Reef, Final report to the State of Queensland Greenhouse Taskforce through the Department of Natural Resources and Mining, Townsville" (2003).
27. S. D. Donner, W. J. Skirving, C. M. Little, M. Oppenheimer, O. Hoegh-Guldberg, *Glob. Change Biol.* **11**, 2251 (2005).
28. C. D. Harvell *et al*., *Science* **296**, 2158 (2002).
29. J. F. Bruno *et al*., *PLoS Biol.* **5**, e124 (2007).
30. K. Newton, I. M. Cote, G. M. Pilling, S. Jennings, N. K. Dulvy, *Curr. Biol.* **17**, 655 (2007)
31. Y. K. Loya *et al*., *Ecol. Lett.* **4**, 122 (2001).
32. S. K. Wilson *et al*., *Glob. Change Biol.* **12**, 2220 (2006).
33. B. Honisch, N. G. Hemming, *Earth Planet. Sci. Lett.* **236**, 305 (2005)
34. L. Mydlarz, L. Jones, C. D. Harvell, *Annu. Rev. Ecol. Evol. Syst.* **37**, 251 (2006).
35. R. S. Steneck, in *Proceedings of the Colloquium on Global Aspects of Coral Reefs: Health, Hazards and History*, R. N. Ginsburg, Ed. (Univ. of Miami Press, FL, 1994).
36. R. W. Grigg *et al., Coral Reefs* **21**, 73 (2002).
37. N. Knowlton, *Am. Zool.* **32**, 674 (1992).
38. R. Rowan, N. Knowlton, A. Baker, J. Jara, *Nature* **388**, 265 (1997).
39. M. Stat, D. Carter, O. Hoegh-Guldberg, *Plant Ecol. Evol. Syst.* **8**, 23 (2006).
40. D. L. Bryant, D. L. Burke, J. McManus, M. Spalding, *Reefs at Risk: A Map-Based Indicator of Threats to the World's Coral Reefs* (World Resources Institute, Washington, DC, 1998).
41. H. Hoegh-Guldberg, O. Hoegh-Guldberg, *Biological, Economic and Social Impacts of Climate Change on the Great Barrier Reef* (World Wildlife Fund, Sydney, 2004).
42. M. J. Caley *et al*., *Annu. Rev. Ecol. Syst.* **27**, 477 (1996).
43. UNEP, "Marine and coastal ecosystems and human well-being: A synthesis report based on the findings of the Millennium Ecosystem Assessment" (United Nations Environmental Programme, 2006).
44. UNEP-WCMC, "In the front line: Shoreline protection and other ecosystem services from mangroves and coral reefs (United Nations Environmental Programme–World Conservation Monitoring Centre, Cambridge, UK, 2006).
45. C. Sheppard, D. J. Dixon, M. Gourlay, A. Sheppard, R. Payet, *Estuar. Coast. Shelf Sci.* **64**, 223 (2005).
46. H. J. S. Fernando, J. L. McCulley, *Eos* **86**, 301 (2005).
47. E. H. Williams Jr., P. J. Bartels, L. Bunkley-Williams, *Glob. Change Biol.* **5**, 839 (1999).
48. P. J. Webster, G. J. Holland, J. A. Curry, H.-R. Chang, *Science* **309**, 1844 (2005)
49. J. L. Sadd, *Bull. Mar. Sci.* **35**, 221 (1984).
50. P. J. Edmunds, R. C. Carpenter, *Proc. Natl. Acad. Sci. U.S.A.* **98**, 5067 (2001).
51. P. J. Mumby, *Ecol. Appl.* **16**, 747 (2006).
52. P. J. Mumby *et al*., *Science* **311**, 98 (2006).
53. J. E. Hansen, *Environ. Res. Lett.* **2**, 024002 (2007).
54. E. Lewis, D. W. R. Wallace, Program Developed for CO_2 System Calculations. ORNL/CDIAC-105 (Carbon Dioxide Information Analysis Center, Oak Ridge National Laboratory, U.S. Department of Energy, Oak Ridge, TN, 1998).

55. This project was supported by the Global Environment Facility, the World Bank, and the University of Queensland through the Coral Reef Targeted Research Program (www.gefcoral.org). We also thank J. Dixon, S. Dove, and D. W. Gledhill for discussions concerning this manuscript, N. Cenacchi for assistance in rendering Fig. 4, and L. Cao for helping with the analysis and preparation of Fig. 3. The manuscript contents are solely the opinions of the authors and do not constitute a statement of policy, decision, or position on behalf of NOAA or the U.S. Government. This paper is dedicated to the memory of Kim Mitchell, who saw the value of and worked hard for the future of the world's natural ecosystems.

Supporting Online Material

www.sciencemag.org/cgi/content/full/318/5857/1737/DC1
SOM Text
Table S1
References

10.1126/science.1152509

Carnivorous Fungi from Cretaceous Amber

Alexander R. Schmidt,[1]* Heinrich Dörfelt,[2] Vincent Perrichot[1]

Carnivorous or predatory fungi have developed distinctive trapping devices such as adhesive hyphae, knobs, and networks or constricting and nonconstricting rings that enable them to exploit nematodes, other small animals, and protozoans as their main nutrition source (*1*–*3*).

Here, we report fossil evidence of carnivorous fungi that have hyphal rings as trapping devices preserved together with their prey, small nematodes, in circa (ca.)-100-million-year-old amber. A later fossil carnivorous fungus is known from Oligocene-Miocene Mexican amber (*4*), but its trapping devices are not clearly identifiable.

Our fossil specimens originate from the highly fossiliferous amber deposit of Archingeay/Les-Nouillers in southwestern France, which is Late Albian in age (*5*, *6*). The specimens are deposited in the Museum of Natural History in Paris (accession numbers MNHN AR-C115.5a, ARC115.13, ARC115.20, and ARC115.22a).

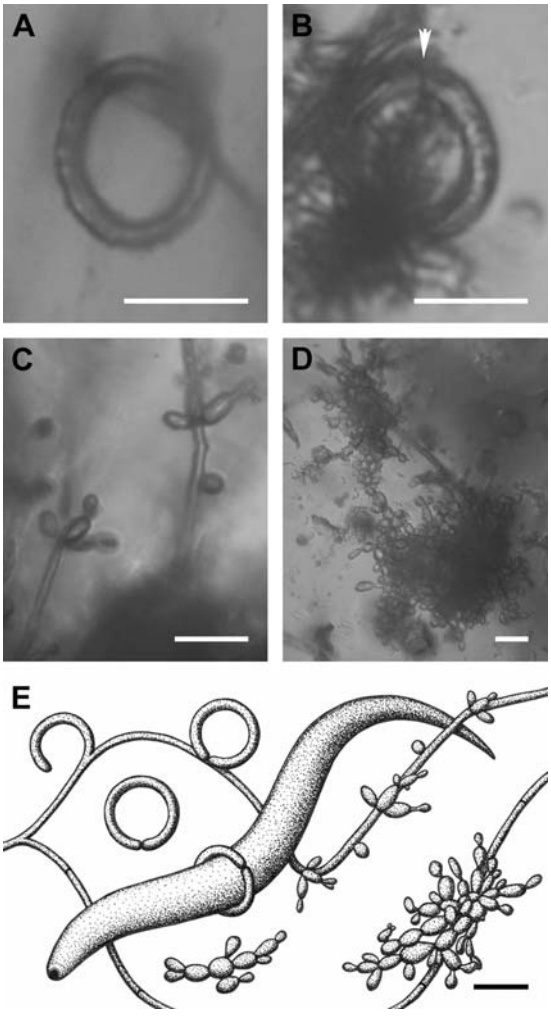

Fig. 1. Dimorphic carnivorous fungus from Cretaceous amber. Scale bars represent 10 μm. (**A**) Trapping ring (MNHN ARC115.13). (**B**) Trapping ring with attached detritus. The arrowhead indicates the only septum (MNHN ARC115.22a). (**C**) Formation of blastospores at a hypha (MNHN ARC115.20). (**D**) Formation of yeast colonies at a hypha (MNHN ARC115.20). (**E**) Reconstructed life cycle with ring formation, fully developed ring at the supporting hypha, disassociated ring, trapped nematode, formation of blastospores, and yeast colonies.

The mycelium consists of irregularly septated branched hyphae, which are 1.5 to 2 μm in diameter. The rings originate from ca.-2-μm-thick lateral branches of the hyphae, forming a loop. In contrast to modern trapping rings consisting of three cells, the rings, which are seen in three specimens of the fungus, are unicellular, forming just a single septum at the junction. Fully developed rings (inner diameter of 8 to 10 μm and outer diameter of 11 to 15 μm) probably detached easily from the supporting hypha and are found disassociated from the mycelium (Fig. 1, A, B, and E). Adhered particles (Fig. 1B and fig. S1A), which are numerous in some samples, indicate that the rings produced a sticky secretion, improving the efficiency of trapping, as known from modern carnivorous fungi trapping with adhesive networks or knobs. Once trapped, the nematodes were probably penetrated and digested by infestation hyphae.

In addition to rings, the fossil fungus also developed blastospores. They are ellipsoid to oviform, are 2 to 4 μm by 1 to 3 μm in size, and bud laterally in whorled position at the hyphae (Fig. 1, C and E). Secondary spores are seen budding primarily apically from the blastospores and form nearly acropetal chains. These cells established yeast colonies (Fig. 1, D and E, and fig. S1B).

Several small nematodes of ca. 100 μm in length are located close to a trapping ring (fig. S1, C and D). Because their maximum diameter falls within the width range of the rings, these animals can be identified as potential prey of the fungus. As a saprotrophic organism and consumer, the fossil fungus was a part of a highly diverse and complex soil biocenosis of an ancient coastal amber forest (*6*). Budding cells of yeast stages are ecologically important in liquid media and are reduced during the course of adaptation to terrestrial habitats. Aquatic representatives of modern carnivorous fungi are considered secondarily aquatic and belong to the same groups as terrestrial soil fungi (*7*). In contrast, the dimorphism exhibited by these fossils may represent an early transitional stage from wet to drier limnetic-terrestrial habitats.

These fossils show that by the Early Cretaceous soil fungi had already developed complex trapping devices to catch motile organisms. As in modern ecosystems, carnivorous fungi formed an ecological group of specialized consumers of small metazoans and protozoans. Today this ecological niche is occupied by more than 200 species of the Zygomycetes and imperfect stages of the Ascomycetes and the Basidiomycetes (*3*). On the basis of the mode of ring formation and the dimorphic mode of life, the fossils cannot be assigned to any recent carnivorous fungus, providing evidence that different groups occupied this ecological niche in the age of dinosaurs and that trapping devices were developed independently multiple times in the course of Earth history. The occurrence of carnivorous fungi in the Mesozoic is an example of complex interactions in early soil ecosystems and suggests that carnivory in fungi may be of ancient origin.

References and Notes

1. G. L. Barron, *The Nematode-Destroying Fungi* (Guelph, Ontario, 1977).
2. D. Ahren, A. Tunlid, *J. Nematol.* **35**, 194 (2003).
3. Y. Yang, E. Yang, Z. An, X. Liu, *Proc. Natl. Acad. Sci. U.S.A.* **104**, 8379 (2007).
4. H.-B. Jansson, G. O. Poinar Jr., *Trans. Br. Mycol. Soc.* **87**, 471 (1986).
5. V. Perrichot, D. Néraudeau, A. Nel, G. De Ploëg, *Afr. Invertebr.* **48**, 213 (2007).
6. Materials and methods are available on *Science* Online.
7. Y. Hao, M. Mo, H. Su, K. Zhang, *Aquat. Microb. Ecol.* **40**, 175 (2005).
8. We thank K. Schmidt and L. Tsuji for discussion and V. Girard, S. Jancke, D. Néraudeau, and S. Struwe for advice. This work was supported by the German Research Foundation and by the Alexander von Humboldt Foundation. This study is a contribution to the project AMBRACE (BLAN07-1-184190) of the French Agence Nationale de la Recherche.

Supporting Online Material

www.sciencemag.org/cgi/content/full/318/5857/1743/DC1
Materials and Methods
Fig. S1
References

30 August 2007; accepted 7 November 2007
10.1126/science.1149947

[1]Museum für Naturkunde der Humboldt-Universität zu Berlin, Invalidenstrasse 43, 10115 Berlin, Germany. [2]Martin-Luther-Universität Halle, Institut für Geobotanik und Botanischer Garten, Neuwerk 21, 06108 Halle/Saale, Germany.

*To whom correspondence should be addressed. E-mail: alexander.schmidt@museum.hu-berlin.de

The Structure of a Human p110α/p85α Complex Elucidates the Effects of Oncogenic PI3Kα Mutations

Chuan-Hsiang Huang,[1,3] Diana Mandelker,[2] Oleg Schmidt-Kittler,[2] Yardena Samuels,[2*] Victor E. Velculescu,[2] Kenneth W. Kinzler,[2] Bert Vogelstein,[2†] Sandra B. Gabelli,[1†] L. Mario Amzel[1†]

PIK3CA, one of the two most frequently mutated oncogenes in human tumors, codes for p110α, the catalytic subunit of a phosphatidylinositol 3-kinase, isoform α (PI3Kα, p110α/p85). Here, we report a 3.0 angstrom resolution structure of a complex between p110α and a polypeptide containing the p110α-binding domains of p85α, a protein required for its enzymatic activity. The structure shows that many of the mutations occur at residues lying at the interfaces between p110α and p85α or between the kinase domain of p110α and other domains within the catalytic subunit. Disruptions of these interactions are likely to affect the regulation of kinase activity by p85 or the catalytic activity of the enzyme, respectively. In addition to providing new insights about the structure of PI3Kα, these results suggest specific mechanisms for the effect of oncogenic mutations in p110α and p85α.

Phosphatidylinositol 3-kinases (PI3Ks) are lipid kinases that phosphorylate phosphatidylinositol 4,5-bisphosphate [PI(4,5)P_2 or PIP_2] at the 3-position of the inositol ring, and thus generate phosphatidylinositol 3,4,5-trisphosphate (PIP_3), which, in turn, initiates a vast array of signaling events. PI3Ks are heterodimers, composed of catalytic and regulatory subunits, that are activated by growth factor–receptor tyrosine kinases (*1*, *2*). PIP_3 levels are tightly regulated by the action of phosphatases, such as the phosphatase and tensin homolog (PTEN) (*3*). PIP_3 produced by PI3Ks acts as a docking site for pleckstrin homology (PH)–containing proteins, such as the Akt serine-threonine kinases (*4*). Once at the membrane, Akt's are activated by phosphorylation at two sites and, in turn, phosphorylate numerous protein targets (*5*–*17*). The biological consequences of Akt activation are broad and include regulation of cell proliferation, survival, and motility (*2*, *18*–*20*).

The PI3K pathway was first linked to cancer when Vogt and colleagues reported that the avian sarcoma virus 16 genome encodes an oncogene that is derived from a cellular PI3K gene (*21*). The finding that PTEN is inactivated by mutations in various tumors solidified the relevance of this pathway to human cancer (*22*–*24*). Other genetic alterations in pathway members have been identified, including occasional mutations in the regulatory subunit p85 of PI3K (*25*–*32*). Particularly exciting was the more recent discovery that *PIK3CA*, the gene encoding the catalytic subunit of PI3Kα, was somatically mutated in a significant fraction of diverse tumor types (*33*–*41*). Most of the reported mutations in *PIK3CA* cluster in conserved regions within the region coding for the helical and kinase domains of p110 α (*33*). As these mutations constitutively activate its kinase activity (*42*–*48*), the enzyme appears to be an ideal target for drug development. Indeed, several low-molecular-weight compounds that inhibit p110α activity have been described (*49*). Most of these compounds, however, are not specific and inhibit other PI3Ks, as well as other kinases. Progress in this area of drug development would be facilitated by knowledge of the structure of the p110α/p85α complex.

The p110α subunit of PI3Kα has five domains: an N-terminal domain called ABD (adaptor-binding domain) that binds to p85α, a Ras-binding domain (RBD), a domain called C2 that has been proposed to bind to cellular membranes, a helical domain of unknown function, and a kinase catalytic domain (Fig. 1A) (*1*, *2*, *18*, *19*). In its basal state, the p110α subunit is bound to and inhibited by the regulatory subunit p85α or p85α-related proteins. The p85α polypeptide also has five known domains including two SH2 domains (the N-terminal nSH2 and C-terminal cSH2) separated by an inter-SH2 (iSH2) domain that binds to the catalytic subunit. When appropriate

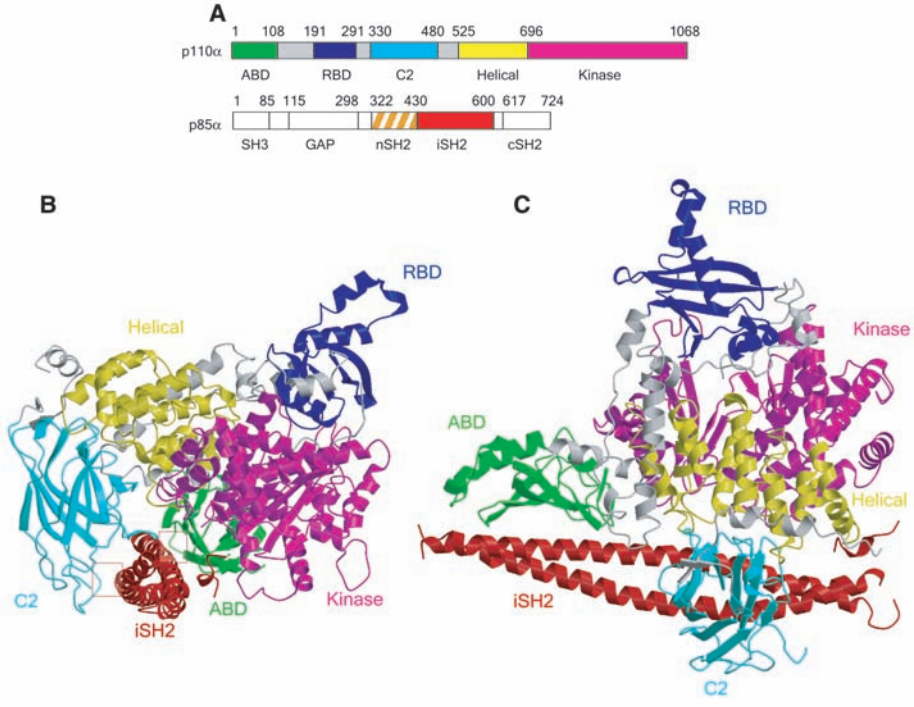

Fig. 1. Overview of the p110α/niSH2 heterodimer. (**A**) Scheme of the domain organization. The same color coding is used throughout this article unless specified. Gray regions are linkers between domains. The nSH2 domain of p85α, denoted by the region with orange stripes, was not traced in the final model but its location in the complex was determined as described in the text. (**B**) Ribbon diagram of the p110α/niSH2 heterodimer. The iSH2 ABD and iSH2 C2 contacts are boxed. (**C**) Ribbon diagram of the p110α/niSH2 heterodimer, alternate view.

[1]Department of Biophysics and Biophysical Chemistry, Johns Hopkins University School of Medicine, Baltimore, MD 21205, USA. [2]Ludwig Center for Cancer Genetics and Therapeutics, and Howard Hughes Medical Institute at the Johns Hopkins Kimmel Cancer Center, Baltimore, MD 21231, USA. [3]Graduate Program in Immunology, Johns Hopkins University School of Medicine, Baltimore, MD 21205, USA.

*Present address: National Human Genome Research Institute, National Institutes of Health, Bethesda, MD 20892, USA.

†To whom correspondence should be addressed. E-mail: mamzel@jhmi.edu (L.M.A.); gabelli@jhmi.edu (S.B.G.); vogelbe@jhmi.edu (B.V.)

cellular stimuli are present, the nSH2 and cSH2 domains bind phosphorylated tyrosines in activated receptors and adapter proteins, and this phosphotyrosine binding activates the p110α catalytic subunit without releasing p85α from p110α.

Although the structures of pig and human p110γ are known (*50*–*52*), the sequence identity between p110α and p110γ is only 35%. In addition, unlike p110α, p110γ does not require binding to a regulatory subunit for its catalytic activity, and the reported structures of p110γ do not include the ABD domain. The crystal structure of a complex between the N-terminal ABD domain of p110α (residues 1 to 108) and the human p85α (iSH2) domain (residues 431 to 600) was recently determined (*53*). The structure of the isolated nSH2 domain has been previously reported (*54*). In the current study, we crystallized and determined the structure of a complex between the full-length human p110α catalytic subunit and the domains of the p85α regulatory subunit critical for its binding and activation.

Results and Discussion. In a baculovirus production system, we found that human p110α was produced at easily detectable levels only when coexpressed with the regulatory p85α protein. However, coexpression of p110α with full-length p85α led to protein aggregation. We tested different truncated versions of p85α, all containing the iSH2 region, and found that residues 322 to 600 (termed niSH2) produced the highest protein yield. The complex was enzymatically active, with a Michaelis constant K_M of 11 μM for adenosine triphosphate (ATP) and of 58 μM for L-α-phosphatidylinositol. It contained all five p110α domains (ABD, residues 1 to 108; RBD, residues 190 to 291; C2, residues, 330 to 480; helical, residues 525 to 696; and kinase, residues 697 to 1068), as well as the nSH2 (residues 322 to 430) and iSH2 (residues 431 to 600) domains of p85α (Fig. 1A). The structure of the p110α/niSH2 heterodimer was determined with data to 3.05 Å resolution and refined to an R_{work}/R_{free} of 26.3/32.3 (Table 1).

Table 1. Data collection and refinement statistics.

Measure	Value
Data collection	
X-ray source	BNL-X29(λ = 1.0809 Å)
Space group	$P2_12_12_1$
Cell dimensions *a*, *b*, *c* (Å)	115.1, 117.1, 151.6
Resolution (Å)	3.05
Measured reflections	270,209
R_{sym}	7.2 (43.3)
$\langle I / \sigma I \rangle$	9.4 (2.1)
Completeness (%)	98.7 (88.2)
Redundancy	7.1 (5.3)
Refinement	
Resolution (Å)	46.4–3.05
No. reflections (work/test set)	36,888/2000
R_{work}/R_{free}	26.3/32.3
No. residues	1133
No. atoms of protein	9365
Average *B*-factor Å^2	85.7
RMSD	
Bond lengths (Å)	0.01
Bond angles (°)	1.5

Highest-resolution shell is shown in parentheses. $R_{sym} = \sum_{hkl} | I(hkl) - \langle I(hkl) \rangle | / \sum_{hkl} I(hkl)$, where $\langle I(hkl) \rangle$ is the mean of the symmetry-equivalent reflections of $I(hkl)$.

Description of the structure. The p110α/niSH2 heterodimer has an overall triangular shape with the long coiled-coil of iSH2 forming the base (Fig. 1C). ABD, which is located near one end of the complex, contacts the iSH2 coiled-coil from the top, burying 2237 Å^2 of surface area, while the C2 domain interacts with the iSH2 from the side and buries an additional 1233 Å^2 (total buried surface area 3470 Å^2) (Fig. 1B). The helical and kinase domains form the bulk of the center of the complex but are not in direct contact with iSH2. The RBD sits at the top corner, farthest away from the iSH2. Adventitiously, the N-terminal portion of the His-tag (residues –27 to –15; complete tag: residues –1 to –28) in the p110α construct, which was not removed before crystallization, is locked in a polar pocket between the RBD and the kinase domains of a neighboring molecule, which may contribute to the stability of the crystals.

ABD and RBD are both small globular domains of about 100 residues in length with an α/β-sandwich topology. A long linker (residues 109 to 189) containing four helices connects these two domains. ABD displays a complex set of interactions with helix α1K of the kinase domain and helix α1L, which is part of the linker between ABD and RBD. The previously reported crystal structure of the ABD domain of p110α in complex with the iSH2 of p85 did not reveal how ABD interacts with the rest of p110α (*53*). Nevertheless, the contacts between the isolated ABD and iSH2 domains, as well as their relative orientations, are in agreement with those we found in the complex between the intact p110α and niSH2.

The C2 domain is a β sandwich of two four-stranded antiparallel sheets. The linker between RBD and C2 is a long coil (residues 292 to 329) with a short helix near its N terminus. Part of this linker (residues 307 to 324), as well as the linker between the C2 and the helical domains (residues 506 to 527), were not traced because their density was not well defined. The C2 domain is the least conserved among the four common domains of class I PI3Ks, with only 27% sequence identity between p110α and p110γ. Although the characteristic eight-stranded antiparallel β-sandwich topology is preserved, there are significant differences between the intervening loops of p110α and p110γ. In particular, the loop connecting β5C2 and β6C2 in p110α (CBR3, residues 406 to 424) is about 10 residues shorter than the corresponding loop in p110γ. As in the C2 domain of p110γ, CBR3 of p110α contains basic residues Lys^{410}, Arg^{412}, Lys^{413}, and Lys^{416}, which appear to be involved in the interaction with the lipid membrane. The reduced length of CBR3 in p110α might be a consequence of the spatial constraint imposed by the interaction between C2 and iSH2.

One unexpected feature of the C2 domain in the p110α/niSH2 crystal structure is its interaction with the iSH2 of p85. It had been suggested that the iSH2 coiled-coil sits in a groove between the C2 and kinase domains (*53*), but the exact position of iSH2 in the complex was not known. In the structure presented here, Asp^{560} and Asn^{564} of iSH2 are within hydrogen-bonding distance (2.8 and 3.0 Å) of Asn^{345} of C2 (Fig 2C). This interaction, not identified in previous studies, forms an important additional contact between iSH2 and p110α.

The helical domain folds as an all α-helical structure. It was proposed to be the core of the molecule to which all other domains attach (*52*). In the p110α/niSH2 structure, however, the main role of the helical domain within the p110α subunit is to bridge the C2 and kinase domains, the only two domains with which it is in direct contact.

The kinase domain harbors the catalytic site of the enzyme. It is a two-lobed structure formed by two α/β subdomains separated by a cleft, an architecture typical of protein and lipid kinases. In p110α, the smaller N-terminal domain comprises residues 697 to 851 and the larger C-terminal domain residues 852 to 1068. On the basis of the structures of other protein kinases, the activation and catalytic loops of p110α were assigned to residues 933 to 957 and 912 to 920, respectively (fig. S1). Residues 941 to 950 of the activation loop, as well as residues beyond 1050, were disordered and were not traced. The structure of this domain is highly conserved among class I PI3Ks, particularly for residues around the substrate-binding pocket situated between the N- and C-terminal lobes of the kinase domain. Alignment of the kinase domains of p110α and p110γ shows a root mean square deviation (RMSD) of 1.8 Å between 288 out of 337 aligned Cα atoms. Analysis of this alignment shows that the major deviation occurs at helix α12K (residues 1032 to 1048) with an RMSD of 3.2Å. Alignment of the kinase domain without helix α12K shows a deviation of 1.6 Å. As discussed below, helix αK12 contains two cancer-related mutations and is close to the activation loop, as well as the nSH2 domain of p85α. This suggests that p85α regulates p110α activity through a helix αK12–mediated conformational change of the activation loop.

To identify the ATP-binding site in p110α, crystals were soaked in ATP-containing mother liquor solutions. Diffraction data, however, did not show density for the nucleotide. Analysis of the crystal structure provides an explanation: The ATP-binding site of p110α participates in a crystal contact and is occupied by a loop (residues 226 to 239) from the RBD domain of a neighboring molecule (fig. S2). The architecture of the portions of p110α that are present in the structure of the human p110γ are similar, despite the low

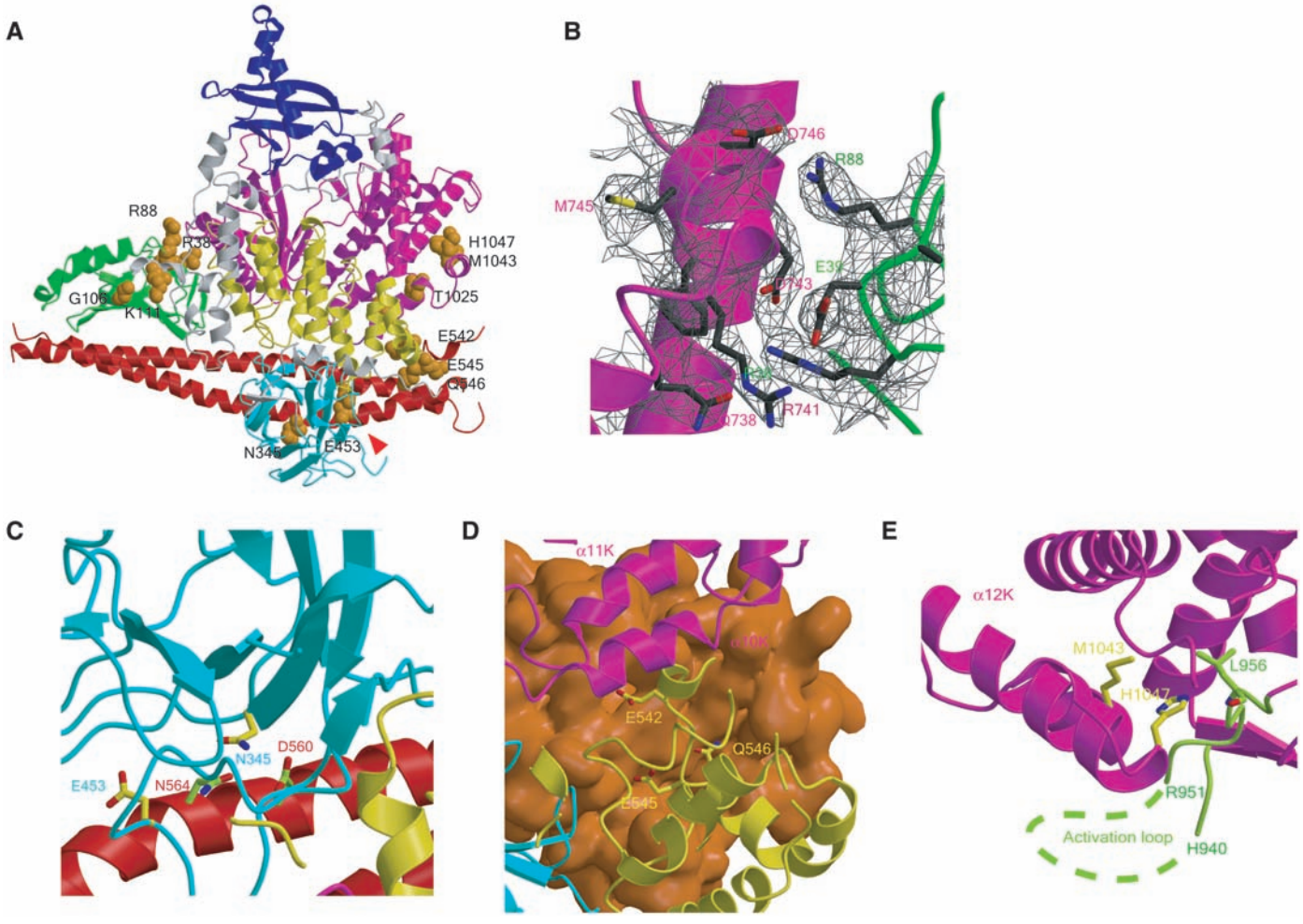

Fig. 2. Mutations in PIK3CA identified in human cancers. (**A**) Distribution of representative mutations within p110α. Residues mutated in cancers are shown as CPK models. The start of the cancer-associated truncation (residue 571 of p85) is shown by the red arrowhead. (**B**) Electron density map of Arg^{38} and Arg^{88} cancer mutations shown at the interface between the ABD and the kinase domains. (**C**) Close-up view of the interface of the C2 domain of p110 with iSH2 of p85. The stick representation of the Asn^{345} mutation of C2 and the residues within iSH2 (Asp^{560} and Asn^{564}) with which it may interact are shown. (**D**) Mutations in the helical domain (Glu^{542}, Glu^{545}, and Gln^{546}), located at the interface with nSH2 (orange surface). (**E**) Mutations of the kinase domain (Met^{1043} and His^{1047}), located near the C-terminal end of the activation loop, are shown in light green. The part of the activation loop between residues 941 and 950 could not be traced (see text).

sequence identity between the two proteins (fig. S1 and fig. S3) (*52*).

Cancer-specific mutations. Cancer-associated mutations have been identified in the ABD, C2, helical, and kinase domains of p110α (*33*). The distribution of representative mutations within the p110α structure is shown in Fig. 2A. Several of these mutations have been shown to result in enhanced enzymatic activity in vitro and in vivo (*33*, *42*, *43*). Mutations located in different domains were thought to act through unrelated mechanisms but this hypothesis was difficult to prove in the absence of structural information. The structure presented here sheds light on the mechanisms through which these mutations may affect kinase activity.

The ABD domain mutations (in which, for example, cysteine, histidine, and glutamine replace arginine at residue 38 and 88) $Arg^{38}Cys$, $Arg^{38}His$, and $Arg^{88}Gln$ were initially thought to disrupt the interaction between ABD and iSH2, but were later found not to be located at the interface in a crystal structure of ABD in complex with iSH2 (*53*). The effect of these mutations, however, was not evident from the structure of ABD-iSH2 heterodimer. The structure of the p110α/niSH2 reveals that both Arg^{38} and Arg^{88} are located at a contact between the ABD and the kinase domains, within hydrogen-bonding distance (<3.2 Å) of Gln^{738}, Asp^{743}, and Asp^{746} of the N-terminal lobe of the kinase domain (Fig. 2B). Mutations of Arg^{38} and Arg^{88} are likely to disrupt these interactions, resulting in a conformational change of the kinase domain that alters enzymatic activity.

Mutations in the C2 domain were thought to change the affinity of p110α for the lipid membrane (*47*). In the structure reported here, Asn^{345}, mutated to Lys in some cancers, is within hydrogen-bonding distance (2.8 Å and 3.0 Å) of Asn^{564} and Asp^{560} of iSH2 (Fig. 2C). This suggests that an Asn^{345} mutation may disrupt the interaction of the C2 domain with iSH2. This would presumably alter the regulatory effect of p85 on p110α, rather than disrupt the interaction of p110α with the lipid membrane. It is intriguing that another mutation identified in cancer, $Glu^{453}Gln$, is also located at the interface between C2 and iSH2. The density for its side chain, however, is not defined well enough in the structure to identify a direct interaction.

The helical domain contains two residues, Glu^{542} and Glu^{545}, that are frequently mutated in cancers ("hot spots"). In the majority of cases, these two residues are mutated to Lys, causing a charge reversal. Glu^{542} and Glu^{545}, as well as the less frequently mutated Gln^{546}, are located on an exposed region of the helical domain (Fig. 2A). Biochemical studies suggested that these residues interact with Lys^{379} and Arg^{340} of the p85 nSH2 domain and that this interaction inhibited the activity of the catalytic subunit (*53*, *55*). Although nSH2 was included in our p110α/niSH2 protein

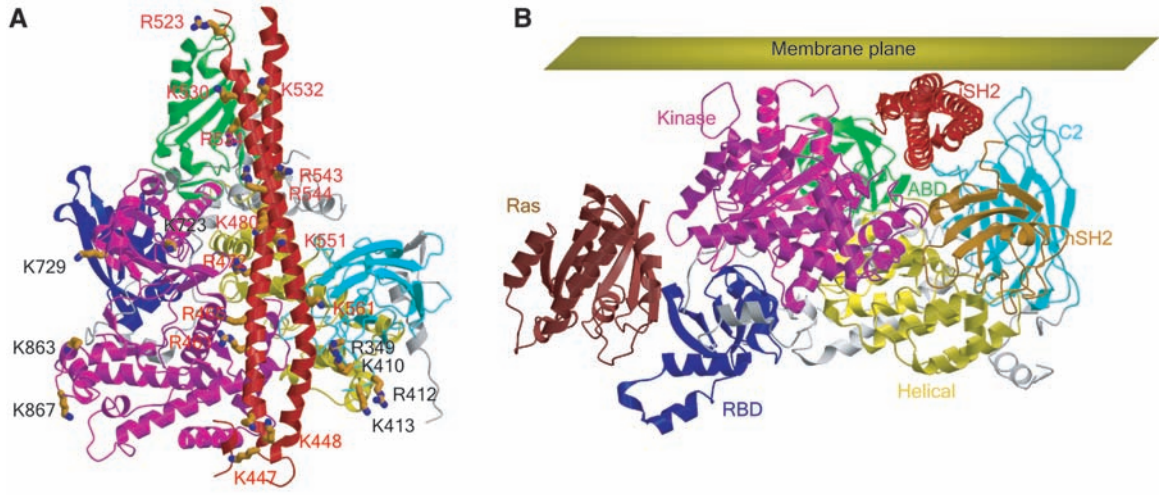

Fig. 3. Model of membrane interaction. (**A**) Positively charged residues on the surface of iSH2 domain of p85α (red) and loops of the C2 and kinase domains of p110α (black) are proposed to contact the negatively charged phospholipid bilayer. (**B**) Model of p110α/niSH2 bound to Ras and its proposed orientation with respect to the lipid membrane.

complex, it was not highly ordered in the crystal. A model of the complete p110α/niSH2 complex was therefore created by placing the previously determined structure of the nSH2 domain of human p85α (*54*) into the weak density of the final $2F_{obs} - F_{calc}$ map of p110α/niSH2, while taking into account the interactions identified biochemically (*53*). In this model, nSH2 is placed close to the interface between the kinase and the helical domain and interacts with both domains. This model is fully consistent with the biochemical experiments of Miled *et al.* (*53*) demonstrating that mutations at residues 542, 545, and 546 abrogate the inhibitory effect of nSH2 (Fig. 2D). Two ways in which the effects of these mutations are communicated to the complex can be identified: Mutations may modify the orientation of nSH2 with respect to the helical and the kinase domains, and by changing the interaction of the helical domain with nSH2, the mutations may alter the relative positions of helices α11K and α12K.

His^{1047} in the kinase domain is another hot spot for somatic mutations in cancer. It is interesting that His^{1047} is mutated to Arg in the majority of cases, yet arginine is normally present at the homologous position in human p110γ (fig. S1). In the structure of the p110α/p85 complex, His^{1047} is located within helix α12K of the C-terminal lobe of the kinase domain and is close to the C-terminal end of the activation loop, possibly forming a hydrogen bond with the main-chain carbonyl of Leu^{956} within the activation loop (Fig. 2E). Mutations of His^{1047} most likely have a direct effect on the conformation of the activation loop, changing its interaction with phosphatidylinositide substrates. Another less frequently observed mutation, $Met^{1043}Ile$, is located on the same helix, and we hypothesize that it also exerts its effect through changes in the activation loop.

Although alterations of p85α in cancers are much less common than those of p110α, several have been reported. Many of these are truncations or deletions starting at or near residue 571 (*32*, *56*). In particular, a truncation mutant known as p65 (eliminating all amino acids C-terminal to residue 571), leads to constitutively increased PI3Kα activity. It has been proposed that residues 581 to 593 constrain the location of the inhibitory nSH2 domain and that deletion of them removes such orienting constraints (*57*). On the basis of the crystal structure of p110/niSH2, an alternative possibility appears more likely: Truncation at residue 571 might destabilize the iSH2 coiled-coil around residues 560 and 564 that make an important contact with Asn^{345} of the C2 domain. Thus, the effect of this truncation may be equivalent to that of mutation of Asn^{345} of the C2 domain discussed above.

Interaction with the lipid membrane. Upon activation, PI3Ks are recruited to the plasma membrane, where the phosphatidylinositide substrates reside. A model of the interaction between p110γ and the lipid membrane based on the known location of the active site and the co-crystal structure of p110γ with Ras (*50*) has been proposed. In this model, loops from the C2 and kinase domains form the major contact sites with the lipid membrane. When this assumed membrane plane is placed in the p110α/niSH2 structure, the exposed surface of the coiled-coil of iSH2 (residues 447 to 561) forms a long rectangular surface that contacts the putative plane of the membrane. This surface of iSH2, as well as two loops from the kinase domain (residues 723 to 729 and 863 to 867) are rich in basic residues (Lys^{447}, Lys^{448}, Arg^{461}, Arg^{465}, Arg^{472}, Lys^{480}, Lys^{530}, Lys^{532}, Arg^{523}, Arg^{534}, Arg^{543}, Arg^{544}, Lys^{551}, and Lys^{561} of the iSH2 and Lys^{723}, Lys^{729}, Lys^{863}, and Lys^{867} of the kinase domain) and are therefore well-suited for interacting with negatively charged phospholipids (Fig. 3A). The region of iSH2 containing these basic residues thus would appear to be the major determinant of interaction with membranes, in agreement with the observation that iSH2 interacts with phospholipids in vitro (*58*). In contrast, the C2 domain, which had been thought to be the main lipid-interacting domain of p110, is partly blocked from membrane interaction by iSH2, although it remains possible for the basic residues of its CBR loops (e.g. Arg^{349}, Lys^{410}, Arg^{412}, Lys^{413}, Lys^{416}) to reach the membrane. Further studies are required to elucidate the relative importance of iSH2 and C2 in lipid membrane interaction.

Ras activates PI3Ks by binding to the RBD of their catalytic subunit. A model of Ras bound to p110α/niSH2, built by aligning the structure of the Ras-binding domain of p110α with the structure of the p110γ/Ras complex (*50*), shows the position of this activator protein in the complex and its relation to the putative membrane plane (Fig. 3B).

The p110α/niSH2 crystal structure reveals the architecture of the complete catalytic subunit of a class IA PI3K, identifies a contact between the C2 domain of p110α and iSH2 domain of p85, and suggests a role for iSH2 in lipid binding. It also sheds new light on the mechanisms by which PIK3CA oncogenic mutations affect PI3Kα activity. Insights obtained from this structure suggest new targets for the design of isoform- or mutation-specific inhibitors for cancer therapeutics.

References and Notes

1. B. Vanhaesebroeck, M. D. Waterfield, *Exp. Cell Res.* **253**, 239 (1999).
2. L. C. Cantley, *Science* **296**, 1655 (2002).
3. T. Maehama, J. E. Dixon, *Trends Cell Biol.* **9**, 125 (1999).
4. B. Vanhaesebroeck, D. R. Alessi, *Biochem. J.* **346**, 561 (2000).
5. B. T. Nave, M. Ouwens, D. J. Withers, D. R. Alessi, P. R. Shepherd, *Biochem. J.* **344**, 427 (1999).
6. B. D. Manning, A. R. Tee, M. N. Logsdon, J. Blenis, L. C. Cantley, *Mol. Cell* **10**, 151 (2002).
7. S. R. Datta *et al.*, *Cell* **91**, 231 (1997).
8. L. del Peso, M. González-Garcia, C. Page, R. Herrera, G. Nuñez, *Science* **278**, 687 (1997).
9. L. D. Mayo, D. B. Donner, *Proc. Natl. Acad. Sci. U.S.A.* **98**, 11598 (2001).
10. B. P. Zhou *et al.*, *Nat. Cell Biol.* **3**, 973 (2001).
11. M. A. Lawlor, P. Rotwein, *Mol. Cell. Biol.* **20**, 8983 (2000).
12. L. Rossig *et al.*, *Mol. Cell. Biol.* **21**, 5644 (2001).
13. M. H. Cardone *et al.*, *Science* **282**, 1318 (1998).
14. J. A. Romashkova, S. S. Makarov, *Nature* **401**, 86 (1999).
15. A. Brunet *et al.*, *Cell* **96**, 857 (1999).

16. S. Guo *et al.*, *J. Biol. Chem.* **274**, 17184 (1999).
17. G. Rena, S. Guo, S. C. Cichy, T. G. Unterman, P. Cohen, *J. Biol. Chem.* **274**, 17179 (1999).
18. I. Vivanco, C. L. Sawyers, *Nat. Rev. Cancer* **2**, 489 (2002).
19. R. Katso *et al.*, *Annu. Rev. Cell Dev. Biol.* **17**, 615 (2001).
20. A. G. Bader, S. Kang, L. Zhao, P. K. Vogt, *Nat. Rev. Cancer* **5**, 921 (2005).
21. H. W. Chang *et al.*, *Science* **276**, 1848 (1997).
22. J. Li *et al.*, *Science* **275**, 1943 (1997).
23. P. A. Steck *et al.*, *Nat. Genet.* **15**, 356 (1997).
24. I. Sansal, W. R. Sellers, *J. Clin. Oncol.* **22**, 2954 (2004).
25. S. P. Staal, *Proc. Natl. Acad. Sci. U.S.A.* **84**, 5034 (1987).
26. A. Bellacosa *et al.*, *Int. J. Cancer* **64**, 280 (1995).
27. J. Q. Cheng *et al.*, *Proc. Natl. Acad. Sci. U.S.A.* **89**, 9267 (1992).
28. J. Q. Cheng *et al.*, *Proc. Natl. Acad. Sci. U.S.A.* **93**, 3636 (1996).
29. L. Shayesteh *et al.*, *Nat. Genet.* **21**, 99 (1999).
30. B. Actor *et al.*, *Genes Chromosomes Cancer* **34**, 416 (2002).
31. C. B. Knobbe, G. Reifenberger, *Brain Pathol.* **13**, 507 (2003).
32. A. J. Philp *et al.*, *Cancer Res.* **61**, 7426 (2001).
33. Y. Samuels *et al.*, *Science* **304**, 554 (2004).
34. D. K. Broderick *et al.*, *Cancer Res.* **64**, 5048 (2004).
35. K. E. Bachman *et al.*, *Cancer Biol. Ther.* **3**, 772 (2004).
36. J. W. Lee *et al.*, *Oncogene* **24**, 1477 (2005).
37. I. G. Campbell *et al.*, *Cancer Res.* **64**, 7678 (2004).
38. D. A. Levine *et al.*, *Clin. Cancer Res.* **11**, 2875 (2005).
39. L. H. Saal *et al.*, *Cancer Res.* **65**, 2554 (2005).
40. Y. Wang, A. Helland, R. Holm, G. B. Kristensen, A. L. Borresen-Dale, *Hum. Mutat.* **25**, 322 (2005).
41. P. K. Vogt, S. Kang, M. A. Elsliger, M. Gymnopoulos, *Trends Biochem. Sci.* **32**, 342 (2007).
42. S. Kang, A. G. Bader, P. K. Vogt, *Proc. Natl. Acad. Sci. U.S.A.* **102**, 802 (2005).
43. T. Ikenoue *et al.*, *Cancer Res.* **65**, 4562 (2005).
44. A. G. Bader, S. Kang, P. K. Vogt, *Proc. Natl. Acad. Sci. U.S.A.* **103**, 1475 (2006).
45. S. J. Isakoff *et al.*, *Cancer Res.* **65**, 10992 (2005).
46. J. J. Zhao *et al.*, *Proc. Natl. Acad. Sci. U.S.A.* **102**, 18443 (2005).
47. M. Gymnopoulos, M. A. Elsliger, P. K. Vogt, *Proc. Natl. Acad. Sci. U.S.A.* **104**, 5569 (2007).
48. Y. Samuels *et al.*, *Cancer Cell* **7**, 561 (2005).
49. Z. A. Knight, K. M. Shokat, *Biochem. Soc. Trans.* **35**, 245 (2007).
50. M. E. Pacold *et al.*, *Cell* **103**, 931 (2000).
51. E. H. Walker *et al.*, *Mol. Cell* **6**, 909 (2000).
52. E. H. Walker, O. Perisic, C. Ried, L. Stephens, R. L. Williams, *Nature* **402**, 313 (1999).
53. N. Miled *et al.*, *Science* **317**, 239 (2007).
54. R. T. Nolte, M. J. Eck, J. Schlessinger, S. E. Shoelson, S. C. Harrison, *Nat. Struct. Biol.* **3**, 364 (1996).
55. J. Yu, C. Wjasow, J. M. Backer, *J. Biol. Chem.* **273**, 30199 (1998).
56. C. Jimenez *et al.*, *EMBO J.* **17**, 743 (1998).
57. S. C. Shekar *et al.*, *J. Biol. Chem.* **280**, 27850 (2005).
58. P. End *et al.*, *J. Biol. Chem.* **268**, 10066 (1993).
59. Support was provided by the Virginia and D. K. Ludwig Fund for Cancer Research. NIH grants CA 43460 to B.V., GM066895 to L.M.A, and GM07309 and GM 07184 to D.M. Brookhaven National Laboratory is gratefully acknowledged for providing Beamlines X29 and X6a of the National Synchrotron Light Source for collection of the diffraction data. We are grateful to Jr-Ming Yang for the identification of the crystallization condition. Coordinates of the p110α/niSH2 have been deposited in the Protein Data Bank (accession number 2RD0, www.rcsb.org).

Supporting Online Material

www.sciencemag.org/cgi/content/full/318/5857/1744/DC1
Materials and Methods
Figs. S1 to S3
References

21 September 2007; accepted 31 October 2007
10.1126/science.1150799

REPORTS

Stored Light in an Optical Fiber via Stimulated Brillouin Scattering

Zhaoming Zhu,[1] Daniel J. Gauthier,[1]* Robert W. Boyd[2]

We describe a method for storing sequences of optical data pulses by converting them into long-lived acoustic excitations in an optical fiber through the process of stimulated Brillouin scattering. These stored pulses can be retrieved later, after a time interval limited by the lifetime of the acoustic excitation. In the experiment reported here, smooth 2-nanosecond-long pulses are stored for up to 12 nanoseconds with good readout efficiency: 29% at 4-nanosecond storage time and 2% at 12 nanoseconds. This method thus can potentially store data packets that are many bits long. It can be implemented at any wavelength where the fiber is transparent and can be incorporated into existing telecommunication networks because it operates using only commercially available components at room temperature.

An information network consists of nodes where information is generated, processed, routed, and stored, and of transmission links that interconnect the nodes. One bottleneck in modern optical information networks is the lack of an all-optical memory for which the storage time is continuously adjustable (*1*). Substantial progress has been made in the development of a memory based on spatial-spectral holography (*2*), but this method requires operation at cryogenic temperatures. Another promising approach is so-called stored or stopped light based on electromagnetically induced transparency (EIT), in which information encoded on an optical beam is impressed upon internal degrees of freedom of a dense atomic ensemble (*3*–*7*). Storage times exceeding 1 s have been observed for a 20-μs-long pulse (*8*), suggesting that this method could be useful as a component in long-distance quantum information networks (*9*, *10*). One limitation of both of these storage methods is that their frequency of operation is highly constrained: The frequency of the stored light must match precisely the resonance frequency of the ions or atoms used. These constraints have been cast aside with the prediction (*11*) that a pulse can be stored in a dynamically controlled microring resonator containing many narrow resonances over a broad spectral range, and a single optical pulse was stored for ~100 ps in a proof-of-concept experiment (*12*).

Here, we demonstrate storage of multiple optical pulses by coherently transferring their information content to an acoustic excitation in a room-temperature optical telecommunication fiber through their interaction with an additional optical "write" pulse. After a controllable storage time, the acoustic excitation is converted back to the optical domain by interaction with a "read" pulse. The process is based on stimulated Brillouin scattering (SBS) (*13*, *14*) and works at any wavelength where the fiber is transparent, including the important telecommunication band in the near-infrared spectral region. The SBS process arises from electrostriction, in which a time-varying electric field creates a time-varying change in density of the material system (i.e., an acoustic excitation). The acoustic wave modulates the refractive index of the medium, which induces both amplifying and absorbing resonances in the vicinity of the applied laser frequencies. Our storage scheme relies on the process of anti-Stokes absorption, which occurs efficiently when the carrier frequency (central frequency) of the incident data pulses is higher than the carrier frequency of the applied write pulse by the Brillouin frequency shift Ω_B, which is proportional to the speed of sound in the material and is approximately 9.6 GHz for our fiber at wavelengths near 1.55 μm. The SBS process works for data pulses at any carrier frequency so long as the write- and read-pulse frequencies are lower than the data-pulse frequency by Ω_B; this condition can be achieved easily using standard tunable-laser technology.

Our experiment to demonstrate light storage in an optical fiber is conceptually very simple. Bits of information, represented by pulses of light, pass through the fiber while, simultaneously, a write pulse passes through the fiber in the opposite direction (Fig. 1A). Through the process of SBS, essentially all the data-pulse energy is depleted and a coherent acoustic excitation is left behind in the

[1]Duke University, Department of Physics, Box 90305, Durham, NC 27708, USA. [2]The Institute of Optics, University of Rochester, Rochester, NY 14627, USA.

*To whom correspondence should be addressed. E-mail: gauthier@phy.duke.edu

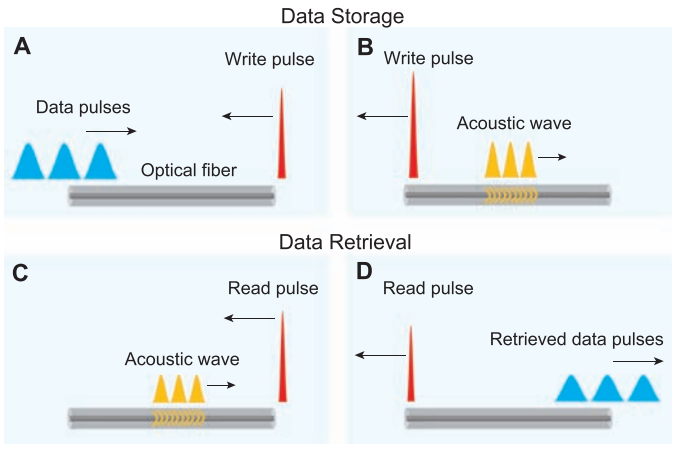

Fig. 1. Storage of data pulses as an acoustic disturbance in an optical fiber and their subsequent retrieval after a controllable time interval. In the storage process, a short, intense write pulse that is detuned to the low-frequency side of the data-pulse frequency by the Brillouin frequency shift causes the data pulses to become depleted (**A**) with the information being stored as an acoustic wave in the medium (**B**). In the retrieval process (**C**), a short, intense read pulse at the same frequency as the write pulse depletes the acoustic wave and converts the data back to the original optical frequency, thereby producing a replica of the incident data pulses (**D**).

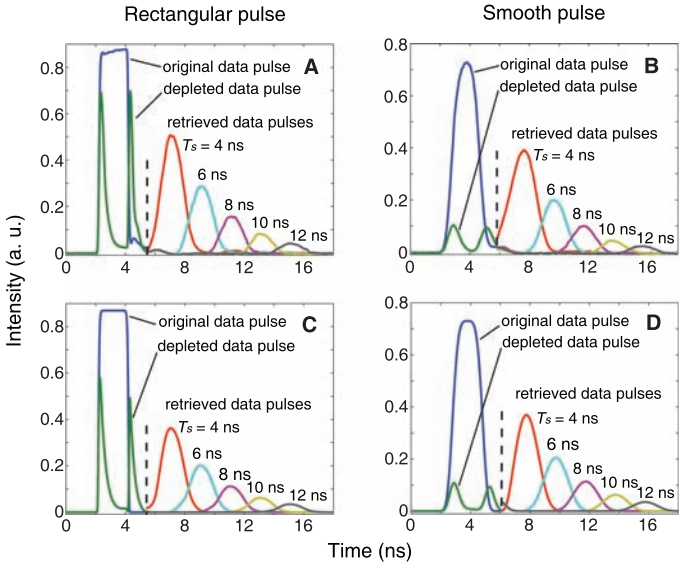

Fig. 2. Observation of stored light. (**A**) shows experimental results for a 2-ns-long rectangular-shaped data pulse, and (**C**) shows the corresponding theoretical simulations. (**B**) shows the case of a 2-ns-long smooth data pulse, with the corresponding simulations shown in (**D**). The retrieved pulses are shown with a multiplication factor of 2 to the right of the dashed vertical line.

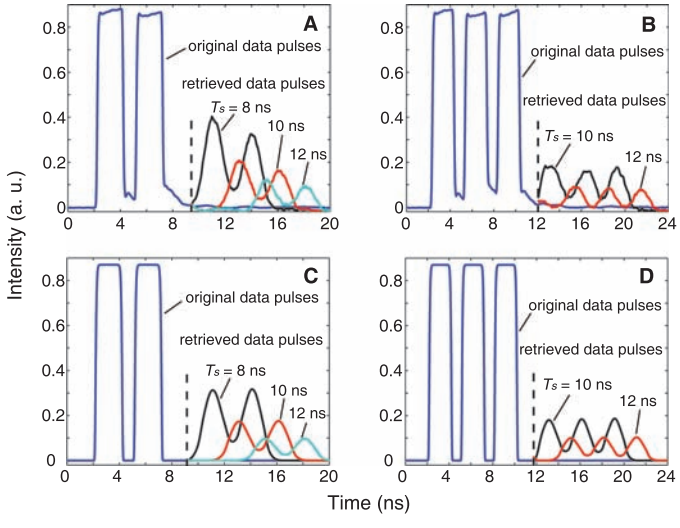

Fig. 3. Storage of pulse sequences. (**A**) shows experimental results for two 2-ns-long data pulses separated by 1 ns, and (**C**) shows the corresponding theoretical simulations. (**B**) shows the case of three 2-ns-long data pulses separated by 1 ns, with the corresponding simulations shown in (**D**). The retrieved pulses are shown with a multiplication factor of 5 to the right of the dashed vertical line. For clarity, the depleted data pulses are not shown.

fiber, which contains the information content of the data pulses (Fig. 1B). Only a small fraction of the data-pulse energy is converted to the acoustic excitation; most of it is transferred to the write pulse. At a later time, a read pulse passes through the fiber in the same direction as the write pulse (Fig. 1C). It depletes the acoustic excitation, and the data pulses are released from the fiber, propagating in the same direction as the original data pulses (Fig. 1D). Energy from the read pulse is transferred to the released data pulses in this process.

Our approach has some relation to previous pulse-storage methods. It can be thought of as a form of real-time holography, and it is related to the process of the stimulated photon echo familiar in magnetic resonance imaging (but operating at much higher efficiency). Also, it has been predicted (*15*, *16*) that light pulses can be stored via Raman backscattering induced in a plasma, although this effect has not been observed experimentally.

As with EIT-based stored-light methods, nearly 100% storage and retrieval efficiency can be obtained in our approach when various conditions are satisfied. In analogy to work with driven two-state systems (such as in nuclear magnetic resonance), we define a pulse area as $\Theta = \sqrt{g_B \upsilon_g n_f \varepsilon_0 c/16\tau_B}\int A_c(t)dt$, where the integration is carried over the duration of the pulse, g_B is the SBS intensity gain coefficient, υ_g is the group velocity of the pulses in the fiber, n_f is the modal refractive index of the fiber, ε_0 is the vacuum permittivity, c is the light speed in vacuum, τ_B is the acoustic lifetime, and A_c is the electric-field envelope of the write or read pulse (*17*). Complete storage of the data waveform is possible when four conditions are met. The first is that $\Theta = \pi/2$ for both the write and read pulses. The second condition is that the write and read pulses must have a duration that is shorter than the shortest-duration data pulse to be stored. Under this condition, the entire spectrum of the data pulses can be faithfully recorded and retrieved. Third, the storage time T_s must be less than the acoustic lifetime τ_B. Last, the spatial extent of the data packet must be less than twice the length of the storage material.

These ideal conditions can be satisfied only approximately in typical experiments, where compromises must be made because of material and equipment limitations. For example, for constant pulse area, the peak power of the write or read pulses scales inversely with the square of the pulse duration. Hence, the shortness of the write and read pulses is limited only by the available pulse power. Also, the readout efficiency decreases rapidly when the storage time exceeds the acoustic lifetime τ_B, which places a bound on the total length of the data packet. For a packet storage time of T_s, the maximum retrieval efficiency is $exp(-T_s/\tau_B)$. The time constant τ_B depends on

material parameters, such as the viscosity, and scales quadratically with the wavelength of the optical pulses. It equals ~3.4 ns for our storage material, so that our current system is most appropriate for high-data-rate communication systems.

We use a short length of commercially available optical fiber and light pulses with a center wavelength around 1.55 μm, which is in the middle of the telecommunication band (*17*). Fig. 2A shows the experimental results for storing and retrieving a single rectangular-shaped 2-ns-long data pulse using identical, 1.5-ns-long write and read pulses with peak powers of ~100 W. To the left of the dashed vertical line, the incident data pulse in the absence and presence of the write and read pulses is shown by the blue and green lines, respectively. The energy storage efficiency of the storage process is very high—equal to ~66%—indicating that we have faithfully encoded the optical pulse information onto the acoustic material excitation.

The data pulses are released from the fiber after a controllable storage time T_s by applying a read pulse, which converts the acoustic material excitation back to the optical domain. The curves to the right of the vertical dashed line are the observed retrieved pulses, where we have scaled them by a factor of 2 for clarity. For T_s = 4 ns, we obtain a readout energy efficiency of 25%, defined as the energy of the released pulse divided by the energy of the incident data pulse. For T_s = 12 ns, the storage time is equal to 6 pulse widths with an efficiency of 1.8%. These observations suggest that this method is useful for a class of high-speed, all-optical information processing applications, such as pulse correlation (*18*). Consistent with the discussion above, we see that the readout efficiency drops with increasing storage time as a result of the decay of the acoustic wave.

The fast rising and falling edges of the data pulse in the time domain contribute to its high-frequency content in the frequency domain. Thus, we hypothesize that the edges are not fully stored because the write-pulse spectrum is not broad enough to fully encompass the data-pulse spectrum; its spectrum is only slightly wider than the data-pulse spectrum. To test this hypothesis, we stored and retrieved a smoothed data pulse, as shown in Fig. 2B. In this case, the energy storage efficiency increases to 86% and the readout efficiencies are improved slightly (~29% for T_s = 4 ns).

To verify the interpretation of our results, we have solved numerically the equations governing the interaction between the optical and acoustic waves in an optical fiber. The simulations (Fig. 2, C and D) are in good agreement with observations (*17*).

Fig. 3, A and B, shows our observations for the storage and retrieval of sequences of two and three data pulses, respectively. For clarity, we show only the input data pulses to the left of the dashed vertical line and to the right we show the retrieved pulses scaled by a factor of 5. The light released from the fiber clearly replicates the input data stream with reasonable fidelity. Again, the numerical simulations (Fig. 3, C and D) are in good agreement with the observations (Fig. 3, A and B).

Our results demonstrate that coherent optical storage can be realized without the use of atomic spin coherence such as that used in EIT-based stored light. Longer storage times may be expected using materials with longer acoustic lifetimes, such as chalcogenide glass fibers (τ_B =12 ns for As_2Se_3 at a wavelength of 1.55 μm) (*19*) or high-pressure gases (τ_B = 80 ns for Xe at 140 atm and a wavelength of 1.55 μm) (*13*). Also, the peak powers of the write and read pulses can be lowered substantially using fibers with a larger SBS gain coefficient (e.g., g_B for As_2Se_3 is 134 times as large as that of silica) (*19*) or smaller core sizes (i.e., smaller mode area). With such improvements, our method should be suitable for use in the buffering of information and for all-optical data processing such as correlation and convolution.

References and Notes

1. R. S. Tucker, P.-C. Ku, C. J. Chang-Hasnain, *J. Lightwave Technol.* **23**, 4046 (2005).
2. H. Lin, T. Wang, T. W. Mossberg, *Opt. Lett.* **20**, 1658 (1995).
3. M. Fleischhauer, S. F. Yelin, M. D. Lukin, *Opt. Comm.* **179**, 395 (2000).
4. C. Liu, Z. Dutton, C. H. Behroozi, L. V. Hau, *Nature* **409**, 490 (2001).
5. D. F. Phillips, A. Fleischhauer, A. Mair, R. L. Walsworth, M. D. Lukin, *Phys. Rev. Lett.* **86**, 783 (2001).
6. A. V. Turukhin *et al*., *Phys. Rev. Lett.* **88**, 023602 (2002).
7. M. D. Lukin, *Rev. Mod. Phys.* **75**, 457 (2003).
8. J. J. Longdell, E. Fraval, M. J. Sellars, N. B. Manson, *Phys. Rev. Lett.* **95**, 063601 (2005).
9. T. Chanelière *et al*., *Nature* **438**, 833 (2005).
10. C. W. Chou *et al*., *Nature* **438**, 828 (2005).
11. M. F. Yanik, W. Suh, Z. Wang, S. Fan, *Phys. Rev. Lett.* **93**, 233903 (2004).
12. Q. Xu, P. Dong, M. Lipson, *Nat. Phys.* **3**, 406 (2007).
13. R. W. Boyd, *Nonlinear Optics, 2nd Ed*. (Academic Press, San Diego, 2003), Ch. 9.
14. G. P. Agrawal, *Nonlinear Fiber Optics, 3rd Ed*. (Academic Press, San Diego, 2001), Ch. 9.
15. I. Y. Dodin, N. J. Fisch, *Phys. Rev. Lett.* **88**, 165001 (2002).
16. I. Y. Dodin, N. J. Fisch, *Opt. Commun.* **214**, 83 (2002).
17. Materials and methods are available as supporting material on *Science* Online.
18. R. Ramaswami, K. N. Sivarajon, *Optical Networks: A Practical Perspective* (Morgan Kaufmann, San Francisco, CA, 2002), Ch. 12.
19. K. F. Abedin, *Opt. Express* **13**, 10266 (2005).

20. We gratefully acknowledge the financial support from the Defense Advanced Research Projects Agency, Defense Sciences Office Slow-Light Program.

Supporting Online Material

www.sciencemag.org/cgi/content/full/318/5857/1748/DC1
Materials and Methods
Figs. S1 and S2
References

10 August 2007; accepted 23 October 2007
10.1126/science.1149066

Mott Transition in VO_2 Revealed by Infrared Spectroscopy and Nano-Imaging

M. M. Qazilbash,[1]* M. Brehm,[2] Byung-Gyu Chae,[3] P.-C. Ho,[1] G. O. Andreev,[1] Bong-Jun Kim,[3] Sun Jin Yun,[3] A. V. Balatsky,[4] M. B. Maple,[1] F. Keilmann,[2] Hyun-Tak Kim,[3] D. N. Basov[1]

Electrons in correlated insulators are prevented from conducting by Coulomb repulsion between them. When an insulator-to-metal transition is induced in a correlated insulator by doping or heating, the resulting conducting state can be radically different from that characterized by free electrons in conventional metals. We report on the electronic properties of a prototypical correlated insulator vanadium dioxide in which the metallic state can be induced by increasing temperature. Scanning near-field infrared microscopy allows us to directly image nanoscale metallic puddles that appear at the onset of the insulator-to-metal transition. In combination with far-field infrared spectroscopy, the data reveal the Mott transition with divergent quasi-particle mass in the metallic puddles. The experimental approach used sets the stage for investigations of charge dynamics on the nanoscale in other inhomogeneous correlated electron systems.

One challenge of contemporary condensed matter physics is the understanding of the emergence of metallic transport in correlated insulators or Mott insulators in which, for example, a temperature change or chemical doping induces anomalous conducting phases (*1*). In such a correlated metal, the mobile charges experience strong competing interactions leading to exotic phases, including the pseudogap state in cuprates and manganites, high-temperature superconductivity, charge stripes in cuprates, and even phase separation in some manganites and cuprates (*1*–*8*). In systems where multiple phases coexist on the nanometer scale, the dynamical properties of these individual electronic phases remain unexplored because methods appropriate to study charge

dynamics (transport, infrared/optical, and many other spectroscopies) lack the required spatial resolution. Scanning near-field infrared microscopy can circumvent this limitation (*9*–*11*). Specifically, we probed coexisting phases in the vicinity of the insulator-to-metal transition in vanadium dioxide (VO_2) at length scales down to 20 nm. This enabled us to identify an electronic characteristic of the Mott transition, namely divergent quasi-particle mass in the metallic puddles, which would otherwise have remained obscured in macroscopic studies that average over the coexisting phases in the insulator-to-metal transition regime.

One particular advantage of VO_2 for the study of electronic correlations is that the transition to the conducting state is initiated by increasing the temperature without the need to modify the stoichiometry. The salient features of the first-order phase transition that occurs at $T_c \approx 340$ K are the orders-of-magnitude increase in conductivity accompanied by a change in the lattice structure (*1*). Compared to the high-temperature rutile metallic (R) phase, the two main features that distinguish the lattice in the low-temperature monoclinic (M1) insulating phase are dimerization (charge-ordering) of the vanadium ions into pairs and the tilting of these pairs with respect to the *c* axis of the rutile metal. The experiments on VO_2 films (*12*, *13*) reported here reveal a strongly correlated conducting state that exists within the insulator-to-metal transition region in the form of nanoscale metallic puddles. Electromagnetic response of these puddles separated by the insulating host displays the signatures of collective effects in the electronic system, including divergent optical effective mass and optical pseudogap. These findings, which were not anticipated by theoretical models, may also help to settle the decades-long debate (*1*, *14*–*20*) on the respective roles played by the lattice and by the electron-electron correlations in the insulator-to-metal transition.

The gross features of the insulator-to-metal transition in VO_2 can be readily identified through the evolution of the far-field optical constants (*13*) obtained with use of spectroscopic ellipsometry and reflectance (Fig. 1). The insulating monoclinic phase ($T \leq 341$ K) displays a sizable energy gap of about 4000 cm^{-1} (≈0.5 eV) in the dissipative part of the optical conductivity, $\sigma_1(\omega)$. The $T \geq 360$ K rutile metallic phase is characterized by a broad Drude-like feature in the optical conductivity, linear temperature dependence of resistivity, and an extremely short elec-

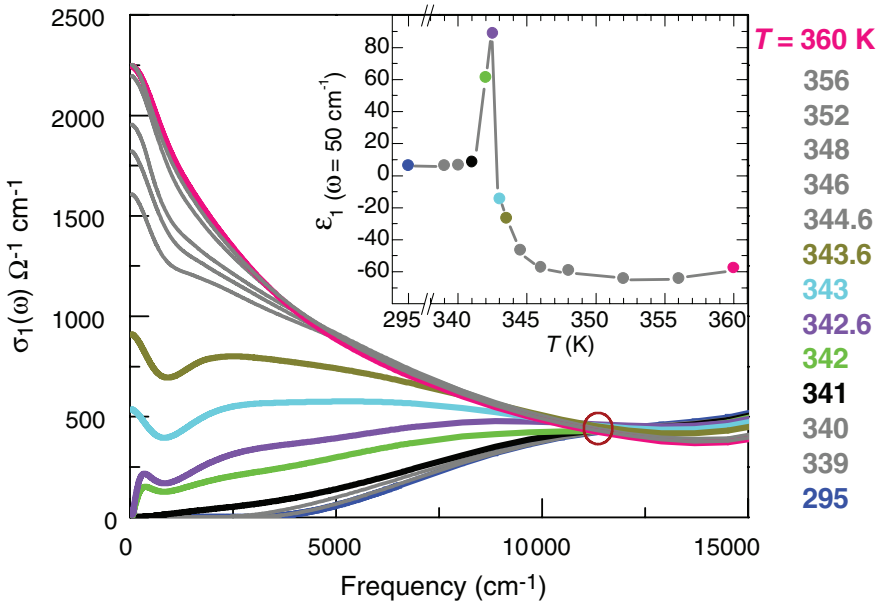

Fig. 1. The real part of the optical conductivity $\sigma_1(\omega) = \frac{\omega\varepsilon_2(\omega)}{4\pi}$ of VO_2 is plotted as a function of frequency for various representative temperatures. The open circle denotes the isosbestic (equal conductivity) point for all spectra. (**Inset**) The temperature dependence of the real part of the dielectric function ε_1 in the low-frequency limit ($\omega = 50$ cm^{-1}).

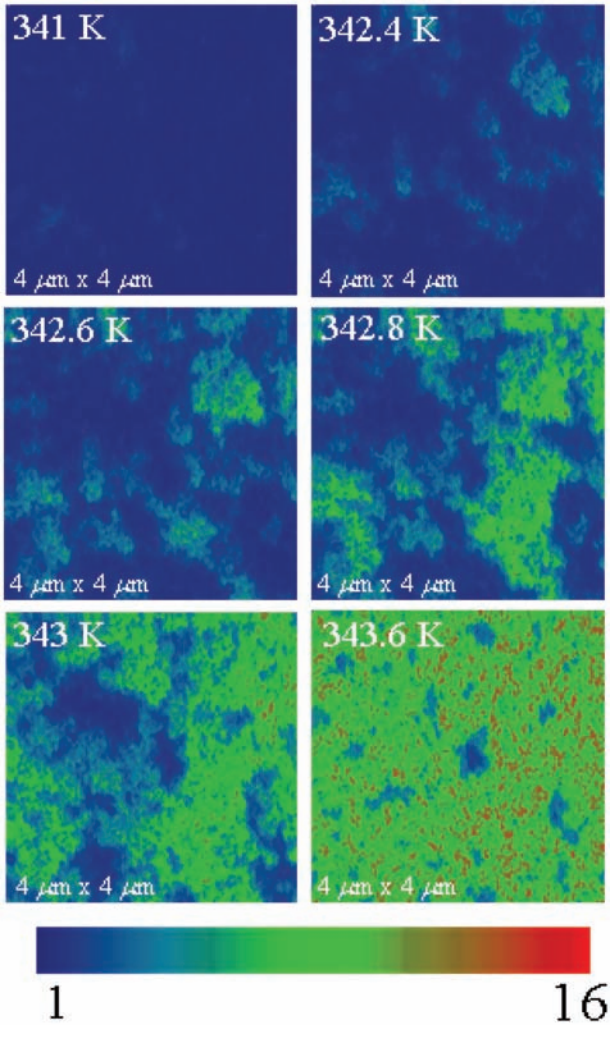

Fig. 2. Images of the near-field scattering amplitude over the same 4-μm-by-4-μm area obtained by s-SNIM operating at the infrared frequency $\omega = 930$ cm^{-1}. These images are displayed for representative temperatures in the insulator-to-metal transition regime of VO_2 to show percolation in progress. The metallic regions (light blue, green, and red colors) give higher scattering near-field amplitude compared with the insulating phase (dark blue color). See (*13*) for details.

[1]Physics Department, University of California–San Diego, La Jolla, CA 92093, USA. [2]Abt. Molekulare Strukturbiologie, Max-Planck-Institut für Biochemie and Center for NanoScience, 82152 Martinsried, München, Germany. [3]IT Convergence and Components Laboratory, Electronics and Telecommunications Research Institute, Daejeon 305-350, Korea. [4]Theoretical Division and Center for Integrated Nanotechnologies, MS B262, Los Alamos National Laboratory, Los Alamos, NM 87545, USA.

*To whom correspondence should be addressed. E-mail: mumtaz@physics.ucsd.edu

tronic mean free path of the order of the lattice constant, reminiscent of "bad metal" behavior in other transition metal oxides, including the cuprates (*21*–*23*). The insulator-to-metal transition is evident from the increase of the conductivity with spectral weight "filling up" the energy gap that has to be contrasted with a gradual decrease of the energy gap magnitude. This feature of the transition, along with an isosbestic point at a frequency of 11,500 ± 125 cm^{-1}, is one of several spectroscopic fingerprints of doped Mott insulators (*1*) identified in this work. The isosbestic point is defined here as the location of equal conductivity for all spectra obtained at different temperatures. Lastly, the divergence of the real part of the dielectric function ε_1 (Fig. 1 inset) signals the percolative nature of the insulator-to-metal transition. This divergence of ε_1 is similar to that observed near the percolative insulator-to-metal transition in ultrathin Au and Pb films (*24*).

Mid-infrared near-field images directly show that in fact the insulating and metallic phases coexist in VO_2 over a finite temperature range in the transition region (Fig. 2). This determination was made by using a scattering scanning near-field infrared microscope (s-SNIM) operating at the infrared frequencies $\omega = 930\ cm^{-1}$ and $\omega = 1725\ cm^{-1}$. S-SNIM is capable of registering contrast between electronic phases according to their optical constants with spatial resolution ≈ 20 nm. Specifically, the scattering amplitude signal demodulated at the second harmonic of the tapping frequency of the tip of our s-SNIM apparatus (maps in Fig. 2) is related to the local value of the complex dielectric function $\tilde{\varepsilon} = \varepsilon_1 + i\varepsilon_2$ of the sample. The amplitude of the scattering signal is expected to increase in metallic regions compared with that in the insulating regions: a behavior grasped well by the so-called dipole model of the near-field infrared contrast (*9*, *10*, *13*).

The amplitude-contrast near-field images in Fig. 2 show the electronic insulator-to-metal transition in progress. At temperatures between 295 and 341 K in the insulating phase, we observed uniform maps of low scattering (dark blue color in Fig. 2). A small increase of temperature radically changes the near-field images. For example, in the T = 342.4 K image we then observed nanoscale clusters in which the amplitude of the scattering signal was enhanced by a factor of 2 to 5 compared with that of the insulating host, indicating a metallic phase. Representative scans showed that the metallic regions nucleate, then grow with increasing temperature, and eventually connect. We did not observe any obvious correlations between the size and/or shape of the metallic clusters and the features in simultaneously collected topographic images. Although the percolative nature of the insulator-to-metal transition had been proposed previously (*25*), it is directly revealed by our scanning near-field infrared measurements reported herein. The insulator-to-metal transition is complete by T = 360 K, at which temperature insulating islands are no longer seen.

With the observation of nanostructured phases in Fig. 2, the far-field infrared spectra in Fig. 1 should be analyzed with use of an effective medium theory (EMT) for such phase-separated systems (*13*, *26*). The effective optical constants of a two-phase heterogeneous system are an average of the optical constants of the insulating and metallic regions weighted by the respective volume fractions. Our near-field images enabled us to determine these fractions. However, a simple weighting of optical constants of the insulating phase and of the rutile metallic phase at T = 360 K within the EMT model does not produce a satisfactory description of the far-field infrared data near the onset of the insulator-to-metal transition in VO_2. This discrepancy indicates that the infrared properties of the metallic puddles, once they first appear at $T \approx 342$ K, may be different from that of the high-temperature rutile metal. We confirmed this hypothesis by extracting the response of the metallic puddles from a combi-

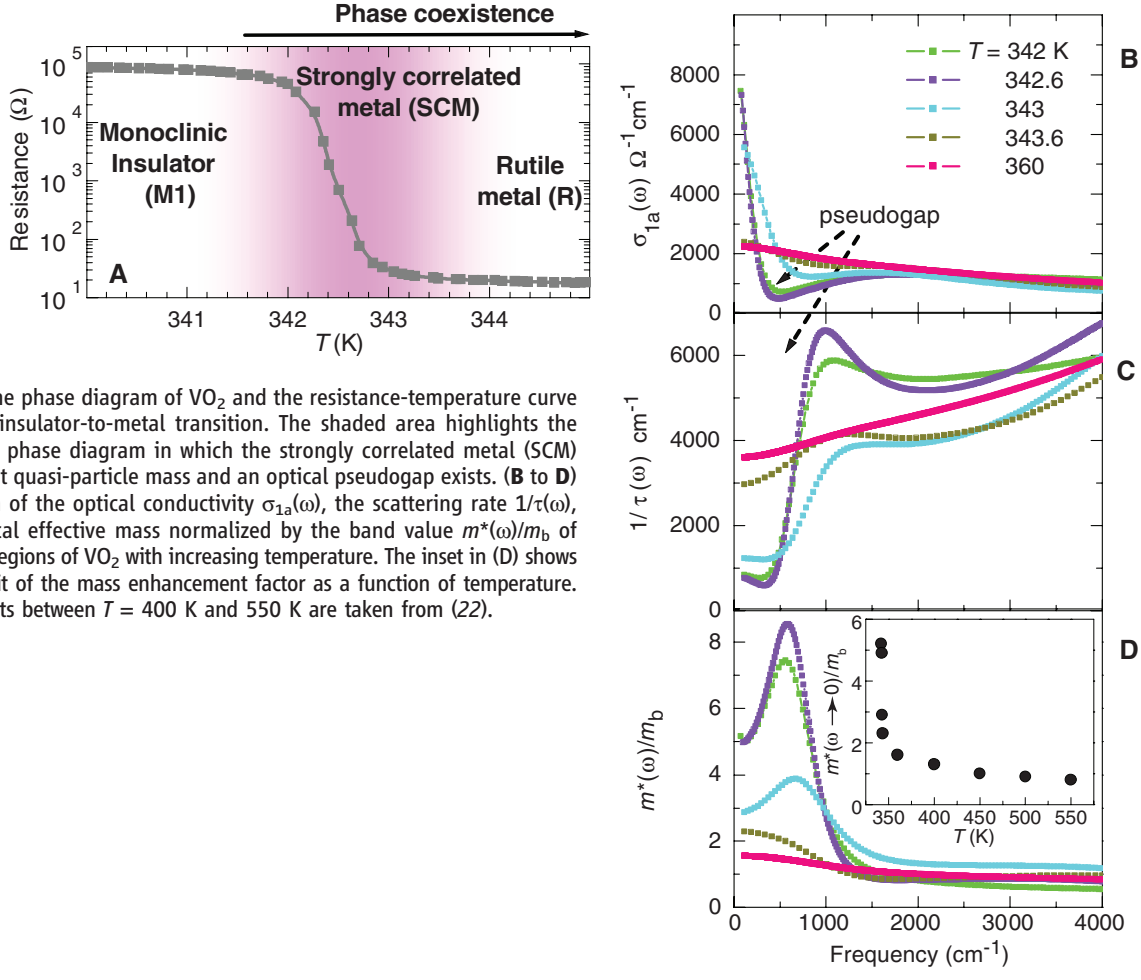

Fig. 3. (**A**) The phase diagram of VO_2 and the resistance-temperature curve showing the insulator-to-metal transition. The shaded area highlights the region of the phase diagram in which the strongly correlated metal (SCM) with divergent quasi-particle mass and an optical pseudogap exists. (**B** to **D**) The evolution of the optical conductivity $\sigma_{1a}(\omega)$, the scattering rate $1/\tau(\omega)$, and the optical effective mass normalized by the band value $m^*(\omega)/m_b$ of the metallic regions of VO_2 with increasing temperature. The inset in (D) shows the $\omega \rightarrow 0$ limit of the mass enhancement factor as a function of temperature. The data points between T = 400 K and 550 K are taken from (*22*).

nation of near-field results and far-field spectra within an EMT analysis described in (*13*).

The real part of the conductivity spectrum, $\sigma_{1a}(\omega)$, of the metallic puddles is plotted in Fig. 3B as it evolves with temperature. When these puddles appear at the onset of the electronic insulator-to-metal transition at $T \approx 342$ K (Fig. 3A), their conductivity spectrum differs markedly from that of the rutile metallic phase at higher temperature, for example, $T = 360$ K. These metallic regions exhibit a narrow Drude-like peak at low frequencies and then a dip, followed by a prominent mid-infrared band that peaked at $\approx$1800 cm^{-1}. Uncertainties in the EMT analysis [detailed in (*13*)] do not exclude the possibility of a nonmonotonic form of $\sigma_{1a}(\omega)$ at the lowest frequencies, a behavior consistent with Drude response modified by localization. These features indicate that the metallic islands are not simply isolated regions of the higher-temperature VO_2 rutile metal.

In order to highlight distinctions between the electrodynamics of the metallic clusters and the rutile metallic phase, we performed the extended Drude analysis (*13*, *27*) on the optical constants of the metallic clusters to extract the scattering rate $1/\tau(\omega)$ and the mass enhancement factor $m^*(\omega)/m_b$ (m_b is the electronic band mass) of the charge carriers (Fig. 3, C and D). In the limit of $\omega \rightarrow 0$, these quantities can be interpreted in terms of lifetime, $\tau(\omega)$, and effective mass, $m^*(\omega)$, of quasiparticles (*27*) in the metallic regions. One can recognize a prominent enhancement of $m^*(\omega \rightarrow 0)/m_b$ at $T = 342$ K that has to be contrasted with much lighter masses in the rutile phase ($T = 360$ K) spectrum in Fig. 3D (*22*). More importantly, the temperature dependence of $m^*(\omega \rightarrow 0)/m_b$, plotted in the inset of Fig. 3D, shows divergent behavior in the vicinity of the insulator-to-metal transition: an unambiguous attribute of the Mott transition (*28*). The spectra of $1/\tau(\omega)$ reveal a threshold structure followed by an overshoot at higher energies up to $\approx$1000 cm^{-1}. This is characteristic of systems with a (pseudo)gap in the electronic density of states (*29*) that is to be contrasted with the relatively smooth variation of $1/\tau(\omega)$ in the rutile phase. We also note that the new electronic state exhibiting an enhanced mass and a gaplike form of the relaxation rate exists only in a narrow temperature range, as shown by the shaded region in Fig. 3A. By $T = 343.6$ K, the optical constants of the metallic regions already resemble those of the rutile metallic phase.

The analysis and discussion above suggest that the classic temperature-induced insulator-to-metal transition in VO_2 occurs from the monoclinic insulator to an incipient strongly correlated metal (SCM) in the form of nanoscale puddles. These metallic puddles exhibit mass divergence, which is a clear signature of electronic correlations due to many-body Coulomb interactions (*28*). The pseudogap and mid-infrared band are consequences of optically induced electronic excitations across a gap on some parts of the Fermi surface. The energy scale of the pseudogap in the SCM state in VO_2 can be determined by the overshoot in $1/\tau(\omega)$ spectra that occurs at $\approx$1000 cm^{-1} (or $\approx 4k_BT_c$). We note that the pseudogap is a common property of doped Mott insulators (*1*, *27*). The pseudogap features in the optical conductivity and $1/\tau(\omega)$ spectra also bear resemblance to those found in metallic systems with a partial charge density wave (CDW) gap (*30*). The pseudogap in VO_2 may result from a complex interplay between electronic correlations and charge ordering.

The Mott transition commonly leads to an antiferromagnetically ordered insulator as in closely related V_2O_3 (*1*). Vanadium dioxide avoids this magnetic ordering via dimerization of vanadium ions in the monoclinic insulating phase (*14*) because of competing effects of charge ordering (Peierls instability) that is likely caused by electron-phonon interactions. Thus, the insulating monoclinic (M1) phase of VO_2 should be classified as a Mott insulator with charge ordering. It remains an open question whether or not the insulator-to-metal transition occurs at a slightly different temperature from the structural transformation associated with charge ordering (*18*, *19*, *31*), and this raises the issue about the precise lattice structure of the metallic nanopuddles we have observed. This issue does not affect our observation of divergent optical mass and can only be resolved by x-ray diffraction measurements on the nanoscale. We also note that the images of phase coexistence and percolation reported here (Fig. 2) are consistent with the thermodynamic evidence of the first-order nature of the phase transition in VO_2 (*21*). Moreover, our experiments show that the collapse of a large $\approx$0.5 eV energy gap and the formation of heavy quasi-particles in the emergent metallic nanopuddles at the onset of the insulator-to-metal transition are due to Mott physics (*1*, *28*) and that percolation occurs at a later stage when these metallic puddles grow and connect (Fig. 2).

A transformation from an insulator to a metal in many correlated electron systems, including high-T_c cuprates, colossal magnetoresistive manganites, and others, occurs through an intermediate pseudogap regime (*1*, *5*, *27*, *29*). At least in the case of cuprates, optical signatures of the pseudogap state are similar to the results in the SCM state of VO_2 (*27*). Furthermore, in many correlated systems, the pseudogap state is in the vicinity of the regime of the bad metal in which resistivity shows a peculiar linear dependence with temperature, whereas the absolute values of the resistivity are so large that the notion of quasiparticles becomes inapplicable (*21*–*23*). Often a crossover from pseudogapped metal to bad metal occupies an extended region of the phase diagram. In VO_2, the boundary between the two electronic regimes is relatively abrupt, and the emergence of bad metal transport in the rutile phase may be linked to the loss of long-range charge order that does not extend into the rutile metal. Then the poor conductivity of rutile VO_2 and other bad metals appears to arise from the collapse of electronically and/or magnetically ordered states in the vicinity of a Mott insulator, thereby causing the resistivity to exceed the Ioffe-Regel-Mott limit of metallic transport (*21*–*23*). Lastly, we note that, in the cuprates, in contrast to VO_2, the effective mass of doped carriers inferred from infrared spectroscopy data (*32*) shows no divergence. However, if electronic phase separation exists in doped cuprates, as suggested by recent scanning probe studies (*6*, *8*), then infrared analysis of the effective quasi-particle mass needs to be revisited with the help of nano-imaging tools used in this work.

References and Notes

1. M. Imada, A. Fujimori, Y. Tokura, *Rev. Mod. Phys.* **70**, 1039 (1998).
2. V. J. Emery, S. A. Kivelson, J. M. Tranquada, *Proc. Natl. Acad. Sci. U.S.A.* **96**, 8814 (1999).
3. M. Uehara, S. Mori, C. H. Chen, S.-W. Cheong, *Nature* **399**, 560 (1999).
4. L. Zhang, C. Israel, A. Biswas, R. L. Greene, A. de Lozanne, *Science* **298**, 805 (2002); published online 19 September 2002 (10.1126/science.1077346).
5. E. Dagotto, *Science* **309**, 257 (2005).
6. J. Lee *et al.*, *Nature* **442**, 546 (2006).
7. Z. Sun *et al.*, *Nat. Phys.* **3**, 248 (2007).
8. K. K. Gomes *et al.*, *Nature* **447**, 569 (2007).
9. B. Knoll, F. Keilmann, *Nature* **399**, 134 (1999).
10. F. Keilmann, R. Hillenbrand, *Philos. Trans. R. Soc. London Ser. A* **362**, 787 (2004).
11. N. Ocelic, A. Huber, R. Hillenbrand, *App. Phys. Lett.* **89**, 101124 (2006).
12. B. G. Chae *et al.*, *Electrochem. Solid-State Lett.* **9**, C12 (2006).
13. See Materials and Methods on *Science* Online.
14. R. M. Wentzcovitch, W. W. Schulz, P. B. Allen, *Phys. Rev. Lett.* **72**, 3389 (1994).
15. T. M. Rice, H. Launois, J. P. Pouget, *Phys. Rev. Lett.* **73**, 3042 (1994).
16. S. Biermann, A. Poteryaev, A. I. Lichtenstein, A. Georges, *Phys. Rev. Lett.* **94**, 026404 (2005).
17. T. C. Koethe *et al.*, *Phys. Rev. Lett.* **97**, 116402 (2006).
18. H.-T. Kim *et al.*, *Phys. Rev. Lett.* **97**, 266401 (2006).
19. H.-T. Kim *et al.*, *N. J. Phys.* **6**, 52 (2004).
20. E. Arcangeletti *et al.*, *Phys. Rev. Lett.* **98**, 196406 (2007).
21. P. B. Allen, R. M. Wentzcovitch, W. W. Schulz, P. C. Canfield, *Phys. Rev. B* **48**, 4359 (1993).
22. M. M. Qazilbash *et al.*, *Phys. Rev. B* **74**, 205118 (2006).
23. V. J. Emery, S. A. Kivelson, *Phys. Rev. Lett.* **74**, 3253 (1995).
24. J. J. Tu, C. C. Homes, M. Strongin, *Phys. Rev. Lett.* **90**, 017402 (2003).
25. H. S. Choi, J. S. Ahn, J. H. Jung, T. W. Noh, D. H. Kim, *Phys. Rev. B* **54**, 4621 (1996).
26. G. L. Carr, S. Perkowitz, D. B. Tanner, in *Infrared and Millimeter Waves*, K. J. Button, Ed. (Academic Press, Orlando, 1985), vol. 13.
27. D. N. Basov, T. Timusk, *Rev. Mod. Phys.* **77**, 721 (2005).
28. W. F. Brinkman, T. M. Rice, *Phys. Rev. B* **2**, 4302 (1970).
29. D. N. Basov, E. J. Singley, S. V. Dordevic, *Phys. Rev. B* **65**, 054516 (2002).
30. G. Gruner, *Density Waves in Solids* (Perseus Publishing, Cambridge, MA, 2000).
31. Y. J. Chang *et al.*, *Phys. Rev. B* **76**, 075118 (2007).
32. W. J. Padilla *et. al., Phys. Rev. B* **72**, 060511(R) (2005).

33. This work was supported by the U.S. Department of Energy, the Deutsche Forschungsgemeinschaft Cluster of Excellence Munich–Centre for Advanced Photonics, and the Electronics and Telecommunications Research Institute (ETRI), Korea.

Supporting Online Material

www.sciencemag.org/cgi/content/full/318/5857/1750/DC1
Materials and Methods
SOM Text
Table S1

5 September 2007; accepted 31 October 2007
10.1126/science.1150124

Stable Magnesium(I) Compounds with Mg-Mg Bonds

Shaun P. Green,[1,2] Cameron Jones,[1]* Andreas Stasch[1]*

The chemistry of the group 2 metals (beryllium, magnesium, calcium, strontium, and barium) is dominated by the +2 oxidation state. Here, we report the reductions of two magnesium(II) iodide complexes with potassium metal in toluene, leading to thermally stable magnesium(I) compounds, (L)MgMg(L) (where L is $[(Ar)NC(NPr^i_2)N(Ar)]^-$ or $\{[(Ar)NC(Me)]_2CH\}^-$, Ar is 2,6-diisopropylphenyl, Me is methyl, and Pr^i is isopropyl) in moderate yields. The results of x-ray crystallographic and theoretical studies are consistent with central Mg_2^{2+} units that have single, covalent magnesium-magnesium bonding interactions with 2.8508 ± 0.0012 (standard deviation) and 2.8457 ± 0.0008 angstrom bond lengths, respectively, and predominantly ionic interactions with the anionic ligands (L).

Magnesium is ubiquitous in living organisms, Earth's crust, and seawater (*1*). Like the other alkaline earth metals (group 2 metals), magnesium is present in all its known stable compounds in the +2 oxidation state. It plays a major role in nature as the central ion in chlorophyll because its redox-inert character is important for the charge separation in photosynthesis (*1*). The reduction of other metal ions has involved the formation of direct metal-metal bonds. For example, homonuclear compounds, RM^IM^IR (where R represents an organic or similar substituent and M is a metal), of *p*- or *d*-block metals have been prepared with the metal centers formally in the +1 oxidation state. Two recent landmark advances in this field are the synthesis of a chromium(I) dimer [L'CrCrL', where L' is $C_6H_3(C_6H_3Pr^i_2\text{-}2,6)_2$-2,6 and Pr^i is isopropyl] containing a metal-metal quintuple bonding interaction (*2*) and the synthesis of a zinc(I) compound, $(\eta^5\text{-}C_5Me_5)ZnZn(\eta^5\text{-}C_5Me_5)$ (where Me is methyl) (*3*). Since the report on the latter, the chemical similarities between zinc and the lighter group 2 metals have prompted theoreticians to examine the possibility of preparing complexes of the type RMMR (where M is Be, Mg, or Ca), with the conclusion that such reduced *s*-block compounds should be stable given the correct choice of ligand (*4*–*6*). A number of magnesium(I) compounds, for example, HMgMgH, have previously been studied under, for example, matrix isolation conditions (*7*), and mononuclear compounds, for example, $Mg^I(NC)$, have been detected in circumstellar clouds (*8*). Moreover, the formation of synthetically important Grignard reagents, RMgX (where X is a halide), has been proposed to proceed via magnesium(I) compounds of the type RMgMgX (*9*). In addition, related cluster compounds, RMg_4X, of undetermined structure have been investigated by using mass spectrometry experiments (*10*). However, no examples of stable molecular group 2 metal(I) compounds have been isolated.

In the past 2 years, we have developed and used the bulky guanidinate ligands, $[(Ar)NC(NR'_2)N(Ar)]^-$ [where Ar is 2,6-diisopropylphenyl and R' is isopropyl (Priso) or cyclohexyl (Giso)] to access complexes of *p*-block elements in the +1 oxidation state, for example, Ga^I(Giso) (*11*) and $[Ge^I(Priso)]_2$ (*12*). The ability of these sterically hindered, N,N'-chelating ligands to stabilize low oxidation state complexes is strikingly similar to that of bulky examples from the well-studied β-diketiminate class of ligand, for example, $\{[(Ar)NC(Me)]_2CH\}^-$ (Nacnac) (*13*). Here, we report the use of both Priso and Nacnac ligands to prepare molecular magnesium(I) compounds that contain structurally characterized magnesium-magnesium bonds. We examined the nature of the bonding in these compounds by theoretical studies and also carried out preliminary reactivity studies.

The new magnesium(II) complex, $(Priso)Mg(\mu\text{-}I)_2Mg(OEt_2)(Priso)$ (OEt_2 is diethyl ether), was prepared as a precursor to one of the target magnesium(I) compounds (*14*). This was spectroscopically characterized, and its x-ray crystal structure was determined (fig. S2). Reduction of $(Priso)Mg(\mu\text{-}I)_2Mg(OEt_2)(Priso)$ and the known compound, $MgI(OEt_2)(Nacnac)$ (*15*), with an excess of potassium metal in toluene over 24 hours led to the crystalline magnesium(I) compounds $[Mg(Priso)]_2$ **1** (colorless, yield of 28.5%) and $[Mg(Nacnac)]_2$ **2** (yellow, yield of 56.5%), respectively, after workup (Fig. 1) (*14*). Although both compounds are air- and moisture-sensitive, they are thermally stable and fully decompose only at temperatures in excess of 170°C and 300°C, respectively, the former with deposition of elemental magnesium. The x-ray crystal structure of each compound was obtained (Figs. 2 and 3) (*16*). Both possess distorted trigonal planar coordination geometries with delocalized ligand backbones. Although their Mg-N distances [2.0736(10) (or ±0.0010) Å for **1** and a mean value of 2.060 Å for **2**; the number in parentheses indicates the standard deviation] are in the known range for Mg-N bonds (*17*), they are longer than all such bonds in complexes in which β-diketiminates ligate three-coordinate magnesium(II) centers. Despite the paucity of Mg-Mg bonds for comparison, the lengths of those interactions in **1** and **2** are similar [2.8508(12) Å and 2.8457(8) Å, respectively]. Although these distances are considerably shorter than those in diatomic or elemental magnesium (3.890 Å and 3.20 Å, respectively) (*18*, *19*), they are longer than the sum of two magnesium covalent radii (2.72 Å) (*19*). The distances are, however, in the range of previously

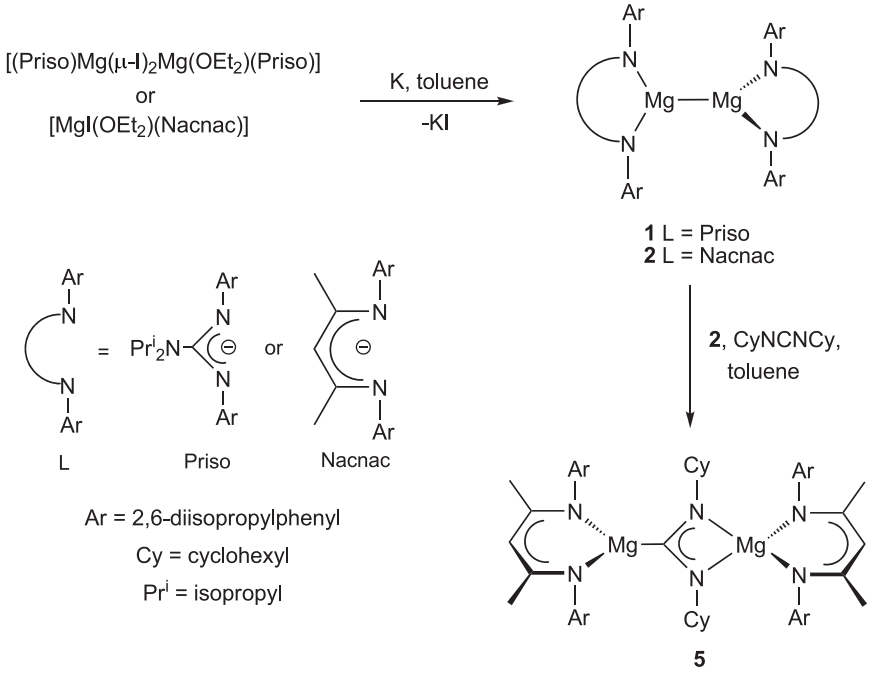

Fig. 1. Formation of compounds **1**, **2**, and **5**.

[1]School of Chemistry, Monash University, Post Office Box 23, Victoria 3800, Australia. [2]School of Chemistry, Main Building, Cardiff University, Cardiff CF10 3AT, UK.

*To whom correspondence should be addressed. E-mail: cameron.jones@sci.monash.edu.au (C.J.); andreas.stasch@sci.monash.edu.au (A.S.)

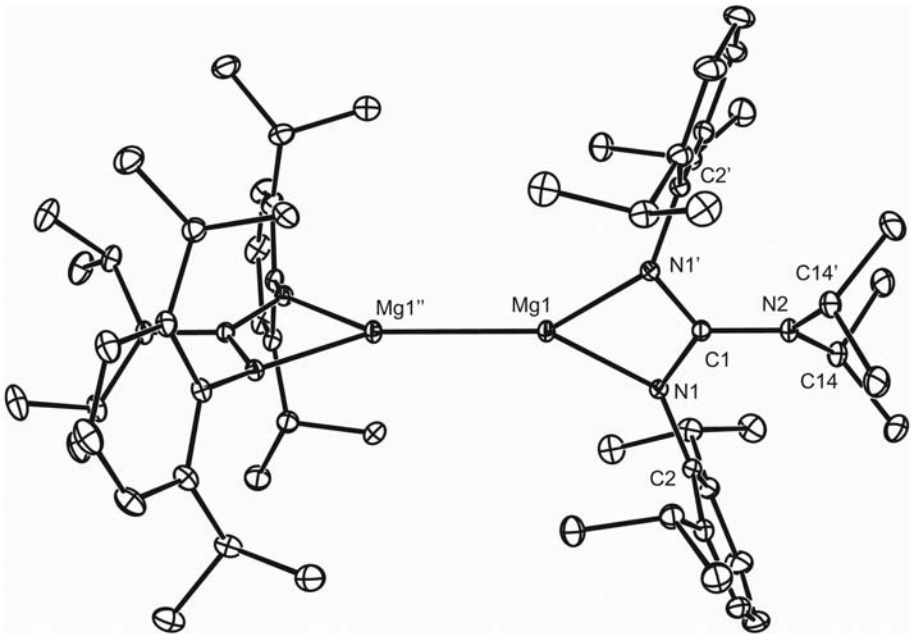

Fig. 2. Molecular structure of **1** (hydrogen atoms omitted, ellipsoids shown at the 20% probability level). Selected bond lengths and angles: Mg(1)-Mg(1)" 2.8508(12) Å, Mg(1)-N(1) 2.0736(10) Å, N(1)-C(1) 1.3497(12) Å, N(2)-C(1) 1.389(2) Å; N(1)-Mg(1)-N(1)' 65.54(5)°, N(1)-C(1)-N(1)' 112.53(13)°, N(1)-Mg(1)-Mg(1)" 147.23(3)°.

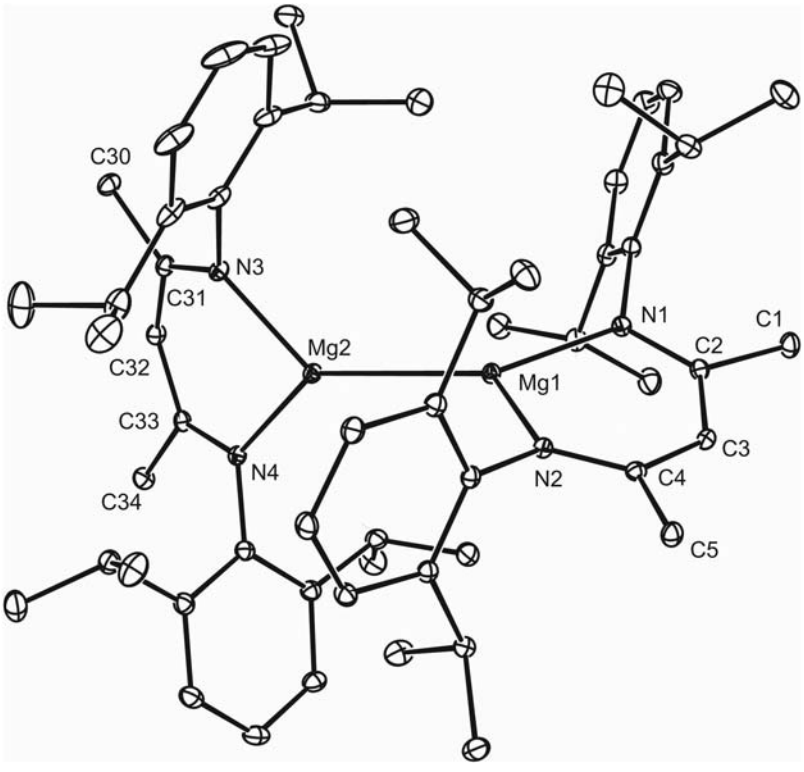

Fig. 3. Molecular structure of **2** (hydrogen atoms omitted, ellipsoids shown at the 20% probability level). Selected bond lengths and angles: Mg(1)-Mg(2) 2.8457(8) Å, Mg(1)-N(2) 2.0547(13) Å, Mg(1)-N(1) 2.0643(13) Å, N(1)-C(2) 1.3354(18) Å, C(1)-C(2) 1.5135(19) Å, Mg(2)-N(3) 2.0571(13) Å, Mg(2)-N(4) 2.0656(12) Å, N(2)-C(4) 1.3251(17) Å, C(2)-C(3) 1.4041(19) Å, N(3)-C(31) 1.3269(18) Å, C(3)-C(4) 1.4041(19) Å, N(4)-C(33) 1.3368(17) Å, C(4)-C(5) 1.5116(19) Å, C(30)-C(31) 1.514(2) Å, C(31)-C(32) 1.409(2) Å, C(32)-C(33) 1.398(2) Å, C(33)-C(34) 1.5157(19) Å; N(2)-Mg(1)-N(1) 91.78(5)°, N(2)-Mg(1)-Mg(2) 128.50(4)°, N(1)-Mg(1)-Mg(2) 139.35(4)°, N(3)-Mg(2)-N(4) 91.80(5)°, N(3)-Mg(2)-Mg(1) 129.65(4)°, N(4)-Mg(2)-Mg(1) 138.24(4)°.

calculated Mg-Mg separations in theoretical molecular compounds, for example, the cyclopentadienyl magnesium(I) dimer, $(C_5H_5)MgMg(C_5H_5)$ [2.776 Å (B3LYP calculations) (*4*) and 2.809 Å (BP86) (*5*)], the 2,6-diphenylphenyl magnesium(I) dimer, $\{[C_6H_3(C_6H_5)_2\text{-}2,6]MgMg[C_6H_3(C_6H_5)_2\text{-}2,6]\}$ [2.838 Å (BP86) (*6*)], and HMgMgH [2.862 Å (B3LYP) (*4*) and 2.884 Å (BP86) (*5*)]. It should also be noted that two nonbonded Mg···Mg interactions in one cluster compound, $[Mg(THF)(\mu\text{-}C_6H_4)]_4$ (THF is tetrahydrofuran) (*20*), are shorter [2.804(2) Å and 2.841(2) Å] than the separations in **1** and **2**.

Considering the relatively long Mg-Mg bonds in **1** and **2**, the possibility that these compounds actually exist as hydride-bridged magnesium(II) dimers, $[Mg(L)(\mu\text{-}H)]_2$ (L is Priso or Nacnac), cannot be overlooked. However, the combined weight of the crystallographic, spectroscopic, theoretical, and chemical evidence discounts this possibility (*vide infra*). First, the heterocycle least squares planes in **1** are orthogonal, whereas compound **2** has close to orthogonal heterocycle planes (dihedral angle is 80.2°) and is isostructural with the related metal(I) dimers, $[M^I(Nacnac)]_2$ [M is Zn (*21*) or Mn (*22*)]. If **1** and **2** were hydride-bridged dimers, their heterocycles would, instead, be expected to be close to coplanar. In addition, in the final difference maps of the structural refinements of both compounds, there were no regions of residual electron density of greater than 0.15 electrons per cubic angstrom close to the Mg-Mg vectors, again suggesting the absence of hydride ligands.

The nuclear magnetic resonance (NMR) spectroscopic data for diamagnetic **1** and **2** are consistent with their proposed formulations. No bridging hydride resonances were observed in the expected chemical shift range in the ^{1}H NMR spectra of the complexes (*23*). In addition, their electron ionization high-resolution accurate mass spectra exhibit molecular ion envelopes with isotopic mass distributions that match well those calculated for the hydride-free complexes (fig. S1). In this respect, the stability of **2** in the gas phase is demonstrated by the fact that it can be sublimed intact at 230°C (circa 10^{-6} mm Hg). The Raman spectra of the compounds display a number of low-frequency absorptions, although none of these can be confidently assigned as arising from Mg-Mg stretching modes. Similarly, little information regarding the structures of the complexes can be obtained from their infrared spectra. Mg-H-Mg stretching absorptions originating from the alternatively formulated complexes, $[Mg(L)(\mu\text{-}H)]_2$, would certainly lie in the fingerprint region (*24*) and would, thus, be difficult to assign due to overlap with low-frequency ligand modes. Because we have not yet been able to prepare authentic samples of $[Mg(L)(\mu\text{-}H)]_2$ by rational routes (*14*), we cannot compare their infrared spectra {and the infrared spectra of their deuterated analogs, $[Mg(L)(\mu\text{-}D)]_2$} with those of **1** and **2**.

In order to examine the nature of the bonding in **1**, density functional theory (DFT) calcula-

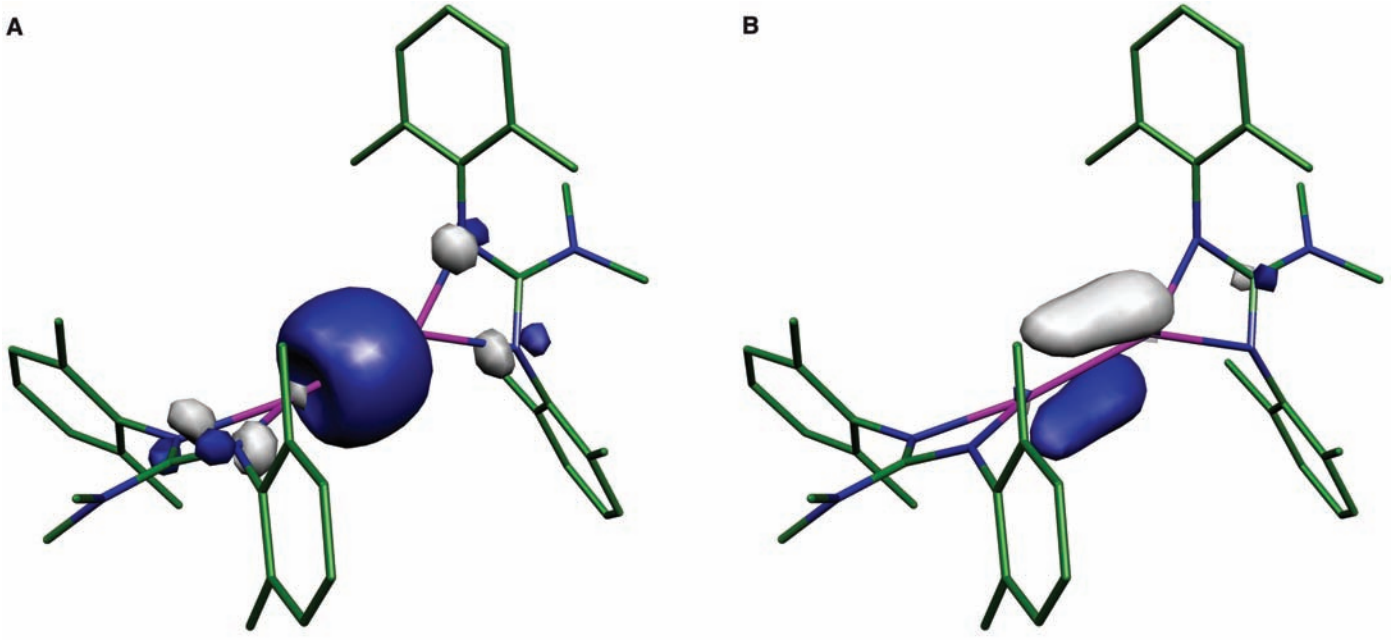

Fig. 4. Representations of (**A**) the HOMO (–4.75 eV) and (**B**) the LUMO (–0.722 eV) of the model system $\{Mg[(Ar'N)_2C(NMe_2)]\}_2$ **3** (Ar' is $C_6H_3Me_2$-2,6).

tions (B3LYP and BP86) (*25*) were carried out on the model complex, $\{Mg[(Ar'N)_2C(NMe_2)]\}_2$ **3** (Ar' is $C_6H_3Me_2$-2,6). The geometry of the optimized structure was found to be in close agreement with that in the crystal structure of **1** (i.e., with effectively orthogonal heterocycle planes) but with slightly underestimated Mg-Mg bond lengths (with B3LYP, 2.828 Å; with BP86, 2.839 Å) and slightly overestimated Mg-N distances (with B3LYP, mean = 2.102 Å; with BP86, mean = 2.114 Å). Figure 4A depicts the highest occupied molecular orbital (HOMO) of the complex, which largely comprises the metal-metal σ-bonding interaction. The two lowest unoccupied orbitals, LUMO (Fig. 4B) and LUMO+1 (fig. S4), are almost degenerate (energy difference of 0.11 eV, 2.6 kcal mol^{-1}) and predominantly encompass metal-metal π-bonding orbitals derived from metal p_x- and p_y-orbital overlaps respectively. A similar arrangement of frontier orbitals has been calculated for $[C_6H_3(C_6H_5)_2$-2,6]ZnZn$[C_6H_3(C_6H_5)_2$-2,6] (*26*). The HOMO-LUMO gap in **3** (4.02 eV, 93.0 kcal mol^{-1}) is comparable with those calculated for both $(C_5H_5)MgMg(C_5H_5)$ (3.87 eV, 89.5 kcal mol^{-1}) (*5*) and $[C_6H_3(C_6H_5)_2$-2,6]ZnZn$[C_6H_3(C_6H_5)_2$-2,6] (4.25 eV, 97.6 kcal mol^{-1}) (*26*). In addition, the results of a natural bonding orbital (NBO) analysis (B3LYP) of the Mg-Mg interaction in **3** indicate a high s-character, single covalent bond (93.2% s-, 6.0% p-, and 0.8% d-character; Wiberg bond index = 0.914), whereas the metal-ligand interactions are predominantly ionic (natural charge for Mg, +0.82 mean, and for N, –0.97 mean). Accordingly, the molecule can be viewed as an anion-stabilized Mg_2^{2+} unit, as has been discussed for other model RMgMgR systems (*4*–*6*).

We were prompted to analyze the theoretical hydride complex, $\{Mg[(Ar'N)_2C(NMe_2)](\mu\text{-}H)\}_2$ **4**, using DFT calculations (B3LYP) for purposes of comparison with **1** and **3**. In contrast to those complexes, the optimized geometry of **4** exhibits coplanar heterocycles, oriented nearly orthogonal to the bridging, symmetrical Mg_2H_2 unit. Scans of the potential energy hypersurface of the less bulky model, $\{Mg[(HN)_2C(NH_2)](\mu\text{-}H)\}_2$, at density functional (B3LYP) and ab initio (MP2) levels of theory, show this conformation to be the global minimum (*14*). Moreover, there are no local minima associated with any conformation of the molecule in which the planes of the magnesium heterocycles are orthogonal or close to orthogonal with each other. Surprisingly, the Mg···Mg separation in **4** at 2.770 Å (Mg-H mean distance = 1.890 Å) is substantially shorter than in **3**, despite a less pronounced metal-metal interaction (Wiberg bond index = 0.307). In this respect, previous theoretical studies have concluded that metal-metal distances in hydride bridged complexes can be shorter than in corresponding hydride-free, metal-metal bonded complexes (*27*). The results of all calculations undertaken are fully consistent with **1** (and by implication **2**) being a magnesium(I) dimer, not a hydride bridged magnesium(II) dimer.

Although **1** and **2** would be expected to be highly reducing, we have found that they do not react with dihydrogen or dinitrogen in toluene, even at elevated temperatures (80°C) or when irradiated with ultraviolet light (λ = 254 nm). The lack of reactivity of the complexes toward dihydrogen is not surprising when it is considered that the closely related addition of H_2 to $[(C_5H_5)MgMg(C_5H_5)]$ [to generate two molecules of $(C_5H_5)MgH$] has been calculated to be an endothermic process (*4*). Surprisingly, exposure of the three-coordinate magnesium centers in **1** and **2** to THF in C_6D_6 solutions does not lead to evidence of THF coordination as judged by ^1H or $^{13}C\{^1H\}$ NMR spectroscopy. However, a weak, transient coordination of THF cannot be ruled out in these experiments on the basis of the results of the reaction of **2** with the carbodiimide CyNCNCy (Cy is cyclohexyl) in toluene at –70°C (Fig. 1). This led to immediate loss of the yellow color of **2** and the isolation of the magnesium magnesioamidinate complex, **5**, after warming the reaction mixture to 20°C (*14*). Presumably, this reaction occurs via an initial coordination of one N-center of the carbodiimide at a magnesium center, followed by a double reduction of the carbodiimide and its concomitant insertion into the Mg-Mg bond of **2** (*28*, *29*). The spectroscopic data for **5** are consistent with the solid-state structure determined by an x-ray crystallographic study (fig. S4). In contrast to the nearly orthogonal Mg(Nacnac) least squares planes in **2**, these planes in **5** are mutually parallel and orthogonal to the CyN-CNCy unit. Reaction of the carbodiimide with the alternative hydride-bridged magnesium(II) complex, $[Mg(Nacnac)(\mu\text{-}H)]_2$, would not be expected to give compound **5** but instead C=N bond hydromagnesiation.

References and Notes

1. W. Kaim, B. Schwederski, *Bioinorganic Chemistry: Inorganic Elements in the Chemistry of Life - An Introduction and Guide* (Wiley, Chichester, 1994), chapters 2 and 4.
2. T. Nguyen *et al.*, *Science* **310**, 844 (2005); published online 22 September 2005 (10.1126/science.1116789).
3. I. Resa, E. Carmona, E. Gutierrez-Puebla, A. Monge, *Science* **305**, 1136 (2004).
4. Y. Xie, H. F. Schaefer III, E. D. Jemmis, *Chem. Phys. Lett.* **402**, 414 (2005).
5. A. Velazquez, I. Fernandez, G. Frenking, G. Merino, *Organometallics* **26**, 4731 (2007).
6. M. Westerhausen *et al.*, *Chem. Eur. J.* **13**, 6292 (2007).
7. X. Wang, L. Andrews, *J. Chem. Phys. A* **108**, 11511 (2004).
8. S. Petrie, *Aust. J. Chem.* **56**, 259 (2003).

9. P. G. Jasien, C. E. Dykstra, *J. Am. Chem. Soc.* **105**, 2089 (1983).
10. L. A. Tjurina *et al.*, *Organometallics* **23**, 1349 (2004).
11. C. Jones, P. C. Junk, J. A. Platts, A. Stasch, *J. Am. Chem. Soc.* **128**, 2206 (2006).
12. S. P. Green, C. Jones, P. C. Junk, K.-A. Lippert, A. Stasch, *Chem. Commun.* 3978 (2006).
13. L. Bourget-Merle, M. F. Lappert, J. R. Severn, *Chem. Rev.* **102**, 3031 (2002).
14. Materials and methods are available on *Science* Online.
15. J. Prust *et al.*, *Z. Anorg. Allg. Chem.* **627**, 2032 (2001).
16. Crystal data for **1** and **2** were obtained at 123(2) K with use of an Enraf-Nonius Kappa charge-coupled device diffractometer and MoK_α radiation ($\lambda = 0.71073$ Å). The crystal data are as follows. For **1**: $a = b = 18.409(3)$ Å, $c = 17.640(4)$ Å, tetragonal, $I4_1/a$, $Z = 4$, R_1 for 3176 [data intensity $I > 2\sigma(I)$] unique data = 0.0448, and wR_2 (all 4353 unique data) = 0.1256. For **2**: $a = 14.444(3)$ Å, $b = 14.203(3)$ Å, $c = 26.742(5)$ Å, $\beta = 94.87(3)°$, monoclinic, $P2_1/c$, $Z = 4$, R_1 for 9054 [data intensity $I > 2\sigma(I)$] unique data = 0.0428, and wR_2 (all 11,843 unique data) = 0.1145.
17. As determined from a survey of the Cambridge Crystallographic Database, September 2007.
18. K. P. Huber, G. Herzberg, *Constants of Diatomic Molecules* (Van Nostrand, New York, 1979), pp. 116 and 394.
19. J. Emsley, *The Elements* (Clarendon, Oxford, ed. 2, 1995).
20. M. A. G. M. Tinga *et al.*, *J. Am. Chem. Soc.* **115**, 2808 (1993).
21. Y. Wang *et al.*, *J. Am. Chem. Soc.* **127**, 11944 (2005).
22. J. Chai *et al.*, *J. Am. Chem. Soc.* **127**, 9201 (2005).
23. R. E. Mulvey *et al.*, *Chem. Commun.* 376 (2002).
24. E. C. Ashby, A. B. Goel, *Inorg. Chem.* **18**, 1306 (1979).
25. M. J. Frisch *et al.*, Gaussian 98, Revision A.10, Gaussian, Incorporated, Pittsburgh, PA (2001).
26. Z. Zhu *et al.*, *Angew. Chem. Int. Ed.* **45**, 5807 (2006).
27. M.-H. Baik, R. A. Friesner, G. Parkin, *Polyhedron* **23**, 2879 (2004).
28. A recent precedent for these reactions exists with the insertions of the carbodiimide, CyN=C=NCy, into the Fe-B bonds of terminal iron borylene complexes, e.g., $(C_5H_5)Fe(CO)_2(BNCy_2)$, to give ferro-amidinate complexes of boron, e.g., $[(C_5H_5)Fe(CO)_2C(NCy)_2]BNCy_2$. These reactions are thought to proceed via initial N-coordination of the carbodiimide at the borylene center (*29*).
29. G. A. Pierce *et al.*, *Angew. Chem. Int. Ed.* **46**, 2043 (2007).

30. We are grateful to the Australian Research Council for providing fellowships to C.J. and A.S. We also thank the Engineering and Physical Sciences Research Council of the UK for a partly funded studentship (S.P.G.). Metrical data for $(Priso)Mg(\mu\text{-}I)_2Mg(OEt_2)(Priso)\cdot(hexane)_{0.5}$, **1**, **2**, and **5**$\cdot(toluene)_2$ are freely available from the Cambridge Crystallographic Database Center (CCDC codes 661565 to 661568).

Supporting Online Material

www.sciencemag.org/cgi/content/full/1150856/DC1
Materials and Methods
Figs. S1 to S4
Tables S1 to S3
References

24 September 2007; accepted 26 October 2007
Published online 8 November 2007;
10.1126/science.1150856
Include this information when citing this paper.

Activity of CeO_x and TiO_x Nanoparticles Grown on Au(111) in the Water-Gas Shift Reaction

J. A. Rodriguez,[1]* S. Ma,[1] P. Liu,[2] J. Hrbek,[1] J. Evans,[3] M. Pérez[3]

The high performance of Au-CeO_2 and Au-TiO_2 catalysts in the water-gas shift (WGS) reaction ($H_2O + CO \rightarrow H_2 + CO_2$) relies heavily on the direct participation of the oxide in the catalytic process. Although clean Au(111) is not catalytically active for the WGS, gold surfaces that are 20 to 30% covered by ceria or titania nanoparticles have activities comparable to those of good WGS catalysts such as Cu(111) or Cu(100). In TiO_{2-x}/Au(111) and CeO_{2-x}/Au(111), water dissociates on O vacancies of the oxide nanoparticles, CO adsorbs on Au sites located nearby, and subsequent reaction steps take place at the metal-oxide interface. In these inverse catalysts, the moderate chemical activity of bulk gold is coupled to that of a more reactive oxide.

Nearly 95% of the hydrogen supply is produced from the reforming of crude oil, coal, natural gas, wood, organic wastes, and biomass (*1*), but this reformed fuel contains 1 to 10% CO, the presence of which degrades the performance of the Pt electrode in fuel cell systems (*2*). To get clean hydrogen for fuel cells and other industrial applications, the water-gas shift (WGS) reaction ($CO + H_2O \rightarrow CO_2 + H_2$) is critical. Current industrial catalysts for the WGS (mixtures of Fe-Cr or Zn-Al-Cu oxides) are pyrophoric and normally require lengthy and complex activation steps before usage (*3*). Au-CeO_2 and Au-TiO_2 nanomaterials have recently been reported to be very efficient catalysts for the WGS (*3*–*5*). This is remarkable because neither bulk Au (*6*) nor bulk ceria and titania are known as WGS catalysts (*3*, *4*).

The nature of the active phase(s) in these metal/oxide nanocatalysts and the WGS reaction mechanism are still unclear. For example, the as-prepared Au-CeO_2 catalysts contain nanoparticles of pure gold and gold oxides (AuO_x) dispersed on a nanoceria support. Each of these gold species could be in the active phase (*3*–*5*), and the ceria support may not be a simple spectator in these systems (*7*). Although pure ceria is a very poor WGS catalyst, the properties of this oxide were found to be crucial for the observed activity of the Au-CeO_2 nanocatalysts (*4*, *6*, *8*). Several studies dealing with metal/oxide powder catalysts and the WGS reaction indicate that the oxide plays a direct role in the reaction (*3*, *4*, *9*, *10*), but because of the complex nature of these systems, there is no agreement on its role. Thus, we performed a series of experiments to test the chemical and catalytic properties of CeO_2 and TiO_2 nanoparticles (NPs) dispersed on a Au(111) template, as inverse model catalysts. Results of density-functional calculations point to a very high barrier for the dissociation of H_2O on Au(111) or Au(100) (*11*), which leads to negligible activity for the WGS process. Even gold NPs cannot dissociate water and catalyze the WGS reaction (*11*).

Part of the experiments described below were carried out in ultrahigh-vacuum (UHV) chambers that have attached a batch reactor (*12*) or have capabilities for scanning tunneling microscopy (STM) (*13*). High-resolution x-ray photoelectron spectroscopy (XPS) spectra, probing only the near-surface region in the oxide/gold systems (*5*, *14*), were acquired at the U7A beamline of the National Synchrotron Light Source. To prepare the TiO_2/Au(111) surfaces, Ti atoms were vapor deposited on a gold substrate covered with NO_2 at 100 K (*15*). The temperature was then raised to 700 K and the $TiNO_x$ particles were transformed into TiO_2. STM images indicated that this methodology produces flat NPs of TiO_2 exhibiting a combination of rutile and anatase phases (*15*). The NPs of ceria were prepared according to two different procedures. In the first one, labeled CeO_2-I here, alloys of $CeAu_x$/Au(111) were exposed to O_2 ($\sim 5 \times 10^{-7}$ torr) at 500 to 700 K for 5 to 10 min (*13*, *14*). The CeO_2 NPs grew dispersed on the herringbone structure of Au(111) (Fig. 1A) and had a rough three-dimensional structure that did not exhibit any particular face of ceria (Fig. 1B). In the second procedure, labeled CeO_2-II here, Ce was vapor deposited onto Au(111) under an atmosphere of O_2 ($\sim 5 \times 10^{-7}$ torr) at 550 K and then heated to 700 K. In these cases, the CeO_2 NPs grew preferentially at the steps between the terraces in the Au(111) substrate (Fig. 1C) and displayed regions with a CeO_2(111) orientation. When there was a deficiency of oxygen, groups or clusters of O vacancies were seen in STM images (Fig. 1D). This result is similar to that found for bulk CeO_{2-x}(111) (*16*). High-resolution XPS showed that Au atoms do not incorporate into the ceria lattice (*14*). Gold 4f spectra taken at photon energies of 240 to 380 eV, probing only two to three layers near the surface, showed the absence of the features expected for Au cations incorporated into ceria (*5*).

In Fig. 2, the WGS activity of a series of TiO_2/Au(111), CeO_2-I/Au(111), and CeO_2-II/Au(111) surfaces is shown. The fraction of the Au(111) substrate covered by the TiO_2 or CeO_2 particles was determined by means of ion-scattering spectroscopy (*5*, *7*). In the kinetics measurements, the sample was transferred from the

[1]Chemistry Department, Brookhaven National Laboratory, Upton, NY 11973, USA. [2]Center for Functional Nanomaterials, Brookhaven National Laboratory, Upton, NY 11973, USA. [3]Facultad de Ciencias, Universidad Central de Venezuela, Caracas, 1020-A Venezuela.

*To whom correspondence should be addressed. E-mail: rodrigez@bnl.gov

UHV chamber to the batch reactor at ~300 K, then the reactant gases were introduced (20 torr of CO and 10 torr of H_2O) and the sample was rapidly heated to the reaction temperature (575 K). Product yields were analyzed by a gas chromatograph (*17*). The amount of product was normalized by the active area exposed by the front of the sample. The sample holder was passivated by extensive sulfur poisoning (exposure to H_2S) and had no catalytic activity (*6*). XPS spectra showed that there was no migration of S from the sample holder to the oxide/gold surfaces. The values reported in Fig. 2 were acquired after 5 min of reaction. In our batch reactor, a steady-state regime for the production of H_2 and CO_2 was reached after 1 to 2 min of reaction time. The kinetics experiments were done in the limit of low conversion (<5%).

The data in Fig. 2 show a substantial increase in catalytic activity at small coverages of CeO_2 and TiO_2. Although clean Au(111) is not catalytically active, gold surfaces that are 20 to 30% covered by the oxide NPs had activities per unit geometric area similar to or larger than those of Cu(111) or Cu(100) under similar conditions (*6*, *17*), noting that Cu is the best known metal catalyst for the WGS (*11*, *17*, *18*).

In Fig. 2, the catalytic activity of the surface reaches a maximum, then decreases and disappears once there is no Au exposed and multilayers of ceria or titania cover the metal substrate (*13*–*15*). As we discuss below, small oxide NPs exhibit the highest chemical reactivity toward CO and H_2O. In general, the effects of ceria on the catalytic activity are greater than those of titania, with TiO_2/Au(111) being as active as Cu(100). In Fig. 2, we compare the relative WGS activities of the CeO_2-I/Au(111) and CeO_2-II/Au(111) surfaces. The procedure followed to prepare the CeO_2-I/Au(111) surfaces yielded a greater dispersion for the oxide NPs on the gold template (compare Fig. 1, A and C), and the NPs had a more disordered structure (compare Fig. 1, B and D). These morphological differences could account for a superior catalytic activity for the CeO_2-I/Au(111) systems.

After collecting the kinetics data, the gases were pumped out from the reaction cell and the surfaces were characterized with XPS, which showed adsorbed CO_x groups with a C 1s binding energy of 289.6 to 289.9 eV. This binding energy matches well those found for formate (HCOO) and carbonate (CO_3) groups bonded to oxides (*19*, *20*). The XPS data also indicated a lack of oxidation of the Au substrate. The catalysts exhibited Au 4f spectra that were practically identical to those of Au(111) and very different from those expected for AuO_x species or Au incorporated into the ceria lattice (*4*, *5*). The lack of oxidation of the Au substrate seen in the XPS data are consistent with in situ measurements of near-edge x-ray absorption spectroscopy for high–surface area catalysts (*3*, *5*), which show that $Au^{\delta+}$ species are not stable under typical WGS conditions.

For the surfaces that have the highest activity in Fig. 2 (the fraction of Au covered < 30%), the Ce 3d and Ti 2p core-level XPS spectra showed a significant reduction of the oxides upon exposure of CeO_2/Au(111) and TiO_2/Au(111) to the reactants of the WGS. After curve-fitting (*7*, *14*) the corresponding Ce 3d and Ti 2p spectra, we found that 14 to 17% of the O atoms in the CeO_2 and TiO_2 NPs were removed to produce partially reduced ceria and titania. The degree of reduction of the CeO_2 and TiO_2 NPs substantially decreased when the fraction of gold covered by the oxide increased above 35%. As an example, we show in Fig. 3 the percentage of O vacancies in ceria after performing the WGS on the CeO_2-I/Au(111) catalysts: The systems with a high catalytic activity also have a significant concentration of O vacancies and associated Ce^{3+} cations.

The high catalytic activity for low coverages of ceria and titania can be attributed to special chemical properties of the oxide NPs and cooperative effects at oxide-metal interfaces. However, it is very difficult to quantify the number of active sites in the oxide/gold catalysts of Figs. 1 and 2. The reaction likely involves O vacancies that are near oxide-gold interfaces. Because O vacancies tend to form groups or ensembles (Fig. 1D) (*16*, *21*), uncovering in this way the metal substrate, oxide-gold interfaces can exist within the oxide NPs. We estimate that the best catalysts in Fig. 2 have a turnover frequency (TOF) that is 40 to 50 times as large as that of Cu(100) (*22*).

Using density-functional theory (DFT) (*11*, *23*, *24*), we investigated the WGS reaction on Au(100) or Au(111), a free Ti_2O_4 cluster [see structure in (*25*)], a free TiO_2 single chain, and over a model TiO_2/Au(111) catalyst that contains chains of TiO_2 over the gold substrate in a (3 × 1) array (Fig. 4). This model catalyst exposes not fully coordinated Ti centers, as expected for a TiO_2 NP, and allows the study of the oxide-metal interface. A very high barrier for the dissociation of water on Au(111) or Au(100) was seen (Fig. 4), but once OH formed, subsequent steps for the WGS process occurred readily on the gold substrate.

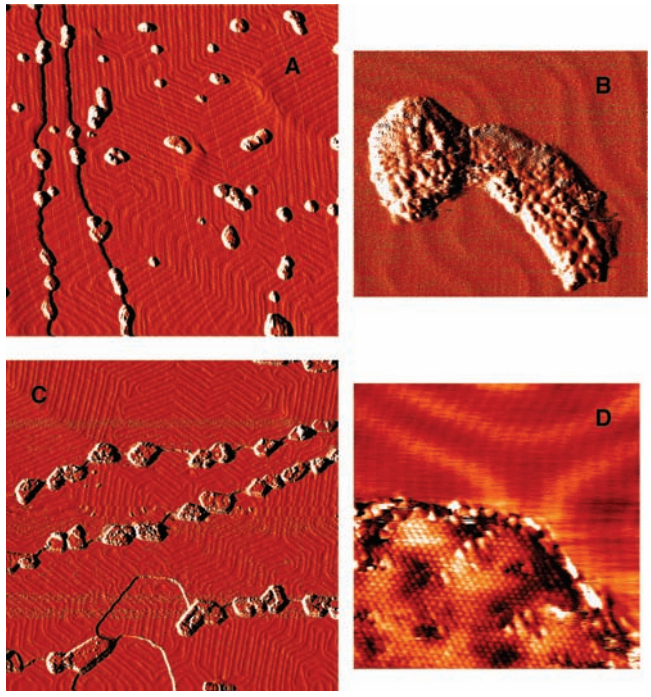

Fig. 1. (**A**) STM image taken after oxidizing a Ce-Au(111) alloy in O_2 at 550 K and subsequent annealing to 690 K. Size: 200 nm by 200 nm; imaging parameters: −1.970 V and 0.03182 nA. (**B**) STM image also taken after oxidizing a Ce-Au(111) alloy in O_2. Size: 30 nm × 25 nm; imaging parameters: −1.709 V and 0.02761 nA. (**C**) STM image acquired after depositing Ce in an atmosphere of 1.5×10^{-7} torr of O_2 at 550 K followed by annealing to 700 K. Size: 200 nm by 200 nm; imaging parameters: 2.463 V and 0.02597 nA. (**D**) STM image also recorded after depositing Ce in an atmosphere of 1.5×10^{-7} torr of O_2 at 550 K followed by annealing to 700 K. Size: 15 nm by 15 nm; imaging parameters: 0.806 V and 0.04404 nA

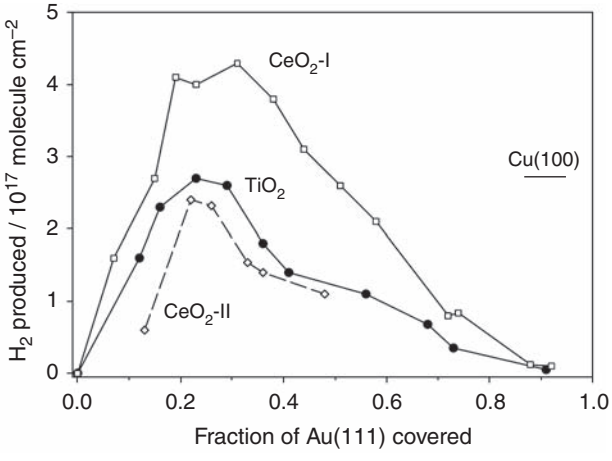

Fig. 2. Production of hydrogen during the WGS reaction on a Au(111) surface partially covered with ceria or titania. The ceria NPs were prepared according to two different methodologies denoted as CeO_2-I and CeO_2-II (see text). Each surface was exposed to a mixture of 20 torr of CO and 10 torr of H_2O at 573 K for 5 min.

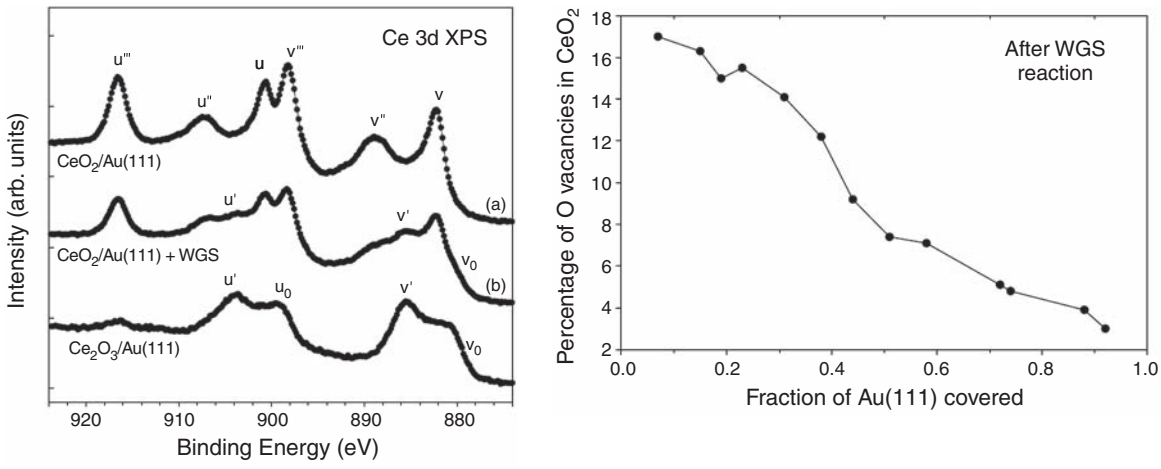

Fig. 3. (**Left**) Ce 3d XPS spectra taken before (trace a) and after (trace b) exposing a CeO_2-I/Au(111) surface to the WGS reaction. The fraction of the Au surface covered by ceria was ~30%. For comparison, we show the corresponding spectrum for a Ce_2O_3/Au(111) system. (**Right**) Percentage of O vacancies in the CeO_2-I/Au(111) catalysts after the WGS reaction (20 torr of CO, 10 torr of H_2O at 573 K for 5 min). The amount of oxygen removed from the ceria was calculated by curve-fitting (*5*, *7*, *14*) the corresponding Ce 3d spectra and obtaining the ratio of Ce^{3+}/Ce^{4+} cations.

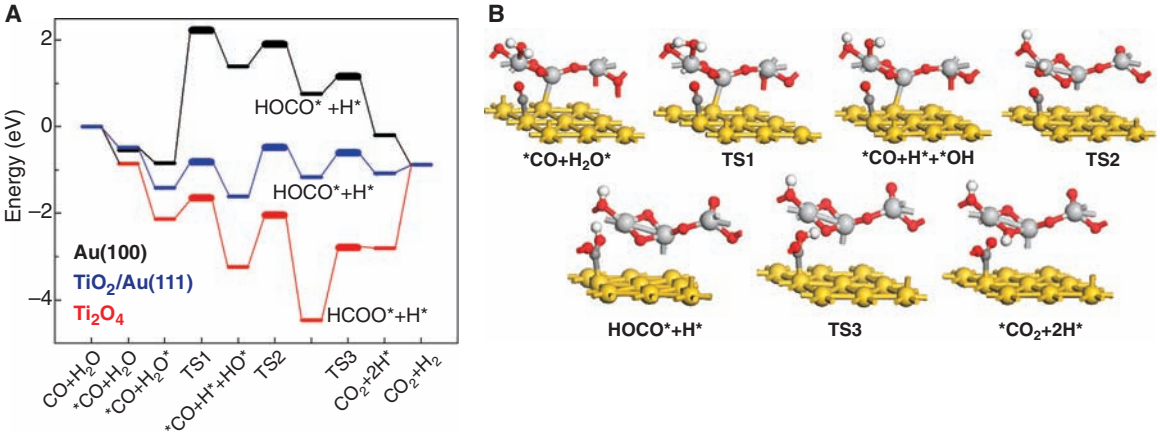

Fig. 4. (**A**) Calculated reaction profile for the WGS on Au(100), a free Ti_2O_4 cluster, and TiO_2/Au(111) model catalysts. Transitions states are denoted as TS1, TS2, and TS3. (**B**) Optimized structures for the different steps of the WGS on TiO_2/Au(111). Large yellow spheres, Au; large gray spheres, Ti; small red spheres, O; small white spheres, H; small dark gray spheres, C. Adsorbed species are denoted by asterisks (*).

Indeed, experimental studies show that CO adsorbs and is chemically active on gold surfaces first covered with oxygen or other chemical species (*26*, *27*). On a free Ti_2O_4 cluster or on a nonsupported TiO_2 single chain, the dissociation of water is not difficult, and is even easier than on Cu(100) (Fig. 4), but the reaction of the formed OH with CO leads to the formation of a stable formate species that prevents the production of H_2 and CO_2.

The DFT calculations for the model TiO_2/Au(111) catalyst show a system that can readily perform the WGS process (Fig. 4). The reaction pathway with the minimum-energy barriers involves the following steps:

$$CO_{gas} \rightarrow CO_{ads} \quad (1)$$

$$H_2O_{gas} \rightarrow H_2O_{ads} \quad (2)$$

$$H_2O_{ads} \rightarrow OH_{ads} + H_{ads} \quad (3)$$

$$CO_{ads} + OH_{ads} \rightarrow HOCO_{ads} \quad (4)$$

$$HOCO_{ads} \rightarrow CO_{2,gas} + H_{ads} \quad (5)$$

$$2H_{ads} \rightarrow H_{2,gas} \quad (6)$$

The adsorption and dissociation of water take place on the oxide, whereas CO adsorbs on sites of the gold substrate located nearby (bifunctional catalyst). All of the subsequent steps occur at an oxide-metal interface. The DF calculations show that the activation energy for the dissociation of water on TiO_2/Au(111), ~0.6 eV, is also much smaller than on Cu(100), ~1.1 eV (*11*), so TiO_2/Au(111) should be a better WGS catalyst than Au(100) and Cu(100), as found above. The intermediate that precedes the formation of CO_2 and H_2 in the WGS process is a HOCO species. CO_x species were observed experimentally on the surface of the catalysts after the WGS, and they could be simple spectators when strongly bound to the oxide nanoparticles.

Our results imply that the high performance of Au-CeO_2 and Au-TiO_2 catalysts in the WGS (*4*, *6*) relies heavily on the direct participation of the oxide-metal interface in the catalytic process. The oxide helps in the dissociation of water, a reaction that extended surfaces and NPs of gold cannot perform (*11*). Experiments in our laboratories have verified that TiO_{2-x}/Au(111) and CeO_{2-x}/Au(111) easily dissociate water, and no decomposition of this adsorbate is seen when no O vacancies exist in the oxide nanoparticles (*14*). Exposure of small coverages of TiO_2 and CeO_2 to CO at 575 K leads to the appearance of O vacancies in the oxide NPs, and these systems become active for the dissociation of water. For the WGS, it is critical that the properties of the oxide facilitate H_2O dissociation, and we have found that this is the case for NPs of CeO_{2-x}, TiO_{2-x}, MoO_{3-x}, and ZnO_{1-x}.

Previous studies indicate that overlayers of Au can be catalytically active for the oxidation of CO, if they are nanosized in one dimension or interact strongly with an oxide support (*28*). In contrast, the situation for the WGS on TiO_{2-x}/Au(111) and CeO_{2-x}/Au(111) takes advantage of the moderate chemical activity of bulk gold by coupling it to that of a more reactive oxide material.

References and Notes

1. J. J. Spivey, *Catal. Today* **100**, 171 (2005).
2. D. J. Suh, C. Kwak, J. H. Kim, S. Kwon, T. J. Park, *J. Power Sources* **142**, 70 (2005).
3. R. Burch, *Phys. Chem. Chem. Phys.* **8**, 5483 (2006).
4. Q. Fu, H. Saltsburg, M. Flytzani-Stephanopoulos, *Science* **301**, 935 (2003).
5. X. Wang, J.A. Rodriguez, J.C. Hanson, M. Perez, J. Evans, *J. Chem. Phys.* **123**, 221 101 (2005).
6. J. A. Rodriguez, P. Liu, J. Hrbek, J. Evans, M. Perez, *Angew. Chem. Int. Ed.* **46**, 1329 (2007).
7. J. A. Rodriguez, M. Pérez, J. Evans, G. Liu, J. Hrbek, *J. Chem. Phys.* **122**, 241101 (2005).
8. Q. Fu, W. Deng, H. Saltsburg, M. Flytzani-Stephanopoulos, *Appl. Catal. B: Environ.* **56**, 57 (2005).
9. S. Ricote *et al.*, *Appl. Catal. Gen.* **303**, 35 (2006).
10. T. Bunluesin, R. J. Gorte, G. W. Graham, *Appl. Catal. Environ.* **15**, 107 (1998).
11. P. Liu, J. A. Rodriguez, *J. Chem. Phys.* **126**, 164705 (2007).

12. The sample could be transferred between the reactor and UHV chamber without exposure to air (*5*, *6*). The UHV chamber (base pressure ~ 1×10^{-10} torr) was equipped with instrumentation for XPS, low-energy electron diffraction, ion-scattering spectroscopy, and thermal-desorption mass spectroscopy.
13. S. Ma, X. Zhao, J. A. Rodriguez, J. Hrbek, *J. Phys. Chem. C* **111**, 3685 (2007).
14. X. Zhao, S. Ma, J. Hrbek, J. A. Rodriguez, *Surf. Sci.* **601**, 2445 (2007).
15. Z. Song, J. Hrbek, R. Osgood, *Nano Lett.* **5**, 1327 (2005).
16. F. Esch *et al.*, *Science* **309**, 752 (2005).
17. J. Nakamura, J. M. Campbell, C. T. Campbell, *J. Chem. Soc. Faraday Trans.* **86**, 2725 (1990).
18. C. V. Ovesen, P. Stoltze, J. K. Nørskov, C. T. Campbell, *J. Catal.* **134**, 445 (1992).
19. J. Zhou, D. R. Mullins, *Surf. Sci.* **600**, 1540 (2006).
20. C. T. Au, W. Hirsch, W. Hirschwald, *Surf. Sci.* **197**, 391 (1988).
21. O. Dulub *et al.*, *Science* **317**, 1052 (2007).
22. To estimate the TOF of CeO_{2-x}/Au(111) surfaces, we took into account the area covered by the oxide NPs and the concentration of O vacancies. It was assumed that all the atoms of a flat Cu(100) surface are active in the WGS reaction. This is a common assumption (*17*, *18*).
23. The unrestricted DF calculations were performed with the DMol3 code, treating molecules, nanostructures, and extended surfaces with the same level of accuracy (*11*, *24*). Au(100), Au(111), and TiO_2/Au(111) were modeled by means of the supercell approach with three-layer gold slabs and an 11 Å vacuum between the slabs (*11*). The top layer of the Au substrate, the oxide nanostructures, and the adsorbates were allowed to fully relax.
24. B. Delley, *J. Chem. Phys.* **92,** 508 (1990); **113,** 7756 (1992).
25. T. Albaret, F. Finocchi, C. Noguera, *Faraday Discuss.* **114**, 285 (1999).
26. V. A. Bondzie, S. C. Parker, C. T. Campbell, *Catal. Lett.* **63**, 143 (1999).
27. B. K. Min, C. M. Friend, *Chem. Rev.* **107**, 2709 (2007).
28. M. S. Chen, D. W. Goodman, *Science* **306**, 252 (2004).
29. N. C. Hernández, J. F. Sanz, J. A. Rodriguez, *J. Am. Chem. Soc.* **128**, 15600 (2006).
29. The work performed at Brookhaven National Laboratory was supported by the U.S. Department of Energy, Office of Basic Energy Sciences, under contract DE-AC02-98CH10886. J.E. and M.P. are grateful to Intevep for partial support of the work carried out at the Universidad Central de Venezuela.

4 September 2007; accepted 22 October 2007
10.1126/science.1150038

Accretion of Mudstone Beds from Migrating Floccule Ripples

Juergen Schieber,[1]* John Southard,[2] Kevin Thaisen[1]

Mudstones make up the majority of the geological record. However, it is difficult to reconstruct the complex processes of mud deposition in the laboratory, such as the clumping of particles into floccules. Using flume experiments, we have investigated the bedload transport and deposition of clay floccules and find that this occurs at flow velocities that transport and deposit sand. Deposition-prone floccules form over a wide range of experimental conditions, which suggests an underlying universal process. Floccule ripples develop into low-angle foresets and mud beds that appear laminated after postdepositional compaction, but the layers retain signs of floccule ripple bedding that would be detectable in the rock record. Because mudstones were long thought to record low-energy conditions of offshore and deeper water environments, our results call for reevaluation of published interpretations of ancient mudstone successions and derived paleoceanographic conditions.

A century ago, Henry Clifton Sorby, one of the pioneers of geology, pointed to the study of muds as one of the most challenging topics in sedimentary geology (*1*). Today, with our knowledge clearly expanded, muddy sediments are still considered highly complex systems that may require as many as 32 variables and parameters for a satisfactory physicochemical characterization (*2*). More research may clarify interdependencies between a number of these parameters and may allow us to consider a smaller number of variables, but the fundamental complexity of muddy sediments is likely to remain. A key issue in mudstone sedimentation is flocculation, a phenomenon in which a number of these parameters, such as settling velocity, floccule size, grain-size distribution, ion exchange behavior, and organic content "come together." A joining of smaller particles to form larger aggregates, flocculation enhances the deposition rate of fine-grained sediments, and its understanding is critical for modeling the behavior of mud in sedimentary environments.

Flocculation is affected by particle concentration within the fluid and intensity of turbulence (*3*, *4*). Over time, floccules enlarge to a maximum equilibrium diameter that is related to the intensity of turbulence (*5*). Floccule deposition is influenced by turbulence, bed shear stress, sediment concentration, and settling velocity. We currently still miss critical data on floccule formation and on the influence of floccule structure and turbulence on the formation of muddy sediments (*6*). We will collect data concerning these issues with new instrumentation in the near future, although the importance of our observations will not be affected. The notion is widely held that slow-moving currents or still water are a prerequisite for substantial mud deposition (*7*, *8*) because shear stress in swift-moving currents disrupts previously formed fragile floccules and prevents their deposition, but our observations suggest an alternative mode of mud deposition that apparently left its imprint in the rock record.

Mudstones constitute up to two-thirds of the sedimentary record and are arguably the most poorly understood type of sedimentary rocks (*9*). Mudstone successions contain a wealth of sedimentary features that provide information about depositional conditions and sedimentary history (*10*–*13*), but presently we lack the information that would allow us to link features observed in the rock record to measurable sets of physical variables in modern environments.

Although various small-scale sedimentary structures have been described from modern muds, these have not been observed in the making. This forces us to infer controlling parameters (e.g., current velocity and density of suspension) from temporally and spatially very limited measurements in the overlying water column (*14*–*17*). Such measurements (e.g., flow velocity, sediment concentration) in modern environments are commonly considered representative of depositional conditions for the uppermost millimeters to decimeters of the accumulating deposits. However, upon close examination, modern sediments show considerable heterogeneity at the millimeter to centimeter scale (*16*), an indication that what we observe in surficial sediments is not a direct response to measured conditions in the overlying water column. To improve on this situation, it is essential to conduct experiments that replicate natural conditions and to compare the experimental sediments to the rock record.

Here, we report experimental insights into the sedimentology of mudstones. In past experimental studies, centrifugal pumps were used to recirculate mud suspensions (*18*–*20*), destroying the clay floccules that are of such key importance in mud transport and deposition. Therefore, to minimize the risk of shredding clay floccules once formed, we built a racetrack flume that uses a paddle belt (*21*) for moving the mud suspension.

The racetrack flume (fig. S1) used for these experiments (*21*) has a 25-cm-wide channel. The effective flow depth was 5 cm. Powdered kaolinite clay (Fig. 1A) was mixed with water and added into the flume, running at 50 cm/s velocity (*21*). Sediment concentrations ranging from 0.03 g/l to 2 g/l were explored, and suspended sediment concentrations were monitored with an optical turbidity sensor. Experiments were conducted in distilled water, fresh (tap) water, and salt water (35 per mil salinity). In a few experiments, Ca-montmorillonite and natural lake mud (sieved to 63 μm) was used.

Addition of clay to the flume resulted within minutes in the formation of "floccule streamers" that mark boundary-layer streaks (*22*). Floccules range in size from 0.1 mm to almost 1 mm (Fig. 1, B to D) and were sampled and examined with a scanning electron microscope (SEM). After establishment of a stable suspended clay concentration, the velocity was stepwise reduced (Fig. 2) until the critical velocity of sedimentation was reached (*23*). At that point, a linear decline of sediment concen-

[1]Department of Geological Sciences, Indiana University, Bloomington, IN 47405, USA. [2]Department of Earth and Planetary Sciences, Massachusetts Institute of Technology, Cambridge, MA 02139, USA.

*To whom correspondence should be addressed. E-mail: jschiebe@indiana.edu

tration was observed and essentially all sediment settled out of the flow (Fig. 2). By shining strong lights from above through the flow, we were able to photograph and film floccule streamers (Fig. 3A), individual migrating floccules, floccule ripples (Fig. 3B), and fields of floccule ripples (Fig. 3C).

Floccules that give rise to "floccule streamers" (Fig. 3A) form even at small sediment concentrations (0.03 g/l), in both distilled water and fresh water, and increase in abundance as velocity is lowered. Below the critical velocity of sedimentation (Fig. 2), patches of floccules form and organize into streamlined ripples that migrate slowly downcurrent (Fig. 3, B to D). The critical velocity for sedimentation depends on initial sediment concentrations and ranges from ~10 cm/s for small sediment concentrations (0.03 g/l) to at least 26 cm/s for sediment concentrations in the 1 to 2 g/l range. In several experiments where flow was stopped suddenly and water was drained and replaced with clear water, floccules were observed on the foreset slopes of floccule ripples (Fig. 3E).

We also conducted experiments in which we introduced multiple sediment pulses and allowed the clay to accumulate at the bottom before adding the next pulse (*21*). A small amount of pulverized hematite (a red powder) was added between clay pulses to mark the tops of successive clay pulses. This addition of clay increments and hematite spikes was repeated until a sediment layer of approximately 2 cm (uncompacted thickness) had accumulated. At the end of the flume run, draining of the water typically revealed that the mud bed carried at its surface elongated ripples that stood up to 3 cm above the flume bottom and were spaced between 30 and 40 cm apart in the downstream direction (Fig. 3D and fig. S2). These experimental mud layers were air-dried to the consistency of soft butter and scraped with a butter knife or spatula to reveal internal layering outlined by hematite drapes. These internal layers were inclined in the downcurrent direction (fig. S3), indicating lateral accretion of clays. Once the clay beds have dried completely, these internal laminae appear to layer parallel on surfaces perpendicular to bedding (Fig. 4A). Drying out, however, also leads to separation of the top portions of layers along bottom-parallel fractures and reveals that the overall deposit is characterized by low-angle, downcurrent-dipping cross-strata (Fig. 4B).

These observations show that ripples composed of clay floccules migrated over the flume bottom at the onset of deposition (Fig. 3) and that a rippled bed topography was present at the end of deposition (fig. S2). In addition, the texture produced by the low-angle, downcurrent-dipping cross-strata in Fig. 4B has a direct textural analog in sandstones, where it is known as "rib and furrow" structure (*24*). The latter is seen on horizontal surfaces cut through sandstone beds that accumulated from migrating ripples. Closer inspection of the surface exposed in Fig. 4B shows the deposits of multiple overriding floccule ripples (fig. S4). Under the microscope, the inclined clay laminae from Fig. 4B show a "bumpy" surface pattern of closely packed ovoid bodies (0.2 to 0.6 mm in size) (fig. S5), the compacted floccules from which the migrating ripples and the accreting clay bed were constructed.

It appears that irrespective of what drives flocculation in a given experiment, flocculation provides deposition-prone particles without fail over a wide range of experimental conditions. Formation of floccule ripples from a variety of clay-size materials (kaolinite, montmorillonite, and lake mud), and over a range of sediment concentrations and salinities (distilled, fresh, and salt water) strongly suggests a universal process at work.

Our observations do not support the notion that muds can only be deposited in quiet environments with only intermittent weak currents (*8*). Instead, bedload transport of flocculated mud and deposition occurs at current velocities that would also transport and deposit sand (*21*). Clay beds can accrete from migrating floccule ripples under swiftly moving currents in the 10 cm/s to 26 cm/s velocity range, a range likely to expand as flows with larger sediment concentrations are explored. Whereas the clay beds formed in our experiments consist of downcurrent-inclined laminae, they appear to be parallel-laminated once fully compacted (Fig. 4A). Because floccule ripples are spaced 30 to 40 cm apart, ancient sediments of this origin are likely to appear parallel-laminated (Fig. 4C) as well. Detection of ripple-accreted muds in the rock record will require carefully defined, and yet to be developed, criteria. Things to look for might be subtle nonparallel lamina geometry, as well as basal downlap and top truncation of laminae. Examination of ancient shale units may, for example, yield low-amplitude bedforms (Fig. 4, D and E) as indicators of lateral accretion and ripple migration. Bedding-oblique orientation of larger flat particles, such as spores, microfossils, plant debris, and mica flakes, could be another indicator. If such particles are deposited on the inclined foresets of floccule ripples, they may record the gentle inclination of the latter even when compaction has rendered the depositional fabric of inclined laminae (Fig. 4B) unrecognizable.

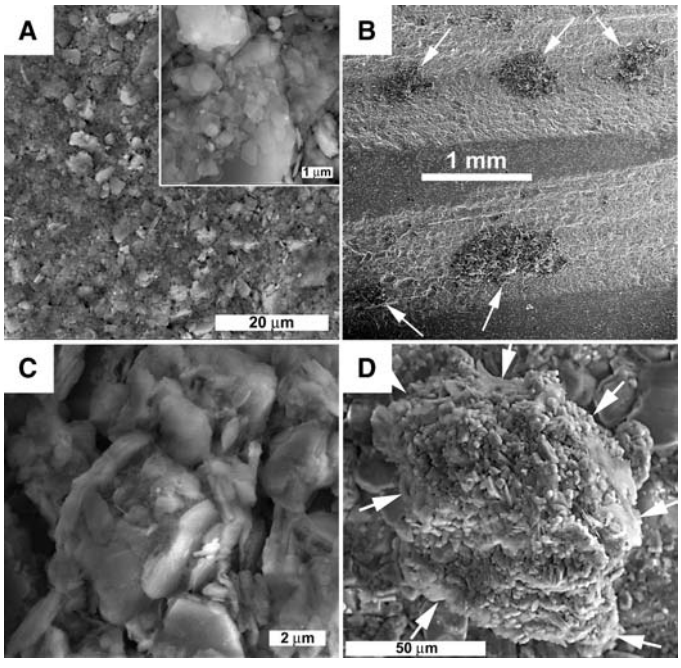

Fig. 1. Flume feed and floccules. (**A**) SEM image of typical kaolinite clay used in the majority of experiments. Inset shows size and morphology of clay flakes. (**B**) SEM image of floccules (pointed out by arrows) that were trapped at the flume bottom with a grooved glass slide. (**C**) Close-up of floccules in (B). (**D**) SEM image of a floccule (outline marked with white arrows). This floccule measures 0.12 mm along the long axis.

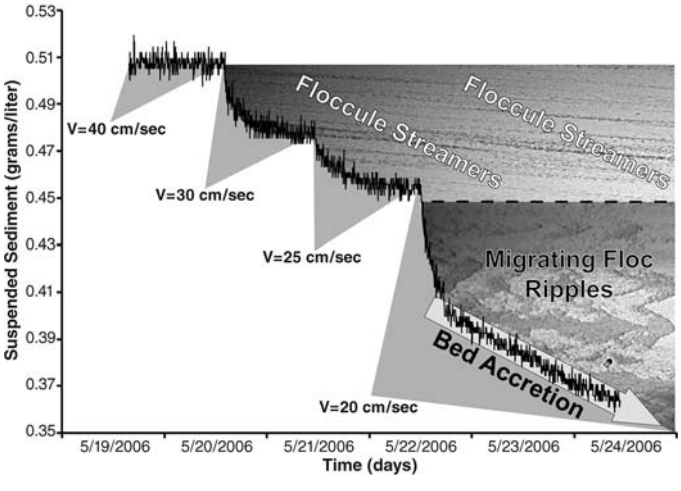

Fig. 2. Example of changes in suspended sediment in the course of an experiment. Vertical axis shows continuously logged suspended sediment concentration, and horizontal axis shows time elapsed (tick marks separate successive days). The critical velocity of sedimentation lies between 25 cm/s and 20 cm/s and coincides with the onset of development of floccule ripples. Its exact determination requires the use of smaller velocity steps.

In the course of two decades of detailed studies of shales and mudstones, one of us (*25*–*27*) has seen comparable low-amplitude bedforms (Fig. 4D) in shale units that were deposited in a wide variety of environments. Examples can be found in the Mid-Proterozoic Belt Supergroup, the Devonian of the eastern United States, the Jurassic Posidonia Shale, the Cretaceous Mancos Shale, and the Eocene Green River Formation. This suggests that mud accretion from migrating floccule ripples probably occurred throughout geologic history. Many ancient shale units, once examined carefully, may thus reveal that they accumulated in the manner illustrated here, rather than having largely settled from slow-moving or still suspensions. This, in turn, will most likely necessitate the reevaluation of the sedimentary history of large portions of the geologic record.

Elucidating the mechanisms of mudstone deposition not only helps to better understand the rock record but also benefits hydrocarbon exploration, hydrogeology, and coastal and shelf engineering. Managing mud is important for the maintenance of harbors, shipping lanes, and water reservoirs, especially given the impact of climate change. How mudstones act as barriers to fluid migration (oil and water) is probably linked to depositional processes that affect mud microfabrics. For example, if a mud accumulated from current-transported floccules, one might expect a network of larger pores, poorer sealing capacity, and easier release of liquid and gaseous hydrocarbons. Conversely, accumulation in still water from dispersed clays and low-density floccules should lower permeability and may produce an oil shale that clings tightly to its generated hydrocarbons. These qualities are also critical for the ability of a mudstone unit to protect aquifers from contamination and to compartmentalize groundwater reservoirs.

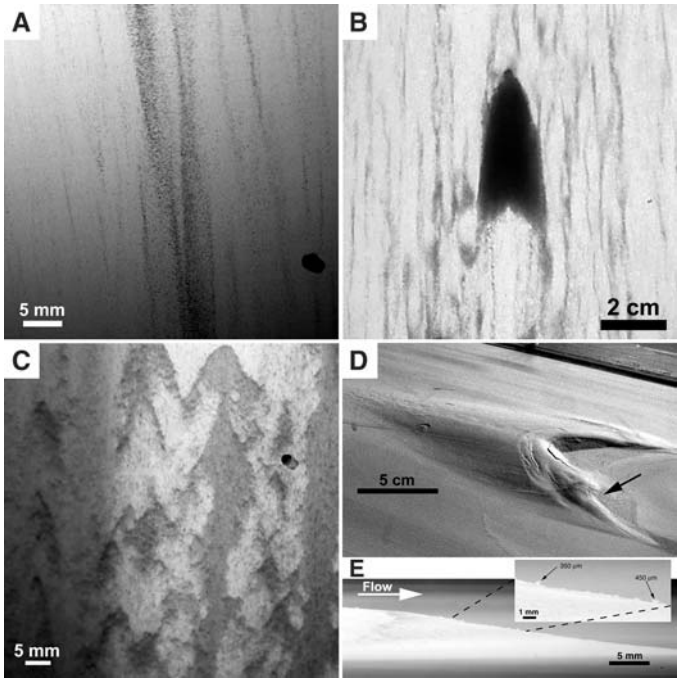

Fig. 3. (**A**) Floccule streamers photographed through the flume bottom (flow velocity 48 cm/s, initial sediment concentration 0.72 g/liter, lake mud in tap water). (**B**) Streamlined floccule ripple and floccule streamers. (**C**) Multiple floccule ripples begin to coalesce. Flow is from top to bottom in images (A), (B), and (C). (**D**) Oblique view of large barchan-shaped migrating floccule ripple. Flow is toward the right. (**E**) Side view of the left horn of this ripple [pointed out by black arrow in (D)]. Inset shows that the surface is covered with small, round bodies, the clay floccules that moved across the ripple during current activity. Numbers indicate floccule size.

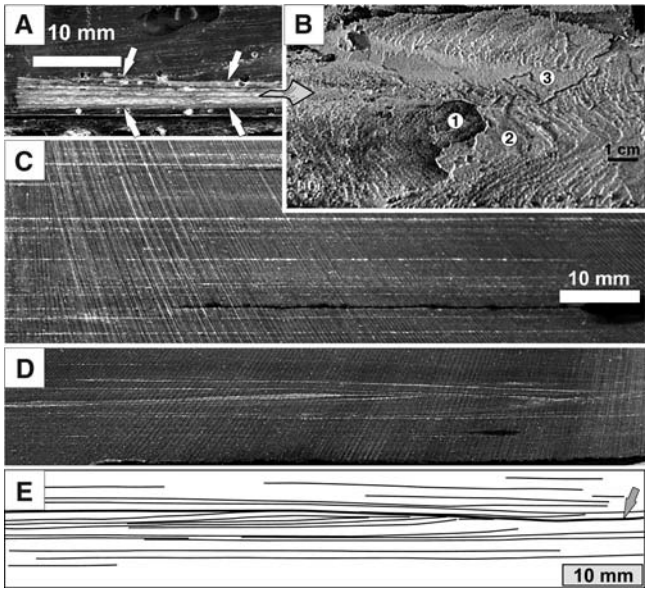

Fig. 4. (**A**) Laminated flume sediment (between white arrows) that was deposited during an experiment with continuous current flow. Sample was embedded in epoxy and cut perpendicular to bedding. Sample is curved due to desiccation. The darker internal laminae are hematite markers. (**B**) Textural detail from the interior of the clay layer in (A) (top view, arrow indicates 90° twist). As the layer dried out, its upper portion formed concave desiccation polygons, whereas its lower portion remained attached to the flume bottom. Removing the upper portion exposes a bottom-parallel surface through the clay layer. The curved lines are the upper terminations of broken foreset laminae of floccule ripples. The foreset laminae are inclined to the right, and the circled numbers indicate a succession of overriding ripples (see also fig. S4). The overall texture resembles "rib and furrow" structures as known from current rippled sandstones (*24*). (**C**) Parallel-laminated black shale, New Albany Shale, Devonian, Indiana. Lighter laminae are silt-enriched. (**D**) Cross-laminated shale collected from the same core box as (C). (**E**) Tracing of silt laminae visible in (D). Arrow marks an internal erosion surface. In the center are inclined (to the left) truncated laminae, forming the outline of a compacted and mud-dominated ripple. The synoptic relief of this ripple is 3 mm, but its original relief would have been ~20 mm (assuming 85% water content), the same magnitude as observed in our experiments.

References and Notes

1. H. C. Sorby, *Q. Geol. Soc. London* **64**, 171 (1908).
2. J. Berlamont, M. Ockenden, E. Toorman, J. Winterwerp, *Coast. Eng.* **21**, 105 (1993).
3. H. A. Einstein, R. B. Krone, *Proc. J. Hydr. Div.* **H12**, 51 (1961).
4. I. N. McCave, in *Fine-Grained Sediments: Deep Sea Processes and Facies*, D. A. V. Stow, D. J. W. Piper, Eds. (Geological Society of London, London, 1984), pp. 35–69.
5. E. Parthenaides, *Proc. J. Hydraulics Div.* **91**, 105 (1965).
6. J. C. Winterwerp, C. Kranenburg, *Fine Sediment Dynamics in the Marine Environment, Proceedings in Marine Science 5* (Elsevier, Amsterdam, 2002).
7. P. E. Potter, J. B. Maynard, W. A. Pryor, *Sedimentology of Shale* (Springer Verlag, New York, 1980).
8. P. E. Potter, J. B. Maynard, P. J. Depetris, *Mud and Mudstones: Introduction and Overview* (Springer, New York, 2005).
9. J. Schieber, in *Shales and Mudstones (vol. 1): Basin Studies, Sedimentology and Paleontology*, J. Schieber, W. Zimmerle, P. Sethi, Eds. (Schweizerbart'sche Verlagsbuchhandlung, Stuttgart, 1998), pp. 131–146.
10. N. R. O'Brien, R. M. Slatt, *Argillaceous Rock Atlas* (Springer Verlag, New York, 1990).
11. J. Schieber, *Sedimentology* **33**, 521 (1986).
12. J. Schieber, *Sedimentology* **36**, 203 (1989).
13. J. Schieber, in *Shales and Mudstones (vol. 1): Basin Studies, Sedimentology and Paleontology*, J. Schieber, W. Zimmerle, P. Sethi, Eds. (Schweizerbart'sche Verlagsbuchhandlung, Stuttgart, 1998), pp. 187–215.
14. S. A. Kuehl, C. A. Nittrouer, D. J. DeMaster, *Cont. Shelf Res.* **6**, 311 (1986).
15. S. A. Kuehl, C. A. Nittrouer, D. J. DeMaster, *J. Sediment. Petrol.* **58**, 12 (1988).
16. S. A. Kuehl, T. M. Hariu, M. W. Sanford, C. A. Nittrouer, D. J. DeMaster, in *Microstructure of Fine-Grained Sediments*, R. H. Bennett, W. R. Bryant, M. H. Hulbert, Eds. (Springer Verlag, New York, 1991), pp. 33–45.
17. M. P. Segall, S. A. Kuehl, *Sediment. Geol.* **93**, 165 (1994).
18. N. Hawley, *Sedimentology* **28**, 699 (1981).
19. K. W. Pasierbiewicz, J. Kotlarczyk, *J. Sediment. Res.* **67**, 510 (1997).
20. J. H. Baas, J. L. Best, *J. Sediment. Res. Sect. A* **72**, 336 (2002).
21. Materials and methods are available as supporting material on *Science* Online.
22. J. R. L. Allen, *Principles of Physical Sedimentology* (George Allen and Unwin, London, 1985).

23. J. Berlamont, M. Ockenden, E. Toorman, J. Winterwerp, *Coast. Eng.* **21**, 105 (1993).
24. W. L. Stokes, *Primary Sedimentary Trend Indicators as Applied to Ore Finding in the Carrizo Mountains, Arizona and New Mexico, Part 1* (U.S. Atomic Energy Commission, Oak Ridge, TN, 1953).
25. J. Schieber, *Sedimentology* **36**, 203 (1989).
26. J. Schieber, in *Shales and Mudstones (vol. 1): Basin Studies, Sedimentology and Paleontology*, J. Schieber, W. Zimmerle, P. Sethi, Eds. (Schweizerbart'sche Verlagsbuchhandlung, Stuttgart, 1998), pp. 187–215.
27. J. Schieber, *J. Sediment. Res.* **69**, 909 (1999).
28. This research was supported by NSF grants EAR-0318769 and EAR-0617128.

Supporting Online Material
www.sciencemag.org/cgi/content/full/318/5857/1760/DC1
Materials and Methods
Figs. S1 to S5

25 June 2007; accepted 30 October 2007
10.1126/science.1147001

A Madden-Julian Oscillation Event Realistically Simulated by a Global Cloud-Resolving Model

Hiroaki Miura,[1]* Masaki Satoh,[1,2] Tomoe Nasuno,[1] Akira T. Noda,[1] Kazuyoshi Oouchi[1]

A Madden-Julian Oscillation (MJO) is a massive weather event consisting of deep convection coupled with atmospheric circulation, moving slowly eastward over the Indian and Pacific Oceans. Despite its enormous influence on many weather and climate systems worldwide, it has proven very difficult to simulate an MJO because of assumptions about cumulus clouds in global meteorological models. Using a model that allows direct coupling of the atmospheric circulation and clouds, we successfully simulated the slow eastward migration of an MJO event. Topography, the zonal sea surface temperature gradient, and interplay between eastward- and westward-propagating signals controlled the timing of the eastward transition of the convective center. Our results demonstrate the potential making of month-long MJO predictions when global cloud-resolving models with realistic initial conditions are used.

A Madden-Julian Oscillation (MJO) is an envelope of active convection thousands of kilometers wide that travels eastward at an average speed of 5 m/s over the Indian and Pacific Oceans (*1*). Given the large-scale (10^3 to 10^4 km horizontally) coupling between the atmospheric circulation and deep convection, an MJO influences not only the intraseasonal (30 to 90 days) variability of the tropics but also tropical cyclone genesis, the onset and break of the Asian-Australian monsoon, and the evolution of the El Niño–Southern Oscillation event (*2*, *3*). Despite its extensive effects on weather events and climate variability, weather prediction and climate models do not simulate the MJO well (*4*). Even recently, most of the coupled atmosphere-ocean general circulation models (GCMs) presented in the Fourth Assessment Report of the Intergovernmental Panel on Climate Change had difficulty simulating the variance and phase speed of the MJO (*5*). It is expected that weather forecasts beyond 10 days could be improved if the MJO representations in global weather prediction models were more realistic (*2*).

The major difficulty in simulating the MJO with GCMs involves cumulus parameterization used to estimate the vertical redistribution of heat and moisture by unresolved convective clouds in GCMs (*4*, *6*). Computational constraints have made it almost impossible to run global cloud-resolving models (GCRMs) that compute the effects of clouds explicitly and do not depend on cumulus parameterizations. However, recent increases in available computer power have begun to eliminate the models' artificial gap between cloud processes and the atmospheric circulation (*7*). Improved MJO simulations with GCMs substituting two-dimensional cloud-resolving models for cumulus parameterizations (*8*, *9*) suggest the importance of representing the variation in quasi-equilibrium states (*10*); that is, the statistical balance between stabilization by convection and destabilization by external forcing, which depends on large-scale atmospheric circulation. Therefore, GCRMs may allow realistic MJO simulations because convective activity can be linked directly to dynamic and thermodynamic atmospheric conditions of large-scale atmospheric circulation and convection. Here we report a numerical simulation of an MJO event that occurred between December 2006 and January 2007.

On the Earth Simulator, we ran a GCRM called the Nonhydrostatic Icosahedral Atmosphere Model (*11*), which has been upgraded as a result of aquaplanet experiments (*12*, *13*) and a realistic tropical cyclone experiment (*14*), with horizontal grids with mesh sizes about 3.5 and 7 km. These resolutions are almost fine enough to resolve the gross behavior of cumulus ensembles, including heating and moistening, as a response to large-scale atmospheric conditions. The 3.5-km grid run covered 1 week, whereas the 7-km grid run covered 30 days, which was long enough to reproduce the eastward migration of the convective center from the Indian to the Pacific Ocean. The initial atmospheric conditions were generated by linear interpolation from the National Centers for Environmental Prediction (NCEP) Global Tropospheric Analyses at 00:00 universal time coordinated (UTC) on 25 December 2006 for the 3.5-km grid run and at 00:00 UTC on 15 December 2006 for the 7-km grid run. We did not use any artificial techniques to nudge the model atmosphere to realistic atmospheric states during the numerical integrations (*15*).

The large-scale convectively active region of the MJO was reproduced approximately by the 3.5-km (Fig. 1) and 7-km (not shown in Fig. 1) grid runs. The convective center was near Borneo on 31 December 2006, and upper tropospheric clouds covered the islands of Southeast Asia and the surrounding seas. The typical multiscale structure of

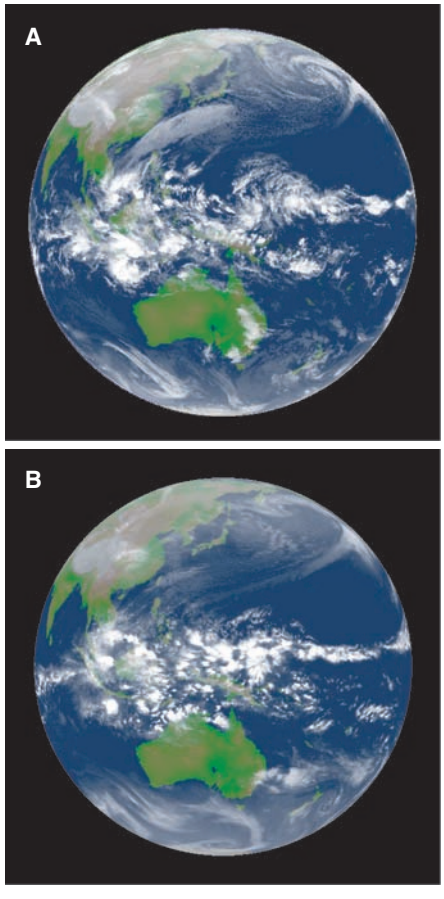

Fig. 1. (**A**) Infrared image from the Multi-Functional Transport Satellite (MTSAT-1R) at 00:30 UTC on 31 December 2006 and (**B**) outgoing longwave radiation from the 3.5-km run averaged from 00:00 UTC to 01:30 UTC on 31 December 2006.

[1]Frontier Research Center for Global Change, Japan Agency for Marine-Earth Science and Technology, 3173-25 Showamachi, Kanazawa-ku, Yokohama, Kanagawa 236-0001, Japan. [2]Center for Climate System Research, University of Tokyo, 5-1-5 Kashiwanoha, Kashiwa, Chiba 277-8568, Japan.

*To whom correspondence should be addressed. E-mail: miurah@jamstec.go.jp

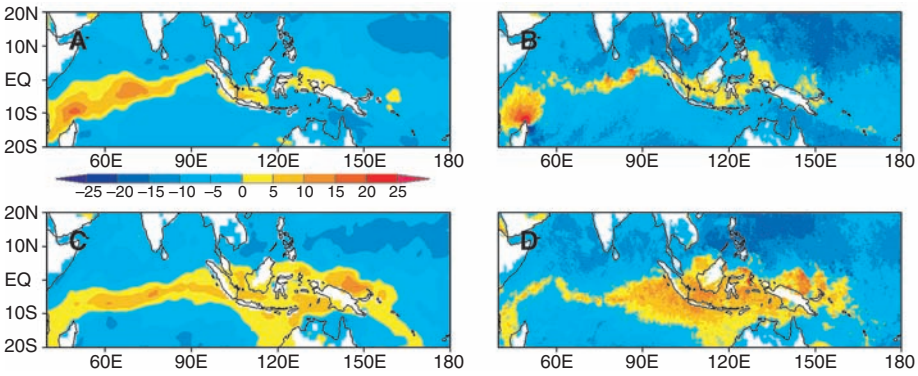

Fig. 2. Spatial distribution of the zonal wind velocity (in meters per second) at the 975-hPa level from (**A** and **C**) the NCEP analyses data and (**B** and **D**) the 7-km grid run at 00:00 UTC on 23 December 2006 [(A) and (B)] and 00:00 UTC on 6 January 2007 [(C) and (D)].

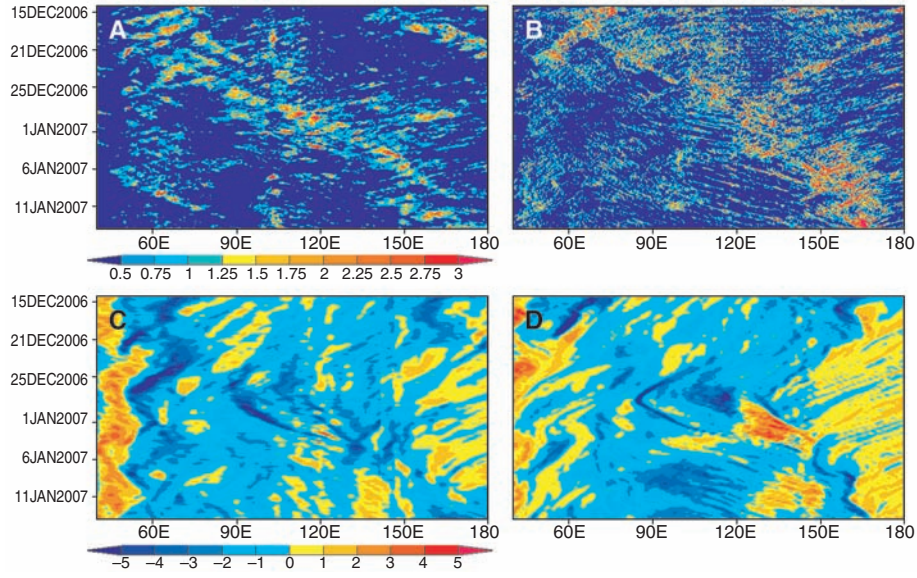

Fig. 3. Time/longitude (Hovmöller) sections. Surface precipitation (in millimeters per hour) averaged between 10°S and 5°N from (**A**) the TRMM 3B42 data and (**B**) the 7-km grid run. The vorticity (10^{-5} per second) at the 850-hPa level averaged between 10°S and 5°S from (**C**) the NCEP analyses and (**D**) the 7-km grid run.

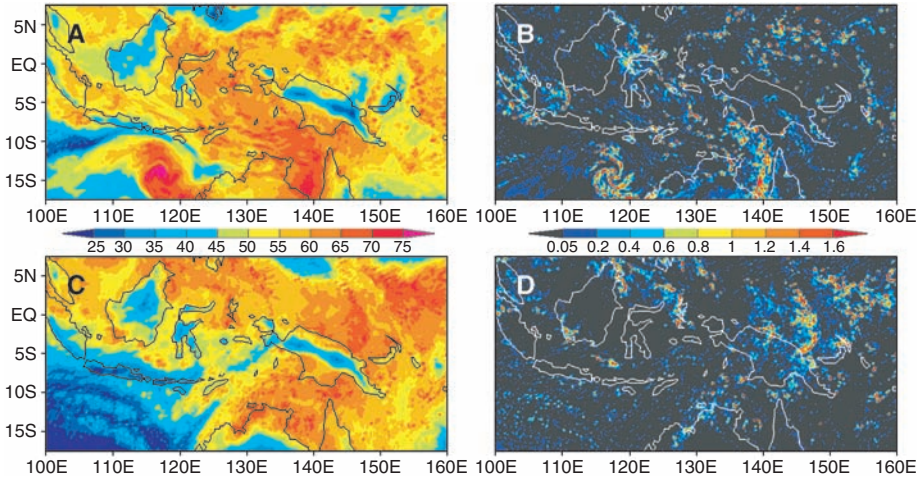

Fig. 4. Longitude/latitude sections of (**A** and **C**) precipitable water (in kilograms per square meter) and (**B** and **D**) column-integrated cloud water (in kilograms per square meter) from the 7-km run at 00:00 UTC on 2 January 2007 [(A) and (B)] and 00:00 UTC on 6 January 2007 [(C) and (D)].

convective systems (*16*, *17*) existed within the convectively active region. The active convective envelope consisted of cloud clusters covering hundreds of kilometers horizontally.

The 7-km grid run simulated the temporal evolution of the large-scale atmospheric circulation realistically during the 30-day integration (Fig. 2 and fig. S1). Before the intense convective activity began, an easterly wind dominated over the Indian and Pacific Oceans on 23 December 2006 (Fig. 2, A and B). Strong westerly and easterly winds near the north end of Madagascar were related to a developing tropical cyclone. As the active convective envelope passed eastward over the Indian Ocean and maritime continents (100° to 150°E), a low-level westerly wind was induced as a response to the latent heating of cloud systems (*18*). On 6 January 2007, the low-level westerly region was about 60° in width (90° to 150°E) at the equator, and strong westerly winds blew around the leading edge of the eastward-moving system (Fig. 2, C and D). The 7-km grid run resolved a strong westerly region northeast of New Guinea that consisted of several archlike structures.

The 7-km grid run computed the slow eastward movement of the convective center at a speed of about 5 m/s (Fig. 3, A and B). Heavy rainfall occurred over the Indian Ocean before 28 December 2006, over the maritime continents from 29 December 2006 to 6 January 2007, and over the Pacific Ocean after 7 January 2007. The slow-moving active convective envelope included internal structures propagating eastward at speeds exceeding 10 m/s, which is in the range of the propagation speeds of convectively coupled Kelvin waves (*19*, *20*). The Indian and Pacific Oceans were connected by a complex of higher-frequency, smaller-scale, eastward-propagating signals (*16*, *17*). The rapidly propagating signals conveyed low-level cool air maintained by consecutive rain evaporation to the east (fig. S2), and the moisture convergence zone shifted eastward following the leading edges of the signals (fig. S3). Over the maritime continents, rapidly propagating signals were generated every 1-day period, suggesting enhancement of the diurnal variation of convection under a moist environment.

The fast eastward-propagating signals faded away at around 150°E before 6 January 2007 (Fig. 3, A and B). The disappearance of the signals appeared to result from interference from topography and a zonal gradient of the sea surface temperature (SST). For example, on 2 January 2007, there was a large amount of moisture over an area between Australia and New Guinea (Fig. 4A), and a large-scale rainband system located at 140°E led the active convective envelope of the MJO (Fig. 4B). Subsequently, the northern part of this rainband system collided with the mountains of New Guinea and weakened rapidly, and the southern part decayed when it encountered drier air over the Coral Sea, where the SST was cooler. As a result, this rainband system did not reach the

Pacific Ocean. Behind the leading edge, counterclockwise and clockwise vortices were generated at the equator and at 15°S, respectively, at around 120°E. The clockwise vortex northwest of Australia corresponded well with a real tropical cyclone named Isobel. The 7-km grid run successfully predicted this tropical cyclone at the proper location and time, even after the integration continued for more than 2 weeks.

On 2 January 2007, a smaller cloud system was simulated at around 105°E in association with a clockwise vortex (Fig. 4B). This clockwise vortex near the south end of Sumatra originated from a tropical depression–type (TD-type) disturbance (*21*), which changed its direction from westward to eastward west of 90°E around 29 December 2006 (Fig. 3, C and D). As the negative-vorticity region proceeded eastward, a rainband system began to grow around 130°E, traveled to the northwest of New Guinea, and developed into a mature system at around 148°E on 6 January 2007 (Fig. 4D). Around 6 January 2007, a large amount of moisture northeast of New Guinea provided suitable atmospheric conditions for the growth of cloud systems (Fig. 4C). Moisture was transported mainly from the central Pacific, where the SST was as warm as in the western Pacific because of an El Niño event (fig. S3). The eastward-propagating rainband system brought low-level cool air into the South Pacific Convergence Zone (fig. S2), and the convective center of the MJO shifted from the maritime continents to the Pacific Ocean. Rainband systems northeast of New Guinea were also observed in the other MJO events during TOGA-COARE IOP (Tropical Ocean Global Atmosphere–Coupled Ocean Atmosphere Response Experiment, Intensive Observation Period) from November 1992 to February 1993 (*22*, *23*).

Overall, the 7-km grid run realistically reproduced the slow eastward migration of the MJO from the Indian to the Pacific Ocean. However, some features could have caused errors in the movement speed of the MJO. The 7-km grid run failed to simulate individual clouds correctly during the month-long integration. The zonal wind velocity tended to be overestimated over the tropics, and the effect of the overvalued surface precipitation might result in inaccuracy in the estimated amount of latent heat release. Despite these imperfections, the leading edge of the active convective envelope was positioned almost identically to that of observational data sets after the integration of more than 3 weeks on 6 January 2007. A possible explanation for the good correspondence between the 7-km grid run and observations is that the temporal evolution of the MJO is dominated by large-scale systems that the 7-km grid can resolve sufficiently. As inferred from the results of resolution-sensitivity studies using cloud-resolving models in limited domains (*24*, *25*), GCRMs probably have the ability to respond to a given large-scale forcing and restore statistical equilibrium states in a realistic time scale, even if a coarse horizontal resolution is used.

Our results demonstrate the potential ability of GCRMs to make month-long MJO predictions when they run with realistic initial conditions. The principal factors governing the realistic eastward migration of the MJO were the interference of preceding rainband systems from New Guinea and drier air over an area with a relatively cool SST, an eastward-propagating signal that originated from a TD-type disturbance, and abundant moisture supply from the east, probably in association with a westward-propagating disturbance. These results support the hypothesis derived from analyses of the TRMM (Tropical Rainfall Measuring Mission) data, which showed that a group of eastward-propagating Kelvin waves and their interaction with westward-propagating equatorial Rossby waves play a crucial role in MJOs (*26*); and they emphasize the influence of topography and the zonal SST gradient on the MJO.

References and Notes

1. R. A. Madden, P. R. Julian, *J. Atmos. Sci.* **29**, 1109 (1972).
2. D. E. Waliser, K. M. Lau, W. Stern, C. Jones, *Bull. Am. Meteorol. Soc.* **84**, 33 (2003).
3. C. Zhang, *Rev. Geophys.* **43**, RG2003 (2005).
4. J. M. Slingo *et al.*, *Clim. Dyn.* **12**, 325 (1996).
5. J.-L. Lin *et al.*, *J. Clim.* **19**, 2665 (2006).
6. E. D. Maloney, D. L. Hartmann, *J. Clim.* **14**, 2015 (2001).
7. R. A. Kerr, *Science* **313**, 1040 (2006).
8. W. W. Grabowski, *J. Atmos. Sci.* **60**, 847 (2003).
9. M. F. Khairoutdinov, D. A. Randall, C. DeMotte, *J. Atmos. Sci.* **62**, 2136 (2005).
10. A. Arakawa, W. H. Schubert, *J. Atmos. Sci.* **31**, 674 (1974).
11. M. Satoh *et al.*, *J. Comput. Phys.*, published online 17 February 2007, 10.1016/j.jcp.2007.02.006.
12. H. Tomita, H. Miura, S. Iga, T. Nasuno, M. Satoh, *Geophys. Res. Lett.* **32**, L08805 (2005).
13. H. Miura *et al.*, *Geophys. Res. Lett.* **32**, L19717 (2005).
14. H. Miura *et al.*, *Geophys. Res. Lett.* **34**, L02804 (2007).
15. The other experimental settings followed the realistic tropical cyclone experiment (*14*), except for updating a boundary-layer scheme to include a partial condensation process (*27*) and introducing a monotone advection scheme (*28*).
16. T. Nakazawa, *J. Meteorol. Soc. Jpn.* **66**, 823 (1988).
17. H. H. Hendon, B. Liebmann, *J. Geophys. Res.* **99**, 8073 (1994).
18. T. Matsuno, *J. Meteorol. Soc. Jpn.* **44**, 25 (1966).
19. Y. N. Takayabu, *J. Meteorol. Soc. Jpn.* **72**, 433 (1994).
20. M. Wheeler, G. N. Kiladis, *J. Atmos. Sci.* **56**, 374 (1999).
21. Y. N. Takayabu, T. Nitta, *J. Meteorol. Soc. Jpn.* **71**, 221 (1993).
22. N. Takahashi, H. Uyeda, *J. Meteorol. Soc. Jpn.* **73**, 427 (1995).
23. S. Satoh, A. Kinoshita, H. Uyeda, *J. Meteorol. Soc. Jpn.* **73**, 443 (1995).
24. W. W. Grabowski, X. Wu, M. W. Moncrieff, W. D. Hall, *J. Atmos. Sci.* **55**, 3264 (1998).
25. M. F. Khairoutdinov, D. A. Randall, *J. Atmos. Sci.* **60**, 607 (2003).
26. H. Masunaga, T. S. L'ecuyer, C. D. Kummerow, *J. Atmos. Sci.* **63**, 2777 (2006).
27. G. L. Mellor, T. Yamada, *Rev. Geophys. Space Phys.* **20**, 851 (1982).
28. H. Miura, *Mon. Weather Rev.* **135**, 4038 (2007).

29. This study was supported by Core Research for Evolutional Science and Technology of the Japan Science and Technology Agency (CREST, JST). The simulations were performed with the Earth Simulator at the Earth Simulator Center of the Japan Agency for Marine-Earth Science and Technology. We thank T. Matsuno, A. Sumi, M. Kimoto, Y. N. Takayabu, H. Tomita, and S. Iga for their advice and comments and T. Inoue, A. Higuchi, and S. Ishikawa for their help in treating the Multi-Functional Transport Satellite (MTSAT-1R) data.

Supporting Online Material

www.sciencemag.org/cgi/content/full/318/5857/1763/DC1
Figs. S1 to S3

27 July 2007; accepted 26 October 2007
10.1126/science.1148443

Deep Ocean Impact of a Madden-Julian Oscillation Observed by Argo Floats

Adrian J. Matthews,[1,2]* Patama Singhruck,[1] Karen J. Heywood[1]

Using the new Argo array of profiling floats that gives unprecedented space-time coverage of the upper 2000 meters of the global ocean, we present definitive evidence of a deep tropical ocean component of the Madden-Julian Oscillation (MJO). The surface wind stress anomalies associated with the MJO force eastward-propagating oceanic equatorial Kelvin waves that extend downward to 1500 meters. The amplitude of the deep ocean anomalies is up to six times the amplitude of the observed annual cycle. This deep ocean sink of energy input from the wind is potentially important for understanding phenomena such as El Niño–Southern Oscillation and for interpreting deep ocean measurements made from ships.

The Madden-Julian Oscillation (MJO) (*1*–*3*) is characterized by large-scale (1000 km across) precipitation anomalies that propagate slowly eastward from the Indian Ocean to the western Pacific. The lifetime of an individual MJO event is between 30 and 60 days. Dynamically, the MJO can be interpreted as a moist atmospheric Kelvin-Rossby wave in the tropics (*4*) and a modified Rossby wave response propagating on the climatological basic state in the extratropics (*5*). The MJO is thermodynamically coupled with the upper layers of the tropical

[1]School of Environmental Sciences, University of East Anglia, Norwich NR4 7TJ, UK. [2]School of Mathematics, University of East Anglia, Norwich NR4 7TJ, UK.

*To whom correspondence should be addressed. E-mail: a.j.matthews@uea.ac.uk

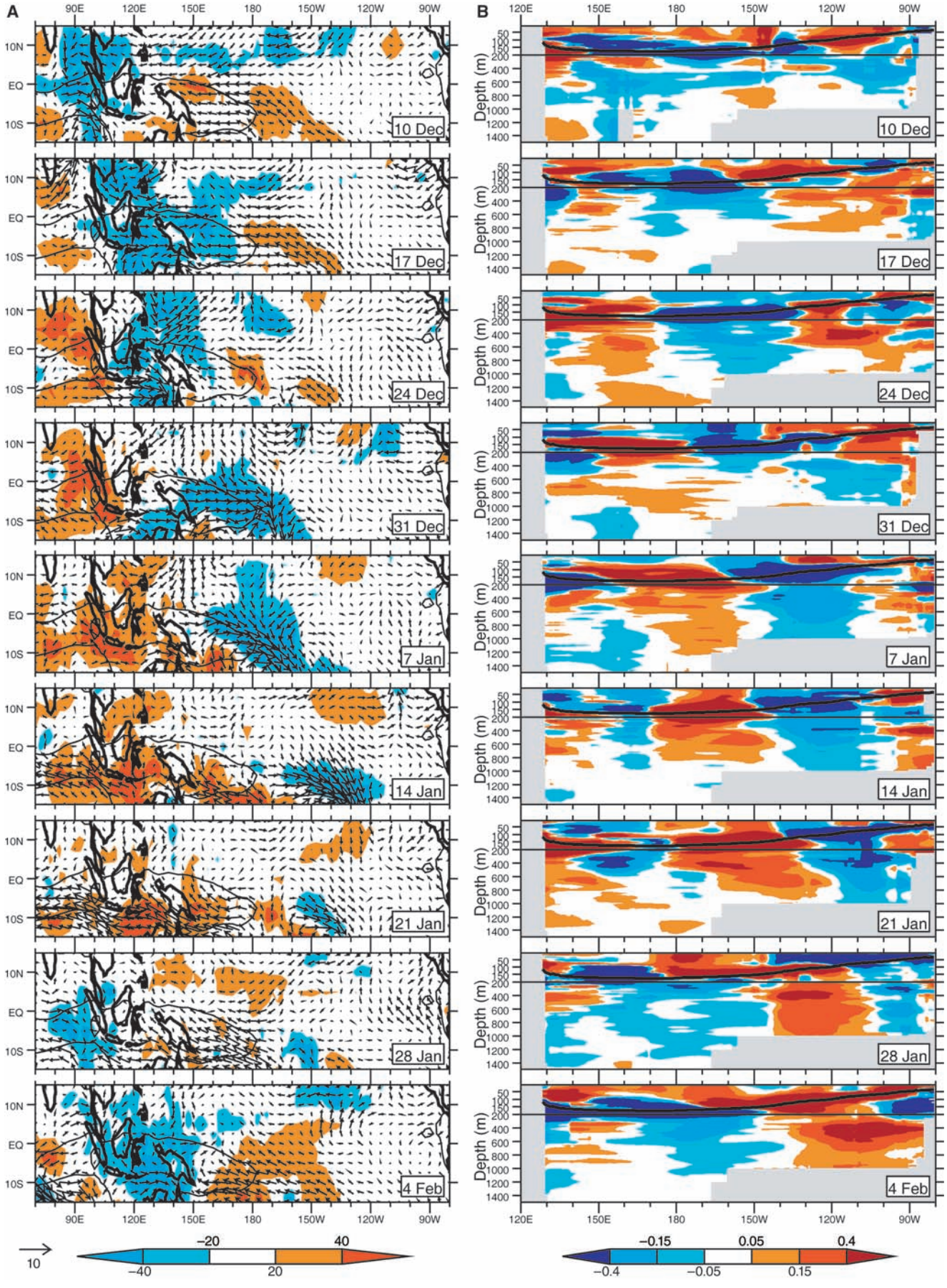
A
B
90E
120E
150E
180
150W
120W
90W
10N
EQ
10S
10 Dec
17 Dec
24 Dec
31 Dec
7 Jan
14 Jan
21 Jan
28 Jan
4 Feb
Depth (m)
50
100
150
200
400
600
800
1000
1200
1400
10
−20
40
−40
20
−0.15
0.05
0.4
−0.4
−0.05
0.15

Fig. 1 (opposite page). Weekly mean anomalies (annual cycle subtracted) from 10 December 2003 to 4 February 2004 in the western Pacific. (**A**) OLR. Shading interval is 20 W m^{-2} (see scale bar); wind vectors are 1000 hPa. The length of the vector arrows is proportional to the magnitude of the wind vector. The standard wind vector in the lower left corner has magnitude 10 m s^{-1}. The zero climatological-mean zonal wind contour is shown by a solid line. (**B**) Longitude-depth sections of Argo temperature along the equator (averaged 5°S to 5°N). Note the change of vertical scale at 200 m. Contours are at ±0.05°, 0.15°, and 0.4°C (see scale bar). The depth of the mean thermocline (20°C isotherm) is shown by the thick line.

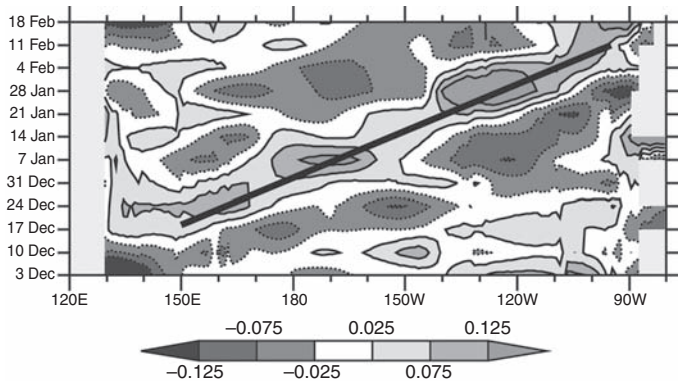

Fig. 2. Longitude-time section (Hovmöller diagram) of equatorial (averaged 5°S to 5°N) Argo temperature anomaly at the 850-dbar level. Contour interval is 0.05°C (see scale bar). The thick solid line indicates the phase propagation of the downwelling Kelvin wave.

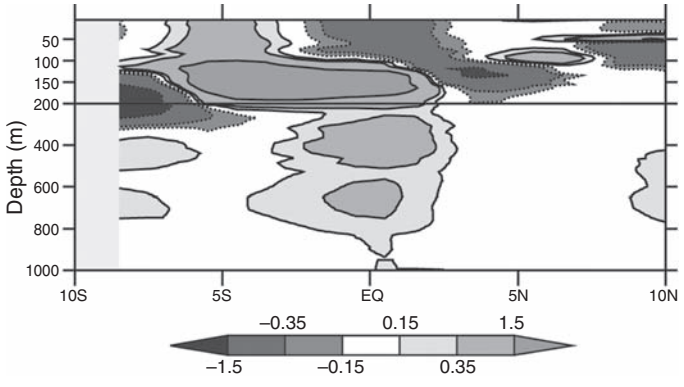

Fig. 3. Latitude-depth section of weekly mean Argo temperature anomaly at 140°W on 21 January 2004. Contours are at ±0.15°, 0.35°, and 1.5°C (see scale bar).

Indian and Pacific oceans (*6*–*8*). Anomalous surface fluxes of shortwave (solar) radiation due to cloudiness changes, and latent heat due to evaporation from the ocean surface through surface wind speed changes, both heat and cool the ocean mixed layer by up to 1°C in a strong MJO event (*6*).

In addition, oceanic equatorial Kelvin waves in the central and eastern Pacific are forced by MJO wind stress anomalies (*9*–*12*). A sequence of MJO events can force a train of eastward-propagating equatorial Kelvin waves along the thermocline in the Pacific, which can trigger an El Niño event (*13*, *14*) such as the event of 1997–1998 (*15*, *16*). The MJO has a direct impact on the ocean biosphere: The MJO-forced oceanic Kelvin waves modulate the surface chlorophyll concentration through vertical entrainment, with implications for the fishing industry (*17*).

The upper tropical ocean component of the MJO has been well documented (*6*–*8*), but the data have not been available to examine whether there is a deep tropical ocean component. The deepest MJO-linked observations in the tropical ocean—from the Tropical Atmosphere Ocean (TAO) moored buoy network in the tropical Pacific—extend down to only 500 m (*9*). A 50-day oscillation has been observed in currents down to 3000 m depth in the Indian Ocean, consistent with a zonally propagating Rossby wave (*18*), but these limited data have not been linked to the MJO or any atmospheric surface forcing. However, the MJO can influence the deep ocean in high latitudes (*19*).

Therefore, it seems plausible that the MJO may influence the deep ocean in the tropics, but the limited hydrographic data that exist do not have the temporal resolution necessary for an analysis of intraseasonal variability. However, this situation has begun to change because of the advent of the Argo ocean observing system (*20*). Argo floats have been deployed since 2000 and are at the core of current efforts to set up a global ocean observing system (*21*). Today almost 3000 floats are operational, providing unprecedented global coverage of the world oceans. Each float drifts at a typical parking depth of 1000 m for ~10 days. In ~2 hours, it then descends to 2000 m, ascends to the surface, measuring a vertical profile of temperature and salinity, then descends again to its parking depth. Argo data have already been used to study mid-depth circulation at high latitudes (*22*) and seasonal temperature variation below the thermocline in the Pacific (*23*). The 10-day temporal resolution provides a new opportunity to study the spatial variability of the deep ocean on intraseasonal time scales.

Here, we used Argo data to reveal the oceanic component of the MJO downward into the deep Pacific, in a case study of the December 2003–February 2004 MJO event. Outgoing longwave radiation (OLR) was used as a proxy for precipitation (*24*), as low values of OLR are indicative of deep clouds and precipitation in the tropics. In the uppermost panel of Fig. 1A, which shows the Argo data for 10 December 2003, the positive OLR anomalies over the western Pacific indicate reduced precipitation (dry phase of MJO) with easterly surface wind anomalies, and the negative OLR anomalies over the eastern Indian Ocean indicate enhanced precipitation (wet phase of MJO) with equatorial westerly wind anomalies. A further region of positive OLR anomalies over the central Indian Ocean indicates the next dry phase of the MJO. These precipitation anomalies then propagate slowly eastward. The 56-day period shown in Fig. 1A covers slightly more than one full cycle of the MJO.

The MJO exerts a thermodynamical control on the ocean mixed layer via changes to the surface shortwave and latent heat fluxes. Negative OLR anomalies imply more deep clouds, a reduction in the downward surface shortwave flux, and a cooling of the ocean surface. Intraseasonal latent heat flux (evaporation) anomalies are mainly controlled by changes in the total (climatological mean plus anomalous) surface wind speed. West of the date line, westerly surface wind anomalies reinforce the mean westerlies there (Fig. 1A). The total wind speed will increase, increasing evaporation from the ocean surface and cooling it. East of the date line, westerly anomalies partially cancel the mean easterlies, reducing the total wind speed and evaporation and providing a warming anomaly to the ocean. The sea surface temperature (SST) response to these changes in the surface fluxes is lagged by approximately one-quarter of the MJO cycle, or 1 to 2 weeks (*6*).

The surface shortwave and latent heat flux anomalies lead to changes in the equatorial western Pacific SST throughout this particular MJO event, as clearly illustrated by the gridded Argo temperature anomalies (*24*). Initially, the positive SST anomalies in the equatorial western Pacific on 10 December (Fig. 1B) are due to the dry MJO phase and increased downward surface shortwave flux, as well as the reduction in evaporation and upward latent heat flux from the anomalous easterlies weakening the total wind speed, over the previous week. These flux anomalies are still present on 10 December, and a week later, on 17 December, there are still

positive SST anomalies over the western Pacific. However, the wet phase of the MJO has now moved over the western Pacific. The associated reduction in the downward surface shortwave flux, and the increased evaporation from surface westerlies enhancing the mean winds, lead to negative SST anomalies there from 24 December 2003 to 14 January 2004. When the next dry phase of the MJO arrives around 7 January, the flux anomalies begin to change sign and positive SST anomalies return from 28 January onward.

The SST anomalies in the equatorial western Pacific that are consistent with thermodynamical forcing by the surface flux anomalies extend down through the mixed layer to about 50 m depth (Fig. 1B). Below this depth, the new Argo data set allows us to document the dynamical ocean mechanisms that become important below the mixed layer. On 10 December, the negative SST anomalies between 100 and 200 m in the western and central Pacific show an upwelling oceanic equatorial Kelvin wave that has arisen as a forced response to the surface easterly wind stress anomalies above. With the arrival of the wet phase of the MJO over the western Pacific on 17 December, the associated surface westerly anomalies (a "westerly wind burst") begin to force a downwelling oceanic equatorial Kelvin wave, with a small region of positive SST anomalies at thermocline depth (180 m; thick line in Fig. 1B) at 150°E. These positive and negative temperature anomalies at the thermocline also extend coherently downward into the deeper ocean, to around 600 m.

By 24 December, the upwelling and downwelling Kelvin waves have propagated eastward along the thermocline. The largest-amplitude Argo temperature anomalies follow the thermocline, as this is the level of greatest vertical temperature gradient. The coherent temperature anomalies extend from the thermocline down to 1500 m, the deepest level of observations. From 31 December to 4 February, the upwelling and downwelling Kelvin waves continue to propagate eastward and also extend downward to at least 1200 m. The deep anomalies have a large amplitude. The maximum anomaly observed at 600 m is 0.45°C (on 4 February at 105°W); at 850 m, the maximum anomaly is 0.25°C (on 28 January at 130°W). These are greater by a factor of 3 to 6 than the amplitude of the annual cycle, which is 0.08° and 0.07°C at these locations, respectively, as calculated from the Argo data (*24*). Their amplitudes are also larger than the predicted deep ocean Kelvin wave response to intraseasonal wind forcing in an ocean model (*25*).

When the next dry phase of the MJO arrives over the western Pacific on 14 January (Fig. 1A), its easterly surface wind stress anomalies force another upwelling equatorial Kelvin wave. The associated negative temperature anomalies then propagate eastward along the thermocline and extend down to 1300 m (Fig. 1B).

The coherent eastward propagation of the upwelling, downwelling, and second upwelling phases of the deep Kelvin wave can be clearly seen in Hovmöller diagrams of the temperature anomalies in the deep ocean at 850 dbar (Fig. 2) and in the thermocline at 150 dbar (fig. S1). The average phase speed of the waves (slope of solid lines in Fig. 2 and fig. S1) is $c = 2.8$ m s^{-1}, consistent with the typical observed phase speed of first-internal-mode equatorial Kelvin waves on the thermocline (*12*, *26*). The vertical tilt of the anomalies can clearly be seen in a comparison of the two Hovmöller diagrams; the temperature anomalies in the thermocline (fig. S1) lead those in the deep ocean (Fig. 2) by a quarter cycle. The latitude-depth section of the temperature anomalies (Fig. 3) shows the characteristic spatial structure of a theoretical equatorial Kelvin wave. This has a maximum at the equator, then decays toward the poles with a Gaussian structure, $\exp(-\beta y^2/2c)$, where y is distance northward from the equator, and $\beta = 2.3 \times 10^{-11}$ m^{-1} s^{-1} is the latitudinal gradient of planetary vorticity. Using the observed value of $c = 2.8$ m s^{-1}, we find that the latitudinal trapping scale is $y_0 = (2c/\beta)^{1/2} = 490$ km $\approx 4.4°$ latitude. This is consistent with the observed latitudinal structure of the deep Argo temperature anomalies in Fig. 3.

The vertical structure of the waves can be interpreted in terms of standing and vertically (downward) propagating components. The vertical phase lines (or, equivalently, zero-anomaly contours) in, for example, the eastern Pacific on 7 January indicate a standing component. Conversely, the phase line (zero-anomaly contour) that tilts downward and eastward in the eastern Pacific on 21 January indicates downward (energy) propagation of the Kelvin wave (*27*, *28*), with a vertical wavelength of about 800 m, which is consistent with the theoretical value (*24*). Alternatively, the tilted phase lines and apparent vertical propagation can be interpreted as a superposition of vertical modes. However, in the Pacific, vertical modes of order 3 and higher are all subjected to critical layer dissipation in the equatorial undercurrent (*25*), and the deep structure is consistent with wave-mean flow interaction effects superimposed on a first-mode baroclinic structure.

The Argo data have facilitated an unprecedented view of the deep tropical Pacific Ocean on short (intraseasonal) time scales. This had not previously been possible, as conventional hydrographic data have inadequate time resolution and spatial coverage, and the TAO moored buoy network has a maximum depth of only 500 m. The MJO has been shown to force eastward-propagating equatorial Kelvin waves that extend downward into the deep ocean. Although intraseasonal Kelvin waves have been well studied in the near-surface layers (*9*, *25*, *26*), there has been no opportunity to observe the deeper signal until now. These Argo-observed deep ocean Kelvin waves have larger amplitude than the annual cycle and model predictions, and they could potentially increase the errors in vertical structure, circulation, and heat content from hydrographic sections (*29*) if a Kelvin wave passed through at the time of the section. The anomalies in the deep (e.g., 600 m) geostrophic zonal currents, calculated from the Argo temperature and salinity data, are typically 1 cm s^{-1}. This is the same magnitude as the mean geostrophic current at these depths (below the equatorial undercurrent). Hence, these anomalies are a large perturbation to the mean currents and represent a substantial transfer of energy from the surface, where they are forced, to the deep ocean, where they must be dissipated.

The propagation of the Kelvin wave into the deep ocean will have effects on deep ocean biology and chemistry, and should be included in coupled models of the MJO. Furthermore, these deep ocean Kelvin waves will have an impact on ocean circulation outside the equatorial wave guide. Upon reaching the eastern boundary, the equatorial Kelvin wave will trigger meridionally propagating coastal Kelvin waves along the coastline of the Americas, which will then trigger westward-propagating Rossby waves back into the ocean interior.

References and Notes

1. R. A. Madden, P. R. Julian, *Mon. Weather Rev.* **122**, 814 (1994).
2. C. Zhang, *Rev. Geophys.* **43**, RG2003 (2005).
3. W. K. M. Lau, D. E. Waliser, Eds., *Intraseasonal Variability in the Atmosphere-Ocean Climate System* (Springer-Praxis, Berlin, 2005).
4. H. H. Hendon, M. L. Salby, *J. Atmos. Sci.* **53**, 1751 (1996).
5. A. J. Matthews, B. J. Hoskins, M. Masutani, *Q. J. R. Meteorol. Soc.* **130**, 1991 (2004).
6. T. Shinoda, H. H. Hendon, J. Glick, *J. Clim.* **11**, 1685 (1998).
7. S. J. Woolnough, J. M. Slingo, B. J. Hoskins, *J. Clim.* **13**, 2086 (2000).
8. M. J. McPhaden, *J. Clim.* **15**, 2632 (2002).
9. W. S. Kessler, M. J. McPhaden, K. M. Weickmann, *J. Geophys. Res.* **100**, 10613 (1995).
10. H. H. Hendon, B. Liebmann, J. D. Glick, *J. Atmos. Sci.* **55**, 88 (1998).
11. C. Zhang, *J. Clim.* **14**, 1309 (2001).
12. P. E. Roundy, G. N. Kiladis, *J. Clim.* **19**, 5253 (2006).
13. C. Zhang, J. Gottschalck, *J. Clim.* **15**, 2429 (2002).
14. K. H. Seo, Y. Xue, *Geophys. Res. Lett.* **32**, L07712 (2005).
15. M. J. McPhaden, *Science* **283**, 950 (1999).
16. K. Kutsuwada, M. J. McPhaden, *J. Phys. Oceanogr.* **32**, 1133 (2002).
17. D. E. Waliser, R. Murtugudde, P. Strutton, J. L. Li, *Geophys. Res. Lett.* **32**, L23602 (2005).
18. K. J. Heywood, E. D. Barton, G. L. Allen, *Oceanol. Acta* **17**, 255 (1994).
19. A. J. Matthews, M. P. Meredith, *Geophys. Res. Lett.* **31**, L24312 (2004).
20. J. Gould, *Eos* **85**, 190 (2004).
21. K. Alverson, D. J. Baker, *Science* **314**, 1657 (2006).
22. K. L. Lavender, R. E. Davis, W. B. Owens, *Nature* **407**, 66 (2000).
23. S. Hosoda, S. Minato, N. Shikama, *Geophys. Res. Lett.* **33**, L13604 (2006).
24. See supporting material on *Science* Online.
25. E. S. Johnson, M. J. McPhaden, *J. Phys. Oceanogr.* **23**, 608 (1993).

26. S. Cravatte, J. Picaut, G. Eldin, *J. Geophys. Res.* **108**, 10.1029/2002JC001511 (2003).
27. A. E. Gill, *Atmosphere-Ocean Dynamics* (Academic Press, San Diego, CA, 1982).
28. W. S. Kessler, J. P. McCreary, *J. Phys. Oceanogr.* **23**, 1192 (1993).
29. M. Tsuchiya, L. D. Talley, *J. Mar. Res.* **54**, 541 (1996).

30. The Argo data were provided by the Argo project (www.argo.ucsd.edu). The interpolated OLR and NCEP reanalysis data were provided by NOAA/Earth System Research Laboratory, Physical Sciences Division, Boulder, Colorado (www.cdc.noaa.gov). P.S. was funded by the University of East Anglia and the Thai government. We thank N. Gillett and two anonymous reviewers for comments on the manuscript.

Supporting Online Material
www.sciencemag.org/cgi/content/full/318/5857/1765/DC1
Materials and Methods
Fig. S1
References

2 July 2007; accepted 12 October 2007
10.1126/science.1147312

Asymmetric Mating Interactions Drive Widespread Invasion and Displacement in a Whitefly

Shu-Sheng Liu,[1]* P. J. De Barro,[2] Jing Xu,[1] Jun-Bo Luan,[1] Lian-Sheng Zang,[1] Yong-Ming Ruan,[1] Fang-Hao Wan[3]

The role of behavioral mechanisms in animal invasions is poorly understood. We show that asymmetric mating interactions between closely related but previously allopatric genetic groups of the whitefly *Bemisia tabaci*, a haplodiploid species, have been a driving force contributing to widespread invasion and displacement by alien populations. We conducted long-term field surveys, caged population experiments, and detailed behavioral observations in Zhejiang, China, and Queensland, Australia, to investigate the invasion process and its underlying behavioral mechanisms. During invasion and displacement, we found increased frequency of copulation leading to increased production of female progeny among the invader, as well as reduced copulation and female production in the indigenous genetic groups. Such asymmetric mating interactions may be critical to determining the capacity of a haplodiploid invader and the consequences for its closely related indigenous organisms.

Biological invasions threaten agricultural and natural systems throughout the world (*1*). Invasive animals often thrive at the expense of indigenous, closely related organisms, and insight into the causes of animal invasions often hinges on detailed assessments of behavioral mechanisms (*2*). Closely related species often have incompletely isolated mate recognition systems conducive to reproductive interactions and interference (*3*), but rarely have such behavioral mechanisms been isolated and tested in an experimental setting to reveal their contribution to invasion biology (*1*). Here, we combined long-term field monitoring, caged population studies, and detailed behavioral observations to investigate the mechanisms underlying the widespread, rapid invasion by a genetic group of the whitefly *Bemisia tabaci* (Gennadius) (Hemiptera: Aleyrodidae).

The whitefly *B. tabaci*, a haplodiploid species, is a genetically diverse group including many morphologically indistinguishable populations that differ in biological characteristics but display clear geographic distributions, with indigenous

[1]Institute of Insect Sciences, Zhejiang University, Hangzhou 310029, China. [2]CSIRO Entomology, 120 Meiers Road, Indooropilly, Queensland 4068, Australia. [3]Institute of Plant Protection, Chinese Academy of Agricultural Sciences, Beijing 100081, China.

*To whom correspondence should be addressed. E-mail: shshliu@zju.edu.cn

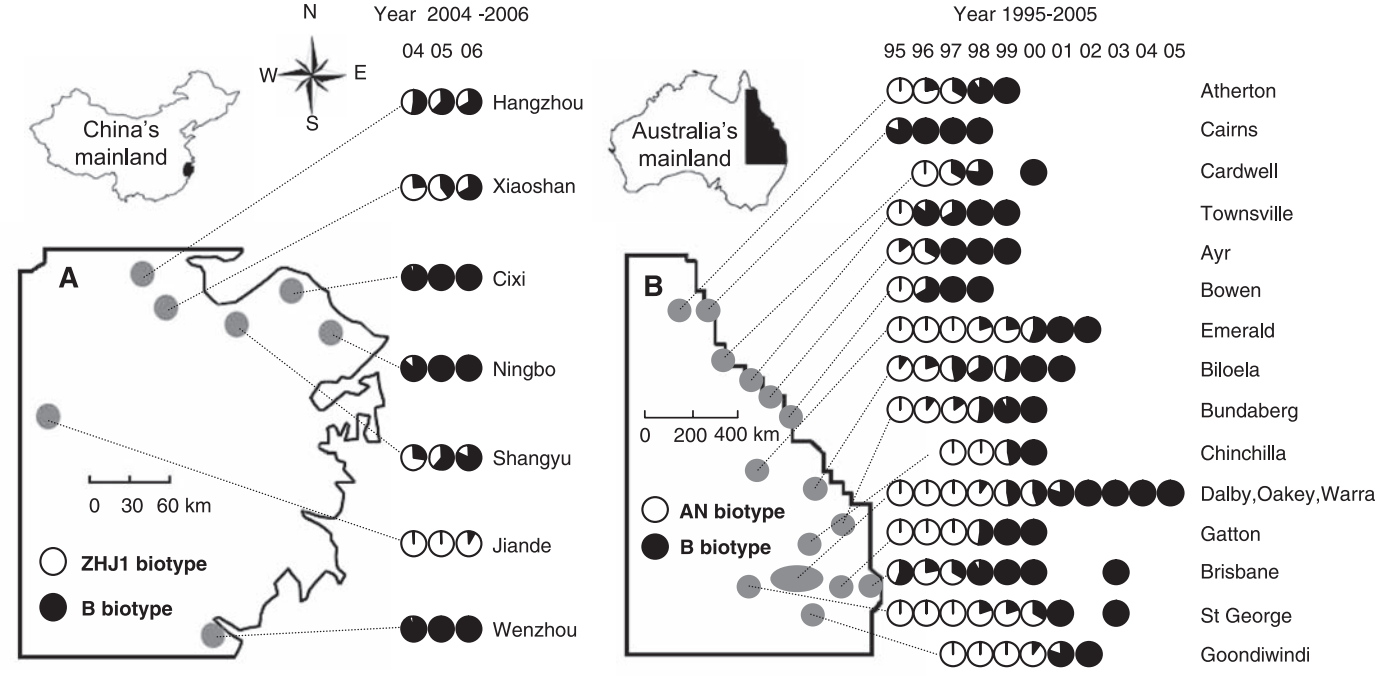

Fig. 1. Changes of the mean proportions of the exotic B biotype and indigenous biotypes of *Bemisia tabaci* after introduction of B. (**A**) ZHJ1 versus B on cotton at seven locations in Zhejiang, China, from 2004 to 2006. The map covers the area 122°E to 119°E from east to west and 27°30′N to 30°N from south to north. Of the seven locations, Jiande is in a western mountainous area with less transport activity relative to the other six locations along the east coast, where transport of vegetables and ornamental plants is frequent. (**B**) AN versus B on *Sonchus oleraceus* at 17 locations in Queensland, Australia, from 1995 to 2005. The map covers the area 153°30′E to 142°E from east to west and 34°S to 14°40′S from south to north. Data from the other 17 locations are not depicted because of space.

populations that span the globe between 30°N and 30°S (*4*–*6*). A recent phylogenetic analysis of *B. tabaci* mitochondrial CO1 and ribosomal ITS1 DNA sequences supports the existence of 12 "major genetic groups" (*5*). The available data indicate reproductive compatibility within each of the major groups but reproductive isolation between them (*7*). As species-level distinctions among the members of *B. tabaci* remain elusive, we use the term "biotypes" to refer to individuals representing the different genetic groups involved in our description of between-group interactions.

A major recent event associated with *B. tabaci* has been the invasion by individuals commonly known as the B biotype [also called *B. argentifolii* (*8*)] from their presumed origin in the Mediterranean–Asia Minor region to much of the rest of the world, with a resulting impact that has led to it being described as one of the top 100 invasive species (*4*–*6*, *9*, *10*). The invasive B biotype has caused considerable damage to crops through phloem feeding, transmission of plant viruses, induction of phytotoxic disorders, and excretion of honeydew (*4*, *6*). Circumstantial evidence indicates that in many regions, introduction of the B biotype has led to the displacement of some relatively innocuous, indigenous *B. tabaci* belonging to different genetic groups (*4*, *11*–*13*). However, the mechanisms for displacement of indigenous populations are not clear, although the role of some form of mating interference has been inferred (*11*, *14*, *15*).

The B biotype entered China in the mid-1990s (*16*) and Australia in the early 1990s (*17*) (Fig. 1). We conducted regular sampling of the field whitefly populations in Zhejiang, China, from 2004 to 2006 and in Queensland, Australia, from 1995 to 2005 to monitor the process of invasion and displacement by B in the two regions (*18*). The data indicate that before invasion, the ZHJ1 biotype, which is indigenous to China (*5*), was widely distributed in Zhejiang, and the AN biotype, which is indigenous to Australia (*5*), was widely distributed in Queensland (Fig. 1). Phylogenetic analysis shows that AN, B, and ZHJ1 belong to different major genetic groups (i.e., Australia, Mediterranean–Asia Minor–Africa, and Asia II, respectively) (*5*). Moreover, mating experiments between B and ZHJ1 and between B and AN indicated that neither could interbreed to produce fertile female offspring (*14*, *19*).

In both regions, the process of invasion and displacement agrees in general with earlier circumstantial evidence collected from other regions of the world (*4*). Thus, in Zhejiang, the earliest invasions by B occurred in locations with the most frequent transport of ornamentals (i.e., Cixi, Ningbo, and Wenzhou), whereas in Australia the incursion was first associated with a major importing wholesale nursery in New South Wales and from there to major wholesale nurseries in Cairns and Brisbane in Queensland (Fig. 1). Rapid and widespread displacement of the indigenous population has occurred in both regions. In Zhejiang, displacement of ZHJ1 was complete by 2005 in three locations and is currently occurring in other locations; in Queensland, displacement of AN was complete in all locations by 2005 or earlier, and in any particular location it usually took 3 to 5 years (Fig. 1).

In parallel with the displacement, we detected significant changes in sex ratio in both the indigenous and alien populations in both regions. In Zhejiang, when populations of either B or ZHJ1 occurred alone, B usually had female ratios of 60 to 70%, which were higher than the 50 to 60% female ratios in ZHJ1 (Fig. 2A and fig. S1). This difference in sex ratio between the two was enhanced by the relative increase of females in B and decrease of females in ZHJ1 when B and ZHJ1 occurred together during displacement (Fig. 2A and fig. S1). Similar differences in the sex ratio between AN and B when each of them occurred alone, as well as a similar

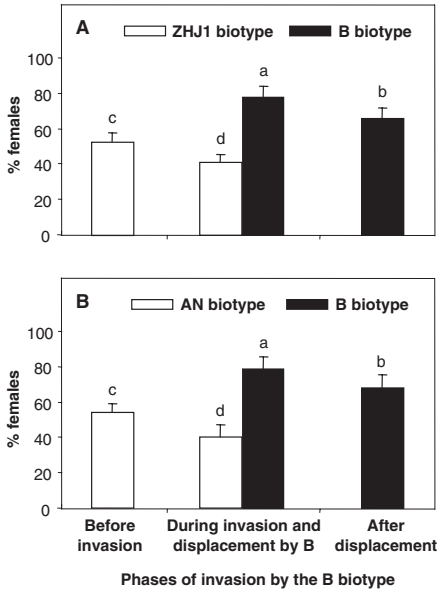

Fig. 2. Changes in mean sex ratios in field populations of the exotic B biotype and indigenous biotypes before, during, and after displacement of the indigenous biotypes by B. (**A**) Female ratios of ZHJ1 and B on cotton from 2004 to 2006; for locations, see Fig. 1. The data set includes 13 samples for ZHJ1 before invasion, 26 samples for ZHJ1 and B during invasion and displacement, and 28 samples for B after displacement. (**B**) Female ratios of AN and B on spurge from 1995 to 2005; for locations, see Fig. 1. The data set includes 74 samples for AN before invasion, 66 samples for AN and B during invasion and displacement, and 77 samples for B after displacement. One-way analysis of variance (ANOVA) and Fisher protected least significant difference (LSD) tests were applied to each of the data sets, based on proportion data transformed by arcsine square root. For (A), $F_{3,89}$ = 224.14, $P < 0.001$; for (B), $F_{3,280}$ = 81.96, $P < 0.001$. Different letters above bars indicate significant differences; error bars indicate SD.

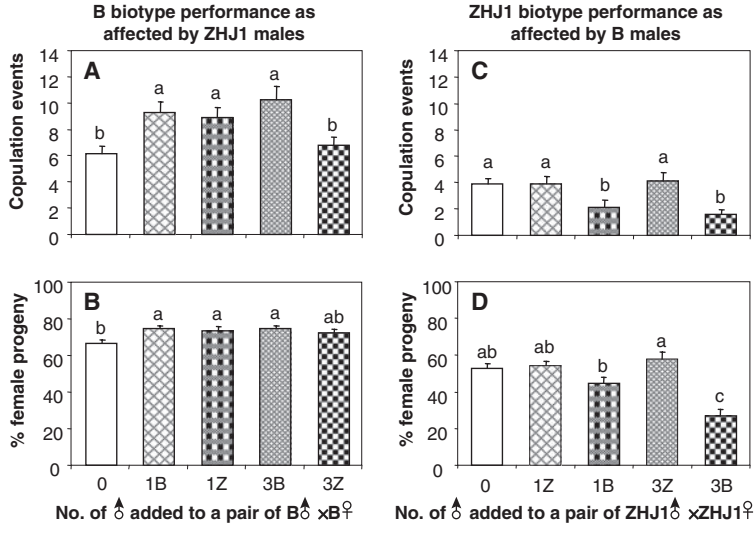

Fig. 3. Changes in the mean number of copulation events during the first 72 hours after emergence and production of progeny for the first 5 days after emergence when a pair of B biotype ♂×♀ was supplemented with one or three ♂ of the B or the indigenous ZHJ1 (Z) biotype (**A** and **B**), or when a pair of ZHJ1 biotype ♂×♀ was supplemented with one or three ♂ of the ZHJ1 or B biotype (**C** and **D**). We conducted 15 to 50 replicates for each of the treatments. One-way ANOVA and LSD tests were applied to each of the four data sets, and the data in (B) and (D) were transformed by arcsine square root before analysis. For (A), $F_{4,106}$ = 5.67, $P < 0.001$; for (B), $F_{4,199}$ = 3.02, P = 0.019; for (C), $F_{4,95}$ = 8.02, $P < 0.001$; and for (D), $F_{4,201}$ = 15.28, $P < 0.001$. Means ± SEM of the number of progeny produced by B females in the five treatments in (B) were 20.8 ± 1.5, 24.1 ± 1.5, 20.3 ± 1.4, 18.4 ± 1.3, and 19.1 ± 1.7, respectively, and the means did not differ significantly ($F_{4,199}$ = 2.31, P = 0.059). Means ± SEM of the number of progeny produced by ZHJ1 females in the five treatments in (D) were 19.6 ± 1.9, 22.7 ± 1.7, 17.5 ± 1.6, 18.1 ± 1.7, and 17.7 ± 1.5, respectively, and the means did not differ significantly ($F_{4,201}$ = 1.74, P = 0.143). Different letters above bars indicate significant differences; error bars indicate SE.

shift in sex ratio when they co-occurred, were observed in Queensland (Fig. 2B and fig. S2).

We then simulated the process of displacement in controlled laboratory and field cage experiments (*18*). In Zhejiang, we reared mixed cohorts of B and ZHJ1, as well as control cohorts of either B or ZHJ1 alone, on caged cotton plants for 225 days (about 10 generations for the earliest-born individuals in every generation) and monitored the changes in relative proportion as well as sex ratio. The mixed cohorts began with 13% B and 87% ZHJ1. The relative proportion of B increased steadily with time and had totally supplanted ZHJ1 after 225 days (fig. S3). Each cohort was initiated with 50% females, and divergences in sex ratio among the different cohorts occurred with time. In cohorts with B only, the female ratio increased in the first 50 days and remained at 60 to 70% thereafter; in cohorts with ZHJ1 only, the female ratio remained at 50 to 60% throughout. In contrast, the female ratio of B in the mixed cohorts increased and reached 70 to 80% from days 50 to 150 when displacement was actively taking place, while that of ZHJ1 decreased to mostly 30 to 40% (fig. S3). In Queensland, we reared mixed cohorts of AN and B, where B made up 10% of the females, as well as control cohorts of either AN or B alone, on spurge plants (*Euphorbia cyathophora*) for five generations in field cages (*18*). In the AN-only cohorts, females made up 56% of the population, whereas 62% of the B-only cohorts were females. However, in the mixed cohort, AN females declined to 22% while B females increased to 76% by the fifth generation (table S1).

Whiteflies, including *B. tabaci*, exhibit haplodiploidy, producing males from unfertilized eggs and females from fertilized eggs (*20*, *21*). In AN, B, and ZHJ1, both females and males start mating soon after emergence and both sexes mate repeatedly (*19*, *21*). We found that for both B and ZHJ1, continuous availability of males to females was essential if the usual level of egg fertilization was to be maintained, and that deprivation of males from mated females resulted in rapid reduction in fertilization and an increase in the proportion of unfertilized eggs leading to male progeny (*18*) (fig. S4). When males and females of B and one of the indigenous biotypes were placed together, they frequently exhibited courtship but never copulated. Furthermore, when two males from different biotypes and a female of a given biotype were placed together, the female was frequently courted by both males and courting and copulation could be interrupted by the second male (*19*, *21*). We thus suspected that changes of sex ratio were related to changes in male availability and copulation events due to interactions between the invader and indigenous individuals.

We next conducted a series of observations to identify the behavioral mechanisms behind the changes in sex ratios. This was done by placing a newly emerged adult female and male of a given biotype on a leaf in a clip cage and supplementing the pair with none, one, or three males of the same or different biotype. Using a video recording system (*21*), we were then able to record the movement and every copulation event that occurred over the following 72 hours (*18*). In parallel with these observations, we examined the progeny production by females of each biotype over the 5-day period after emergence, using the same numbers and combinations of males as in the observations on copulation events (*18*).

When a pair of B individuals on cotton was supplemented with one male of either B or ZHJ1, or with three males of B, the numbers of copulation events of the B females increased, as did the percentage of female progeny, but the numbers of progeny produced remained unchanged; however, the addition of three ZHJ1 males did not affect either copulation events or progeny sex ratio (Fig. 3, A and B). When a pair of ZHJ1 individuals was supplemented with one or three ZHJ1 males, the number of copulation events of the ZHJ1 females remained unchanged; in contrast, when a pair of ZHJ1 was supplemented with one or three B males, the numbers of copulation events as well as the percentage of females in the progeny decreased (Fig. 3, C and D). The observations made with B and AN on spurge showed that the responses of B to the addition of either B or AN males were similar to those of B on cotton when interacting with ZHJ1, in terms of both number of copulation events and progeny sex ratio (Fig. 4, A and B). Likewise, the responses of AN to the addition of either AN or B males were similar to those of ZHJ1 interacting with B (Fig. 4, C and D). Identification of the progeny produced using nuclear DNA markers detected no hybrids, demonstrating reproductive isolation between B and ZHJ1 and between B and AN (*18*). These results showed that B interacting with an indigenous biotype could increase production of female progeny by increasing its frequency of copulation, and at the same time could reduce the production of female progeny by the indigenous females through reducing copulation by the latter.

Detailed analysis of the movement of whitefly adults revealed behavioral elements related to the increase and decrease in copulation events (*18*). In B and ZHJ1, both females and males of the two biotypes differed in mating behavior and interactions in three important ways (tables S2 and S3). First, in the absence of interference by a second male, males of the two biotypes courted at a similar frequency, but B females accepted courtships leading to copulation more frequently than did ZHJ1 females. Second, when a second male of the same biotype was present in the same arena, males of both biotypes increased their frequency of uninterrupted courtships despite some interference between the males, but the responses of females differed: B females increased their acceptance of courtships, leading to more events of copulation, whereas ZHJ1 females did not. Third,

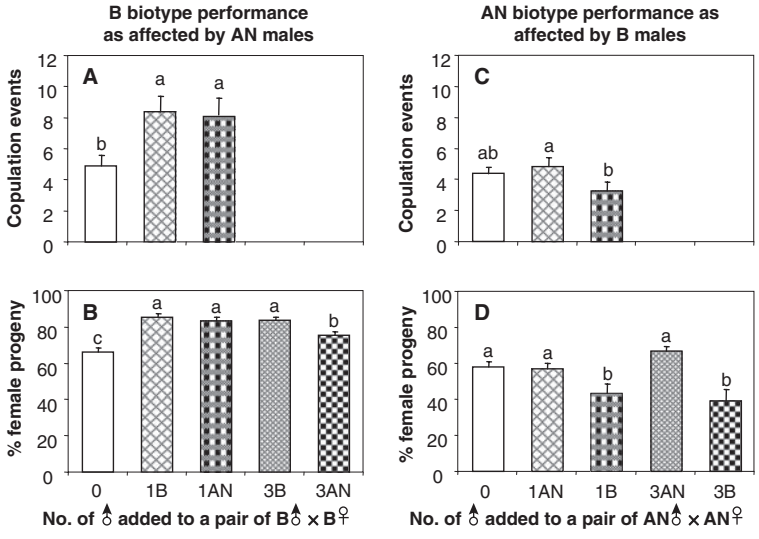

Fig. 4. Changes in the mean number of copulation events during the first 72 hours after emergence and production of progeny for the first 5 days after emergence when a pair of B biotype ♂×♀ was supplemented with one or three ♂ of the B or the indigenous AN biotype (**A** and **B**), or when a pair of the AN biotype ♂×♀ was supplemented with one or three ♂ of the AN or B biotype (**C** and **D**). We conducted 15 to 30 replicates for each of the treatments. One-way ANOVA and LSD tests were applied to each of the four data sets, and the data in (B) and (D) were transformed by arcsine square root before analysis. For (A), $F_{2,42} = 3.28$, $P = 0.048$; for (B), $F_{4,115} = 15.76$, $P < 0.001$; for (C), $F_{2,57} = 3.24$, $P = 0.047$; and for (D), $F_{4,133} = 7.16$, $P < 0.001$. Means ± SEM of the number of progeny produced by B females in the five treatments in (B) were 36.7 ± 2.7, 37.8 ± 2.9, 35.0 ± 2.8, 38.4 ± 2.7, and 36.2 ± 2.6, respectively, and the means did not differ significantly ($F_{4,115} = 0.248$, $P = 0.910$). Means ± SEM of the number of progeny produced by AN females in the five treatments in (D) were 44.2 ± 2.7, 44.8 ± 1.7, 41.5 ± 3.0, 41.0 ± 3.2, and 47.7 ± 3.0, respectively, and the means did not differ significantly ($F_{4,133} = 0.83$, $P = 0.505$). Different letters above bars indicate significant differences; error bars indicate SE.

when males of two biotypes were present with a female of a given biotype in the same arena, the B male and female responded by increasing their frequency of courtships, leading to more copulation events, whereas the ZHJ1 male and female did not do so. Moreover, although courtships between the two biotypes occurred, copulation never resulted; this confirmed that both B and ZHJ1 share incompletely isolated mate recognition systems. Further, B males not only courted females of either biotype more frequently than did ZHJ1 males, they also interfered more frequently with the courtships initiated by ZHJ1 males than did ZHJ1 males with courtships initiated by B males (tables S2 and S3). The mating behavior and interactions between B and AN differed in ways similar to what we found for B and ZHJ1, although details varied between the two combinations (*18*) (tables S4 and S5).

These results help to explain the underlying basis of the B biotype's capacity to invade and displace indigenous populations. The strong competitive ability of B results partly from its capacity to adjust sex ratio in favor of its population increase, and partly from its capacity to interfere with the mating of indigenous individuals. When the proportion of males is increased, B adults respond by increasing the frequency of copulation and consequently increasing the proportion of female progeny. Critical to this is that B responds independently of whether the males are all B or a mix. This interaction is extraordinary because the indigenous males actually help to promote copulation among the invaders and consequently increase the invaders' competitive capacity. In contrast, the indigenous females do not respond to increased numbers of adult males. Moreover, copulation by indigenous individuals is partly blocked by B males that readily attempt to court with females of either biotype—a behavior not reciprocated by the indigenous males. These asymmetric mating interactions have obvious population-level implications because the increase in the proportion of B females and the concomitant decrease in the proportion of indigenous females results in an immediate higher population growth rate for B and a lower growth rate for the indigenous population. As the abundance of B increases relative to the indigenous individuals, the increased allocation of eggs to female progeny and the active interference of mating of indigenous males by B males combine to drive the indigenous population to local extinction.

Mating interactions between closely related but reproductively isolated genetic groups are likely a common phenomenon (*3*, *22*–*24*) and are expected given the widespread existence of hybridization and introgression (*25*). Although examples of asymmetric competition are well known (*26*–*28*), asymmetric mating interactions are less well described (*28*). The rarity of examples may be, as illustrated by this study, the consequence of such interactions leading to the rapid displacement of the disadvantaged organisms. Biological invasions offer opportunities to gauge and characterize the potential magnitude and form of asymmetric mating interactions before species are lost through competitive exclusion or before the importance of competition is reduced over evolutionary time through niche partitioning and character displacement.

Allopatric species often demonstrate greater similarity in mating signals than do sympatric species, even when they have been diverging for a similar length of time (*3*). As a consequence of biological invasions, previously allopatric species are brought together and their partially similar mate recognition systems may promote asymmetric mating interactions between them. As we have shown, these interactions may play a critical role in determining the capacity of the invader to establish itself and the consequences for indigenous species.

References and Notes

1. J. L. Lookwood, M. F. Hoopes, M. P. Marchetti, *Invasion Ecology* (Blackwell, Malden, MA, 2007).
2. D. A. Holway, A. V. Suarez, *Trends Ecol. Evol.* **14**, 328 (1999).
3. R. Butlin, in *Speciation and the Recognition Concept, Theory and Application*, D. M. Lambert, H. G. Spencer, Eds. (Johns Hopkins Univ. Press, Baltimore, 1995), pp. 327.
4. J. K. Brown, D. R. Frohlich, R. C. Rosell, *Annu. Rev. Entomol.* **40**, 511 (1995).
5. L. M. Boykin *et al.*, *Mol. Phylogenet. Evol.* **44**, 1306 (2007).
6. M. Jiu *et al.*, *PLoS ONE* **2**, e182 (2007).
7. P. J. De Barro, J. W. H. Trueman, D. R. Frohlich, *Bull. Entomol. Res.* **95**, 193 (2005).
8. T. M. Perring *et al.*, *Science* **259**, 74 (1993).
9. International Union for the Conservation of Nature and Natural Resources (IUCN) list (www.issg.org).
10. R. Rekha, M. N. Maruthi, V. Muniyappa, J. Colvin, *Entomol. Exp. Appl.* **117**, 221 (2005).
11. T. M. Perring, in *Bemisia 1995: Taxonomy, Biology, Damage, Control and Management*, D. Gerling, R. T. Mayer, Eds. (Intercept, Andover, UK, 1996), p. 3–16.
12. L. H. C. Lima *et al.*, *Genet. Mol. Biol.* **25**, 217 (2002).
13. L. S. Zang, W. Q. Chen, S. S. Liu, *Entomol. Exp. Appl.* **121**, 221 (2006).
14. P. J. De Barro, P. J. Hart, *Bull. Entomol. Res.* **90**, 103 (2000).
15. P. J. De Barro, A. Bourne, S. A. Khan, V. A. L. Brancatini, *Biol. Invas.* **8**, 287 (2006).
16. C. Luo *et al.*, *Acta Entomol. Sin.* **45**, 759 (2002).
17. R. V. Gunning *et al.*, *J. Aust. Entomol. Soc.* **34**, 116 (1995).
18. See supporting material on *Science* Online.
19. L. S. Zang, S. S. Liu, *J. Insect Behav.* **20**, 157 (2007).
20. D. N. Byrne, T. S. Bellows, *Annu. Rev. Entomol.* **36**, 431 (1991).
21. Y. M. Ruan, J. B. Luan, L. S. Zang, S. S. Liu, *Entomol. Exp. Appl.* **124**, 229 (2007).
22. D. K. Mclain, D. J. Shure, *Oikos* **49**, 291 (1987).
23. B. Takafuji, E. Kuno, H. Fujimoto, *Exp. Appl. Acarol.* **21**, 379 (1997).
24. J. Yoshimura, W. T. Starmer, *Res. Popul. Ecol. (Kyoto)* **39**, 191 (1997).
25. J. M. Rhymer, D. Simberloff, *Annu. Rev. Ecol. Syst.* **27**, 83 (1996).
26. J. H. Lawton, M. P. Hassell, *Nature* **289**, 793 (1981).
27. R. F. Denno, M. S. McClure, J. R. Ott, *Annu. Rev. Entomol.* **40**, 297 (1995).
28. S. R. Reitz, J. T. Trumble, *Annu. Rev. Entomol.* **47**, 435 (2002).

29. We thank J. Liu, L. Zhang, K.-K. Lin, Z.-Y. Xiao, and G.-H. Yan for technical assistance, and J. Colvin, M. Dicke, A. Hoffmann, J. Trumble, T. Turlings, and M. Zalucki for comments and discussion. Supported by the National Basic Research and Development Program of China, National Natural Science Foundation of China, Ministry of Education of China, CSIRO Entomology, Horticulture Australia, and the Grains and Cotton Research and Development Corporations.

Supporting Online Material

www.sciencemag.org/cgi/content/full/1149887/DC1
Materials and Methods
SOM Text
Figs. S1 to S4
Tables S1 to S5
References

29 August 2007; accepted 11 October 2007
Published online 8 November 2007;
10.1126/science.1149887
Include this information when citing this paper.

Declining Wild Salmon Populations in Relation to Parasites from Farm Salmon

Martin Krkošek,[1,2]† Jennifer S. Ford,[3] Alexandra Morton,[4] Subhash Lele,[1] Ransom A. Myers,[3]* Mark A. Lewis[1,2]

Rather than benefiting wild fish, industrial aquaculture may contribute to declines in ocean fisheries and ecosystems. Farm salmon are commonly infected with salmon lice (*Lepeophtheirus salmonis*), which are native ectoparasitic copepods. We show that recurrent louse infestations of wild juvenile pink salmon (*Oncorhynchus gorbuscha*), all associated with salmon farms, have depressed wild pink salmon populations and placed them on a trajectory toward rapid local extinction. The louse-induced mortality of pink salmon is commonly over 80% and exceeds previous fishing mortality. If outbreaks continue, then local extinction is certain, and a 99% collapse in pink salmon population abundance is expected in four salmon generations. These results suggest that salmon farms can cause parasite outbreaks that erode the capacity of a coastal ecosystem to support wild salmon populations.

The decline in ocean fisheries (*1*, *2*) and rise in global demand for fish have driven the rapid growth of aquaculture (*3*, *4*). Although aquaculture may augment fish supply (*3*), there are ecological risks, including competition and interbreeding of escaped farm fish with wild fish (*5*, *6*), depletion of wild fish caught to feed farm fish (*3*, *4*), and the spread of infec-

tion from farm fish to wild fish (*7*, *8*). Disease threats of aquaculture to wild fish populations have long been contentious because of the uncertainty in impacts on those populations (*9*–*12*). We assess the impact of recurrent aquaculture-induced salmon lice (*L. salmonis*) infestations on wild pink salmon (*O. gorbuscha*) populations.

The salmon louse is a native marine ectoparasitic copepod of salmonids that feeds on surface tissues and causes stress, osmotic failure, viral or bacterial infection, and ultimately death (*13*). Lice are directly transmitted via planktonic nauplii and copepodids that can persist for several days. In areas without salmon farms, the prevalence of *L. salmonis* on juvenile pink salmon 2 to 3 months after marine emergence is low (<5%) (*14*–*16*), because returning adult salmon are mostly offshore when juvenile salmon enter the sea (*16*, *17*). Louse infestations of wild juvenile salmon have occurred throughout the Broughton Archipelago in Pacific Canada (Fig. 1) from 2001 to 2005 (*7*, *8*, *14*, *18*, *19*). There, salmon farms situated in inlets and channels near rivers can increase copepodid densities above background levels for more than 80 km of wild salmon migration routes or, equivalently, for the first 2.5 months of the wild salmon's marine life (*8*). In response to a pink salmon population collapse in 2002, a primary migration corridor was fallowed in 2003 (i.e., farm salmon were removed from aquaculture facilities in Tribune Channel through Fife Sound, but farms peripheral to this route remained active) (Fig. 1). For that salmon cohort, *L. salmonis* abundance declined (*19*), and pink salmon marine survival increased (*20*).

To test for effects of lice on salmon population dynamics, we compiled Fisheries and Oceans Canada escapement data (the number of salmon per river), from 1970 to the present, for all pink salmon populations from rivers in the central coast of British Columbia, Canada (Fig. 1). There were 64 rivers whose salmon populations were not exposed to salmon farms and 7 rivers whose salmon populations must migrate past at least one salmon farm. Because pink salmon have a 2-year life cycle, there are distinct odd- and even-year lineages (*21*), which amount to 128 unexposed populations and 14 exposed populations. Rivers with substantial enhancement (e.g., spawning channels) were excluded because any increased salmon abundances in these rivers confound our estimates of natural changes in abundance. Unexposed populations had been and continue to be commercially fished. Exposed populations were commercially fished before the infestations, but the fishery remains closed since the onset of the infestations, when the data show a marked decline in productivity (Fig. 2 and fig. S1).

The analysis was based on the Ricker model (*22*), which is commonly used to model time-series data from density-dependent populations (*23*–*26*), including pink salmon (*24*, *26*), and provides robust estimates of population growth rates (*24*). The model is $n_i(t) = n_i(t-2)\exp[r - bn_i(t-2)]$, where $n_i(t)$ is the abundance of population i in year t, r is the population growth rate, and b determines density-dependent mortality. Upon log transformation to $\log[n_i(t)/n_i(t-2)] = r - bn_i(t-2)$, the Ricker equation becomes a linear model with intercept r and slope b that can be estimated by linear regression and hierarchical mixed-effects modeling (*23*, *24*, *27*, *28*). A preliminary model selection analysis did not support including random effects on r or b (fig. S2 and tables S1 and S2) (*27*). We therefore pooled data from multiple populations (*27*) and used linear regression to estimate parameters and parametric bootstrapping to construct 95% confidence intervals (CIs) on the parameter estimates (*23*). This allowed us to statistically compare parameters from pooled populations subjected to infestations, which is not possible with hierarchical mixed-effects models because there are only two data points per population during infestation years.

We compared parameter estimates among three groups: unexposed populations, exposed

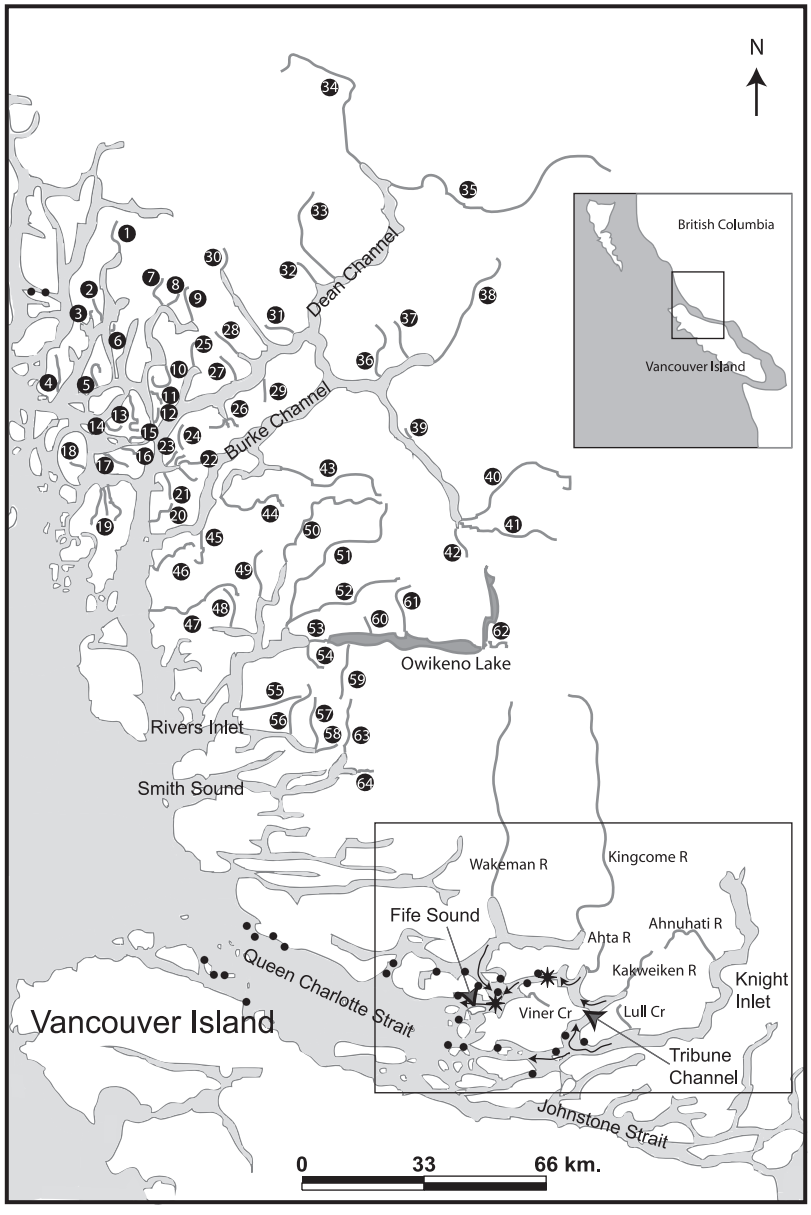

Fig. 1. Study area in the Broughton Archipelago (boxed area in inset), depicting pink salmon populations from unexposed rivers (numbered circles) and exposed rivers (directly labeled within the lower rectangular frame). Inferred migration routes in the Broughton Archipelago are shown by the small arrows. Salmon farms are shown by black dots and sample sites by stars. Salmon farms south of Knight Inlet are not shown. Identities of the numbered (unexposed) rivers are provided in data set S1 (*28*).

[1]Centre for Mathematical Biology, Department of Mathematical and Statistical Sciences, University of Alberta, Edmonton, AB, Canada. [2]Department of Biological Sciences, University of Alberta, Edmonton, AB, Canada. [3]Biology Department, Dalhousie University, Halifax, NS, Canada. [4]Salmon Coast Field Station, Simoom Sound, BC, Canada.

*Deceased.

†To whom correspondence should be addressed. E-mail: mkrkosek@ualberta.ca

preinfestation populations, and exposed populations during infestations (excluding the fallow year). The groups did not differ in b, and so we reanalyzed the data with b fixed among the three groups. Unexposed populations did not differ from exposed preinfestation populations in growth rate (unexposed populations: $r = 0.62$, 95% CI: 0.55 to 0.69; exposed preinfestation populations: $r = 0.68$, 95% CI: 0.46 to 0.90). The growth rate of exposed populations during the infestations was significantly lower and significantly negative ($r = –1.17$, 95% CI: –1.71 to –0.59; Fig. 3), meaning that if infestations are sustained, then local extinction is certain (*29*). Population viability analysis (*28*, *29*) revealed the mean time to 99% population collapse is 3.9 generations, with the 95% CI from 3.7 to 4.2. During two generations of infestations, some exposed populations have declined to <1%, whereas others have exceeded their historical abundance. We initially excluded the fallow data, because they contain only 1 year of observations and correspond to a nonrandom management action. By fixing $b = 0.64$, as estimated above, and estimating r from the remaining seven data points, we found the growth rate of fallow populations was significantly increased ($r = 2.50$, 95% CI: 1.28 to 3.62). The maximum reproductive rate for pink salmon is $r^* = 1.2$ (*24*). Fishing mortality probably reduced r for unexposed and exposed preinfestation populations. The depressed growth rate of exposed salmon populations during the infestations indicates that previous fishing mortality (now ceased) has been greatly exceeded by louse-induced mortality.

To estimate the mortality of pink salmon caused by lice, we extended the Ricker model to directly accommodate louse data collected from exposed populations during the infestations (*14*, *18*, *19*, *28*). We constrained the model by fixing $b = 0.64$ and by requiring $r = r^* = 1.2$, because there was no fishing mortality. Louse-induced mortality is represented by multiplying by $\exp[-aP_i(t-1)]$, where P is the mean abundance of motile (adult and preadult) lice per juvenile salmon from population i that spawned in year t. We log-transformed the model to $\log[n_i(t)/n_i(t-2) = r - bn_i(t-2) - aP_i(t)]$ and used linear regression to estimate a. The term $\exp[-aP_i(t-1)]$ significantly improved the fit of the model ($t = –5.019$, df = 33, $P = 1.74 \times 10^{-5}$; fig. S3), and results remained strong when the data were restricted by averaging populations and excluding some population groups ($P < 0.005$ for all groups; table S3). The parameter a corresponds to the rate of parasite-induced host mortality multiplied by the time that juvenile salmon are exposed to the parasites, $a = \alpha T$. The exposure time, T, is about 2 months (based on the migration speed of juvenile pink salmon through the archipelago), and the value of α has been estimated at 0.022 (motile lice × day)$^{-1}$ (based on survival experiments of naturally infected juvenile pink salmon) (*8*). Dividing the estimated $a = 0.89$ (95% credible intervals are from 0.46 to 1.34) by 60 days reveals an excellent correspondence between these two independent estimates of pathogenicity ($a/60 = 0.015$, with 95% credible estimates from 0.0077 to 0.022). Using a hierarchical Bayesian simulation (*28*) that represents uncertainty in the model fit as well as in the distribution of r^* (*12*), we found the estimated mortality of pink salmon, $1 - \exp[-aP_i(t-1)]$, caused by lice ranged from 16% to over 97% and was commonly over 80% (Table 1). The lowest mortality comes from fallow populations when louse abundance was nevertheless elevated, possibly resulting from transmission from active farms outside the fallowed corridor (*7*, *19*, *20*).

These results provide strong empirical evidence that salmon farm–induced *L. salmonis* infestations of juvenile pink salmon have depressed wild pink salmon populations and may lead to their local extinction. However, this parasite threat may not exist at low farm salmon abundances; the delay between the onset of salmon aquaculture in 1987 and louse infestations in 2001 (Fig. 2) may be explained by farm fish abundance crossing a host density threshold above which outbreak conditions occur (*30*). It is unlikely that another factor is responsible: The increased growth rate in response to fallowing rules out other factors that could have affected exposed, but not unexposed, populations. The results rely on extensive spatial replication to compensate for short time series in infestation

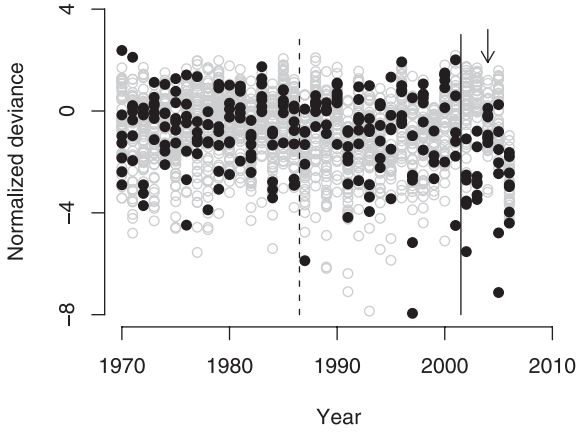

Fig. 2. Time series of normalized population deviances {$\log[N_i(t)/m_i]$, where $N_i(t)$ is the population estimate for population i in year t and m_i is the time-series mean abundance for population i} for 128 control populations of pink salmon (open gray circles) and 14 pink salmon populations exposed to salmon farms (black circles). The vertical dashed line marks the beginning of salmon aquaculture in the Broughton Archipelago. The vertical solid line marks the onset of louse infestations (and the commercial fishery closure) affecting the exposed populations. The arrow indicates data for exposed pink salmon cohorts that, as juveniles, experienced a fallowed migration corridor.

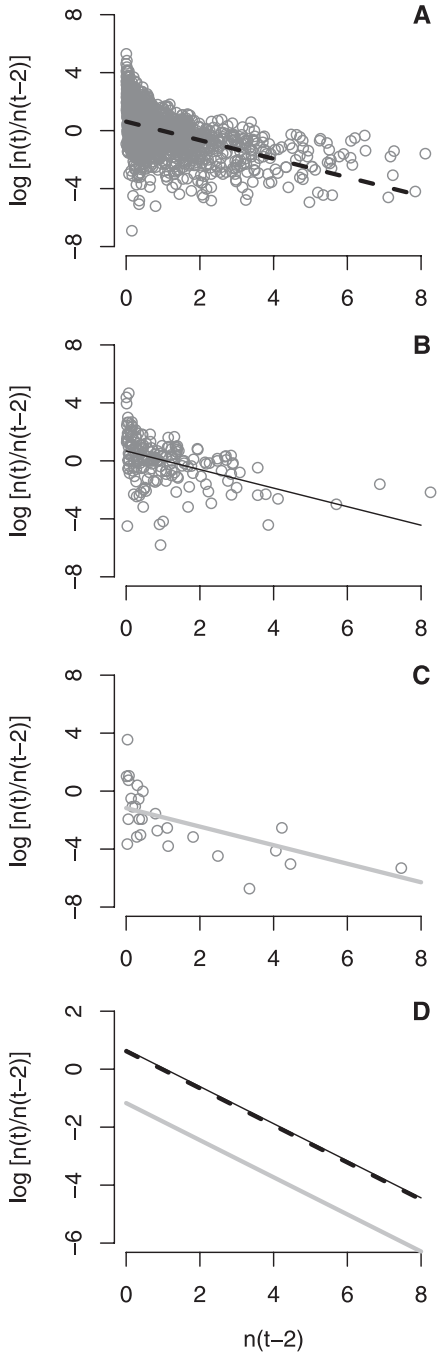

Fig. 3. Fits of the log-transformed Ricker model to escapement data for unexposed populations (**A**), exposed populations before infestations (**B**), and exposed populations during the infestations (**C**), and a comparison of the log-transformed Ricker model for the three groups in panels (A) to (C) (**D**). The intercept (growth rate) is lower for the exposed population during the infestations than for exposed populations before the infestations and the unexposed populations.

Table 1. Mean abundances, *P*, of motile *L. salmonis* on juvenile pink salmon and estimated parasite-induced host mortality, *M* (with upper and lower bounds of the 95% credible interval in parentheses), for exposed populations during infestations.

River	2002		2003		2004*		2005		2006	
	P	*M*	*P*	*M*	*P*	*M*	*P*	*M*	*P*	*M*
Ahta	3.4	95.21 (79.07, 98.95)	1.0	59.09 (36.87, 73.82)	0.3	23.52 (12.89, 33.10)	2.6	90.21 (69.76, 96.93)	0.4	30.06 (16.81, 41.49)
Kakweiken	3.4	95.21 (79.07, 98.95)	1.0	59.09 (36.87, 73.82)	0.3	23.52 (12.89, 33.10)	2.6	90.21 (69.76, 96.93)	0.4	30.06 (16.81, 41.49)
Viner	4.0	97.20 (84.12, 99.53)	2.2	86.00 (63.65, 94.76)	0.2	16.37 (8.79, 23.51)	2.3	87.20 (65.29, 95.41)	1.4	71.39 (47.48, 84.68)
Wakeman	4.0	97.20 (84.12, 99.53)	2.2	86.00 (63.65, 94.76)	0.2	16.37 (8.79, 23.51)	2.3	87.20 (65.29, 95.41)	1.4	71.39 (47.48, 84.68)
Kingcome	4.0	97.20 (84.12, 99.53)	2.2	86.00 (63.65, 94.76)	0.2	16.37 (8.79, 23.51)	2.3	87.20 (65.29, 95.41)	1.4	71.39 (47.48, 84.68)
Ahnuhati	2.6	90.21 (69.76, 96.93)	0.7	46.51 (27.53, 60.86)	0.2	16.37 (8.79, 23.51)	1.9	81.70 (58.27, 92.16)	0.3	23.52 (12.89, 33.10)
Lull	2.6	90.21 (69.76, 96.93)	0.7	46.51 (27.53, 60.86)	0.2	16.37 (8.79, 23.51)	1.9	81.70 (58.27, 92.16)	0.3	23.52 (12.89, 33.10)

*These data correspond to the salmon cohort responding to the fallow treatment in 2003.

years. The time to reach sufficient temporal replication to support hierarchical mixed-effects modeling, say 10 generations (which equals 20 years), greatly exceeds the predicted time to extinction. That is, there is a major risk associated with waiting for large data sets to accumulate before implementing conservation policy. Industrial aquaculture is rapidly expanding to new species, regions, and habitats (*31*), which can create parasite outbreaks that contribute to the decline of ocean fisheries and ecosystems.

References and Notes

1. J. B. C. Jackson *et al.*, *Science* **293**, 629 (2001).
2. R. A. Myers, B. Worm, *Nature* **423**, 280 (2003).
3. R. L. Naylor *et al.*, *Nature* **405**, 1017 (2000).
4. R. Goldburg, R. Naylor, *Front. Ecol. Environ.* **3**, 21 (2005).
5. I. A. Fleming *et al.*, *Proc. R. Soc. London Ser. B* **267**, 1517 (2000).
6. J. P. Volpe, B. R. Anholt, B. W. Glickman, *Can. J. Fish. Aquat. Sci.* **58**, 197 (2001).
7. M. Krkošek, M. A. Lewis, J. P. Volpe, *Proc. R. Soc. London Ser. B* **272**, 689 (2005).
8. M. Krkošek, M. A. Lewis, A. Morton, L. N. Frazer, J. P. Volpe, *Proc. Natl. Acad. Sci. U.S.A.* **103**, 15506 (2006).
9. A. H. McVicar, *ICES J. Mar. Sci.* **54**, 1093 (1997).
10. D. J. Noakes, R. J. Beamish, M. L. Kent, *Aquaculture* **183**, 363 (2000).
11. A. H. McVicar, *Aquac. Res.* **35**, 751 (2004).
12. R. Hilborn, *Proc. Natl. Acad. Sci. U.S.A.* **103**, 15277 (2006).
13. A. W. Pike, S. L. Wadsworth, *Adv. Parasitol.* **44**, 233 (2000).
14. A. Morton, R. Routledge, C. Peet, A. Ladwig, *Can. J. Fish. Aquat. Sci.* **61**, 147 (2004).
15. C. R. Peet, thesis, University of Victoria (2007).
16. M. Krkošek *et al.*, *Proc. R. Soc. London Ser. B* **274**, 3141 (2007).
17. C. Groot, L. Margolis, Eds. *Pacific Salmon Life Histories* (UBC Press, Vancouver, 1991).
18. A. B. Morton, R. Williams, *Can. Field Nat.* **117**, 634 (2003).
19. A. Morton, R. D. Routledge, R. Williams, *N. Am. J. Fish. Manage.* **25**, 811 (2005).
20. R. J. Beamish *et al.*, *ICES J. Mar. Sci.* **63**, 1326 (2006).
21. W. R. Heard, in (*17*), pp. 119–230.
22. W. E. Ricker, *J. Fish. Res. Board Can.* **11**, 559 (1954).
23. B. Dennis, M. L. Taper, *Ecol. Monogr.* **64**, 205 (1994).
24. R. A. Myers, K. G. Bowen, N. J. Barrowman, *Can. J. Fish. Aquat. Sci.* **56**, 2404 (1999).
25. B. W. Brook, C. J. A. Bradshaw, *Ecology* **87**, 1445 (2006).
26. F. J. Mueter, R. M. Peterman, B. J. Pyper, *Can. J. Fish. Aquat. Sci.* **59**, 456 (2002).
27. J. C. Pinheiro, D. M. Bates, *Mixed-Effects Models in S and S-PLUS* (Springer, New York, 2004).
28. Materials and methods are available as supporting material on *Science* Online.
29. B. Dennis, P. L. Munholland, J. M. Scott, *Ecol. Monogr.* **61**, 115 (1991).
30. J. O. Lloyd-Smith *et al.*, *Trends Ecol. Evol.* **20**, 511 (2005).
31. C. M. Duarte, N. Marbá, M. Holmer, *Science* **316**, 382 (2007).

32. We dedicate this paper to our coauthor, Ransom Myers, who passed away before the completion of this work. We thank J. Volpe, J. Reynolds, L. Dill, M. Wonham, B. Connors, and A. Gottesfeld for helpful comments; A. Park for assistance in preparing data and figures; and Fisheries and Oceans Canada stock assessment scientists who collected and shared data. Funding came from the Natural Science and Engineering Research Council of Canada, the Canadian Mathematics of Information Technology and Complex Systems National Centre of Excellence Network on Biological Invasions and Dispersal Research (with nonacademic participants including the David Suzuki Foundation, Canadian Sablefish Association, Wilderness Tourism Association, and Finest at Sea), the National Geographic Society, Tides Canada, a University of Alberta Bill Shostak Wildlife Award, the Lenfest Ocean Program, Census of Marine Life, and a Canada Research Chair.

Supporting Online Material

www.sciencemag.org/cgi/content/full/318/58571772/DC1
Materials and Methods
Figs. S1 to S3
Tables S1 to S3
Dataset S1

2 August 2007; accepted 2 November 2007
10.1126/science.1148744

Habitat Split and the Global Decline of Amphibians

Carlos Guilherme Becker,[1,2] Carlos Roberto Fonseca,[2]* Célio Fernando Baptista Haddad,[3] Rômulo Fernandes Batista,[4] Paulo Inácio Prado[5]

The worldwide decline in amphibians has been attributed to several causes, especially habitat loss and disease. We identified a further factor, namely "habitat split"—defined as human-induced disconnection between habitats used by different life history stages of a species—which forces forest-associated amphibians with aquatic larvae to make risky breeding migrations between suitable aquatic and terrestrial habitats. In the Brazilian Atlantic Forest, we found that habitat split negatively affects the richness of species with aquatic larvae but not the richness of species with terrestrial development (the latter can complete their life cycle inside forest remnants). This mechanism helps to explain why species with aquatic larvae have the highest incidence of population decline. These findings reinforce the need for the conservation and restoration of riparian vegetation.

Amphibian populations are declining worldwide (*1*, *2*). Among the factors determining the amphibian declines are habitat loss and fragmentation, which affect amphibians just as they affect any other organisms: through population isolation, inbreeding, and edge effects (*3*–*5*). Another important factor is the fungus *Batrachochytrium dendrobatidis*, a highly virulent pathogen that attacks many amphibian species and has been responsible for the decline of many populations even in undisturbed environments (*6*, *7*). Amphibians can also be threatened by climate shifts (*7*), ultraviolet-B radiation (*8*), introduction of exotic species (*9*), and agrochemical contaminants (*10*). We investigated the role of a further factor, which we define as "habitat split."

Amphibian species with aquatic larvae typically undergo a major ontogenetic niche shift, whereby tadpoles and adults occupy two distinct habitats (*11*). In pristine environments, the aquatic habitat of the tadpoles and the terrestrial habitat of the postmetamorphics grade into each other. However, in landscapes occupied by humans, land use has often resulted in a spatial separation between remnants of terrestrial habitat and breeding sites (*12*). Adults of species with aquatic larvae, in order to breed, are obliged to abandon forest remnants to reach water bodies, and at the end of the reproductive season, both

adults and juveniles are forced to locate and return to forest remnants (fig. S1). During this compulsory migration, they face multiple hazards that are associated with environmental conditions within the intervening matrix, such as dehydration, predation, agrochemicals, and other pollutants (*10*, *13*). Amphibians with terrestrial development, however, should not respond to habitat split, because they may be able to successfully reproduce irrespective of the presence or absence of water bodies. In human-altered landscapes, habitat split can be expected to reduce population sizes, decrease the extent and occupancy rates of metapopulations, and affect negatively the richness of local communities.

We tested the effect of habitat split on the richness of local amphibian communities, taking into account the influence of two additional landscape properties, habitat loss and fragmentation. The study was conducted in Brazil, which harbors a rich amphibian fauna (*14*, *15*). We focused particularly on the Atlantic Forest, one of the five most endangered biodiversity hot spots (*16*), which has more than 480 amphibian species (about 80% with aquatic larvae). Because less than 7% of the Atlantic Forest remains, habitat loss and fragmentation have been suggested as the main causes of the high frequency of threatened and declining amphibian species in the region (*14*–*17*). Although the Atlantic Forest riparian vegetation is in principle protected by legislation (Brazilian Forest Code 4771/65), land occupation has often been concentrated in valleys where water is readily available for agriculture, industry, and human consumption (*18*). This historical process has favored the occurrence of a large number of "dry fragments" that are disconnected at the landscape level from streams and other water sources (*18*), causing habitat split. Here, habitat loss is measured as the percentage of non-natural vegetation cover, habitat fragmentation is the ratio between the perimeter of forest edge and forest area, and habitat split is the percentage of the total stream length that does not overlap with forest cover; all of these metrics are calculated on a circular landscape of 15-km diameter (*19*).

Across the Atlantic Forest biome, habitat split was the best predictor of the species richness of leaf-litter forest amphibians [simple linear regression: $\beta = -0.140 \pm 0.026$ (SEM), $F_{1,10} = 29.040$, $P < 0.001$, $r^2 = 0.744$], followed by habitat loss ($\beta = -0.122 \pm 0.027$, $F_{1,10} = 21.321$, $P = 0.001$, $r^2 = 0.681$) and habitat fragmentation ($\beta = -7.643 \pm 2.509$, $F_{1,10} = 9.277$, $P = 0.012$, $r^2 = 0.481$). A path analysis, looking simultaneously at the effect of these three explanatory factors, showed that habitat split was the only significant factor negatively affecting the richness of leaf-litter amphibians (standardized path coefficient $= -1.025 \pm 0.514$, $P < 0.05$).

As expected, habitat split had a strong negative effect on the richness of species with aquatic larvae (simple linear regression: $\beta = -0.097 \pm 0.019$, $F_{1,10} = 25.134$, $P = 0.001$, $r^2 = 0.715$) and no effect on the richness of species with terrestrial development ($\beta = -0.042 \pm 0.027$, $F_{1,10} = 2.450$, $P = 0.149$, $r^2 = 0.197$; Fig. 1). Path analyses showed that habitat split was the single landscape metric affecting the richness of species with aquatic larvae (standardized path coefficient $= -1.944 \pm 0.433$, $P < 0.001$; Fig. 2A). In contrast, none of the three landscape metrics affected the richness of species with terrestrial development, although habitat loss exhibited the strongest path (Fig. 2B). The predominance of habitat split as the strongest factor influencing the richness of species with aquatic larvae remained unaltered after controlling, in turn, for latitude, altitude, altitudinal range, and mean annual rainfall (*19*).

Although herpetologists have recognized the importance of small-scale connections between the habitat of immatures and that of adults (*20*, *21*), our results suggest that the absence of these links might be a key driver of the loss of amphibian biodiversity. Habitat loss has an immediate direct effect on the size of amphibian populations by redefining the boundaries of their natural habitats (*3*). Habitat fragmentation acts on a longer time scale through population isolation, inbreeding, and edge effects (*3*–*5*). Habitat split is a strong force that can modify population size, structure, and distribution in a single generation.

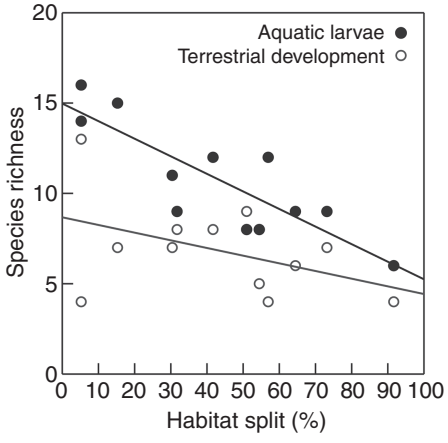

Fig. 1. Effect of habitat split on species richness of leaf-litter amphibians with aquatic larvae and with terrestrial development across 12 Brazilian Atlantic Forest landscapes. Habitat split is calculated as the percentage of the total stream length that does not overlap with natural forest cover. Linear regression lines are shown.

Habitat split should most strongly affect species with aquatic larvae. This can contribute to explaining why a disproportionate number of records of population declines are from amphibian species that have aquatic larvae, especially stream-breeders (*14*, *17*, *22*–*24*). Water-transmitted diseases and water pollution are also important factors producing this bias (*6*, *10*). Our study evaluated the effect of habitat split in relation to streams, but it can also be accessed in relation to other breeding habitats, such as ponds. For instance, the occupancy of ponds by North American anurans and salamanders with aquatic larvae was affected by the distance to the nearest vegetation patch (*20*).

Habitat split is likely to be a major influence on other taxa that undergo ontogenetic habitat shifts, including many terrestrial invertebrates with aquatic larvae. Other vertebrates can also suffer from habitat split. The reproductive migration of a wide variety of freshwater fishes is known to be blocked or jeopardized by dams (*25*). Continental migration of waterbirds has been put at risk with the loss of stopover wetlands reducing the connectivity between breeding and foraging sites (*26*).

A wide range of conservation strategies has been proposed to halt the global decline of amphibians, including a recent international call for ex situ conservation facilities (*27*–*29*). Where pristine environments are still available, as in the Amazon, the establishment of large biological reserves comprising whole hydrographic catchments is the best in situ conservation strategy. In landscapes undergoing modification, specific laws for conserving riparian zones connecting terrestrial and aquatic habitats should be introduced or enforced. Where habitat split has already occurred, restoration programs (*30*) should be undertaken to reverse its negative effects on amphibian diversity.

[1]Departamento de Zoologia, Universidade Estadual de Campinas, 13083-970 Campinas SP, Brazil. [2]Laboratório de Interação Animal-Planta, Universidade do Vale do Rio dos Sinos, 93022-970 São Leopoldo RS, Brazil. [3]Departamento de Zoologia, Universidade Estadual Paulista Júlio de Mesquita Filho, Cx. Postal 199, 13506-900 Rio Claro SP, Brazil. [4]Secretaria Estadual do Meio Ambiente e Desenvolvimento Sustentável do Amazonas, 69050-030 Manaus AM, Brazil. [5]Departamento de Ecologia, Instituto de Biociências, Universidade de São Paulo, 05508-900 São Paulo SP, Brazil.

*To whom correspondence should be addressed. E-mail: cfonseca@unisinos.br

References and Notes

1. R. A. Alford, S. J. Richards, *Annu. Rev. Ecol. Syst.* **30**, 133 (1999).
2. T. J. C. Beebee, R. A. Griffiths, *Biol. Conserv.* **125**, 271 (2005).
3. S. A. Cushman, *Biol. Conserv.* **128**, 231 (2006).
4. R. H. MacArthur, E. O. Wilson, *The Theory of Island Biogeography* (Princeton Univ. Press, Princeton, NJ, 1967).
5. I. Hanski, *Nature* **396**, 41 (1998).
6. K. R. Lips *et al.*, *Proc. Natl. Acad. Sci. U.S.A.* **103**, 3165 (2006).
7. J. A. Pounds *et al.*, *Nature* **439**, 161 (2006).
8. A. R. Blaustein, P. T. Johnson, *Front. Ecol. Environ.* **1**, 87 (2003).
9. L. B. Kats, R. P. Ferrer, *Divers. Distrib.* **9**, 99 (2003).
10. R. A. Relyea, *Ecol. Appl.* **15**, 1118 (2005).
11. E. E. Werner, J. F. Gilliam, *Annu. Rev. Ecol. Syst.* **15**, 393 (1984).
12. J. B. Dunning, B. J. Danielson, H. R. Pulliam, *Oikos* **65**, 169 (1992).
13. M. J. Mazerolle, A. Desrochers, *Can. J. Zool.* **83**, 455 (2005).
14. IUCN, Conservation International, NatureServe, Global Amphibian Assessment (www.globalamphibians.org), accessed 20 May 2007.

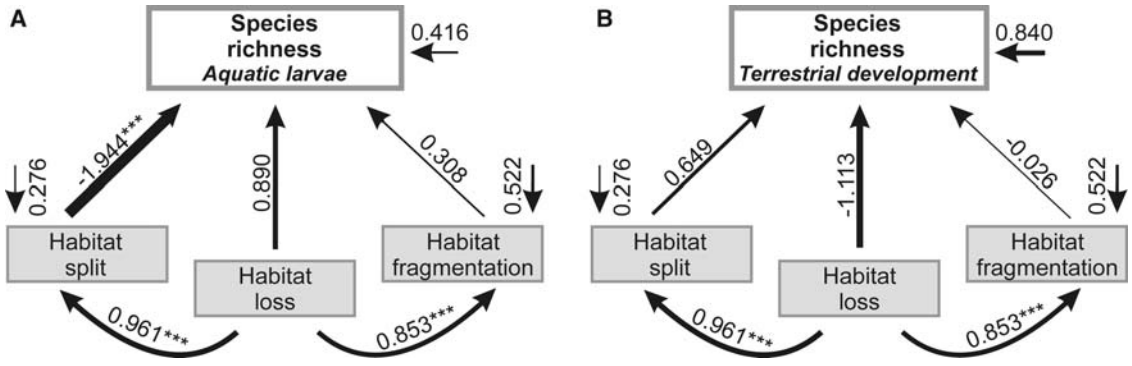

Fig. 2. Path analysis models showing the relative strength of habitat split, habitat loss, and habitat fragmentation on species richness of Brazilian Atlantic Forest leaf-litter amphibians (N = 12 study sites). (**A**) Species with aquatic larvae. (**B**) Species with terrestrial development. Numbers are standardized path coefficients (***P < 0.001). The thickness of the arrows represents the relative strength of the relationship.

15. D. L. Silvano, M. V. Segalla, *Conserv. Biol.* **19**, 653 (2005).
16. R. A. Mittermeier *et al.*, *Hotspots Revisited: Earth's Biologically Richest and Most Endangered Terrestrial Ecoregions* (Univ. of Chicago Press, Chicago, 2005).
17. P. C. Eterovick *et al.*, *Biotropica* **37**, 166 (2005).
18. V. M. Viana, A. A. J. Tabanez, J. L. F. Batista, in *Tropical Forest Remnants: Ecology, Management and Conservation of Fragmented Communities*, W. F. Laurance, R. O. Bierregaard, Eds. (Univ. of Chicago Press, Chicago, 1997), pp. 347–365.
19. See supporting material on *Science* Online.
20. A. D. Guerry, M. L. Hunter, *Conserv. Biol.* **16**, 745 (2002).
21. T. A. G. Rittenhouse, R. D. Semlitsch, *Wetlands* **27**, 153 (2007).
22. K. R. Lips, J. D. Reeve, L. R. Witters, *Conserv. Biol.* **17**, 1078 (2003).
23. R. M. Bustamante, S. R. Ron, L. A. Coloma, *Biotropica* **37**, 180 (2005).
24. J. M. Hero, S. E. Williams, W. E. Magnusson, *J. Zool.* **267**, 221 (2005).
25. J. Carolsfeld, B. Harvey, C. Ross, A. Baer, Eds., *Migratory Fishes of South America: Biology, Fisheries and Conservation Status* (IDRC Press, Victoria, BC, Canada, 2004).
26. J. M. Amezaga, L. Santamaria, A. J. Green, *Acta Oecol.* **23**, 213 (2002).
27. J. R. Mendelson III *et al.*, *Science* **313**, 48 (2006).
28. J. A. Pounds *et al.*, *Science* **314**, 1541 (2006).
29. J. R. Mendelson III *et al.*, *Science* **314**, 1541 (2006).
30. B. Wuethrich, *Science* **315**, 1070 (2007).

31. We thank K. Lips, A. Pounds, C. Gascon, T. Halliday, J.-M. Hero, T. Gardner, M. Almeida-Neto, T. Grant, P. Eterovick, R. Loyola, A. Freitas, E. G. F. Benya, and M. F. Kersch for critically reviewing previous versions of the manuscript; S. Stuart, J. Chanson (World Conservation Union–Global Amphibian Assessment), T. Halliday, and J. Kauffman (Declining Amphibian Populations Task Force) for providing updated versions of their database; M. Dixo, M. Hartmann, I. Martins, and C. Oliveira for performing some of the field surveys; and J. Giovanelli and U. Kubota for assistance in spatial and statistical analyses. Supported by a scholarship from the Fundação de Amparo à Pesquisa do Estado de São Paulo (FAPESP: 04/13132-3) (C.G.B.), fellowships from the Conselho Nacional de Desenvolvimento Científico e Tecnológico (CNPq: 305428/2005-5, 302512/2005-5) (C.R.F. and C.F.B.H.), Programa BIOTA/FAPESP (01/13341-3, 02/08558-6), and Universidade do Vale do Rio dos Sinos.

Supporting Online Material

www.sciencemag.org/cgi/content/full/318/5857/1775/DC1
Materials and Methods
Fig. S1
Table S1
References

17 August 2007; accepted 6 November 2007
10.1126/science.1149374

Serine-7 of the RNA Polymerase II CTD Is Specifically Required for snRNA Gene Expression

Sylvain Egloff,[1] Dawn O'Reilly,[1] Rob D. Chapman,[2] Alice Taylor,[1] Katrin Tanzhaus,[1] Laura Pitts,[1] Dirk Eick,[2] Shona Murphy[1]*

RNA polymerase II (Pol II) transcribes genes that encode proteins and noncoding small nuclear RNAs (snRNAs). The carboxyl-terminal repeat domain (CTD) of the largest subunit of mammalian RNA Pol II, comprising tandem repeats of the heptapeptide consensus Tyr[1]-Ser[2]-Pro[3]-Thr[4]-Ser[5]-Pro[6]-Ser[7], is required for expression of both gene types. We show that mutation of serine-7 to alanine causes a specific defect in snRNA gene expression. We also present evidence that phosphorylation of serine-7 facilitates interaction with the snRNA gene–specific Integrator complex. These findings assign a biological function to this amino acid and highlight a gene type–specific requirement for a residue within the CTD heptapeptide, supporting the existence of a CTD code.

Human snRNA genes transcribed by Pol II, including those encoding U1 and U2 spliceosomal RNAs, have specialized promoters comprising conserved proximal and distal sequence elements (PSE and DSE) (*1*). Rather than polyadenylation signals, 3′ box elements direct the cotranscriptional formation of the primary 3′ end of transcripts (*2*, *3*). The 3′ end of these precursor snRNAs (pre-snRNAs) is further processed in the cytoplasm to yield mature nonpolyadenylated snRNAs (*2*). Removal of the CTD of the large subunit of mammalian Pol II strongly affects expression of both snRNA and protein-coding genes (*2*–*4*). The CTD has a distinctive structure composed of multiple repeats containing residues that undergo reversible phosphorylation during transcription (*5*). For example, phosphorylation of Ser[5] by cyclin-dependent kinase 7 (CDK7) facilitates promoter release and RNA capping, whereas Ser[2] phosphorylation by CDK9 is associated with processive elongation and 3′ end processing (*5*, *6*). No role has yet been ascribed to Ser[7].

The mammalian Pol II CTD comprises 52 repeats, 25 of which deviate from the consensus at position 7. The mainly consensus repeats 1 to 25 activate snRNA 3′ end processing more effectively than repeats 27 to 52, which have few serines at position 7 (*2*). In contrast, both halves of the CTD are equally effective in activating polyadenylation (*7*). We have tested the requirement for Ser[7] for expression of snRNA [U2–globin (U2G) (*2*)] and mRNA [cytomegalovirus promoter-driven heterogeneous nuclear ribonucleoprotein K (pCMV-hnRNPK) (*8*)] templates in human embryonic kidney (HEK) 293 cells by introducing mutations into consensus (Con) CTD repeats in an α-amanitin–resistant Pol II large subunit (Rpb1) (*9*) (Fig. 1A and fig. S1A). The large subunit of endogenous Pol II is very sensitive to inhibition by α-amanitin, facilitating complementation studies (*9*). A CTD with at least 25 consensus repeats [(Con)[25]] was used because this supports efficient production and cotran-

[1]Sir William Dunn School of Pathology, University of Oxford, South Parks Road, Oxford OX1 3RE, UK. [2]Institute of Clinical Molecular Biology and Tumour Genetics, Gesellschaft fuer Strahlung Forschung (GSF)-Research Centre of Environment and Health, Munich Center for Integrated Protein Science (CiPSM), Marchioninistrasse 25, 81377 Munich, Germany.

*To whom correspondence should be addressed. E-mail: shona.murphy@path.ox.ac.uk

scriptional 3′ end processing of transcripts from snRNA and protein-coding templates, whereas five CTD repeats (Δ5) do not (*2*, *4*) (fig. S2, A and B).

Mutation of Ser^7 to the non-phosphoacceptor alanine (S7A) in a background of 25 repeats reduces the level of properly processed U2G transcripts (Proc) and increases the ratio of unprocessed transcripts (Unproc). However, this mutation affects neither the level nor 3′ end processing of hnRNPK transcripts (Fig. 1A and fig. S1B). Mutation of Ser^7 to alanine in a background of 48 consensus repeats [$(Con)^{48}$] (*10*) has a similarly strong effect on U2G transcripts, without affecting hnRNPK transcripts. This mutation does not affect expression of Rpb1 or Ser^2/Ser^5 phosphorylation (fig. S1C). Thus, Ser^7 is specifically required for efficient production of properly 3′ end–processed transcripts from an snRNA template.

Mutation of Ser^7 to the phosphomimic glutamic acid (S7E) has a strong effect on the level and 3′ end processing of transcripts from both the U2G and hnRNPK templates (Fig. 1A), possibly resulting from a defect in Pol II recruitment or association caused by charged residues. The increase in –111Unproc may reflect a defect in termination of transcription of U2G resulting from the defect in 3′ end processing (*2*, *11*, *12*). The S7E mutation abolishes recognition by antibodies to phosphoserine 2 (Ser^2-P) (fig. S1C), reflecting a drop in Ser^2 phosphorylation and/or interference with antibody recognition. A drop in Ser^2 phosphorylation would account for the defect in 3′ end processing and indicate that mutations can have secondary effects. Rpb2 is not affected by α-amanitin treatment in the same way as Rpb1 (fig. S1C), indicating that not all Pol II–specific subunits are subject to α-amanitin–induced turnover in HEK 293 cells.

Mutation of Ser^2 to alanine (S2A) affects 3′ end formation of U2G and hnRNPK transcripts, whereas transcript levels are strongly reduced by mutation to glutamic acid (S2E) (fig. S2, A, B, and D) (*6*). S2A accumulates to a higher level than $(Con)^{25}$ and S2E is undetectable (fig. S2C), suggesting that phosphorylation of Ser^2 is involved in Rpb1 turnover. Introduction of alanine at position 5 (S5A) reduces steady-state U2G and hnRNPK transcript levels and processing (fig. S2, A, B, and D). This likely reflects the requirement for Ser^5 phosphorylation for addition of the 5′ cap, which protects the RNA and activates 3′ end processing (*5*, *13*). Although introduction of glutamic acid at position 5 restores RNA levels, suggesting that capping now occurs, 3′ end processing is still inefficient, demonstrating that a charged amino acid does not fully compensate for the lack of a serine. The increase in –111Unproc accompanies loss of processing of U2G transcripts in all cases (fig. S2A) and likely reflects a termination defect. In contrast to mutations in Ser^7, mutations in Ser^2 and Ser^5 affect production of snRNAs and mRNAs in largely the same way.

Mutation of Ser^2 to alanine and Ser^5 to alanine does not reduce recognition by antibodies to Ser^5-P and Ser^2-P, respectively (fig. S2C), suggesting that both phosphorylation events can occur independently. Mutation of Ser^5 to glutamic acid reduces recognition by the antibody to Ser^2-P, reflecting a drop in Ser^2 phosphorylation and/or interference with antibody recognition. A drop in Ser^2 phosphorylation would again account for the defect in 3′ end processing (fig. S2, A and B).

To determine whether Ser^7 is required for expression of endogenous snRNA genes, we used cells with stably integrated α-amanitin–resistant Rpb1 genes controlled by a tetracycline-regulated promoter (*10*) (Fig. 1B). U2 pre-snRNA (pre-U2) and stable mature U2 snRNA (U2) are readily detected in RNA from cells expressing α-amanitin–resistant Rpb1 with $(Con)^{48}$. A third minor protection product corresponds to transcripts that have escaped 3′ box–directed processing (U2Unproc) (*2*). Because fully processed snRNAs are very stable (*14*), there is little change in U2 levels when Ser^7 is mutated to alanine. However, accumulation of pre-U2 and U2Unproc is severely impaired, although expression of the α-amanitin–resistant Rpb1 is unaffected. Quantitative reverse transcription–polymerase chain reaction (qRT-PCR) analysis of the RNA indicates that this mutation decreases the level of pre-U2 to less than 30%, whereas mRNA encoding the transcription factor hElf-1 is unaffected. Chapman *et al*. (*15*) have independently determined that this

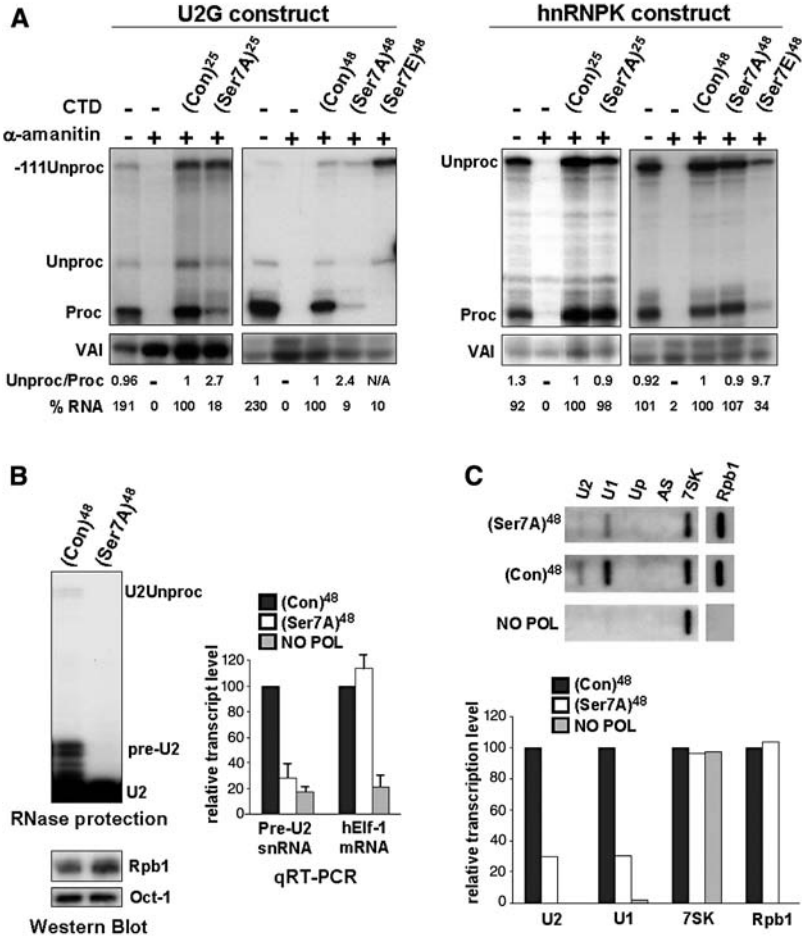

Fig. 1. Ser^7 is required for expression of snRNA but not protein-coding templates. (**A**) Ribonuclease (RNase) protection analysis of RNA transcribed from U2G or pCMV-hnRNPK constructs after ectopic expression of α-amanitin–resistant Rpb1 (fig. S1A). (Con) designates consensus CTD heptapeptides. Ser7A, S7A; Ser7E, S7E; VAI, virus-associated RNA I. (**B**) RNase protection analysis of transcripts from endogenous U2 genes in cells stably expressing α-amanitin–resistant Rpb1 and Western blot analysis of Rpb1 expression. qRT-PCR analysis of U2 pre-snRNA and hElf-1 mRNA in total RNA normalized to 7SK RNA with α-amanitin–treated cells expressing no Rpb1 as negative control (NO POL). Error bars indicate the range of values from three independent experiments. (**C**) Run-on analysis of endogenous U1 and U2 snRNA genes in cells transfected with α-amanitin–resistant Rpb1s. AS and Up are negative controls (*12*). Quantitation of this data is shown in the bar graph.

mutation does not have a general effect on expression of protein-coding genes. Mutation of Ser^7 to alanine also reduces transcription of U1 and U2 genes to less than 30%, as measured by nuclear run-on analysis (Fig. 1C), whereas transcription of the transfected CMV promoter-driven Rpb1 template and the Pol III–dependent 7SK gene is unaffected.

Taken together, these results indicate that Ser^7 is required for endogenous snRNA gene expression. Mutating Ser^7 to alanine does not affect the level of Rpb1 associated with γ-actin and glyceraldehyde phosphate dehydrogenase (GAPDH) protein-coding genes, as measured by chromatin immunoprecipitation (ChIP) (Fig. 2A), indicating that Pol II is recruited efficiently. Unexpectedly, the mutant Pol II is also recruited efficiently to U1 and U2 genes, indicating that transcription of snRNA genes is affected at a post-recruitment step.

The transcription factor PTF/PBP/SNAP$_C$ (PSE-binding transcription factor/PSE-binding protein/snRNA-activating protein complex), which recognizes the PSE (*1*, *16*), and the Integrator complex, which plays a role in 3′ end processing of snRNAs (*17*), are the only known factors specifically involved in expression of Pol II–transcribed snRNA genes. Because Integrator interacts with the CTD (*17*), we analyzed the effect of Ser^7 mutation on recruitment of this complex. When the CTD contains 48 consensus repeats, tandem affinity purification (TAP)–tagged Integrator subunit 9/RC-74 (TAP-Int9) (*17*, *18*) is clearly detectable on snRNA genes but not on γ-actin and GAPDH genes (Fig. 2A and fig. S3A). Association with snRNA genes is lost when Ser^7 is mutated to alanine. In contrast, association of PTF with the promoters of snRNA genes is Pol II–independent (fig. S3B).

When transcribing snRNA genes, Pol II is phosphorylated on Ser^7 (Fig. 2B), raising the possibility that CTD phosphorylation plays a role in Integrator recruitment. To investigate this, we performed glutathione *S*-transferase (GST) pull-down analysis using consensus or S7A repeats. Phosphorylation on Ser^2, Ser^5, and Ser^7 is detected after in vitro phosphorylation (fig. S3C). Int11/RC-68 (*17*, *18*), presumably as part of the Integrator complex, interacts strongly with the consensus repeats only after phosphorylation, and the interaction increases with the number of repeats (Fig. 2C). Mutation of Ser^7 to alanine has a strong effect on Integrator binding, although Ser^2 and Ser^5 phosphorylation still occur (fig. S3D), strongly suggesting that Ser^7 phosphorylation participates in this interaction.

Taken together, these experiments suggest that phosphorylation of conserved Ser^7 residues within the CTD is critical for association with the Integrator complex in vivo. Disruption of this interaction would account for the defect in 3′ end processing and may also be responsible for the defect in transcription (Fig. 2D). It was proposed that different combinations of phosphorylation of Ser^2 and Ser^5 and proline isomerization could constitute a CTD "code" (*19*). Ser^7 phosphorylation would provide an additional, important element of this code in mammals.

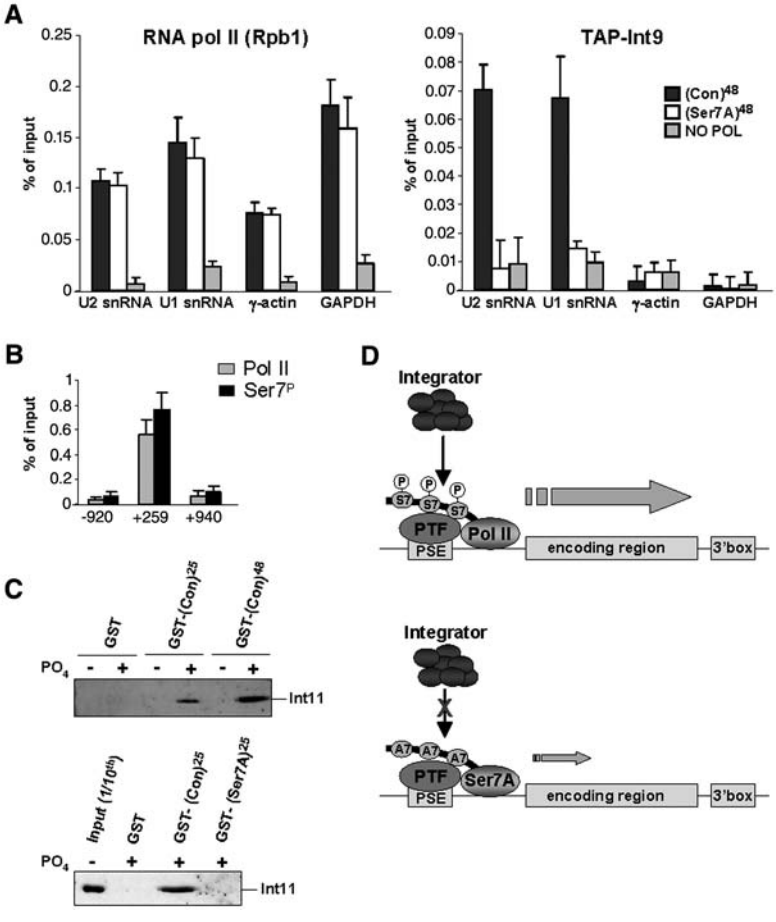

Fig. 2. Mutation of Ser^7 to alanine affects association of Integrator with snRNA genes. (**A**) ChIP analysis of Rpb1 and TAP-Int9 associated with U1, U2, γ-actin, and GAPDH promoters. (**B**) ChIP analysis of endogenous U2 genes with antibodies to Rpb1 (Pol II) or Ser^7-P (Ser7^P). Error bars in (A) and (B) indicate the range of values from three independent experiments. (**C**) Western blot analysis of GST-CTD pull down of Integrator with antibodies to Int11 (*18*). (**D**) Phosphorylation of Ser^7 is required for efficient interaction of Integrator with Pol II. Disruption of this interaction may cause a defect in a post-recruitment step of transcription, in addition to affecting 3′ end processing.

References and Notes

1. N. Hernandez, *J. Biol. Chem.* **276**, 26733 (2001).
2. J. E. Medlin, P. Uguen, A. Taylor, D. L. Bentley, S. Murphy, *EMBO J.* **22**, 925 (2003).
3. E. Y. Jacobs, I. Ogiwara, A. M. Weiner, *Mol. Cell. Biol.* **24**, 846 (2004).
4. S. McCracken *et al.*, *Nature* **385**, 357 (1997).
5. H. P. Phatnani, A. L. Greenleaf, *Genes Dev.* **20**, 2922 (2006).
6. J. Medlin *et al.*, *EMBO J.* **24**, 4154 (2005).
7. N. Fong, G. Bird, M. Vigneron, D. L. Bentley, *EMBO J.* **22**, 4274 (2003).
8. S. Lu, B. R. Cullen, *RNA* **9**, 618 (2003).
9. H. P. Gerber *et al.*, *Nature* **374**, 660 (1995).
10. R. D. Chapman, M. Conrad, D. Eick, *Mol. Cell. Biol.* **25**, 7665 (2005).
11. P. Cuello, D. C. Boyd, M. J. Dye, N. J. Proudfoot, S. Murphy, *EMBO J.* **18**, 2867 (1999).
12. Materials and methods are available as supporting material on *Science* Online.
13. P. Uguen, S. Murphy, *Nucleic Acids Res.* **32**, 2987 (2004).
14. M. G. Fury, G. W. Zieve, *Exp. Cell Res.* **228**, 160 (1996).
15. R. D. Chapman *et al.*, *Science* **318**, 1780 (2007).
16. J. B. Yoon, S. Murphy, L. Bai, Z. Wang, R. G. Roeder, *Mol. Cell. Biol.* **15**, 2019 (1995).
17. D. Baillat *et al.*, *Cell* **123**, 265 (2005).
18. Z. Dominski, X. C. Yang, M. Purdy, E. J. Wagner, W. F. Marzluff, *Mol. Cell. Biol.* **25**, 1489 (2005).
19. S. Buratowski, *Nat. Struct. Biol.* **10**, 679 (2003).

20. We thank Z. Dominski for antibody to RC-68, J. B. Yoon and R. G. Roeder for antibody to PTFγ, B. R. Cullen for pCMV-hnRNPK, J. Corden for mutant CTD constructs, and P. R. Cook and N. J. Proudfoot for comments on the manuscript. This work was supported by Medical Research Council (UK) and Wellcome Trust Grants to S.M. and a Deutsche Forschungsgemeinschaft, Sonderforschungsbereich-Transregio 5 Grant to D.E.

Supporting Online Material

www.sciencemag.org/cgi/content/full/318/5857/1777/DC1
Materials and Methods
Figs. S1 to S3
References

4 June 2007; accepted 19 October 2007
10.1126/science.1145989

Transcribing RNA Polymerase II Is Phosphorylated at CTD Residue Serine-7

Rob D. Chapman,[1] Martin Heidemann,[1] Thomas K. Albert,[2]* Reinhard Mailhammer,[1] Andrew Flatley,[2] Michael Meisterernst,[2]* Elisabeth Kremmer,[2] Dirk Eick[1]†

RNA polymerase II is distinguished by its large carboxyl-terminal repeat domain (CTD), composed of repeats of the consensus heptapeptide Tyr[1]-Ser[2]-Pro[3]-Thr[4]-Ser[5]-Pro[6]-Ser[7]. Differential phosphorylation of serine-2 and serine-5 at the 5′ and 3′ regions of genes appears to coordinate the localization of transcription and RNA processing factors to the elongating polymerase complex. Using monoclonal antibodies, we reveal serine-7 phosphorylation on transcribed genes. This position does not appear to be phosphorylated in CTDs of less than 20 consensus repeats. The position of repeats where serine-7 is substituted influenced the appearance of distinct phosphorylated forms, suggesting functional differences between CTD regions. Our results indicate that restriction of serine-7 epitopes to the Linker-proximal region limits CTD phosphorylation patterns and is a requirement for optimal gene expression.

Differential phosphorylation of CTD residues of the large subunit of eukaryotic RNA polymerase II (Pol II) occurs during the transcription cycle and appears to orchestrate the recruitment, activation, and displacement of various factors involved in transcription and mRNA processing (*1*, *2*). A variety of kinases have been identified, with phosphorylation activity directed toward the amino acids tyrosine-1 (Abl1/2), serine-2 (CTDK1, CDK9, and DNA-PK), serine-5 (ERK1/2 and CDK7-9), and serine-7 (DNA-PK) (*3*). The mammalian CTD is >99% conserved across species and possesses almost double the length of its yeast counterparts (*4*). A minimum length of CTD is required to support the growth of yeast or mammalian cells. However, this is dependent on the number and position of consensus and nonconsensus repeats, which suggests that CTD function is composed of both sequence and length (*5*–*8*). Of the 52 mammalian CTD repeats, 21 obey the consensus sequence and lie largely proximal to the Linker region (fig. S1). The distal C-terminal region deviates from this consensus, predominantly at position 7. These nonconsensus repeats may affect the binding of specific factors or may serve to prevent phosphorylation at the position of deviation. Indeed, studies in vivo suggest that they are equivalent to consensus repeats for functions such as splicing of the fibronectin extra domain I exon (*9*) but not for maintenance of long-term cell viability (*5*, *6*).

To investigate the role of the CTD repeat structure on its phosphorylation, we have established a system that allows the comparison of CTDs of different lengths and repeat compositions in vivo. Recombinant polymerases are engineered with a point mutation conferring resistance to α-amanitin, allowing the endogenous polymerase to be inhibited (and degraded) after addition of α-amanitin but without affecting recombinant polymerase activity (*5*, *10*). Monoclonal antibodies (mAbs) were produced against the CTD phosphoserine epitopes Ser[2]-P, Ser[5]-P, and Ser[7]-P (Fig. 1A and fig. S2). In preparing these antibodies, we considered earlier findings that

[1]Institute of Clinical Molecular Biology and Tumour Genetics, GSF-Research Center of Environment and Health, Munich Center for Integrated Protein Science (CiPSM), Marchioninistrasse 25, 81377 Munich, Germany. [2]Institute of Molecular Immunology, GSF-Research Center of Environment and Health, Munich Center for Integrated Protein Science, Marchioninistrasse 25, 81377 Munich, Germany.

*Present address: Institute of Tumor Biology, University Muenster, Robert-Koch-Strasse 43, 48149 Muenster, Germany.
†To whom correspondence should be addressed. E-mail: eick@gsf.de

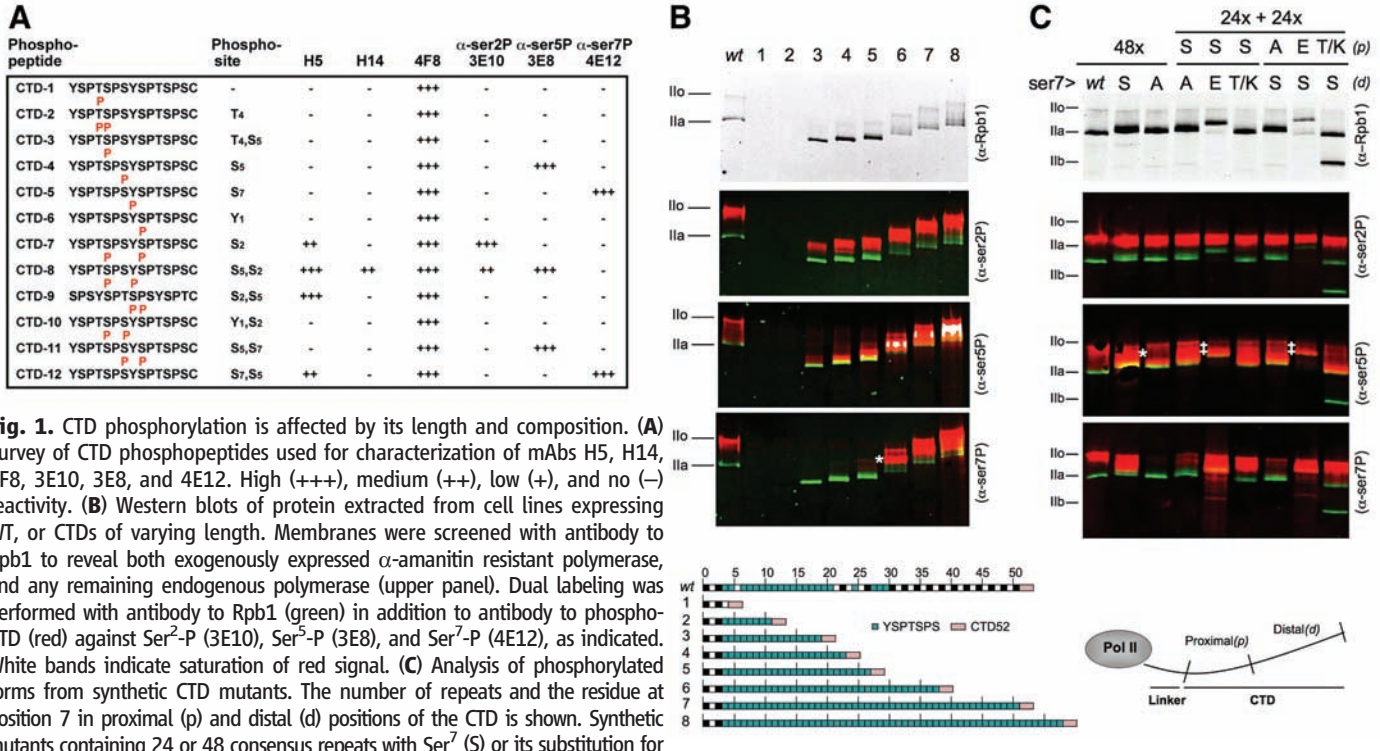

Fig. 1. CTD phosphorylation is affected by its length and composition. (**A**) Survey of CTD phosphopeptides used for characterization of mAbs H5, H14, 4F8, 3E10, 3E8, and 4E12. High (+++), medium (++), low (+), and no (–) reactivity. (**B**) Western blots of protein extracted from cell lines expressing WT, or CTDs of varying length. Membranes were screened with antibody to Rpb1 to reveal both exogenously expressed α-amanitin resistant polymerase, and any remaining endogenous polymerase (upper panel). Dual labeling was performed with antibody to Rpb1 (green) in addition to antibody to phospho-CTD (red) against Ser[2]-P (3E10), Ser[5]-P (3E8), and Ser[7]-P (4E12), as indicated. White bands indicate saturation of red signal. (**C**) Analysis of phosphorylated forms from synthetic CTD mutants. The number of repeats and the residue at position 7 in proximal (p) and distal (d) positions of the CTD is shown. Synthetic mutants containing 24 or 48 consensus repeats with Ser[7] (S) or its substitution for alanine (A) confirm the specificity of the 4E12 mAb. Chimeras of consensus repeats (lanes labeled S) and repeats with Ser[7] mutated to alanine (A), glutamic acid (E), and threonine/lysine (T/K) affect the appearance of a Ser[5]-P/Ser[7]-P reactive band when Ser[7] is absent in the Linker proximal region. Mutants containing T/K-rich sequences at position 7, proximal to the Linker, result in degradation of polymerase to the CTD-less, Pol IIb form.

showed that the functional unit of the CTD is not the heptad repeat itself but is in a sequence lying within heptapeptide pairs (*11*, *12*). Thus, in the production and testing of our antibodies, a panel of di-heptapeptides with various modifications was used. Analysis of our antibodies and commercially available antibodies revealed that some recognition profiles were limited by modifications on neighboring repeats. For example, the α-Ser^7-P antibody (4E12) is affected by upstream, but not downstream, Ser^5-P (Fig. 1A).

Combining these tools, we compared the phosphorylation of wild-type (WT) CTD with that of different lengths of consensus repeats (Fig. 1B). If all repeats are equally accessible to CTD kinases, we should expect intensities of phosphorylation signals for WT and mutants 1 to 8 proportional to CTD length. Dual labeling of membranes with α-Rpb1 antibody (green signal) (mAb Pol3/3 recognizes an epitope outside the CTD) and with α-phospho-CTD antibody (red signal) reveals forms of different mobility—the rapidly migrating, unmodified IIa form and the slower, modified IIo form. For mutants containing 16 to 24 consensus repeats (mutants 3 to 5), the majority of Pol II is not efficiently phosphorylated and accumulates in the IIa form (green). Mutants 1 and 2 are no longer visible at this time point because they are unable to support their own expression. Within the IIo form, Ser^2-P appears in a sharp, slow migrating band, whereas in longer CTDs (mutants 6 to 8), Ser^5-P appears largely in a band (white saturation) migrating between the Ser^2-P band and IIa, which suggests that at least two populations of phosphorylated CTD exist in vivo at any time: Ser^2-P alone and Ser^5-P alone. These data are supported by both the recognition profiles of the antibodies and previous work showing a shift in IIo to a faster migrating form upon treatment with a Ser^2-kinase inhibitor (*13*). Antibody raised against Ser^7-P revealed the existence of this epitope in vivo, which is distributed among the major Ser^2-P and Ser^5-P reactive bands. The epitope is lacking from the Ser^5-P band that appears just above the IIa form. Strong reactivity of α-Ser^7-P is detectable for a band between IIa and IIo (Fig. 1B, *). Furthermore, although Ser^2-P and Ser^5-P appear in all mutants, Ser^7-P appears only in mutants with more than 24 repeats (mutants 4 to 8).

To investigate the effect of nonconsensus repeats on the distribution of phosphorylation, a panel of CTD mutants (fig. S3) was analyzed for their reactivity against phospho-CTD antibodies (Fig. 1C). α-Ser^7-P does not recognize a mutant lacking Ser^7 (48xS7A) but strongly recognizes mutants containing Ser^7 substituted with glutamic acid (S7E), indicating either that this antibody recognizes a CTD conformation or that S7E can structurally mimic Ser^7-P for antibody recognition. Furthermore, replacement of Ser^7 with alanine prevents recognition of the intermediate band between IIa and IIo (Fig. 1C, *) by α-Ser^5-P, suggesting that this form may be Ser^7-P–dependent.

Because deviations from serine at position 7 in the WT CTD are concentrated in its distal region, chimeras were produced to assess the effect of proximal and distal positioning of nonconsensus repeats. The two chimeras of consensus repeats, and repeats containing S7E substitutions, produce a form that migrates between IIa and IIo (Fig. 1C, ‡). The proximal positioning of nonconsensus repeats (S7A and S7T/K) affects the appearance of a form similar in mobility to the intermediate IIo Ser$^{5/7}$-P–reactive band (Fig. 1, B and C, *) seen in mutants of >35 pure consensus repeats. (Fig. 1, B and C; for more detail, see fig. S4).

To determine whether Ser^7 phosphorylation is a physiological event during the transcription cycle, chromatin immunoprecipitation (ChIP) experiments were conducted. A detailed example is shown for the T cell receptor beta (TCRβ) gene locus (Fig. 2A). Ser^7 was phosphorylated on transcribing Pol II, appearing strongly at the promoter and increasing toward the 3′ region of TCRβ (Fig. 2B). The differences in Ser^2 phosphorylation that we observe, compared with earlier data, may result from the antibodies used, because the H5 antibody preferentially recognizes repeats with phosphorylated Ser^2 and Ser^5 (Fig. 1A).

Given that Ser^7 is phosphorylated across TCRβ and all other genes tested (*GAPDH*, *RPLPO*, and *RPS27*), the ability of synthetic polymerases to transcribe and produce mature mRNA from the *c-myc* (Fig. 2C) and *pes1* genes (fig. S5) was analyzed. The effect on *c-myc* and *pes1* mRNA levels of Ser^7 substitution to E or K/T appears dependent on its position, either proximal or distal to the Linker, suggesting again that functional differences exist between these regions. Substitution of Ser^7 to the non-phosphoacceptor, alanine, did not obviously affect mRNA levels, nor did it affect the long-term growth of cell lines, although viability was compromised (fig. S6). This may be due to the effect of this mutation on small nuclear RNA genes (*14*).

ChIP experiments revealed that S7E-containing mutants do not stably associate with any of the genes tested, providing an explanation for the deficit in mRNA observed for mutants containing S7E in the Linker-proximal region. Mutants containing either 48 consensus or S7A repeats appear to be recruited to protein coding genes at similar levels (*14*).

We conclude that the nature of the amino acid at position 7 of the Linker-proximal CTD region is important in steps involved in the stable association of Pol II with class II genes. Accumulation of Ser^7-P in the 3′ region of the TCRβ gene may suggest a role in transcription and/or 3′ RNA processing of some protein-coding genes. We are now able to expand previous models for the cycle of CTD modification across genes that are transcribed by RNA polymerase II (*15*), not only to show how potential phosphorylation patterns change from 5′ to 3′ regions across a gene but also to speculate as to the region of the CTD in which they occur. Phosphorylation of Ser^7 in the proximal part of CTD and replacement of Ser^7 by other amino

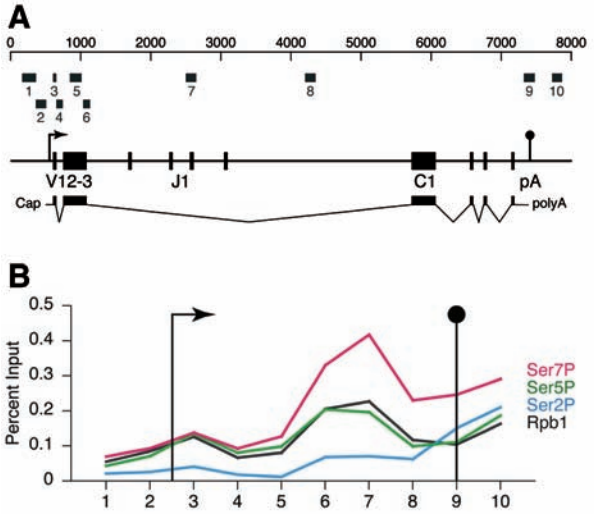

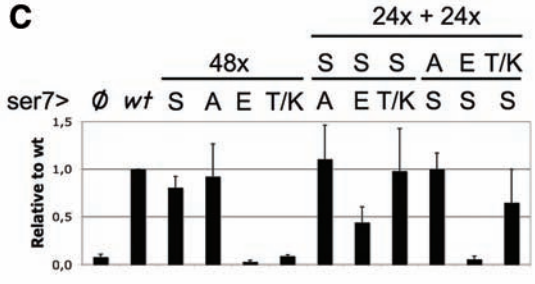

Fig. 2. ChIP analysis of CTD modifications. (**A**) Scale drawing of the rearranged TCRβ gene, with black boxes indicating exons of the variable segment V12-3, of the joining region cluster J1, and of the constant region C1. Gray boxes on top show relative location of ChIP quantitative real-time polymerase chain reaction (QPCR) amplicons 1 to 10. (**B**) QPCR analysis of ChIP analyses in Jurkat cells with antibodies against Rpb1 and indicated phospho-CTD antibodies. The relative location of the transcriptional start site (arrow) and pA (lollipop) are indicated. (**C**) Transcriptional activity of CTD mutants. QPCR of *c-myc* mRNA using primers specific for the mature, spliced form. To control for the effects of α-amanitin treatment, values were normalized against a *7SK* RNA control for the same sample. Myc expression is shown relative to WT levels. Labeling as in Fig. 1B; Ø, without recombinant Pol II. Error bars, SD.

acids in the distal part of CTD may constitute an added layer of gene regulation by mammalian RNA polymerases.

References and Notes

1. A. Meinhart, T. Kamenski, S. Hoeppner, S. Baumli, P. Cramer, *Genes Dev.* **19**, 1401 (2005).
2. H. P. Phatnani, A. L. Greenleaf, *Genes Dev.* **20**, 2922 (2006).
3. B. Palancade, O. Bensaude, *Eur. J. Biochem.* **270**, 3859 (2003).
4. E. Barron-Casella, J. L. Corden, *J. Mol. Evol.* **35**, 405 (1992).
5. M. S. Bartolomei, N. F. Halden, C. R. Cullen, J. L. Corden, *Mol. Cell. Biol.* **8**, 330 (1988).
6. R. D. Chapman, M. Conrad, D. Eick, *Mol. Cell. Biol.* **25**, 7665 (2005).
7. M. L. West, J. L. Corden, *Genetics* **140**, 1223 (1995).
8. Y. Pei, S. Hausmann, C. K. Ho, B. Schwer, S. Shuman, *J. Biol. Chem.* **276**, 28075 (2001).
9. M. de la Mata, A. R. Kornblihtt, *Nat. Struct. Mol. Biol.* **13**, 973 (2006).
10. M. Meininghaus, R. D. Chapman, M. Horndasch, D. Eick, *J. Biol. Chem.* **275**, 24375 (2000).
11. J. W. Stiller, M. S. Cook, *Eukaryot. Cell* **3**, 735 (2004).
12. E. Vojnic, B. Simon, B. D. Strahl, M. Sattler, P. Cramer, *J. Biol. Chem.* **281**, 13 (2006).
13. J. Medlin *et al.*, *EMBO J.* **24**, 4154 (2005).
14. S. Egloff *et al.*, *Science* **318**, 1777 (2007).
15. S. Buratowski, *Nat. Struct. Biol.* **10**, 679 (2003).

16. Supported by grants from the Deutsche Forschungsgemeinschaft (SFB/TR5 and SFB684), Bundesministerium für Bildung und Forschung (QuantPRO, 0313860), Boehringer Ingelheim Fonds, and Fonds der Chemischen Industrie. We thank A. Meinhart and P. Cramer for critical comments on this manuscript.

Supporting Online Material

www.sciencemag.org/cgi/content/full/318/5857/1780/DC1
Materials and Methods
Figs. S1 to S6
References

4 June 2007; accepted 30 October 2007
10.1126/science.1145977

A 3-Hydroxypropionate/4-Hydroxybutyrate Autotrophic Carbon Dioxide Assimilation Pathway in Archaea

Ivan A. Berg,[1] Daniel Kockelkorn,[1] Wolfgang Buckel,[2] Georg Fuchs[1]*

The assimilation of carbon dioxide (CO_2) into organic material is quantitatively the most important biosynthetic process. We discovered that an autotrophic member of the archaeal order Sulfolobales, *Metallosphaera sedula*, fixed CO_2 with acetyl–coenzyme A (acetyl-CoA)/propionyl-CoA carboxylase as the key carboxylating enzyme. In this system, one acetyl-CoA and two bicarbonate molecules were reductively converted via 3-hydroxypropionate to succinyl-CoA. This intermediate was reduced to 4-hydroxybutyrate and converted into two acetyl-CoA molecules via 4-hydroxybutyryl-CoA dehydratase. The key genes of this pathway were found not only in *Metallosphaera* but also in *Sulfolobus*, *Archaeoglobus*, and *Cenarchaeum* species. Moreover, the Global Ocean Sampling database contains half as many 4-hydroxybutyryl-CoA dehydratase sequences as compared with those found for another key photosynthetic CO_2-fixing enzyme, ribulose-1,5-bisphosphate carboxylase-oxygenase. This indicates the importance of this enzyme in global carbon cycling.

The dominant extant autotrophic pathway is the Calvin-Bassham-Benson cycle, which may have evolved late in evolution (*1*). Three additional autotrophic pathways are known: the reductive citric acid cycle (Arnon-Buchanan cycle), the reductive acetyl-CoA pathway (Wood-Ljungdahl pathway), and the 3-hydroxypropionate cycle. These pathways differ in several ways [e.g., with respect to energy demand, available reducing compounds, requirement for metals (Fe, Co, Ni, and Mo), usage of coenzymes, and oxygen sensitivity of enzymes]. These criteria determine the distribution of the pathways in autotrophic organisms in different habitats, in addition to their phylogeny.

In the thermoacidophilic Archaea *Sulfolobus*, *Acidianus*, and *Metallosphaera* spp., CO_2 fixation appears to proceed via a modified, but until now unresolved, variant of the 3-hydroxypropionate cycle (*2*–*6*) (Fig. 1). The 3-hydroxypropionate cycle was originally discovered in the phototrophic bacterium *Chloroflexus aurantiacus* (*7*, *8*); it involves the carboxylation of acetyl-CoA to malonyl-CoA by the biotin-dependent acetyl-CoA carboxylase. Because Archaea contain only trace amounts of fatty acids, if any, in their lipids, acetyl-CoA carboxylase cannot serve as the key enzyme of fatty acid synthesis. It seems that this enzyme functions in another metabolic pathway. Malonyl-CoA is reduced via malonate semialdehyde to 3-hydroxypropionate, which is further reductively converted to propionyl-CoA. Propionyl-CoA is carboxylated to (*S*)-methylmalonyl-CoA by a carboxylase, which is similar or identical to acetyl-CoA carboxylase. (*S*)-Methylmalonyl-CoA is isomerized to (*R*)-methylmalonyl-CoA, followed by carbon rearrangement to succinyl-CoA by coenzyme vitamin B_{12}–dependent methylmalonyl-CoA mutase. In *Chloroflexus*, succinyl-CoA is converted to (*S*)-malyl-CoA, which is cleaved by (*S*)-malyl-CoA lyase to acetyl-CoA (thus regenerating the CO_2-acceptor molecule) and glyoxylate (*8*). However, this succinyl-CoA conversion via (*S*)-malyl-CoA was not verified in Sulfolobales (*3*, *4*, *6*), leaving the problem of how acetyl-CoA is regenerated in this group of organisms.

A comparison of the genomes of autotrophic Archaea that have acetyl-CoA carboxylase genes revealed several groups, which differ with respect to the pattern of other characteristic genes and enzymes (table S1). One group comprising autotrophic members of the genera *Metallosphaera*, *Sulfolobus*, *Archaeoglobus*, and *Cenarchaeum* contains the genes for acetyl-CoA/propionyl-CoA carboxylase and methylmalonyl-CoA mutase. These organisms differ considerably in their energy metabolism and habitats. *Metallosphaera* and *Sulfolobus* spp. metabolize sulfur, pyrite, or hydrogen in volcanic areas (*9*); *Archaeoglobus* spp. are anaerobic sulfate reducers (*10*); and *Cenarchaeum* sp. is a symbiont of marine animals (*11*), which is closely related to *Nitrosopumilus* sp., a marine ammonia oxidizer (*12*). All these organisms contain the gene for 4-hydroxybutyryl-CoA dehydratase, a [4Fe–4S] cluster and flavin adenine dinucleotide–containing enzyme, which catalyzes the elimination of water from 4-hydroxybutyryl-CoA by a ketyl radical mechanism yielding crotonyl-CoA (*13*, *14*). This reaction is known to play a role in a few anaerobic bacteria such as *Clostridium aminobutyricum*, which ferment 4-aminobutyrate via 4-hydroxybutyryl-CoA (*15*).

We suspected that this group of Archaea is able to reduce succinyl-CoA to 4-hydroxybutyrate and convert it with the participation of 4-hydroxybutyryl-CoA dehydratase into two molecules of acetyl-CoA. Cell extracts of *M. sedula*, indeed, catalyzed a rapid (500 nmol min^{-1} mg^{-1} protein at 65°C) reduction of succinyl-CoA via succinate semialdehyde to 4-hydroxybutyrate with NADPH, the reduced form of nicotinamide adenine dinucleotide phosphate ($NADP^+$) (*16*). Extracts also converted 4-hydroxy[1-^{14}C]butyrate to [^{14}C]acetyl-CoA at 50 nmol min^{-1} mg^{-1} protein at 65°C in the presence of Mg–adenosine triphosphate (MgATP), CoA, and nicotinamide adenine dinucleotide (NAD^+) (Fig. 2A). High-performance liquid chromatography (HPLC) analysis of the reaction course revealed labeled 4-hydroxybutyryl-CoA, crotonyl-CoA, and 3-hydroxybutyryl-CoA as intermediates (Fig. 2B). A plot of the relative amounts of radioactivity in the individual products versus time indicated that the order of intermediates was as expected and that acetyl-CoA was the end product (Fig. 2C). The organism grows at 75°C in a $H_2/O_2/CO_2$ mixture with a minimum generation time of 8 hours, which corresponds to a specific carbon fixation rate in vivo of 120 nmol min^{-1} mg^{-1} protein (*17*). Because two molecules of carbon are fixed in the proposed pathway, the minimal in

[1]Mikrobiologie, Fakultät Biologie, Universität Freiburg, Schänzlestraße 1, D-79104 Freiburg, Germany. [2]Mikrobiologie, Fachbereich Biologie, Universität Marburg, D-35032 Marburg, Germany.

*To whom correspondence should be addressed. E-mail: georg.fuchs@biologie.uni-freiburg.de

vivo specific activity of enzymes in the cycle is 60 nmol min^{-1} mg^{-1} protein. All enzymes required for the postulated succinyl-CoA conversion to two acetyl-CoA were detected, and their specific activities met this expectation (see Table 1, which also summarizes the other enzyme activities; for cofactor specificity, see Fig. 1).

Some of the enzymes, for which no likely candidate gene could be identified in the genome, were purified, and the relevant genes were deduced from internal peptide sequences (Table 1). Succinyl-CoA reductase (NADPH) with a 39-kD subunit is identical to malonyl-CoA reductase, a paralog of aspartate semialdehyde dehydrogenase (*17*). Succinate semialdehyde reductase (NADPH) with a 40-kD subunit belongs to Zn-containing alcohol dehydrogenases. 4-Hydroxybutyryl-CoA synthetase [adenosine monophosphate (AMP)–forming] with a 50-kD subunit belongs to acyl-CoA synthetases. Similar genes were present in the sequenced Sulfolobales genomes (figs. S1 to S3).

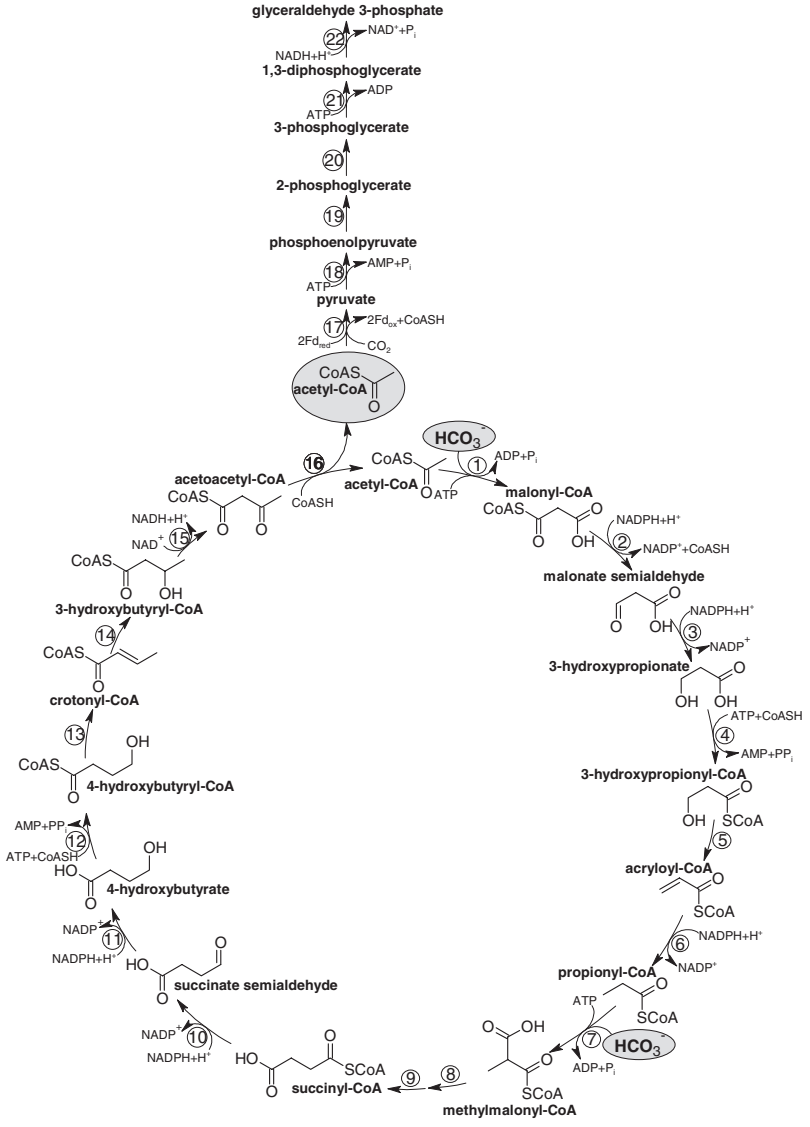

Fig. 1. Proposed autotrophic 3-hydroxypropionate/4-hydroxybutyrate cycle in *M. sedula*. Reactions of the cycle are shown. Enzymes: 1, acetyl-CoA carboxylase; 2, malonyl-CoA reductase (NADPH); 3, malonate semialdehyde reductase (NADPH); 4, 3-hydroxypropionyl-CoA synthetase (AMP-forming); 5, 3-hydroxypropionyl-CoA dehydratase; 6, acryloyl-CoA reductase (NADPH); 7, propionyl-CoA carboxylase; 8, methylmalonyl-CoA epimerase; 9, methylmalonyl-CoA mutase; 10, succinyl-CoA reductase (NADPH); 11, succinate semialdehyde reductase (NADPH); 12, 4-hydroxybutyryl-CoA synthetase (AMP-forming); 13, 4-hydroxybutyryl-CoA dehydratase; 14, crotonyl-CoA hydratase; 15, 3-hydroxybutyryl-CoA dehydrogenase (NAD^+); 16, acetoacetyl-CoA β-ketothiolase. The proposed pathway of glyceraldehyde 3-phosphate synthesis from acetyl-CoA and CO_2 is also shown. Enzymes: 17, pyruvate synthase; 18, pyruvate, water dikinase [phosphoenolpyruvate (PEP) synthase]; 19, enolase; 20, phosphoglycerate mutase; 21, 3-phosphoglycerate kinase; 22, glyceraldehyde 3-phosphate dehydrogenase. The activities of pyruvate synthase and PEP synthase at 75°C were 10 to 25 nmol min^{-1} mg^{-1} protein (*6*) and 25 nmol min^{-1} mg^{-1} protein, respectively.

Hence, the proposed 3-hydroxypropionate/4-hydroxybutyrate cycle, illustrated in Fig. 1, can be divided into two parts. The first transforms acetyl-CoA and two bicarbonate molecules to succinyl-CoA, and the second part converts succinyl-CoA to two acetyl-CoA molecules. In most Archaea, only one copy of genes for the acetyl-CoA/propionyl-CoA carboxylase subunits is present, which suggests that this is a promiscuous enzyme that acts on both acetyl-CoA and propionyl-CoA, as shown for *Acidianus brierleyi* (*18*) and *M. sedula* (*19*) and proposed for *Cenarchaeum symbiosum* (*20*).

A comparison of the proposed 3-hydroxypropionate/4-hydroxybutyrate cycle with the Calvin-Bassham-Benson cycle reveals important differences. The formation of one molecule of glyceraldehyde 3-phosphate from three molecules of CO_2 follows the equation: 3 CO_2 + 6 NAD(P)H + 9 ATP → 1 triosephosphate + 6 $NAD(P)^+$ + 9 adenosine diphosphate (ADP) + 8 inorganic phosphate (P_i). This does not account for the loss of energy and reducing power from the oxygenase activity of ribulose-1,5-bisphosphate carboxylase-oxygenase (RuBisCO). Triosephosphate formation via the proposed cycle (Fig. 1) follows the equation: 2 bicarbonate + 1 CO_2 + 5 NAD(P)H + 2 reduced ferredoxin + 6 ATP → 1 triosephosphate + 5 $NAD(P)^+$ + 2 oxidized ferredoxin + 3 ADP + 4 P_i + 3 AMP + 2 inorganic pyrophosphate (PP_i). Hence, in energetic terms, the two processes are comparable [because ATP cleavage to AMP is equivalent to the loss of two energy-rich compounds, and reduced ferredoxin has a stronger reduction potential than NAD(P)H], but oxygenase activity of RuBisCO renders the Calvin-Bassham-Benson cycle energetically inferior.

The active "CO_2" species is CO_2 in the Calvin-Bassham-Benson cycle, whereas it is bicarbonate as cosubstrate for acetyl-CoA/propionyl-CoA carboxylase in the 3-hydroxypropionate/4-hydroxybutyrate cycle, with CO_2 as cosubstrate for pyruvate synthase (Fig. 1). The turnover number of RuBisCO (average: 5 s^{-1}) reflects a low catalytic efficiency that requires large amounts of enzyme (*21*, *22*). *M. sedula* acetyl-CoA/propionyl-CoA carboxylase catalyzing both carboxylation reactions has a turnover number at 65°C of 28 s^{-1} (*19*). The Michaelis constant (K_m) value of RuBisCO for dissolved CO_2 [the average value is 0.05 mM, but it may be as high as 0.34 mM in some marine cyanobacteria (*21*)] is lower than or even comparable to the apparent K_m value of archaeal acetyl-CoA/propionyl-CoA carboxylase for bicarbonate [0.3 mM (*19*)]. However, the CO_2 concentration in water equilibrated with air (1 atm pressure, 20°C, 370 parts per million CO_2) is 0.012 mM at pH 7.4 (which is the assumed intracellular pH), and the bicarbonate concentration under the same conditions is 0.26 mM. The concentration of bicarbonate will be even higher at pH 7.8 to 8.2 of seawater (apparent dissociation constant pK_{app} for CO_2/HCO_3^- is 6.3, 20°C). Thus, the acetyl-CoA carboxylase affinity for the

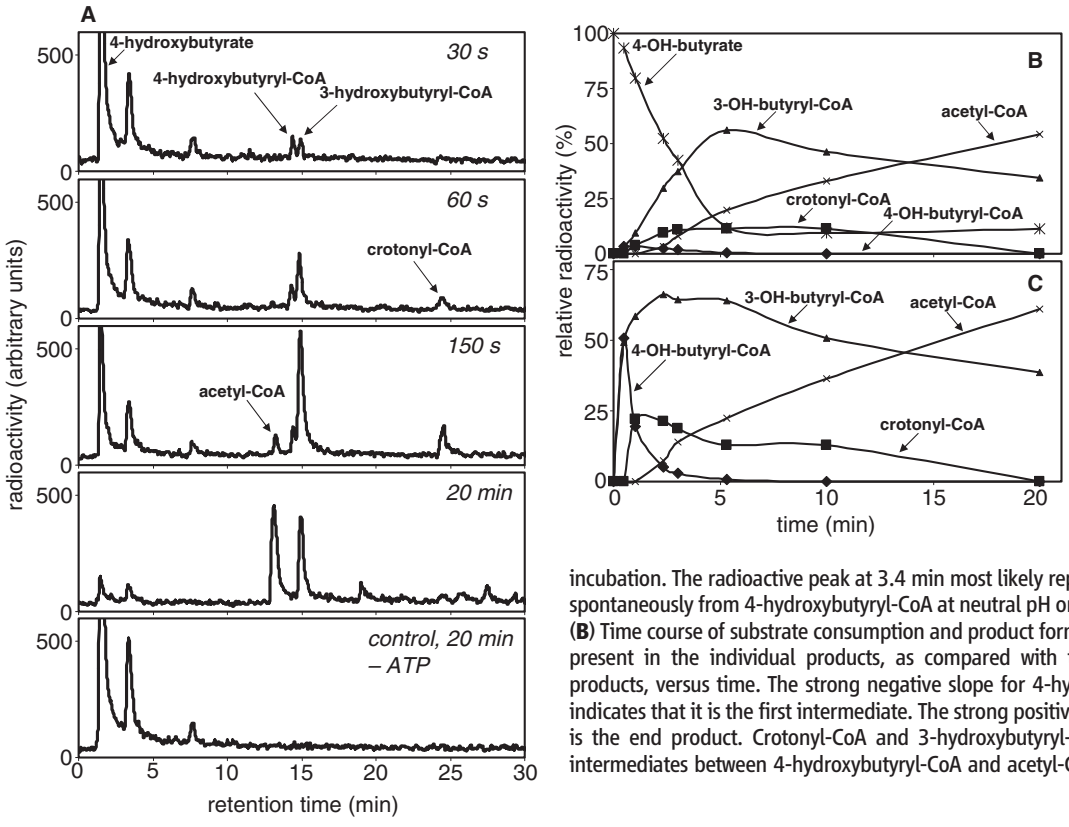

Fig. 2. Conversion of 4-hydroxy [^{14}C]butyrate to [^{14}C]acetyl-CoA at 65°C by cell extracts of *M. sedula*. The reaction mixture (0.5 ml) contained 100 mM Mops/KOH (pH 7.2), 3 mM $MgCl_2$, 5 mM dithiothreitol, 1 mM 4-hydroxy[1-^{14}C]butyrate (160 kilobecquerels ml^{-1}), 3 mM ATP, 2 mM CoA, and 2 mM NAD^+. The reaction was started by the addition of 10 μl of cell extract (to the final concentration of 0.4 mg protein ml^{-1} in the assay). (**A**) HPLC separation of labeled substrate and products and ^{14}C detection by flow-through scintillation counting. The figure shows samples (50 μl) taken after 30-s, 60-s, 150-s, and 20-min incubation, as well as a control experiment lacking ATP after 20-min incubation. The radioactive peak at 3.4 min most likely represents γ-butyrolactone, which forms spontaneously from 4-hydroxybutyryl-CoA at neutral pH or from 4-hydroxybutyrate at acidic pH. (**B**) Time course of substrate consumption and product formation. (**C**) Percentage of radioactivity present in the individual products, as compared with the total radioactivity in all labeled products, versus time. The strong negative slope for 4-hydroxybutyryl-CoA (4-OH-butyryl-CoA) indicates that it is the first intermediate. The strong positive slope for acetyl-CoA indicates that it is the end product. Crotonyl-CoA and 3-hydroxybutyryl-CoA (3-OH-butyryl-CoA) behave like intermediates between 4-hydroxybutyryl-CoA and acetyl-CoA.

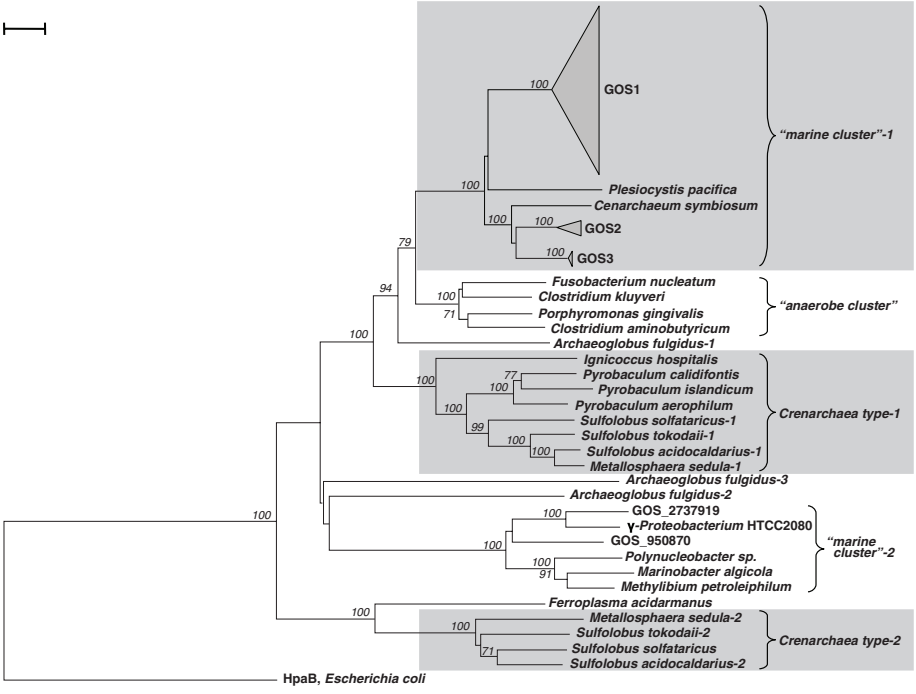

Fig. 3. Phylogenetic tree of representative 4-hydroxybutyryl-CoA dehydratase proteins. The tree is based on amino acid sequence analysis and rooted with 4-hydroxyphenylacetate 3-monooxygenase (HpaB) from *Escherichia coli*, which is a flavoprotein that resembles the flavin-binding domain of 4-hydroxybutyryl-CoA dehydratase. Tree topography and evolutionary distances are given by the neighbor-joining method with Poisson correction. The phylogenetic trees constructed by other algorithms (maximum parsimony, distance matrix, and maximum likelihood) resulted in identical topologies for principal clade grouping. The scale bar represents a difference of 0.1 substitutions per site. Numbers at nodes indicate the percentage bootstrap values for the clade of this group in 1000 replications. Only values above 70% were considered. The tree represents all full gene sequences from the GOS database and the sequences belonging to the major clusters on the tree. The accession numbers are listed in table S2, and the alignment is shown in fig. S4.

active "CO_2" species appears not to be inferior to that of RuBisCO. In addition, in volcanic gases and in animal hosts, the CO_2 concentration is much higher than in ambient air. Although 4-hydroxybutyryl-CoA dehydratase is slowly inactivated by oxygen, it may be sufficiently stable at low oxygen tensions to maintain activity, especially in the protected environment of the cell. There is no additional clue from the genome as to how these Crenarchaeota protect one of their key enzymes of CO_2 fixation from oxygen inactivation.

The 4-hydroxybutyryl-CoA dehydratase gene was not found in heterotrophic Crenarchaea, yet it is present in the genomes of autotrophic *Ignicoccus* and *Pyrobaculum* spp. (table S1), although these genera lack the genes required for part 1 of the proposed pathway. *I. hospitalis* forms succinyl-CoA from acetyl-CoA via pyruvate, phosphoenolpyruvate, and oxaloacetate (*23*) and may use the second half of the 3-hydroxypropionate/4-hydroxybutyrate cycle for the regeneration of the CO_2-acceptor acetyl-CoA from succinyl-CoA. *Pyrobaculum* spp. use a reductive citric acid cycle

Table 1. Enzymes of the proposed 3-hydroxypropionate/4-hydroxybutyrate cycle in *M. sedula.* Because of the use of mesophilic coupling enzymes and the instability of some substrates, the indicated assay temperatures were used; the growth temperature was 75°C. The values are average values of several determinations, the mean deviations are about 10%, depending also on the batch of cells. The genes for 4-hydroxybutyryl-CoA synthetase, acryloyl-CoA reductase, succinate semialdehyde reductase, and one of the copies of 3-hydroxybutyryl-CoA dehydrogenase form a cluster in the *M. sedula* genome. ND, not determined.

Enzyme	Assay temperature (°C)	Specific activity (nmol min^{-1} mg^{-1} protein)		Genes in *M. sedula*
		Measured	Tentatively extrapolated to 75°C*	
Acetyl-CoA carboxylase	65	55–70 (*19*)	110–140	Msed_0147/Msed_0148/Msed_1375†
Malonyl-CoA reductase (NADPH)	65	≥210 (*17*)	≥420	Msed_0709
Malonate semialdehyde reductase (NADPH)	65	1,500	3,000	Unknown
3-Hydroxypropionyl-CoA synthetase (AMP-forming)	55	≥60 (*4*)	≥240	Msed_1456
3-Hydroxypropionyl-CoA dehydratase	55	≥60 (*4*)	≥240	Msed_2001
Acryloyl-CoA reductase (NADPH)	55	≥60 (*4*)	≥240	Msed_1426
Propionyl-CoA carboxylase	65	60–75 (*19*)	120–150	Msed_0147/Msed_0148/Msed_1375†
Methylmalonyl-CoA epimerase	55	Qualitatively shown by HPLC (*4*)	ND	Msed_0639
Methylmalonyl-CoA mutase	55	Qualitatively shown by HPLC (*4*)	ND	Msed_0638/Msed_2055†
Succinyl-CoA reductase (NADPH)	65	500	1,000	Msed_0709
Succinate semialdehyde reductase (NADPH)	65	2,500	5,000	Msed_1424
4-Hydroxybutyryl-CoA synthetase (AMP-forming)	65	150	300	Msed_1422
4-Hydroxybutyryl-CoA dehydratase	42	40	390	Msed_1220, Msed_1321
Crotonyl-CoA hydratase [(*S*)-3-hydroxybutyryl-CoA–forming]	42	1,500	15,000	Five possible candidates (Msed_0399, Msed_0384, Msed_0385, Msed_0336, Msed_0566)
(*S*)-3-Hydroxybutyryl-CoA dehydrogenase (NAD^+)	65	800	1,600	Four possible candidates (Msed_1423, Msed_0399, Msed_1993, Msed_0389)
Acetoacetyl-CoA β-ketothiolase	65	530	1,060	Seven possible candidates (Msed_0656, Msed_1647, Msed_1290, Msed_0396, Msed_0386, Msed_0271, Msed_0270)

*The specific activity at 75°C was calculated based on the assumption that a 10°C rise in temperature doubles the reaction rates. At high temperatures, enzymes may become inactivated in vitro, in contrast to the protected environment of the cell. †Subunits of multicomponent enzyme.

for CO_2 fixation, which results in acetyl-CoA formation from citrate (*6*); however, pyruvate synthase activity appears to be lacking in autotrophically grown cells (*24*). This enzyme is normally responsible for the reductive carboxylation of acetyl-CoA to pyruvate in autotrophic anaerobes. In the absence of pyruvate synthase, the second half of the proposed cycle may be used in the reverse direction to assimilate two molecules of acetyl-CoA into succinyl-CoA, to give a modified reductive citric acid cycle. Several heterotrophic Thermococcales and Halobacteriales harbor the characteristic genes for the first part of the cycle but lack those for the second part (table S1). Because their genomes appear to lack the genes for isocitrate lyase and malate synthase, which are key enzymes of the glyoxylate cycle, these organisms may thus use the first part of the cycle for the assimilation of acetyl-CoA, instead of the glyoxylate cycle, as well as for propionate assimilation.

4-Hydroxybutyryl-CoA dehydratase was originally described in a few strict anaerobes that use it in fermentation (*15*, *25*). These strictly anaerobic Bacteria form a separate "anaerobe cluster" in the 4-hydroxybutyryl-CoA dehydratase phylogenetic tree (Fig. 3). Two independent clusters are formed by hyperthermophilic Crenarchaea that are unable to ferment, with type 1 being more common than type 2. Another cluster is associated with mesophilic Crenarchaea such as *Cenarchaeum* sp., a member of the "marine group"–1 Crenarchaeota, as well as with many marine environmental metagenomes from the Global Ocean Sampling (GOS) database (*26*, *27*). The Basic Local Alignment Search Tool (BLAST) search identified 189 specific genes (18 complete genes and 171 fragments) of 4-hydroxybutyryl-CoA dehydratase in the GOS database, most of which (84%) group in the "marine cluster"–1 (Fig. 3). It is unlikely that the bearers of this gene conduct fermentation in the oxic seawater. The number of identified 4-hydroxybutyryl-CoA dehydratase gene sequences in the GOS database is comparable with that of the gene of RuBisCO large subunit (344 specific genes, including 26 complete genes and 318 fragments). This indicates that a group of abundant mesophilic autotrophic Crenarchaea in the sea (*28*–*30*) may use the proposed 3-hydroxypropionate/4-hydroxybutyrate pathway for CO_2 fixation; yet, such comparisons depend on the cloning efficiency of the required genes. Because these Crenarchaea probably use ammonia as an electron donor (*12*, *20*, *30*), their contribution to the carbon cycle should be much lower than that of phototrophs [~1% of annual marine production (*29*)].

It should be stressed that, in other Archaea, not all individual reactions of the proposed cycle may be catalyzed by the same kind of enzyme. For instance, various alcohol dehydrogenases, aldehyde dehydrogenases, acyl-CoA synthetases, or enoyl-CoA hydratases may fulfill the same

function; yet, each superfamily of those enzymes comprises different enzyme families, from which genes may have been recruited. Also, the pathway of acetyl-CoA assimilation and phosphoenolpyruvate formation may differ. At last, one may be able to trace back the roots of the individual enzymes and come to tentative conclusions regarding the evolution of this cycle. Carboxyphosphate, which is used in the biotin-dependent carboxylase reactions, is an attractive model for carbon fixation during chemoevolution.

Several questions remain. What is the function of two different copies of 4-hydroxybutyryl-CoA dehydratase genes in autotrophic Sulfolobales? What are the functions of acetyl-CoA carboxylase and the enzymes of part 1 of the previously unrecognized pathway in various heterotrophic Archaea? Does the second part of the pathway, when operated in the reverse direction, serve as an acetyl-CoA assimilation route in some Archaea that lack the first part of the cycle? Which of the potential autotrophic pathways is operating in *Archaeoglobus*, which harbors the genes for the reductive acetyl-CoA pathway, for the proposed new pathway, and for RuBisCO (*31*, *32*)?

References and Notes

1. G. Wächtershäuser, *Proc. Natl. Acad. Sci. U.S.A.* **87**, 200 (1990).
2. O. K. Kandler, K. O. Stetter, *Zentbl. Bakteriol. Mikrobiol. Hyg. 1 Abt. Orig. C* **2**, 111 (1981).
3. M. Ishii *et al.*, *Arch. Microbiol.* **166**, 368 (1997).
4. C. Menendez *et al.*, *J. Bacteriol.* **181**, 1088 (1999).
5. N. P. Burton, T. D. Williams, P. R. Norris, *Arch. Microbiol.* **172**, 349 (1999).
6. M. Hügler, H. Huber, K. O. Stetter, G. Fuchs, *Arch. Microbiol.* **179**, 160 (2003).
7. H. Holo, *Arch. Microbiol.* **151**, 252 (1989).
8. G. Strauss, G. Fuchs, *Eur. J. Biochem.* **215**, 633 (1993).
9. H. Huber, K. O. Stetter, in *Bergey's Manual of Systematic Bacteriology, Vol. 1*, D. R. Boone, R. W. Castenholz, Eds. (Springer-Verlag, New York, ed. 2, 2001), pp. 198–202.
10. K. O. Stetter, *Syst. Appl. Microbiol.* **10**, 172 (1988).
11. C. M. Preston, K. Y. Wu, T. F. Molinski, E. F. DeLong, *Proc. Natl. Acad. Sci. U.S.A.* **93**, 6241 (1996).
12. M. Könneke *et al.*, *Nature* **437**, 543 (2005).
13. B. M. Martins, H. Dobbek, I. Çinkaya, W. Buckel, A. Messerschmidt, *Proc. Natl. Acad. Sci. U.S.A.* **101**, 15645 (2004).
14. U. Näser *et al.*, *Bioorg. Chem.* **33**, 53 (2005).
15. A. Gerhardt, I. Çinkaya, D. Linder, G. Huisman, W. Buckel, *Arch. Microbiol.* **174**, 189 (2000).
16. Materials and methods are available as supporting material on *Science* Online.
17. B. Alber *et al.*, *J. Bacteriol.* **188**, 8551 (2006).
18. S. Chuakrut, H. Arai, M. Ishii, Y. Igarashi, *J. Bacteriol.* **185**, 938 (2003).
19. M. Hügler, R. S. Krieger, M. Jahn, G. Fuchs, *Eur. J. Biochem.* **270**, 736 (2003).
20. S. J. Hallam *et al.*, *PLoS Biol.* **4**, e95 (2006).
21. G. G. B. Tcherkez, G. D. Farquhar, T. J. Andrews, *Proc. Natl. Acad. Sci. U.S.A.* **103**, 7246 (2006).
22. R. J. Ellis, *Trends Biochem. Sci.* **4**, 241 (1979).
23. U. Jahn, H. Huber, W. Eisenreich, M. Hügler, G. Fuchs, *J. Bacteriol.* **189**, 4108 (2007).
24. Y. Hu, J. F. Holden, *J. Bacteriol.* **188**, 4350 (2006).
25. U. Scherf, B. Söhling, G. Gottschalk, D. Linder, W. Buckel, *Arch. Microbiol.* **161**, 239 (1994).
26. S. Yooseph *et al.*, *PLoS Biol.* **5**, e16 (2007).
27. D. B. Rusch *et al.*, *PLoS Biol.* **5**, e77 (2007).
28. M. B. Karner, E. F. DeLong, D. M. Karl, *Nature* **409**, 507 (2001).
29. A. E. Ingalls *et al.*, *Proc. Natl. Acad. Sci. U.S.A.* **103**, 6442 (2006).
30. C. A. Francis, J. M. Beman, M. M. M. Kuypers, *ISME J.* **1**, 19 (2007).
31. H.-P. Klenk *et al.*, *Nature* **390**, 364 (1997).
32. M. W. Finn, F. R. Tabita, *J. Bacteriol.* **185**, 3049 (2003).

33. This work is dedicated to O. Kandler. We thank P. Friedrich (Universität Marburg) for help with the 4-hydroxybutyryl-CoA dehydratase assay; N. Gad'on and C. Ebenau-Jehle (Universität Freiburg) for growing cells and maintaining the laboratory; and M. Hügler and B. Alber, who substantially contributed to earlier studies on *Metallosphaera*. The U.S. Department of Energy Joint Genome Institute is acknowledged for the early release of archaeal genomic sequence data. This work was supported by the Deutsche Forschungsgemeinschaft, Evonik-Degussa GmbH, Land Nordrhein-Westfalen, and the Fonds der Chemischen Industrie.

Supporting Online Material

www.sciencemag.org/cgi/content/full/318/5857/1782/DC1
Materials and Methods
Figs. S1 to S7
Tables S1 and S2
References

31 August 2007; accepted 22 October 2007
10.1126/science.1149976

Rev-erbα, a Heme Sensor That Coordinates Metabolic and Circadian Pathways

Lei Yin,[1] Nan Wu,[1] Joshua C. Curtin,[1] Mohammed Qatanani,[1] Nava R. Szwergold,[1] Robert A. Reid,[2] Gregory M. Waitt,[2] Derek J. Parks,[3] Kenneth H. Pearce,[3] G. Bruce Wisely,[3] Mitchell A. Lazar[1]*

The circadian clock temporally coordinates metabolic homeostasis in mammals. Central to this is heme, an iron-containing porphyrin that serves as prosthetic group for enzymes involved in oxidative metabolism as well as transcription factors that regulate circadian rhythmicity. The circadian factor that integrates this dual function of heme is not known. We show that heme binds reversibly to the orphan nuclear receptor Rev-erbα, a critical negative component of the circadian core clock, and regulates its interaction with a nuclear receptor corepressor complex. Furthermore, heme suppresses hepatic gluconeogenic gene expression and glucose output through Rev-erbα–mediated gene repression. Thus, Rev-erbα serves as a heme sensor that coordinates the cellular clock, glucose homeostasis, and energy metabolism.

Circadian rhythms are intrinsic time-keeping mechanisms conserved throughout the animal kingdom (*1*–*3*). Many aspects of mammalian behavior and physiology, including sleep-wake cycles, blood pressure, body temperature, and metabolic pathways are controlled by the circadian clock (*3*–*5*). At the molecular level, cellular rhythms are generated and maintained through interconnected transcriptional-translational feedback loops of clock genes, which are conserved in the central pacemaker and in peripheral tissues (*2*, *3*). The nuclear receptor Rev-erbα has been identified as a link between positive and negative loops of the circadian clock by controlling rhythmic expression of the *Bmal1* gene (*6*–*9*). This repression function is dependent on recruitment of the nuclear receptor corepressor–histone deacetylase 3 (NCoR-HDAC3) complex directly to the *Bmal1* gene.

Several genomewide expression studies have highlighted that genes involved in glucose metabolism, lipid metabolism, heme biosynthesis, and mitochondrial adenosine triphosphate (ATP) synthesis all exhibit a circadian pattern of expression (*1*, *10*–*12*). For example, gluconeogenic genes such as phosphoenol pyruvate carboxykinase (PEPCK) and glucose 6-phosphatase (G6Pase) are typical clock-controlled metabolic-related genes (*12*). Furthermore, mice deficient in either *Bmal1* or *Clock* genes exhibit abnormal metabolic activities (*13*–*15*). Despite the evidence linking circadian clocks and metabolism, the mechanism by which the circadian clock is integrated into metabolic systems remains poorly understood.

To investigate the role of Rev-erbα in metabolic gene regulation, we first depleted Rev-erbα from HepG2 human hepatoma cells with small interfering RNA molecules (siRNAs). Expression of genes encoding gluconenogenic enzymes G6Pase and PEPCK was significantly increased when Rev-erbα amounts were reduced (Fig. 1A). By contrast, loss of Rev-erbα did not affect the expression of acetyl–coenzyme A (CoA) carboxylase or fatty acid synthase, which are involved fatty acid metabolism (fig. S1). Overexpression of full-length Rev-erbα in HepG2 cells decreased expression of G6Pase, PEPCK, and the known Rev-erbα target Bmal1 (Fig. 1B). Further, Rev-erbα repressed expression of a luciferase

[1]Division of Endocrinology, Diabetes, and Metabolism; Department of Medicine; and Institute for Diabetes, Obesity, and Metabolism, University of Pennsylvania School of Medicine, Philadelphia, PA 19104, USA. [2]Department of Computational and Structural Chemistry, Molecular Discovery Research, GlaxoSmithKline, Research Triangle Park, NC 27709–3398, USA. [3]Department of Biological Reagents and Assay Development, Molecular Discovery Research, GlaxoSmithKline, Research Triangle Park, NC 27709–3398, USA.

*To whom correspondence should be addressed. E-mail: lazar@mail.med.upenn.edu

function; yet, each superfamily of those enzymes comprises different enzyme families, from which genes may have been recruited. Also, the pathway of acetyl-CoA assimilation and phosphoenolpyruvate formation may differ. At last, one may be able to trace back the roots of the individual enzymes and come to tentative conclusions regarding the evolution of this cycle. Carboxyphosphate, which is used in the biotin-dependent carboxylase reactions, is an attractive model for carbon fixation during chemoevolution.

Several questions remain. What is the function of two different copies of 4-hydroxybutyryl-CoA dehydratase genes in autotrophic Sulfolobales? What are the functions of acetyl-CoA carboxylase and the enzymes of part 1 of the previously unrecognized pathway in various heterotrophic Archaea? Does the second part of the pathway, when operated in the reverse direction, serve as an acetyl-CoA assimilation route in some Archaea that lack the first part of the cycle? Which of the potential autotrophic pathways is operating in *Archaeoglobus*, which harbors the genes for the reductive acetyl-CoA pathway, for the proposed new pathway, and for RuBisCO (*31*, *32*)?

References and Notes

1. G. Wächtershäuser, *Proc. Natl. Acad. Sci. U.S.A.* **87**, 200 (1990).
2. O. K. Kandler, K. O. Stetter, *Zentbl. Bakteriol. Mikrobiol. Hyg. 1 Abt. Orig. C* **2**, 111 (1981).
3. M. Ishii *et al.*, *Arch. Microbiol.* **166**, 368 (1997).
4. C. Menendez *et al.*, *J. Bacteriol.* **181**, 1088 (1999).
5. N. P. Burton, T. D. Williams, P. R. Norris, *Arch. Microbiol.* **172**, 349 (1999).
6. M. Hügler, H. Huber, K. O. Stetter, G. Fuchs, *Arch. Microbiol.* **179**, 160 (2003).
7. H. Holo, *Arch. Microbiol.* **151**, 252 (1989).
8. G. Strauss, G. Fuchs, *Eur. J. Biochem.* **215**, 633 (1993).
9. H. Huber, K. O. Stetter, in *Bergey's Manual of Systematic Bacteriology, Vol. 1*, D. R. Boone, R. W. Castenholz, Eds. (Springer-Verlag, New York, ed. 2, 2001), pp. 198–202.
10. K. O. Stetter, *Syst. Appl. Microbiol.* **10**, 172 (1988).
11. C. M. Preston, K. Y. Wu, T. F. Molinski, E. F. DeLong, *Proc. Natl. Acad. Sci. U.S.A.* **93**, 6241 (1996).
12. M. Könneke *et al.*, *Nature* **437**, 543 (2005).
13. B. M. Martins, H. Dobbek, I. Çinkaya, W. Buckel, A. Messerschmidt, *Proc. Natl. Acad. Sci. U.S.A.* **101**, 15645 (2004).
14. U. Näser *et al.*, *Bioorg. Chem.* **33**, 53 (2005).
15. A. Gerhardt, I. Çinkaya, D. Linder, G. Huisman, W. Buckel, *Arch. Microbiol.* **174**, 189 (2000).
16. Materials and methods are available as supporting material on *Science* Online.
17. B. Alber *et al.*, *J. Bacteriol.* **188**, 8551 (2006).
18. S. Chuakrut, H. Arai, M. Ishii, Y. Igarashi, *J. Bacteriol.* **185**, 938 (2003).
19. M. Hügler, R. S. Krieger, M. Jahn, G. Fuchs, *Eur. J. Biochem.* **270**, 736 (2003).
20. S. J. Hallam *et al.*, *PLoS Biol.* **4**, e95 (2006).
21. G. G. B. Tcherkez, G. D. Farquhar, T. J. Andrews, *Proc. Natl. Acad. Sci. U.S.A.* **103**, 7246 (2006).
22. R. J. Ellis, *Trends Biochem. Sci.* **4**, 241 (1979).
23. U. Jahn, H. Huber, W. Eisenreich, M. Hügler, G. Fuchs, *J. Bacteriol.* **189**, 4108 (2007).
24. Y. Hu, J. F. Holden, *J. Bacteriol.* **188**, 4350 (2006).
25. U. Scherf, B. Söhling, G. Gottschalk, D. Linder, W. Buckel, *Arch. Microbiol.* **161**, 239 (1994).
26. S. Yooseph *et al.*, *PLoS Biol.* **5**, e16 (2007).
27. D. B. Rusch *et al.*, *PLoS Biol.* **5**, e77 (2007).
28. M. B. Karner, E. F. DeLong, D. M. Karl, *Nature* **409**, 507 (2001).
29. A. E. Ingalls *et al.*, *Proc. Natl. Acad. Sci. U.S.A.* **103**, 6442 (2006).
30. C. A. Francis, J. M. Beman, M. M. M. Kuypers, *ISME J.* **1**, 19 (2007).
31. H.-P. Klenk *et al.*, *Nature* **390**, 364 (1997).
32. M. W. Finn, F. R. Tabita, *J. Bacteriol.* **185**, 3049 (2003).

33. This work is dedicated to O. Kandler. We thank P. Friedrich (Universität Marburg) for help with the 4-hydroxybutyryl-CoA dehydratase assay; N. Gad'on and C. Ebenau-Jehle (Universität Freiburg) for growing cells and maintaining the laboratory; and M. Hügler and B. Alber, who substantially contributed to earlier studies on *Metallosphaera*. The U.S. Department of Energy Joint Genome Institute is acknowledged for the early release of archaeal genomic sequence data. This work was supported by the Deutsche Forschungsgemeinschaft, Evonik-Degussa GmbH, Land Nordrhein-Westfalen, and the Fonds der Chemischen Industrie.

Supporting Online Material

www.sciencemag.org/cgi/content/full/318/5857/1782/DC1
Materials and Methods
Figs. S1 to S7
Tables S1 and S2
References

31 August 2007; accepted 22 October 2007
10.1126/science.1149976

Rev-erbα, a Heme Sensor That Coordinates Metabolic and Circadian Pathways

Lei Yin,[1] Nan Wu,[1] Joshua C. Curtin,[1] Mohammed Qatanani,[1] Nava R. Szwergold,[1] Robert A. Reid,[2] Gregory M. Waitt,[2] Derek J. Parks,[3] Kenneth H. Pearce,[3] G. Bruce Wisely,[3] Mitchell A. Lazar[1]*

The circadian clock temporally coordinates metabolic homeostasis in mammals. Central to this is heme, an iron-containing porphyrin that serves as prosthetic group for enzymes involved in oxidative metabolism as well as transcription factors that regulate circadian rhythmicity. The circadian factor that integrates this dual function of heme is not known. We show that heme binds reversibly to the orphan nuclear receptor Rev-erbα, a critical negative component of the circadian core clock, and regulates its interaction with a nuclear receptor corepressor complex. Furthermore, heme suppresses hepatic gluconeogenic gene expression and glucose output through Rev-erbα–mediated gene repression. Thus, Rev-erbα serves as a heme sensor that coordinates the cellular clock, glucose homeostasis, and energy metabolism.

Circadian rhythms are intrinsic time-keeping mechanisms conserved throughout the animal kingdom (*1*–*3*). Many aspects of mammalian behavior and physiology, including sleep-wake cycles, blood pressure, body temperature, and metabolic pathways are controlled by the circadian clock (*3*–*5*). At the molecular level, cellular rhythms are generated and maintained through interconnected transcriptional-translational feedback loops of clock genes, which are conserved in the central pacemaker and in peripheral tissues (*2*, *3*). The nuclear receptor Rev-erbα has been identified as a link between positive and negative loops of the circadian clock by controlling rhythmic expression of the *Bmal1* gene (*6*–*9*). This repression function is dependent on recruitment of the nuclear receptor corepressor–histone deacetylase 3 (NCoR-HDAC3) complex directly to the *Bmal1* gene.

Several genomewide expression studies have highlighted that genes involved in glucose metabolism, lipid metabolism, heme biosynthesis, and mitochondrial adenosine triphosphate (ATP) synthesis all exhibit a circadian pattern of expression (*1*, *10*–*12*). For example, gluconeogenic genes such as phosphoenol pyruvate carboxykinase (PEPCK) and glucose 6-phosphatase (G6Pase) are typical clock-controlled metabolic-related genes (*12*). Furthermore, mice deficient in either *Bmal1* or *Clock* genes exhibit abnormal metabolic activities (*13*–*15*). Despite the evidence linking circadian clocks and metabolism, the mechanism by which the circadian clock is integrated into metabolic systems remains poorly understood.

To investigate the role of Rev-erbα in metabolic gene regulation, we first depleted Rev-erbα from HepG2 human hepatoma cells with small interfering RNA molecules (siRNAs). Expression of genes encoding gluconenogenic enzymes G6Pase and PEPCK was significantly increased when Rev-erbα amounts were reduced (Fig. 1A). By contrast, loss of Rev-erbα did not affect the expression of acetyl–coenzyme A (CoA) carboxylase or fatty acid synthase, which are involved fatty acid metabolism (fig. S1). Overexpression of full-length Rev-erbα in HepG2 cells decreased expression of G6Pase, PEPCK, and the known Rev-erbα target Bmal1 (Fig. 1B). Further, Rev-erbα repressed expression of a luciferase

[1]Division of Endocrinology, Diabetes, and Metabolism; Department of Medicine; and Institute for Diabetes, Obesity, and Metabolism, University of Pennsylvania School of Medicine, Philadelphia, PA 19104, USA. [2]Department of Computational and Structural Chemistry, Molecular Discovery Research, GlaxoSmithKline, Research Triangle Park, NC 27709–3398, USA. [3]Department of Biological Reagents and Assay Development, Molecular Discovery Research, GlaxoSmithKline, Research Triangle Park, NC 27709–3398, USA.

*To whom correspondence should be addressed. E-mail: lazar@mail.med.upenn.edu

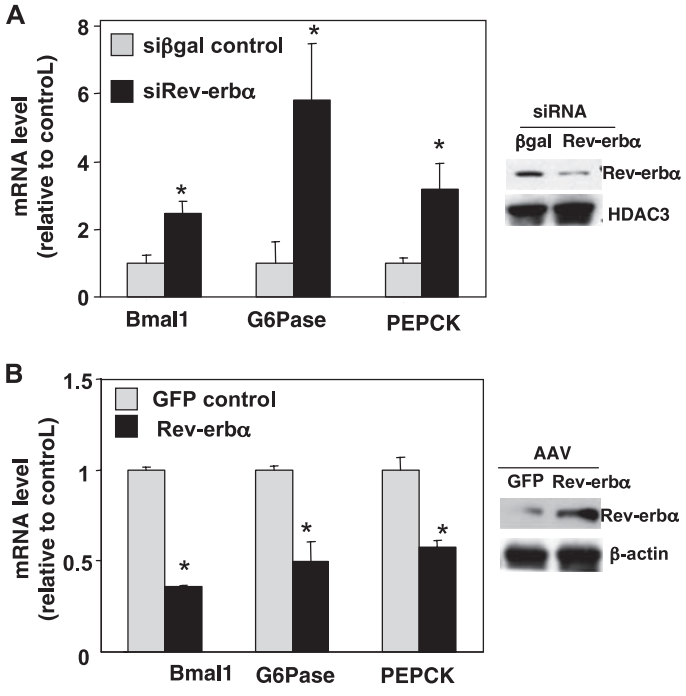

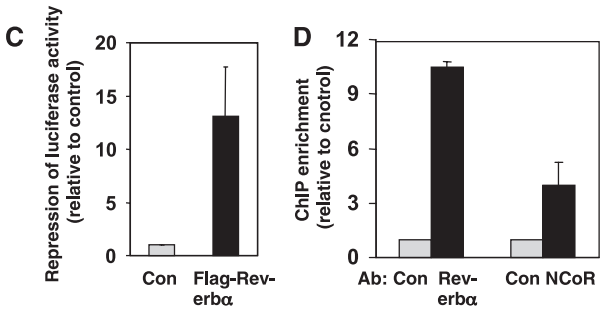

Fig. 1. Basal repression of gluconeogenic genes mediated by Rev-erbα. (**A**) siRNA knockdown of either β-galactosidase (control) or human Rev-erbα in HepG2 liver cells. Bmal1, G6Pase, and PEPCK mRNA concentrations were quantitated by reverse transcription polymerase chain reaction (RT-PCR) and normalized to those of cyclophilin. Mean ± SD of three independent experiments is shown. **P* < 0.05 compared with control by Student's *t* test. Proteins were detected by immunoblotting. (**B**) HepG2 cells were infected with recombinant adeno-associated virus (AAV) expressing either green fluorescent protein (GFP) or Rev-erbα, and Bmal1, G6Pase, and PEPCK mRNAs were measured. Mean ± SD of three independent experiments is shown. **P* < 0.05 compared with GFP control. Expression of Flag-tagged mouse Rev-erbα and β-actin control were determined by immunoblot. (**C**) Activity of a luciferase reporter gene driven by the human G6Pase promoter in HepG2 cells transfected with Rev-erbα or control plasmid. Results are expressed as mean ± SD of triplicate samples. (**D**) ChIP assays to detect association of endogenous Rev-erbα and NCoR with the proximal region of the human G6Pase promoter. Anti-GFP was used as a negative control. Mean ± range of duplicate samples is shown.

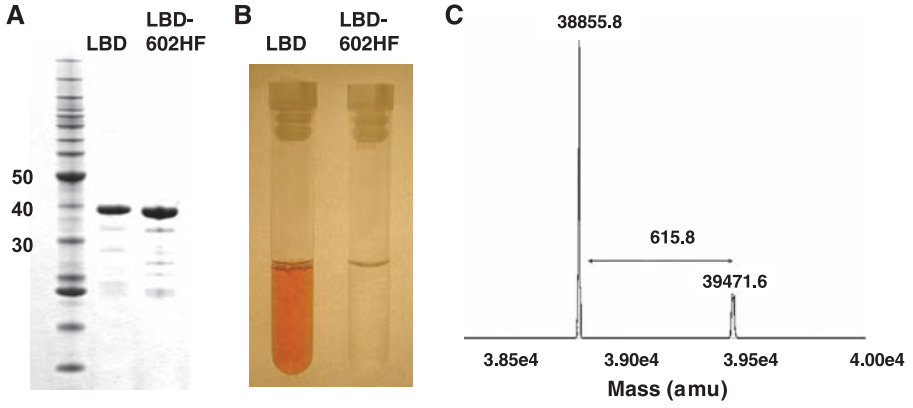

Fig. 2. Binding of heme to Rev-erbα. (**A**) Purified Rev-erbα LBD and 602HF mutant in *E. coli* in the presence of 75 mM hemin. 1 μl of purified protein was separated by SDS–polyacrylamide gel electrophoresis and stained by Coomassie blue. Numbers to the left indicate molecular mass in kD. (**B**) Rev-erbα LBD, but not the 602HF mutant, is red. Both proteins are shown at concentrations of 3.7 mg/ml. (**C**) Mass spectrometric determination of Rev-erbα LBD-bound hemin. amu, atomic mass units.

reporter driven by the human G6Pase promoter (Fig. 1C). With chromatin immunoprecipitation (ChIP), we observed Rev-erbα, along with NCoR, in the vicinity of potential Rev-erbα binding sites (ROREs) (Fig. 1D). Deletion of the distal RORE from human G6Pase promoter abrogated Rev-erbα–dependent repression activity on this promoter (fig. S2). Taken together, these results suggest that Rev-erbα recruits the NCoR-HDAC3 corepressor complex to actively repress the expression of gluconeogenic genes and in turn may have a role in circadian oscillation of gluconeogenesis.

Heme serves as a prosthetic group for a large number of cellular proteins with diverse biological functions, including mitochondrial respiration, hormone synthesis and metabolism, and nitric oxide synthesis (*16*–*18*). Heme has been identified as the prosthetic group of two clock proteins, NPAS2 (*19*) and PER2 (*20*), and implicated in the coregulation of heme biosynthesis and circadian rhythm (*20*, *21*). The homolog of Rev-erbα in *Drosophila melanogaster*, E75, binds heme, which regulates E75 function by increasing protein stability (*22*, *23*). When the Rev-erbα ligand binding domain (LBD, amino acids 281 to 614, optimized for production and purification) was purified from *Escherichia coli* grown in the presence of hemin (Fig. 2A), the protein was red (Fig. 2B). This red color was abolished when His^{602} (H602) was mutated to phenylalanine (602HF, Fig. 2B). Ultraviolet-visible spectrophotometric analysis revealed that the Rev-erbα LBD contained a chromophore with λ_{max} of 414 nm that shifted to 428 nm in the presence of dithionite (fig. S3), suggesting that heme was bound. By contrast, little absorbance in the 400 to 430 nM range was observed for the 602HF mutant. Mass spectrometric analysis of the Rev-erbα LBD revealed the presence of heme (Fig. 2C), which was not identified in the 602HF mutant (fig. S4). These results demonstrate that Rev-erbα binds to heme and that H602 is critical for this function. Heme bound to the Rev-erbα LBD was displaced by molar excess of heme analogs (fig. S5), indicating that heme binding to Rev-erbα is exchangeable and reversible.

We next assessed the biological function of heme binding to Rev-erbα in mammalian cells. In human embryonic kidney 293T cells, the 602HF mutant that does not bind heme was at least as stable as wild-type (WT) Rev-erbα (Fig. 3A). However, the repression function of this mutant was attenuated on a *Bmal1*-luciferase vector (*9*) (Fig. 3B). A similar impairment of the 602HF mutant in repression was observed by using two additional reporter gene constructs that are repressed by WT Rev-erbα (fig. S6). ChIP demonstrated that the 602HF mutant bound at least as well as WT Rev-erbα to the Rev-erbα–responsive *Bmal1*. By contrast, recruitment of both NCoR and HDAC3 by the 602HF mutant was diminished relative to that of WT Rev-erbα (Fig. 3C). When Flag epitope–tagged Rev-erbα was stably expressed and immunoprecipitated from HeLa cells, WT Rev-erbα was associated with NCoR and HDAC3, whereas the 602HF mutant was not

(Fig. 3D). Thus, the 602HF mutation specifically impaired recruitment of the NCoR-HDAC3 complex to Rev-erbα.

To test whether heme binding to Rev-erbα directly regulates its interaction with the NCoR-HDAC3 corepressor complex, we cultured HeLa cells that stably express Rev-erbα in serum-free medium supplemented with succinylacetone (SA) to deplete heme (*24*, *25*). Heme depletion was confirmed by the characteristic increase in abundance of mRNA encoding δ-aminolevulinate synthase 1 (ALAS1) (fig. S7). The interaction between Rev-erbα and NCoR-HDAC3 was nearly abolished in heme-depleted cells (Fig. 4A). This was reversed by incubation of the cells with hemin for 6 hours, whereas the porphyrin-like vitamin B12 did not stabilize the Rev-erbα–corepressor complex (Fig. 4B). In vitro, stable association of the NCoR-HDAC3 complex with Rev-erbα occurred within 5 min of hemin treatment of extracts from heme-depleted cells (Fig. 4C). Furthermore, the ability of heme to stabilize the association between Rev-erbα and NCoR-HDAC3 was dependent on heme concentration (Fig. 4D and fig. S8). Interaction of bacterially expressed Rev-erbα LBD with a short peptide derived from NCoR suggested that heme stabilization of the interaction between full-length Rev-erbα and endogenous NCoR depends on factors other than the LBD alone (fig. S9).

We tested whether the heme-dependent recruitment of the NCoR-HDAC3 corepressor complex affected expression of circadian and metabolic Rev-erbα target genes. Consistent with our biochemical findings, heme depletion significantly increased the expression of the core clock gene *Bmal1* (fig. S10A), whereas hemin treatment significantly suppressed Bmal1 expression (fig. S10B), indicating that intracellular heme concentrations might regulate this Rev-erbα target. Hemin treatment also repressed transcription of the PEPCK and G6Pase genes in human HepG2 liver cells (Fig. 5A). Conversely, heme depletion by knockdown of ALAS1 (fig. S12) significantly induced G6Pase expression and in a manner that was reversed by addition of hemin (Fig. 5B), demonstrating the dependence of G6Pase transcription on heme concentrations. The repressive effect of heme was abrogated when the abundance of Rev-erbα was reduced by siRNA, indicating that the heme effect was Rev-erbα–dependent (Fig. 5C). Moreover, heme-dependent recruitment of NCoR and HDAC3, and a concomitant reduction in histone acetylation, was observed by ChIP at the endogenous *G6Pase* gene (Fig. 5D). Hemin treatment also repressed the expression of G6Pase and PEPCK in primary mouse hepatocytes (fig. S10) and blunted production of glucose (Fig. 5E), demonstrating the metabolic relevance of heme binding to Rev-erbα.

The circadian expression of Rev-erbα is regulated both transcriptionally, by BMAL1-CLOCK (*26*) and by Rev-erbα itself (*27*), as well as posttranslationally, by glycogen synthe-

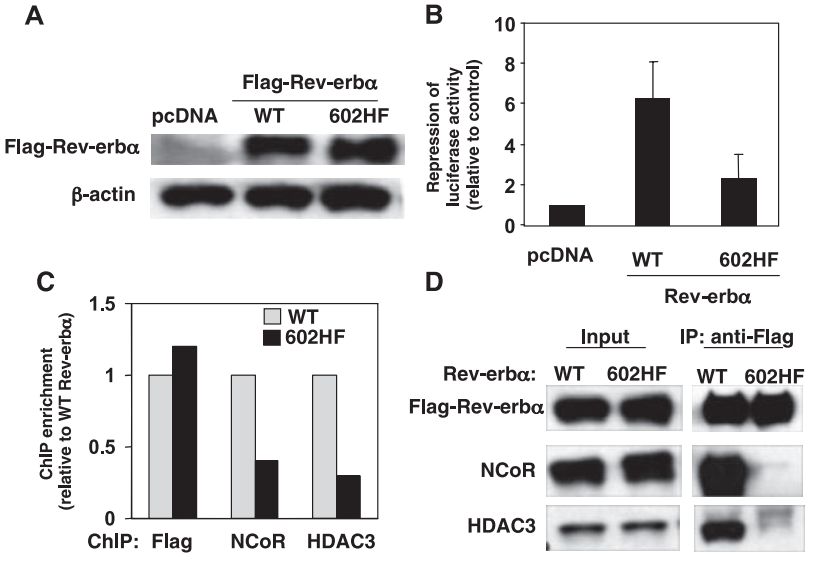

Fig. 3. Impaired transcriptional repression by the Rev-erbα 602HF mutant and failure to recruit the NCoR-HDAC3 corepressor complex. (**A**) Stability of Flag-tagged full-length Rev-erbα WT and 602HF mutant transfected into 293T cells. Proteins were detected by immunoblotting. (**B**) Repression of *Bmal1*-luciferase reporter in cells transfected with empty vector (pcDNA), WT Rev-erbα, or Rev-erbα-602HF. Results are expressed as mean ± SD of at least three independent experiments. (**C**) ChIP assay for recruitment of Rev-erbα, NCoR, and HDAC3 performed 36 hours after transfection of 293T cells with Flag-tagged Rev-erbα WT or 602HF vector and the *Bmal1* luciferase plasmid. (**D**) Protein-protein interaction between Rev-erbα WT or 602HF and NCoR-HDAC3 corepressor complex in Hela Tet-on cells stably transfected with an inducible expression vector expressing either WT or 602HF Flag-tagged Rev-erbα. Cells were lysed and subjected to immunoprecipitation (IP) with FlagM2-conjugated agarose beads. The presence of NCoR and HDAC3 was examined by immunoblotting.

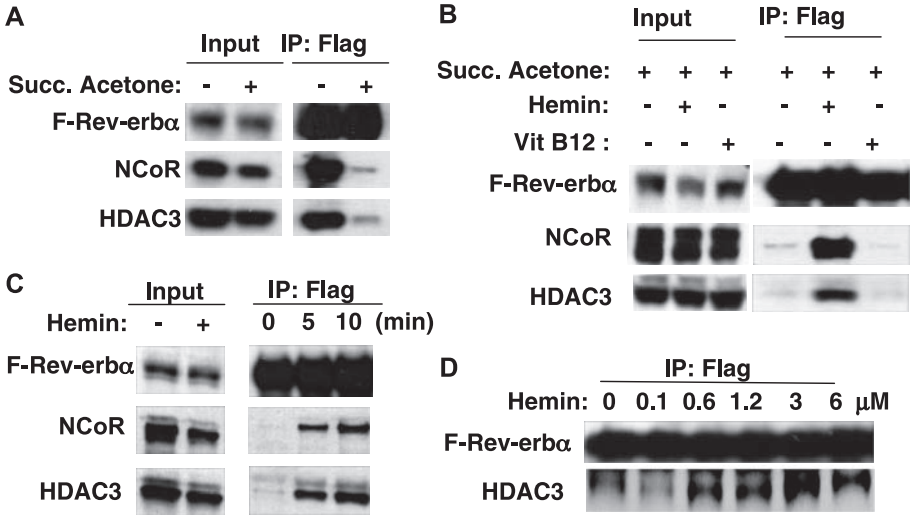

Fig. 4. Effect of alteration of heme concentration on the interaction between Rev-erbα and NCoR-HDAC3 corepressor complex. (**A**) Hela cells stably expressing WT Flag-tagged Rev-erbα were treated with SA (5 mM) for 16 hours to deplete intracellular heme. Amounts of NCoR and HDAC3 copurified with Flag–Rev-erbα were determined by immunoblotting. (**B**) Hela cells expressing Rev-erbα were first treated with SA for 16 hours and then treated with either dimethyl sulfoxide (DMSO), hemin (6 μM), or VitB12 (5 mg/ml) for 6 hours. Cells were then lysed and assayed for coimmunoprecipitation of NCoR-HDAC3 with Rev-erbα. (**C**) Time course of restoration of Rev-erbα binding to NCoR-HDAC3 after treatment with hemin for various times before immunoprecipitation. (**D**) Concentration dependence of hemin effect of Rev-erbα binding to NCoR-HDAC3.

sis kinase 3β–mediated phosphorylation and stabilization (*28*). We have demonstrated that alteration of heme modulates the interaction between Rev-erbα and the NCoR-HDAC3 corepressor complex. Heme concentrations oscillate in a circadian manner (*10*, *20*), and heme is also required by proteins that control various metabolic pathways and biological processes, making it a candidate for integrating circadian clock and metabolic systems. Heme negatively affects

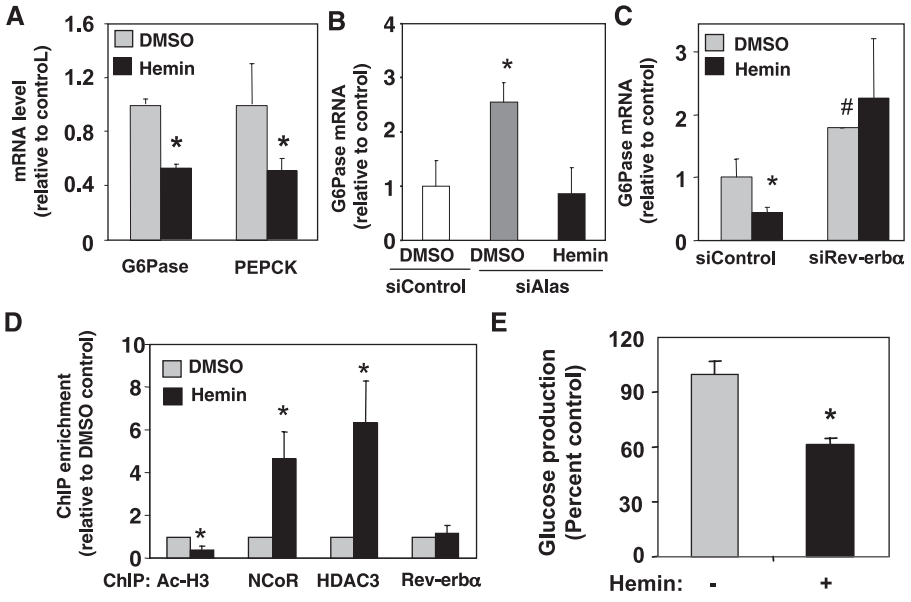

Fig. 5. Suppression of the expression of gluconeogenic genes and glucose production in liver cells treated with hemin. (**A**) Expression of G6Pase and PEPCK genes in HepG2 cells treated with either DMSO or hemin (6 μM) for 6 hours. Amounts of mRNA were quantitated by RT-PCR and normalized to cyclophilin. Mean ± SD of three independent experiments is shown. *$P < 0.05$ compared with control by Student's *t* test. (**B**) Expression of G6Pase gene in HepG2 cells treated with control or ALAS1-targeting siRNA and then stimulated with DMSO or hemin for 16 hours. Mean ± SD ($n = 3$),*$P < 0.05$ compared with siRNA control treated with DMSO. (**C**) Effect of hemin on the expression of G6Pase gene in cells depleted of Rev-erbα. Mean ± SD ($n = 3$), *P <0.05 compared with DMSO-treated cells transfected with control siRNA. Pound symbol indicates $P < 0.05$ compared with DMSO-treated cells transfected with control siRNA. (**D**) Effect of hemin on the occupancy of Rev-erbα, HDAC3, NCoR, or acetylated H3 (Ac-H3) at the *G6Pase* promoter in cells. Results of hemin-treatment are normalized to DMSO results. Mean ± SD ($n = 4$). *$P < 0.05$ compared with control. (**E**) Primary mouse hepatocytes were treated with dexamethasone and 8-(4-chlorophenyl-thio)-adenosine 3′,5′-cyclic monophosphate along with DMSO or hemin for 16 hours, then glucose in the medium was measured. Mean ± SD of triplicate samples is shown, and four independent experiments gave similar results. *$P < 0.05$ compared with control.

BMAL1-NPAS2–dependent transcription activation (*19*–*21*) while enhancing Rev-erbα–mediated transcription repression, providing a potential means of maintaining the amplitude of circadian rhythms.

Expression of the gene encoding ALAS1, the rate-limiting enzyme in heme biosynthesis, increased in response to peroxisome proliferator activated receptor coactivator–1α (*29*), a regulator of mitochondriogenesis that increases flux through the Krebs cycle (*30*). This first and rate-limiting enzyme in heme biosynthesis requires succincyl CoA, a Krebs cycle intermediate (*17*, *29*). Gluconeogenesis competes with the Krebs cycle for metabolic intermediates whose depletion compromises heme biosynthesis as well as mitochondrial oxidative metabolism (fig. S13). The ability of Rev-erbα to function as a receptor for heme could provide a general mechanism for coordinating these processes.

References and Notes

1. F. Gachon, E. Nagoshi, S. A. Brown, J. Ripperger, U. Schibler, *Chromosoma* **113**, 103 (2004).
2. S. M. Reppert, D. R. Weaver, *Annu. Rev. Physiol.* **63**, 647 (2001).
3. P. L. Lowrey, J. S. Takahashi, *Annu. Rev. Genomics Hum. Genet.* **5**, 407 (2004).
4. A. Kohsaka, J. Bass, *Trends Endocrinol. Metab.* **18**, 4 (2007).
5. M. Stratmann, U. Schibler, *J. Biol. Rhythms* **21**, 494 (2006).
6. M. Akashi, T. Takumi, *Nat. Struct. Mol. Biol.* **12**, 441 (2005).
7. N. Preitner *et al.*, *Cell* **110**, 251 (2002).
8. T. K. Sato *et al.*, *Neuron* **43**, 527 (2004).
9. L. Yin, M. A. Lazar, *Mol. Endocrinol.* **19**, 1452 (2005).
10. M. F. Ceriani *et al.*, *J. Neurosci.* **22**, 9305 (2002).
11. K. Oishi *et al.*, *J. Biol. Chem.* **278**, 41519 (2003).
12. S. Panda *et al.*, *Cell* **109**, 307 (2002).
13. K. Oishi *et al.*, *FEBS Lett.* **580**, 127 (2006).
14. R. D. Rudic *et al.*, *PLoS Biol.* **2**, e377 (2004).
15. F. W. Turek *et al.*, *Science* **308**, 1043 (2005); published online 21 April 2005 (10.1126/science.1108750).
16. H. Atamna, *Ageing Res. Rev.* **3**, 303 (2004).
17. P. Ponka, *Am. J. Med. Sci.* **318**, 241 (1999).
18. A. S. Tsiftsoglou, A. I. Tsamadou, L. C. Papadopoulou, *Pharmacol. Ther.* **111**, 327 (2006).
19. E. M. Dioum *et al.*, *Science* **298**, 2385 (2002); published online 20 November 2002 (10.1126/science.1078456).
20. K. Kaasik, C. C. Lee, *Nature* **430**, 467 (2004).
21. D. Boehning, S. H. Snyder, *Science* **298**, 2339 (2002).
22. E. de Rosny *et al.*, *Biochemistry* **45**, 9727 (2006).
23. J. Reinking *et al.*, *Cell* **122**, 195 (2005).
24. S. Sassa, A. Kappas, *J. Clin. Investig.* **71**, 625 (1983).
25. Y. Zhu, T. Hon, W. Ye, L. Zhang, *Cell Growth Differ.* **13**, 431 (2002).
26. J. A. Ripperger, *Chronobiol. Int.* **23**, 135 (2006).
27. G. Adelmant, A. Begue, D. Stehelin, V. Laudet, *Proc. Natl. Acad. Sci. U.S.A.* **93**, 3553 (1996).
28. L. Yin, J. Wang, P. S. Klein, M. A. Lazar, *Science* **311**, 1002 (2006).
29. C. Handschin *et al.*, *Cell* **122**, 505 (2005).
30. S. C. Burgess *et al.*, *J. Biol. Chem.* **281**, 19000 (2006).

31. We thank R. Gampe, D. Steger, T. Stanley, M. Walker, J. Williams, and T. Willson for helpful discussions. This work was supported by National Institute of Diabetes and Digestive and Kidney Diseases grant R01 DK45586 (M.A.L.).

Supporting Online Material

www.sciencemag.org/cgi/content/full/1150179/DC1
Materials and Methods
Figs. S1 to S13
References

6 September 2007; accepted 28 September 2007
Published online 15 November 2007;
10.1126/science.1150179
Include this information when citing this paper.

The *Arabidopsis* Circadian Clock Incorporates a cADPR-Based Feedback Loop

Antony N. Dodd,[1] Michael J. Gardner,[1] Carlos T. Hotta,[1] Katharine E. Hubbard,[1] Neil Dalchau,[1] John Love,[1]* Jean-Maurice Assie,[1] Fiona C. Robertson,[1] Mia Kyed Jakobsen,[1]† Jorge Gonçalves,[2] Dale Sanders,[3] Alex A. R. Webb[1]‡

Transcriptional feedback loops are a feature of circadian clocks in both animals and plants. We show that the plant circadian clock also incorporates the cytosolic signaling molecule cyclic adenosine diphosphate ribose (cADPR). cADPR modulates the circadian oscillator's transcriptional feedback loops and drives circadian oscillations of Ca^{2+} release. The effects of antagonists of cADPR signaling, manipulation of cADPR synthesis, and mathematical simulation of the interaction of cADPR with the circadian clock indicate that cADPR forms a feedback loop within the plant circadian clock.

Circadian clocks are adaptations to the daily rotation of the planet. In plants and cyanobacteria, benefits occur when the clock is resonant with the environment (*1*–*3*). This requires the oscillator to be robust yet flexible, which may explain the evolution of molecular clocks with multiple feedback loops (*4*–*6*). We tested the hypothesis that plant circadian oscillators also incorporate cytosolic signaling molecules because there are circadian rhythms in the

concentration of cytosolic free Ca^{2+} ($[Ca^{2+}]_{cyt}$) (*7*, *8*). We investigated the function within the plant circadian system of cyclic adenosine diphosphate ribose (cADPR), a cytosolic ligand that promotes the release of Ca^{2+} into the cytosol from internal stores through cation channels (*9*).

To identify potential interactions between plant circadian and Ca^{2+} signaling pathways, we examined the overlap between a circadian transcriptome and transcriptomes for known regulators of $[Ca^{2+}]_{cyt}$ (table S1) (*10*). We obtained a new near whole-genome transcriptome in constant light (LL) under conditions allowing circadian $[Ca^{2+}]_{cyt}$ oscillations (*10*, *11*). This was necessary because previous circadian transcript analyses used plants grown on 3% sucrose (*12*, *13*), which abolishes circadian $[Ca^{2+}]_{cyt}$ oscillations (*7*). On the basis of a threshold multiple measures–corrected probability of rhythmicity (pMMC) of 0.15, 2282 (12.08%) transcripts were circadian-regulated (spreadsheet S1 and fig. S1) (*12*, *14*).

A cADPR-regulated transcript set (*15*) had the most statistically significant overlap with our circadian transcriptome [(Fig. 1A and table S1) $P = 5.15 \times 10^{-52}$]. The overlap was significantly larger than the 93 transcripts expected for a chance overlap of two similarly sized datasets selected randomly from the *Arabidopsis* genome. We noted that 252 transcripts were both circadian- and cADPR-regulated (Fig. 1A and spreadsheet S2). There was a phase relation between circadian- and cADPR-regulation of transcript abundance: The majority of cADPR–up-regulated rhythmic transcripts reached peak abundance at zeitgeber time (ZT) ZT8 or ZT12, and the majority of cADPR-repressed rhythmic transcripts reached peak abundance between ZT20 and ZT4 (Fig. 1B).

Because a phase relation existed between circadian- and cADPR-regulated genes and the circadian-regulated evening element was significantly overrepresented in cADPR–up-regulated genes (spreadsheet S3), we reasoned that cADPR signaling might be circadian-regulated (*12*, *15*). We measured [cADPR] in extracts of aerial tissues of seedlings in LL (*10*). [cADPR] was circadian-regulated, because [cADPR] was significantly higher during subjective light (mean ± SEM, 0.27 ± 0.04 pmol · μg protein^{-1}) than subjective dark (0.16 ± 0.02 pmol · μg protein^{-1}) (Fig. 2, A and B, and fig. S2), [cADPR] variations persisted through the second and third days of LL and were eliminated in plants overexpressing *CIRCADIAN CLOCK ASSOCIATED1* (*CCA1*-ox) (Fig. 2A). *CCA1*-ox abolishes all known plant circadian rhythms (*2*, *16*).

We tested whether circadian [cADPR] variations cause circadian rhythms of $[Ca^{2+}]_{cyt}$. Under LL, we monitored $[Ca^{2+}]_{cyt}$ in seedlings treated every 3 hours with Ca^{2+} signaling antagonists (Fig. 2, C and D). Nicotinamide (10 mM) reduced the amplitude of the $[Ca^{2+}]_{cyt}$ oscillation, and 50 mM nicotinamide abolished the oscillation (Fig. 2C) (*10*). Nicotinamide is an antagonist of cADPR signaling that, at 50 mM, inhibits the synthesis of cADPR from NAD^+ by adenosine diphosphate ribosyl cyclase (ADPRc) (*17*). Circadian $[Ca^{2+}]_{cyt}$ oscillations were unaltered by $GdCl_3$, which inhibits extracellular Ca^{2+} influx (*18*) (Fig. 2D), and the phospholipase C (PLC) inhibitor U73122, which inhibits production of inositol 1,4,5-trisphosphate (IP_3) at 1 μM (*19*) (Fig. 2D). *Arabidopsis* ADPRc activity (*10*, *20*) was inhibited in vitro by 40 mM nicotinamide (fig. S3), which suggests that nicotinamide prevents cADPR synthesis in plants. Because 50 mM nicotinamide abolished circadian $[Ca^{2+}]_{cyt}$ oscillations, and circadian [cADPR] and $[Ca^{2+}]_{cyt}$ alterations had a similar phase, circadian cADPR oscillations are likely to drive circadian $[Ca^{2+}]_{cyt}$ rhythms.

Several genes encoding components of the circadian clock are cADPR-regulated (*15*). *GIGANTEA* (*GI*), *CRYPTOCHROME2* (*CRY2*), *GLYCINE-RICH BINDING PROTEIN7* (*GRP7*), *GRP8*, and *PSEUDO-RESPONSE REGULATOR5* (*PRR5*) and *PRR7* are cADPR–up-regulated, and *LATE ELONGATED HYPOCOTYL* (*LHY*) and *CCA1* are down-regulated. *TIMING OF CHLOROPHYLL A/B BINDING PROTEIN* (*TOC1*) is unaffected (spreadsheet S2) (*15*). To understand how circadian function might be affected by cADPR-induced changes in transcript abundance, we performed a simulation using a previously described mathematical model (*21*). In that model, 13 equations define an approximation for the *Arabidopsis* circadian oscillator. We controlled the parameters of this model to constrain *CCA1/LHY*, *GI*, and *TOC1* transcripts to adopt the fold-changes that are caused by cADPR in plants (figs. S4 and S5) (*10*, *15*). First, we constrained the parameters transiently, because increasing cADPR synthesis by inducing the *Aplysia ADPR cyclase* gene, fused to a β-estradiol–inducible promoter (*XVE:ADPRc*), causes transient alterations in clock transcripts although [cADPR] remains elevated (*15*). Depending on the parameters that were constrained, there was a short disruption to the modeled oscillator that sometimes caused phase changes, but the period remained 24 hours (Fig. 3A and fig. S5C). Next, we constrained the parameters continuously to evaluate the effects of continuous cADPR-induced alteration in clock transcripts. Depending on the parameters that were constrained, the circadian period often changed and remained altered throughout the simulation (Fig. 3B). Finally, we inverted the permanent constraint of the parameters to understand the possible effects of removal of cADPR-regulation of clock transcripts. Most of the parameters that did not lead to arrhythmia caused the simulations to run with a longer period (Fig. 3C). These simulated outcomes provided a framework with which to interpret the effects of cADPR on the plant circadian clock.

We experimentally tested how transient [cADPR]-induced alterations in circadian clock transcripts affect circadian behavior. We elevated [cADPR] in two independent lines by inducing the *XVE:ADPRc* transgene (*15*) with 100 μM β-estradiol. [cADPR] increased 13.5-fold (line 1) and 27-fold (line 2) relative to controls (fig. S6). The circadian period and phase of leaf position were unaltered when *XVE:ADPRc* was induced at ZT2 under LL (Fig. 4A and fig. S7, A, B, and G), or at two times during the final LD cycle before LL (fig. S7, C to G). Circadian $[Ca^{2+}]_{cyt}$ oscillations were unaltered by *XVE:ADPRc* induction (Fig. 4B). The invariance of circadian period may be explained by the simulated evidence that transient cADPR-induced alterations in oscillator transcripts do not alter circadian period. This invariance also reveals remarkable stability of the oscillator.

We investigated whether continuous [cADPR] synthesis alters circadian behavior. We overexpressed *Aplysia ADPRc* using the constitutive 35*S* promoter (*35S:ADPRc*) (*10*). This approximately doubled [cADPR] [0.38 ± 0.09 pmol · μg protein^{-1} (line 1); 0.45 ± 0.13 pmol · μg

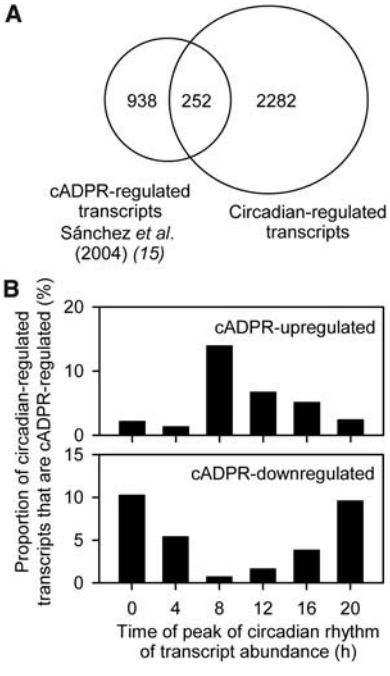

Fig. 1. Circadian- and cADPR-regulated transcripts overlap significantly. (**A**) The numbers of circadian- and cADPR-regulated transcripts (*15*), and the number common to both transcriptomes. (**B**) The proportion of circadian-regulated transcripts that were cADPR-regulated, binned according to the circadian peak of abundance.

[1]Department of Plant Sciences, University of Cambridge, Downing Street, Cambridge CB2 3EA, UK. [2]Department of Engineering, University of Cambridge, Trumpington Street, Cambridge CB2 1PZ, UK. [3]Department of Biology, University of York, York YO10 5YW, UK.

*Present address: School of Biosciences, Geoffrey Pope Building, University of Exeter EX4 4QD, UK.
†Present address: Institute for Plant Biology, Copenhagen University, Thorvaldsensvej 40, 1871 Frederiksberg, Denmark.
‡To whom correspondence should be addressed. E-mail: alex.webb@plantsci.cam.ac.uk

protein^{-1} (line 2), 0.23 ± 0.05 pmol · μg protein^{-1} (wild type); n = 5]. [cADPR] was not measured over a circadian time course because of poor *35S:ADPRc* plant growth, which was consistent with a lesion to stress and circadian signaling (*2*, *3*). The mean period of circadian rhythms in leaf position was unaltered in *35S:ADPRc* [P = 0.51 by two-sample t test (fig. S8, A and B)]. However, there was a broader period length distribution compared with the wild type when all replicates with all lines were considered, as indicated by both the spread and significantly different standard deviation [(Fig. 4C) Ws-2 wild type: SD = 0.71 hours, spread = 22.3 to 25.8 hours, n = 45; *35S:ADPRc*: SD = 0.96 hours, spread = 21.9 to 26.3 hours, n = 106; test of homogeneity of variances Levene statistic = 5.81, P = 0.017**]. ADPRc overexpression disturbed the sinusoidal circadian $[Ca^{2+}]_{cyt}$ oscillations (fig. S9) and increased the relative amplitude error (RAE) (*22*) of the oscillations [(Fig. 4D) wild-type RAE, 0.28 ± 0.02; line 1, 0.42 ± 0.03; line 2, 0.55 ± 0.06]. The greater RAE indicated a poorer Fourier fit to the data. Because $[Ca^{2+}]_{cyt}$ images were obtained from groups of 15 to 20 seedlings (*23*), the increased RAE of circadian $[Ca^{2+}]_{cyt}$ oscillations could reflect increased variability of the $[Ca^{2+}]_{cyt}$ oscillation period between individuals. The simulations suggested that oscillator period is affected by high [cADPR] (Fig. 3B). We found that *35S:ADPRc* affected oscillator period by increasing variability, which might be a consequence of differing levels of cADPR between seedlings and cells having different effects on period.

Finally, we investigated how continuously suppressed cADPR signaling affected the clock by treating seedlings with nicotinamide. The circadian period of rhythms of leaf position was significantly longer with 10 mM or 50 mM nicotinamide compared with water and osmotic controls. The period increase was nicotinamide concentration–dependent [(Fig. 4, E and F, and table S2) control period 23.6 ± 0.3 hours; 10 mM nicotinamide, 24.5 ± 0.3 hours, $P < 0.001$; 50 mM nicotinamide, 26.6 ± 0.4 hours, P = 0.002; comparisons by two-sample t tests]. Circadian rhythms of leaf position were unaltered by other chemical modifiers of Ca^{2+} signaling [$CaCl_2$, $GdCl_3$, $LaCl_3$, EGTA, or U73122 (table S2)]. At 50 mM, nicotinamide also lengthened circadian period of *CAB2:luciferase* luminescence [nicotinamide, 25.3 ± 0.4 hours; 50 mM mannitol, 26.6 ± 0.5 hours (Fig. 4G and fig. S10)], the

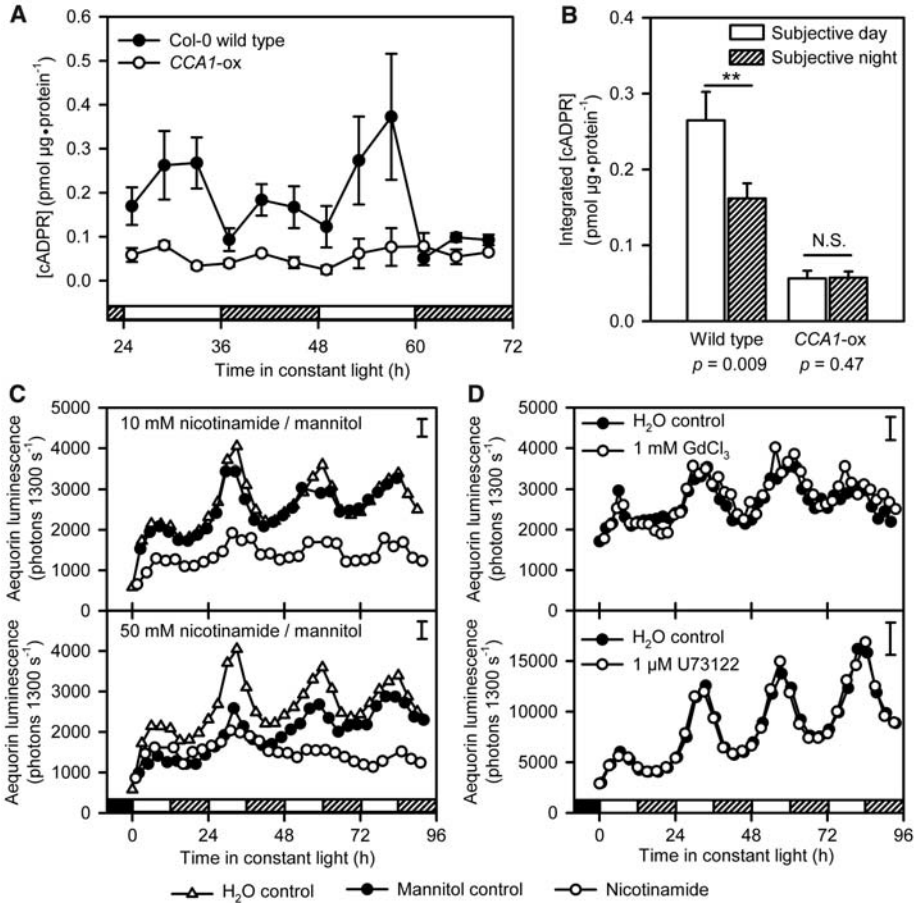

Fig. 2. [cADPR] oscillates with a circadian rhythm and a cADPR signaling antagonist inhibits circadian $[Ca^{2+}]_{cyt}$ oscillations. (**A**) [cADPR] during 48 hours of constant light in Col-0 wild type and arrhythmic *CCA1*-ox (n = 5; ± SEM). Seedlings were transferred to LL 24 hours before sampling. (**B**) Data from (A) binned according to subjective day and night, P values from two-sample t tests indicated. (**C** and **D**) Circadian $[Ca^{2+}]_{cyt}$ oscillations in 11-day-old seedlings dosed every 3 hours with (C) nicotinamide, mannitol (osmotic control), or water; (D) $GdCl_3$ and U73122. n = 12; greatest SEM for each panel at top right. On x axes are black bars, darkness; white bars, light, hatched bars, subjective dark under LL.

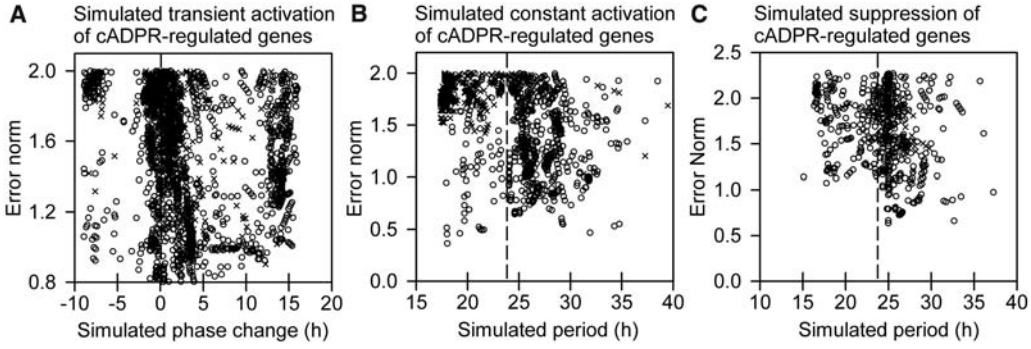

Fig. 3. Constraint of a mathematical model for the *Arabidopsis* circadian clock (*21*) to explore how cADPR-induced alterations in *CCA1/LHY*, *GI*, and *TOC1* transcript abundance alter clock function. (**A**) Transient constraint of model parameters to impose cADPR-induced alterations in clock transcript abundance caused variable phase changes that depended on parameters constrained. (**B** and **C**) For uniform parameter constraints analogous to continuous cADPR signaling (B) and repression (C), the period changed by a magnitude that depended on the parameters constrained. (A to C) Each point represents a different parameter pair that correctly constrained simulated transcripts when cADPR synthesis was induced between ZT20 to 6 or ZT20 to 24 (crosses) and ZT11 to 19 (circles); explained in fig. S5B. Broken lines indicate period or phase of unperturbed simulated oscillator. Phase and period calculated after simulated 480 hours in LL; arrhythmic simulations excluded from plots because perturbation of cADPR signals in plants (Fig. 4) did not cause arrhythmia.

period of *CAB2* transcript abundance [(Fig. 4H) 50 mM nicotinamide, 26.0 hours; H_2O control, 23.3 hours; 50 mM mannitol, 22.3 hours], and *CCA1*, *TOC1*, and *LHY* transcript abundance (Fig. 4H) (*10*). Inhibition of cADPR synthesis, therefore, lengthened the period of the clock and its outputs.

Our data demonstrate the existence of a feedback loop within the plant circadian clock that incorporates cADPR, because [cADPR] is regulated by the circadian oscillator and cADPR, in turn, regulates the abundance of clock gene transcripts. Circadian oscillations in [cADPR] also regulate circadian $[Ca^{2+}]_{cyt}$ oscillations. It has been suggested that diurnal variations in $[Ca^{2+}]_{cyt}$ are regulated by the Ca^{2+} sensor CAS through an IP_3-mediated system (*24*). Our data indicate that IP_3 does not contribute to the control of circadian $[Ca^{2+}]_{cyt}$ oscillations (Fig. 2D). The circadian feedback loop incorporating cADPR may interface the clock with exogenous stimuli that transiently elevate intracellular [cADPR] and $[Ca^{2+}]_{cyt}$ and so optimize the adaptive value of circadian control during unpredictable short-term environmental variations. We have established that cytosolic signaling molecules represent a hitherto unrecognized class of circadian clock components.

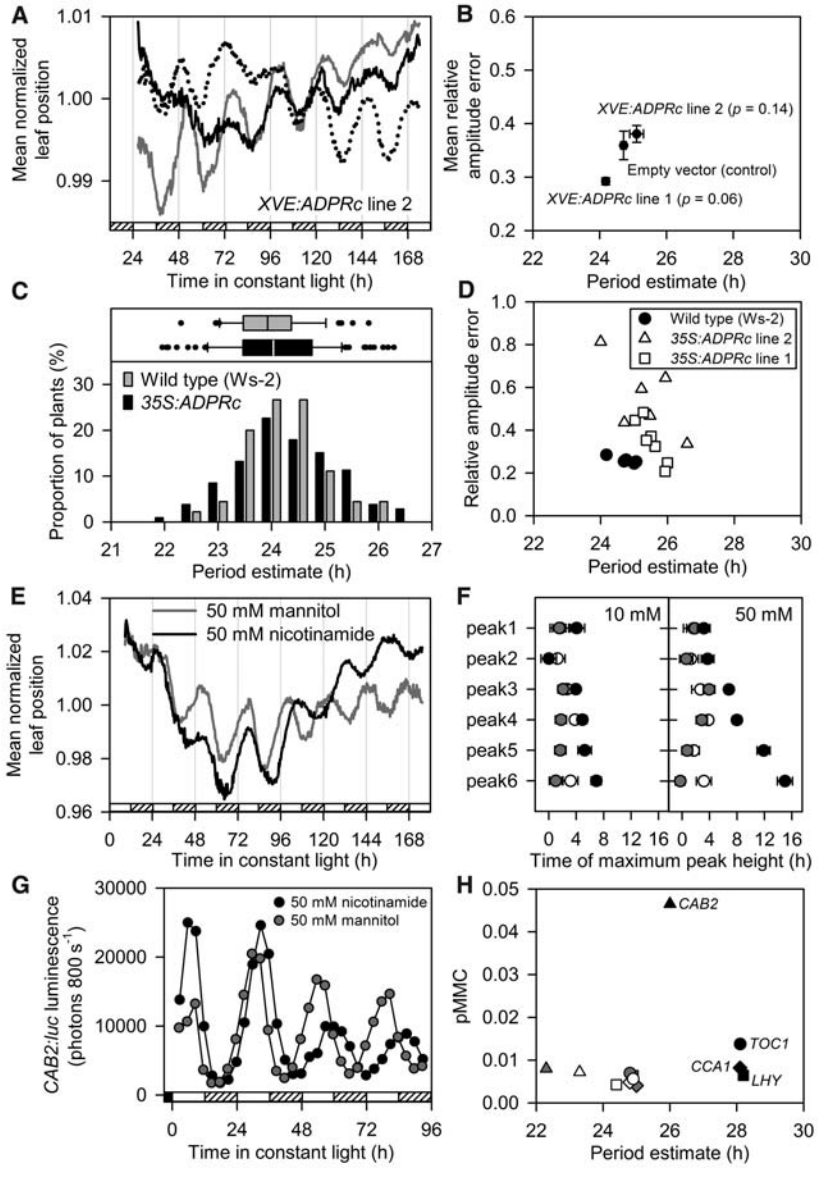

Fig. 4. The circadian clock and its outputs are altered by continuous disruption of cADPR signaling. (**A** and **B**) *XVE:ADPRc* induction at ZT2 on day 1 of LL, (A) circadian rhythm of leaf position (n = 30 to 32) and (B) analysis of circadian $[Ca^{2+}]_{cyt}$ oscillations; P values from two-sample t test comparisons of period to control are indicated and were not significant. Relative amplitude error quantifies the rhythmic robustness (0 is sine wave and 1 is poor Fourier fit; n = 4; mean ± SEM). In (A), black is 100 μM β-estradiol (XVE inducer), gray is empty vector control (P = 0.38 in two-sample t test period comparison with induced plants), broken line, 0.1% DMSO solvent control (P = 0.32). (**C** and **D**) In *35S:ADPRc*, (C) distribution of period lengths of circadian rhythms of leaf position for all replicates and both lines; (D) analysis of circadian $[Ca^{2+}]_{cyt}$ oscillations for *35S:ADPRc* line 1, line 2, and Ws-2 wild type. (**E**) Circadian rhythm of leaf position of seedlings treated at ZT2 with a single dose of 50 mM nicotinamide or 50 mM mannitol (n = 46). (**F**) Time of circadian peaks of leaf position in seedlings treated as for (E) (n = 5 to 26). (**G**) Circadian rhythm of *CAB2:luciferase* luminescence in seedlings dosed every 3 hours with 50 mM nicotinamide (mannitol control shown for clarity). (**H**) Circadian period of *CAB2* (triangles), *TOC1* (circles), *LHY* (squares), and *CCA1* (diamonds) transcript abundance in seedlings dosed every 3 hours with 50 mM nicotinamide. (E to H) Treatment designations: open is H_2O control; gray is mannitol control; black is nicotinamide. For comparability with (E and F), alterations in circadian rhythms of $[Ca^{2+}]_{cyt}$ and *CAB2* promoter activity after single doses of 50 mM nicotinamide are in fig. S10.

References and Notes

1. Y. Ouyang, C. R. Andersson, T. Kondo, S. S. Golden, C. H. Johnson, *Proc. Natl. Acad. Sci. U.S.A.* **95**, 8660 (1998).
2. A. N. Dodd *et al.*, *Science* **309**, 630 (2005).
3. R. M. Green, S. Tingay, Z. Y. Wang, E. M. Tobin, *Plant Physiol.* **129**, 576 (2002).
4. D. A. Rand, B. V. Shulgin, J. D. Salazar, A. J. Millar, *J. Theor. Biol.* **238**, 616 (2006).
5. S. Panda, J. B. Hogenesch, S. A. Kay, *Nature* **417**, 329 (2002).
6. D. Alabadí *et al.*, *Science* **293**, 880 (2001).
7. C. H. Johnson *et al.*, *Science* **269**, 1863 (1995).
8. M. Ikeda *et al.*, *Neuron* **38**, 253 (2003).
9. G. J. Allen, S. R. Muir, D. Sanders, *Science* **268**, 735 (1995).
10. Materials and methods are available on *Science* Online.
11. Microarray data deposited at ArrayExpress (www.ebi.ac.uk/arrayexpress/), accession E-TABM-331.
12. S. L. Harmer *et al.*, *Science* **290**, 2110 (2000).
13. K. D. Edwards *et al.*, *Plant Cell* **18**, 639 (2006).
14. M. Straume, *Methods Enzymol.* **383**, 149 (2004).
15. J. P. Sánchez, P. Duque, N. H. Chua, *Plant J.* **38**, 381 (2004).
16. Z. Y. Wang, E. M. Tobin, *Cell* **93**, 1207 (1998).
17. J. K. Sethi, R. M. Empson, A. Galione, *Biochem. J.* **319**, 613 (1996).
18. A. A. Véry, J. M. Davies, *Proc. Natl. Acad. Sci. U.S.A.* **97**, 9801 (2000).
19. I. Staxén *et al.*, *Proc. Natl. Acad. Sci. U.S.A.* **96**, 1779 (1999).
20. R. M. Graeff, T. F. Walseth, K. Fryxell, W. D. Branton, H. C. Lee, *J. Biol. Chem.* **269**, 30260 (1994).
21. J. C. Locke *et al.*, *Mol. Syst. Biol.* **1**, E9 (2005).
22. J. D. Plautz *et al.*, *J. Biol. Rhythms* **12**, 204 (1997).
23. J. Love, A. N. Dodd, A. A. R. Webb, *Plant Cell* **16**, 956 (2004).
24. R. H. Tang *et al.*, *Science* **315**, 1423 (2007).

25. The authors thank N.-H. Chua for inducible *XVE:ADPRc* lines; H. Okamoto, S. Takasawa, H.-C. Lee, and R. Graeff for *Aplysia ADPRc*; H.-C. Lee, R. Graeff, E. Zocchi, and S. Bruzzone for advice; B. Handley for programming assistance; and J. C. Gray, E. A. C. MacRobbie, and J. Carr for critical reading. Research funded by the U.K. Biotechnology and Biological Sciences Research Council (BBSRC), the Royal Society of London, the Broodbank Foundation Cambridge, the Gates Foundation, Corpus Christi College Cambridge, Coordenação de Aperfeiçoamento de Pessoal de Nível Superior (CAPES) Brazil, and the Danish Research Council.

Supporting Online Material

www.sciencemag.org/cgi/content/full/1146757/DC1
Materials and Methods
Figs. S1 to S10
Tables S1 to S2
References
Spreadsheets S1 to S3

20 June 2007; accepted 27 September 2007
Published online 15 November 2007;
10.1126/science.1146757
Include this information when citing this paper.

Microwave System for Electron Microscopy

The Leica EM AMW is a microwave system for electron microscopy that automatically dehydrates, infiltrates, and polymerizes specimens in resin. The system reduces the time to prepare samples to a matter of hours instead of days. Leica's automated, patented technology for tissue embedding allows results to be reproduced at any time and documented seamlessly. The combination of a microwave chamber and an automatic reagent changer minimizes the manual effort and the time from specimen dehydration to polymerization. The Leica EM AMW automatically guides the reagents into the microwave chamber that contains the specimens and brings the specimens into contact with the correct fluid for a defined time and defined temperature. The monomode microwave chamber focuses the energy on a defined area, resulting in a uniform microwave field and uniform action on specimen and reagent, without hot or cold points and without the need for additional water loads. The user can select either continuous or pulsed microwave power. An infrared sensor controls and monitors the temperature.

Leica For information 800-248-0123 www.leica-microsystems.com

Microliter Accessories

The nanoVette microliter accessory for DU 730 and DU 800 UV/Vis Spectrophotometers is suitable for DNA and protein applications. The cuvette-sized nanoVette accepts sample sizes as small as 0.7 µl and is offered with interchangeable 0.2 mm and 1 mm pathlength lids. Designed for precise fit in the Beckman Coulter spectrophotometers, the nanoVette can be loaded and cleaned without being removed from the instrument, saving time and maximizing throughput. The sample can also be recovered for future analysis. The DU 730 includes advanced tools for protein and nucleic acid analysis, including determination of dye incorporation percentage for microarrays and a set of DNA/protein calculation and conversion tools. The DU 800 adds an advanced interface and additional tools for molecular biology, proteomics, and enzyme kinetic studies. The nanoVette expands the application of both systems to include very low-volume samples.

Beckman Coulter For information 714-993-8955 www.beckmancoulter.com

DNA Sequencing Platform

The SOLiD System is a next-generation DNA sequencing platform designed to enable new ways of performing genetic analysis applications. The system achieves a raw base accuracy of greater than 99.94% due to two-based encoding, a mechanism that distinguishes random or systematic errors from true single nucleotide polymorphisms. The system combines scalable bead technology with mate-paired library preparation, which helps researchers cost-effectively identify specific genomic regions where structural variations are located. A study has shown that structural variation accounts for almost 74% of the variant DNA sequence in the human genome. Identifying the location of structural variation in genomes is expected to be crucial to understanding the role of genetic variation in health and disease.

Applied Biosystems For information +44 (0) 1494 816062 www.appliedbiosystems.com

Phosphatase Substrate Systems

The RedPhos Microwell Phosphatase Substrate System is a sensitive new colorimetric phosphatase for microwell assays that can detect less than 0.5 pg of phosphatase. The color produced is stable, linear over a wide dynamic range, and generates a strong red color that is easily read by eye. The RedPhos Membrane Phosphatase Substrate is suitable for immunoblotting and dot blot procedures. It produces a strong red reaction product with sensitivity in the low nanogram range, sharp band resolution, and a clear image. The color is linear over a wide dynamic range and resists fading when exposed to light.

KPL For information 301-948-7755 www.kpl.com

Peptide Cleavage Device

The P12 is a new accessory for the Activo-P11 peptide synthesizer that allows the system to be used on the lab bench while peptide-resin cleavage and side chain deprotection are undertaken in a nearby fume hood. The success of solid-phase peptide synthesis using 9-fluorenylmethoxycarbonyl (Fmoc) amino acids is often limited by deleterious side reactions that occur during trifluoroacetic acid (TFA) peptide-resin cleavage and side-chain deprotection. Most of these side reactions modify susceptible residues with TFA-liberated side-chain protecting groups and linkers. The use of scavengers to suppress these side reactions is well-established; however, common scavengers such as thioanisole are best not used in an open laboratory due to their noxious odor. To overcome this problem, the new P12 cleavage device has been designed to directly accept the easily removed disposable reactor from the Activo-P11 peptide synthesizer. In this way, the peptide synthesizer can be maintained in the open lab while cleavage and deprotection procedures can be performed simply, speedily, and safely on the P12 in the fume hood.

Activotec For information +44 1223 260008 www.activotec.com

Dispensing Pump

The Furon Precision Dispense Pump (DPD) makes use of cutting-edge technology to deliver extremely accurate doses of media with unprecedented repeatability. Patented PTFE rolling diaphragm technology coupled with precision stepper motor control enables precise dispensing of aggressive or ultra-pure media. Innovative zero-displacement-valve technology enables pulsation-free dispensing. In addition, a programmable suckback capability provides complete control over residual drops of liquid, ensuring recipe accuracy and maximizing chemical efficiency. The Furon PDP is driven by its own onboard microprocessor. It can be operated via its own graphical user interface or controlled remotely via a built-in RS-485 interface. All wetted surfaces are constructed from high-purity fluoropolymers to suit dispensing of ultra-pure chemicals used in the semiconductor, pharmaceutical, and medical industries.

Saint-Gobain Performance Plastics For information 800-833-5661. www.microelectronics.saint-gobain.com

Newly offered instrumentation, apparatus, and laboratory materials of interest to researchers in all disciplines in academic, industrial, and government organizations are featured in this space. Emphasis is given to purpose, chief characteristics, and availability of products and materials. Endorsement by *Science* or AAAS of any products or materials mentioned is not implied. Additional information may be obtained from the manufacturer or supplier.